Optimisation and validation of virtual physiological human lung models in asthma

Christos Nikolaou

IMPERIAL COLLEGE LONDON

FACULTY OF MEDICINE

NATIONAL HEART AND LUNG INSTITUTE

SECTION OF INFLAMMATION, REPAIR AND DEVELOPMENT

A thesis submitted for the degree of

Doctor of Philosophy

October 2025

Declaration of Originality

I declare that the work presented in this thesis was conducted by me unless otherwise stated or referenced. Where information has been obtained or used from others or other sources this has been appropriately referenced throughout the thesis.

Copyright statement

The copyright of this thesis rests with the author. Unless otherwise indicated, its contents are licensed under a Creative Commons Attribution-Non Commercial 4.0 International Licence (CC BY-NC).

Under this licence, you may copy and redistribute the material in any medium or format. You may also create and distribute modified versions of the work. This is on the condition that: you credit the author and do not use it, or any derivative works, for a commercial purpose.

When reusing or sharing this work, ensure you make the licence terms clear to others by naming the licence and linking to the licence text. Where a work has been adapted, you should indicate that the work has been changed and describe those changes.

Please seek permission from the copyright holder for uses of this work that are not included in this licence or permitted under UK Copyright Law.

Acknowledgements

First and foremost, I would like to express my gratitude to the primary supervisor of this PhD project, Professor Salman Siddiqui (National Heart and Lung Institute), and the secondary supervisor of this PhD project Dr Wenjia Bai (Department of Computing & Department of Brain Sciences) for their support and guidance throughout the project. Secondly, I would like to thank Dr Brody Foy (Department of Laboratory Medicine & Pathology, University of Washington) for their support in my early training and for providing me with the foundational knowledge that enabled this research. My gratitude extends to Professor Craig Galban and Dr Alexander Bell (Michigan Medicine) who have shared valuable data, which without the completion of this thesis would not have been possible. I am further grateful to Dr Carl Witfield (University of Manchester) who has provided me with insights into mathematical approaches for lung structure scaling and has also provided me with a mathematical scaling method, relevant to the methods of Chapter 2, and section 7.1. Finally, I would like to express my gratitude to Professor Grace Parraga, Sam Tcherner (Robarts Research Institute and Department of Medical Biophysics, Western University) and Dr Alexander Matheson (Cincinnatti Childrens Hospital) for sharing their knowledge and expertise on hyperpolarized ^{129}Xe MRI, whom without the completion of Chapter 4 of this thesis would not have been possible.

Publications arising from this thesis

Abstract

Nikolaou, C., Bai, W., Foy, B. H. & Siddiqui, S. Understanding the determinants of CO gas-transfer test through a computational lung model. *European Respiratory Journal* 62, (2023).

Abstract

Physiological tests assessing abnormal lung function due to ventilation (V) and perfusion (Q) mismatch, and ventilation heterogeneity (VH)–such as the CO gas transfer and forced oscillation techniques (FOT)–provide valuable but global measurements of whole-lung function. However, lung disease is spatially diverse. Advanced imaging techniques can capture this localised nature of lung disease, but are limited in their ability to simulate hypothetical, unseen scenarios that provide insight into structure-function relationships. This thesis addresses this challenge by presenting new personalised computational methods aimed at enabling more sensitive regional investigation of the determinants of VH and V/Q.

The project comprises three major components. The first focuses on optimising an established, imaging-informed FOT model by enhancing its patient-specificity. Regression models were trained with personalised imaging biomarkers to predict personalised viscoelastic lung tissue parameters obtained through an adaptive grid-search in a large cohort of asthmatic patients and healthy volunteers. The predicted parameters improved the correlation between simulated and measured FOT outputs, demonstrating that the regression models can improve simulation accuracy.

The second aim focuses on developing an imaging-informed mechanistic model spatially localising the CO gas-transfer test, and its validation by comparing hypothetical disease simulations with published data. The model, operating with demographic, physiologic, and lung-morphology-related inputs, comprised simplifying mathematical assumptions governing the test's physics and V/Q dynamics. The results demonstrate that the model can capture expected output responses to physiologic perturbations.

Finally, this thesis presents an approach to personalise blood-gas-barrier function by coupling the developed model with hyperpolarised xenon-129 magnetic resonance imaging (MRI). The results show potential to integrate spatially resolved Xe-MRI data to the model for regional blood-gas-barrier function parametrisation.

Taken together, these contributions establish a framework that enhances the (spatial) accuracy of the two patient-specific digital twins investigated in this work, which, when combined with complementary models, could inform real-time clinical decision-making.

Hypothesis, aims and thesis structure

Hypothesis

It is hypothesised that development and optimisation of physiological digital-twins – that spatially localise pulmonary function tests (PFTs) to evaluate ventilation heterogeneity (VH) and ventilation-perfusion (V/Q) matching – using patient-specific lung information extracted from biomedical imaging, will enable more sensitive regional investigation of the determinants of VH and V/Q in respiratory disease than conventional PFTs.

Aim 1: To examine if prediction of patient-specific constant-phase model (CPM) parameters using imaging biomarkers would increase concordance between forced oscillation technique (FOT) simulations and measurements in ATLANTIS (the Assessment of Small Airways Involvement in Asthma) (Postma *et al.*, 2019; Kraft *et al.*, 2022).

Objectives

1: Participant selection (ATLANTIS) and quality-control of centrelines extracted from CT scans.

2: Patient-specific identification of the CPM viscoelastic parameters G (tissue damping) and H (tissue elastance) (by minimising error between simulations and measurements)

3: Clinical and physiologic validation of G and H.

4: Computed Tomography (CT) biomarkers selection to train regression models for the prediction of G and H.

5: Simulation of the FOT using predicted G and H values and comparison with measured FOT values to assess whether optimisation has been achieved.

Aim 2: To develop a spatial digital-twin of the CO gas-transfer test and validate it.

Objectives

1: Simplifying mathematical assumptions selection, best describing the test's physics and physiological effects on outputs.

2: CO gas-transfer simulation in hypothetical disease by application of changes to physiologic inputs according to literature and simulation of outputs' dependence on Va.

3: Validation by comparison of results obtained from Objective 2 with literature.

Aim 3: To improve personalisation of the CO gas-transfer digital-twin through its coupling with Xenon-129 magnetic resonance imaging (MRI) gas exchange efficiency analogues.

Objectives

1: Mathematical equation derivation considering key ^{129}Xe MRI red blood cell (RBC) and blood-gas barrier outputs.

2: CO gas-transfer simulation in 10 patients with asthma and 5 healthy individuals using ^{129}Xe MRI ventilation defect percent (VDP), RBC and barrier outputs.

3: Comparison of results from Objective 2 with measured values.

Thesis Structure

Chapter 1 - Introduction

The thesis begins with a broad introduction to the field of study, namely the lungs as an oxygen delivery system through their main function which is gas-exchange and the challenges we are faced with in understanding this function better in-silico through computational modelling. This chapter dives into the challenges and opportunities of early diagnosis and early intervention to prevent organ damage in respiratory disease and provides a comprehensive overview of the physiology of the respiratory system. Following an introduction to the physiology of the pulmonary system, this chapter offers an overview of the assessment of key respiratory functions through pulmonary function testing techniques, imaging techniques and computational modelling techniques. The chapter then provides a historical overview of the digital twins' concept, the recent advancements of digital twins in chronic lung diseases as well as the challenges the deployment of this concept on a large scale is faced with. The chapter finally focuses on asthma, providing an introduction to the disease itself, which the current thesis is focuses on, and outlines the recent applications of computational modelling in asthma.

Chapter 2 - Forced Oscillation Technique - model optimisation

Chapter 2 focuses on the analysis implemented relevant to aim 1 of the project which is the examination of whether the prediction of patient-specific CPM parameters using imaging biomarkers would increase concordance between FOT simulations and measurements. The chapter starts with the rational for why the study was implemented. The rationale covers the importance of the FOT test in clinic and asthma as well as the derivation of the imaging biomarkers which are used in the study. The rationale is followed by a subsection describing in detail materials and methods used in the study. These constitute of the patients' and healthy volunteers' data as well as the statistical methods and mathematical models used. The results of the study are included in the following subsection which is then followed by a discussion and summary sections.

Chapter 3 - V/Q model development

The chapter starts with the rationale of why the study was implemented. This study is relevant to aim 3 of the project which is the development and validation of a spatial digital twin of the CO gas-transfer test. The rationale includes a background on the importance of the test in clinical practice and asthma as well as the physics underlying the test and the choice of hypothetical diseases for its validation. A materials and methods subsection follows, which describes the development of the model including the physics and mathematical assumptions used in its development as well as how physiological information was personalised within the model with global lung function initiative's (GLI) reference equations and finally how the validation was implemented. The results are then reported and are followed by a discussion and summary sections.

Chapter 4 - V/Q model coupling with hyperpolarised Xe^{129} MRI

This chapter outlines the analysis implemented relevant to aim 3 of this project which is the improvement of personalisation of the CO gas-transfer digital twin through its coupling with hyperpolarised Xenon-129 MRI gas exchange efficiency analogues. The chapter starts with a rationale of why the study was implemented which includes a background on the hyperpolarised Xenon imaging as well as the function of the blood-gas barrier and how this is monitored clinically. A materials and methods subsection follows, which describes the clinical characteristics of the participants included in the validation study as well as any adaptations implemented on the model from the methods of chapter 3. The results are reported in a subsequent separate subsection, followed by a discussion and summary subsections.

Chapter 5 - Conclusion

The thesis concludes with a chapter outlining the clinical importance of the findings of this study as well as future research recommendations.

Chapter 6 - References

Chapter 7 - Appendices - Code

This chapter includes appendices of the MATLAB code used to implement various analyses across the thesis including the FOT model, scaling of the complete conducting zone airway structures, and V/Q model.

Chapter 8 - Appendices - Permissions

This chapter is an appendix of the permissions requested for the use of figures from other literature sources.

Table of Contents

Declaration of Originality 3

Publications arising from this thesis 6

Abstract 6

Abstract 7

Hypothesis, aims and thesis structure 9

Hypothesis 9

Aim 1 9

Objectives 9

Aim 2 9

Objectives 9

Aim 3: 10

Objectives 10

Thesis Structure 11

Chapter 1 - Introduction 11

Chapter 2 - Forced Oscillation Technique - model optimisation 11

Chapter 3 - V/Q model development 12

Chapter 4 - V/Q model coupling with hyperpolarised Xe^{129} MRI 12

Chapter 5 - Conclusion 12

Chapter 6 - References 12

Chapter 7 - Appendices - Code 13

Chapter 8 - Appendices - Permissions 13

Table of Figures 20

List of Tables 24

Nomenclature 26

1. Introduction 33

1.1 Respiratory disease 34

1.2 Respiratory system physiology 35
1.2.1 Anatomy of the pulmonary system 35
1.3 Pulmonary Function Testing – Current practices 39
1.3.1 Spirometry 39
1.3.2 Multiple Breath Washout 41
1.3.3 Lung Impedance 42
1.3.4 Ventilation (V) and Perfusion (Q) matching 46
1.3.5 Blood-gas barrier function 48
1.3.6 Questionnaires 50
1.3.7 Differential Cell Counts 52
1.4 Spatial tests and medical imaging 53
1.5 Mathematical modelling of pulmonary function 55
1.5.1 Digital Twins in Healthcare 56
1.6 Application of modelling in Asthma 62
2. Forced Oscillation Technique – model optimisation 65
2.1 Rationale 65
2.2 Materials and methods 66
2.2.1 Data Collection 66
2.2.2 Scaling of lung structures 68
2.2.3 Clinical Characteristics and Structure Morphology 73
2.2.4 Imaging biomarkers 80
2.2.5 Mathematical assumptions for the FOT model 81
2.2.5 Simulation of the FOT in study cohort 83
2.2.6 Tissue Parameter Identification through grid-search 83
2.2.6 Validation of grid-search-obtained G and H 85
2.2.7 Assessment of markers in across asthma severity 85
2.2.8 Prediction of G and H using imaging biomarkers 85
2.2.9 Validation of predicted G and H 87

2.3 Results ... 88
2.3.1 Grid-search for personalised G & H identification ... 88
2.3.2 Prediction of G & H using imaging biomarkers ... 96
2.3.3 Summary of results ... 109
2.4 Discussion ... 112
2.4.1 Grid search ... 113
2.4.2 Imaging Biomarkers and morphometric markers ... 116
2.4.3 Prediction of G and H ... 117
2.5 Summary ... 119
3. V/Q model Development ... 122
3.1 Rationale ... 122
3.1.1 Single-breath CO gas-transfer test in clinical practice ... 123
3.2 Materials and Methods ... 126
3.2.1 Mathematical assumptions for V/Q model development ... 127
3.2.2 Personalisation of structural lung information ... 134
3.2.3 Simulations of hypothetical disease ... 135
3.2.4 Validation with healthy behaviour in Va reduction ... 136
3.2.5 Validation with structural alterations in disease ... 136
3.3 Results ... 138
3.3.1 Healthy behaviour in alveolar volume reduction ... 138
3.3.2 Sensitivity to a blend of structural alterations in disease ... 140
3.3.4 Results expressed relative to GLI healthy reference values ... 149
3.4 Discussion ... 154
3.5 Summary ... 158
4. V/Q model, hyperpolarised Xe^{129} MRI coupling ... 160
4.1 Rationale ... 160
4.1.1 Hyperpolarised Xenon 129 and Blood-gas barrier ... 160
4.2 Materials and methods ... 161

4.2.1 Data Collection 162
4.2.2 Coupling of V/Q model with Xenon 129 MRI 163
4.2.3 Scaling of permeation analogue RBC:barrier ratio 163
4.2.4 Simulations with patient and healthy volunteer data 164
4.3 Results 165
4.3.1 Simulations in Asthma and Health 165
4.4 Discussion 168
4.5 Summary 169
5. Conclusion 172
5.1 Clinical Importance 173
5.2 Future work and recommendations 174
5.2.1 Impedance Model 174
5.2.2 V/Q Model 176
6. References 179
7. Appendices - Code 209
7.1 Lambert's Scaling MATLAB code 209
7.2 FOT Code 210
7.3 MATLAB Function of V/Q Digital Twin 213
7.4 MATLAB code for hypothetical disease simulations 216
7.5 MATLAB code for Figure 20 227
8. Appendices - Permissions 230

Table of Figures

Figure 1– Anatomy of the pulmonary system. 36

Figure 2– Airway tree schematic of the various zones across Weibel generations of bifurcations. 37

Figure 3 – Illustration of ^{129}Xe Magnetic resonance spectrum graph 50

Figure 4 – ATLANTIS Consort Diagram. 67

Figure 5 – Illustration of lung volumes resulting from spirometry. 70

Figure 6 – Overview of the FOT Mathematical model and the full conducting zone airway lung structures 79

Figure 7 – Personalised viscoelastic CPM parameter identification through grid-search for FOT model optimisation 84

Figure 8 – FOT outputs R_5, R_{20}, R_5-R_{20}, X_5, and AX simulated with personalised viscoelastic CPM parameters G and H post grid-search, against their in-clinic measured corresponding values 89

Figure 9 – Personalised grid-search-obtained Tissue Damping (G) separation across (A) xPFavg or ΔHU^{AP} quartiles – which represents lung spatial deformation gradient in the anterior-posterior axis and (B) asthma severity groups. 90

Figure 10 – Spearman correlation coefficients dendrogram of clinical characteristics 91

Figure 11 – Spearman correlation coefficients heatmap of clinical characteristics and viscoelastic CPM parameters (top 3 rows and first 3 columns from the right) 92

Figure 12 – Spearman correlation coefficients dendrogram of imaging biomarkers 95

Figure 13 – Spearman correlation coefficients heatmap and viscoelastic CPM parameters (top 3 rows and first 3 columns from the right) 96

Figure 14 - FOT measurements compared to simulations obtained with predicted Tissue Damping (G) and Elastance (H) 100

Figure 15 – Separation of predicted (A) Tissue Damping, G and (B) Elastance, H across quartiles of xPFavg or ΔHU^{AP} quartiles – which represents lung spatial deformation gradient in the anterior-posterior axis 101

Figure 16 - Separation of predicted (A) Tissue Damping, G and (B) Hysteresivity, η across quartiles of zPFavg or ΔHU^{IS} quartiles – which represents lung spatial deformation gradient in the inferior-superior axis 102

Figure 17 – Spearman correlation coefficients heatmap of clinical characteristics and predicted viscoelastic CPM parameters (top 3 rows and 3 first columns from the right) 103

Figure 18 – Spearman correlation coefficients heatmap of imaging biomarkers and predicted viscoelastic CPM parameters (top 3 rows and 3 first columns from the right of heatmap) 109

Figure 19 – V/Q Model Overview 134

Figure 20 – Validation of the Digital Twin in reduction of alveolar volume. ... 139

Figure 21 - Comparison of reported real-world test outputs (blue) with digital-twin-simulated outputs as a percentage of a healthy baseline simulation (black) following application of expected physiologic changes for 4 disease cases. 141

Figure 22 - Visualisation of the model's sensitivity to input alterations for ILD (A) and PH (B). 142

Figure 23 - Visualisation of the model's sensitivity to input alterations for Right Lung (RL) Pneumonectomy (A) and Asthma (B). 143

Figure 24 – 2D visualisation of the model's sensitivity to alterations of 2 inputs simultaneously for Interstitial Lung Disease (ILD). 145

Figure 25 – 2D visualisation of the model's sensitivity to alterations of 2 inputs simultaneously for Pulmonary Hypertension (PH). 146

Figure 26 – 2D visualisation of the model's sensitivity to alterations of 2 inputs simultaneously for Right Lung Pneumonectomy. 147

Figure 27 – 2D visualisation of the model's sensitivity to alterations of 2 inputs simultaneously for Asthma. 148

Figure 28 – Results of simulated disease cases as compared to their GLI predicted DLCO and KCO. 149

Figure 29 – PAH simulation of DLCO and KCO % predicted 151

Figure 30 – ILD simulation of DLCO and KCO % predicted 151

Figure 31 – Asthma simulation of DLCO and KCO % predicted 152

Figure 32 – Pneumonectomy simulation of DLCO and KCO % predicted 153

Figure 33 – Schematic of proposed use of the V/Q model in a clinical setting . 157

Figure 34 – Box plots of DLCO and KCO simulation results in asthma (n=10) and health (n=5). 166

Figure 35 – Correlation plots of simulated outputs against measured DLCO and KCO in asthma (n=10) and health (n=5) using hyperpolarised Xenon^{129} MRI gas exchange analogues. 167

List of Tables

Table 1 - Clinical Characteristics of individuals included in the study 74

Table 2 - Morphometric properties calculated from bifurcations of the lung structures 76

Table 3 - Description of morphometric markers – For each individual, these markers represent the mean value obtained by averaging measurements across the full conducting airway tree. 77

Table 4 –Imaging Biomarkers and their description 80

Table 5 - Spearman correlation coefficients of spirometry compared to CPM parameters. 95

Table 6 – Comparison of statistically significant imaging biomarkers and morphometric markers across asthma severity groups 97

Table 7 - Spearman correlation coefficients of spirometry compared to predicted CPM parameters. 108

Table 8 - Comparison of grid-search obtained and predicted CPM parameters across asthma severity groups 111

Table 9 - Investigative physiologic input data. Input Alterations for 4 hypothetical disease cases and simulated DLCO and KCO results. 137

Table 10 – Participant Demographics for V/Q model validation with hyperpolarised ^{129}Xe data 162

Nomenclature

Acronyms

ACM	Alveolar-capillary membrane
ACQ-6	Asthma control questionnaire (6 questions)
ACT	Asthma control test
AHR	Airway hyper-responsiveness
ALL	Alveolar lining layer
ANOVA	One-way analysis of variance
ARTP	Association of respiratory technicians and physiologists
ATLANTIS	Assessment of small airways involvement in asthma
ATS	American thoracic society
AUC	Area under the receiver operating characteristic curve
BGB	Blood-gas barrier
BHT	Breath-hold time
BMI	Body-mass index
BTPS	Body temperature (i.e., 37°C), ambient pressure, saturated with water vapour
BTS	British thoracic society
CBC	Complete blood count
CFD	Computational fluid dynamics
COPD	Chronic obstructive pulmonary disease
CPM	Constant-phase model

CRD	Chronic respiratory disease
CT	Computed tomography
CXR	Chest radiography
DT	Digital twin
ERS	European Respiratory Society
EuroQol	Health-related quality of life questionnaire
FOT	Forced oscillation technique
FRC	Functional residual capacity
GINA	Global initiative for asthma
GLI	Global lung function initiative
HAA	High attenuation areas
HPV	Hypoxic pulmonary vasoconstriction
HRCT	High-resolution computed tomography
ICS	Inhaled corticosteroids
ILD	Interstitial lung disease
IOS	Impulse oscillometry
IPF	Idiopathic pulmonary fibrosis
IQR	Interquartile range
LLL	Left-lower lobe
LUL	Left-upper lobe
MATLAB	Matrix Laboratory – Software by Mathworks
MBW	Multiple-breath washout
MDCT	Multi-detector computed tomography
MIGET	Multiple inert gas elimination technique

MRI	Magnetic resonance imaging
Ns	Not significant
OCT	Optical coherence tomography
PD	Parenchymal disease
PFT	Pulmonary function test
PH	Pulmonary hypertension
PPM	Parts per million
Q	Perfusion
qCT	Quantitative computer tomography
RBC	Red blood cell
RLL	Right-lower lobe
RML	Right-middle lobe
RMSE	Root mean squared error
ROI	Region of interest (e.g. whole lung, left/right lung, lobe)
RUL	Right-upper lobe
RV	Residual volume
SA	Surface area
SAA	Stratified axial analysis
SAD	Small airways disease
SPECT	Single photon emission computed tomography
STPD	Standard temperature (0°C) and pressure (1 atmosphere – 101.325 kPa, 760 mmHg)
TLC	Total lung capacity
V	Ventilation

Va	Alveolar volume
VDP	Ventilation defect percent
VH	Ventilation heterogeneity
VOI	Volume of interest
VPH	Virtual physiological human
V/Q	Ventilation / Perfusion
YACTA	Yet another computed tomography analyser

Symbols

°C	Degrees Celsius
CO	Carbon monoxide
D	Diffusion rate
dt	Time increment
$DLCO_h$	Reference DLCO for a healthy subject
E_{CO}	Existing amount of carbon monoxide in the compartment
G	Constant-phase model tissue damping
H	Constant-phase model tissue elastance
h	Length of a cylinder
Hb	Haemoglobin
He	Helium
L/D	Dimensionless ratio of length/diameter of an airway branch
N_{CO}	New amount of carbon monoxide in the compartment
P_b	Alveolar gas pressure

P_{blood}	Partial pressure of blood – 0 mmHg
P_{acin}	Alveolar CO partial pressure of compartment at 37 °C – 713 mmHg
P_C	Compartmental capillary blood volume % contribution to the total (%)
r	Radius
V_C	Capillary blood volume
V_{CS}	Total capillary blood volume of a subject
V_{CH}	Healthy capillary blood volume of a two-lung structure
Vd	Anatomical dead Space
VDV	Ventilation defect volume / unventilated volume
VT	Tidal volume
VV	Ventilated volume
Xe	Xenon
ΔHU	Change in Hounsfield units
η	Hysteresivity – Ratio of G/H
θ	Angle
μ	Mean/average
ρ	Spearman correlation coefficient
σ	Standard deviation
τ	Thickness
φ	Angle between the plane made by a parent and sibling airway branch and the plane made by their child airway branches

Test indices

AX	Area of reactance (FOT/IOS)
DLCO	Diffusing capacity of the lungs for carbon monoxide
FEV_1	Forced expiratory volume in 1 second (spirometry)
FVC	Forced vital capacity (spirometry)
FEF	Forced expiratory flow (spirometry)
FeNO	Fractional exhaled nitric oxide
IVC	Inspiratory vital capacity
KCO	Carbon monoxide transfer coefficient
LCI	Lung clearance index (Multiple-breath washout)
PEF	Peak expiratory flow
R_5	Resistance at 5Hz (FOT/IOS)
R_{20}	Resistance at 20Hz (FOT/IOS)
S_{acin}	Washout acinar zone slope (Multiple-breath washout)
S_{cond}	Washout conducting zone slope (Multiple-breath washout)
VC	Vital capacity
X_5	Reactance at 5Hz (FOT/IOS)

1. Introduction

The human lungs' functional ability to exchange gas is determined largely by their structural design. Their design is a result of bioengineering optimisation, serving their gas exchange function well and efficiently (Weibel, 2009). The structural and functional complexities of the lungs have evolved to meet a group of unique challenges such as the efficient delivery of inhaled air to all lung units inside a limited thoracic space, to construct of a large surface area for gas exchange that is connected with a blood-gas barrier membrane of minimal thickness and a microscopic vasculature/capillary network accommodating cardiac output while enduring mechanical stresses varying in magnitude from exercise to resting conditions (Hsia, Hyde and Weibel, 2016). Linking the lung's complex structure to its function is the foundation of medical diagnosis and supports our understanding of how this organ works. Due to the lung's extreme complexity and inaccessible gas-exchange tissue and small airways, understanding this link remains a major challenge (Tawhai and Bates, 2015). A critical role in addressing this challenge is played by computational models which allow the integration of the large amount of information we possess about the lungs into a framework which could enable the prediction of the organ's response to therapy, behaviour, and interaction with delivery devices (Tawhai and Bates, 2015). Computational modelling provides a platform for integration of structure-function data measured at various scales, imaging data, and respiratory mechanics to simulate, understand and predict dynamics of the lungs in health and disease (Neelakantan *et al.*, 2022). Furthermore, the integration of in silico experimental modelling with biological data provides the potential for development of "digital twins" or virtual human lung models which hold promise for discovering of new therapeutic strategies and enhancing our understanding of disease (Lam *et al.*, 2025). The growing burden and prevalence of respiratory disease emphasizes the urgent need for advanced predictive modelling tools (Lam *et al.*, 2025). An important challenge in the development of such modelling tools is our limited understanding of underlying biological pathways and their mechanisms inside the lungs. The iterative process of modelling the pulmonary function and informing in silico models with new discoveries as new and advanced technologies emerge,

will lead to a virtual lung capable of simulating impacts of structural perturbations on the lungs' function.

1.1 Respiratory disease

Chronic respiratory diseases (CRDs) affected around half a billion people globally and were the third leading cause of mortality responsible for four million deaths in 2019 (Momtazmanesh *et al.*, 2023). More specifically, asthma affects around 300 million people worldwide (Porsbjerg *et al.*, 2023) while chronic obstructive pulmonary disease (COPD) around 200 million people. Lung diseases obstructive in nature, such as COPD and asthma, tend to stay undiagnosed until the occurrence of at least moderate disease severity (Mapel *et al.*, 2011; Usmani *et al.*, 2021). Most therapies therefore, target changes in the physiology and their associated symptoms (occurring as a result of chronic lung disease), by reducing inflammation and improving smooth muscle tone (Mapel *et al.*, 2011; Usmani *et al.*, 2021). There has been limited success in efforts for development of therapies aimed to reverse pathogenesis and stop the progression of long-term lung disease, indicating that existing therapies address insufficiently the mechanisms underlying obstructive lung disease (Tashkin *et al.*, 2008; Covar *et al.*, 2012; Vestbo *et al.*, 2016; Usmani *et al.*, 2021). This may be due to the lack of measurable outcomes (endpoints), able to measure changes in the small airways that are not detectable by the usual clinical tests (subclinical), and due to inadequate understanding of the pathophysiology of the early stages of disease (Mannino, 2015; Usmani *et al.*, 2021). Examination of early changes in obstructive lung disease pathology showed significant dysfunction of the small airways before any apparent airway obstruction was detectable by usual spirometry techniques (Hogg, Macklem and Thurlbeck, 1968; Crisafulli *et al.*, 2017; Deepak *et al.*, 2017; Koo *et al.*, 2018; Usmani *et al.*, 2021). It should therefore be possible, by identifying new endpoints for measurement of subclinical changes, and enhancing our understanding of small airways dysfunction in early disease and early disease progression, to predict and measure with enhanced sensitivity, disease progression in mildly symptomatic or asymptomatic obstructive lung disease. Earlier diagnosis of respiratory disease, brings

opportunities for earlier treatment and higher chances of slowing progression of disease (Usmani *et al.*, 2021). Earlier diagnosis also brings higher potential for physiological recovery before small airways damage becomes irreversible (Usmani *et al.*, 2021). Patients with diseases such as interstitial lung disease (ILD) are faced with significant diagnostic delay (Spagnolo *et al.*, 2021). Early diagnosis may improve outcomes as evidence is emerging in idiopathic pulmonary fibrosis (IPF) (Lamas *et al.*, 2011) that delayed access to care provision is linked to a higher mortality rate and earlier care provision is linked to preserved lung function, and longer time to death (Brereton *et al.*, 2020). In COPD and asthma, clinical care provided to people, previously undiagnosed, was associated with health benefit (Aaron *et al.*, 2024) indicating the importance of early diagnosis. The small airways' (≤ 2mm in diameter) involvement in COPD and asthma pathogenesis is increasingly recognised and early detection of their function is vital for disease management (Arshad *et al.*, 2020). Early recognition of the small airways' involvement in COPD and asthma coupled with timely management could lessen long-term illness in these conditions (Deepak *et al.*, 2017).

1.2 Respiratory system physiology

To facilitate understanding of the research aims and the challenges in respiratory disease, this section provides a summary of the physiology and the anatomy of the pulmonary system at a micro and macro scales. Information about the physiology and anatomy of the respiratory system was sourced from (Lumb and Thomas, 2021c) unless otherwise stated.

1.2.1 Anatomy of the pulmonary system

The human respiratory system consists of two lungs; each separated into lobes by fissures as shown in **Figure 1**. The right lung is composed of three lobes, the superior or upper lobe (RUL), the middle lobe (RML) and the inferior or lower lobe (RLL), while the left lung is only composed of two lobes, the superior or upper lobe (LUL) and the inferior or lower lobe (LLL). Breathing occurs through either the mouth or nose, with nasal breathing being the norm offering two significant advantages over mouth breathing – better humidification of inhaled gas and filtration of particulate matter. These two air passages converge in the pharynx, where

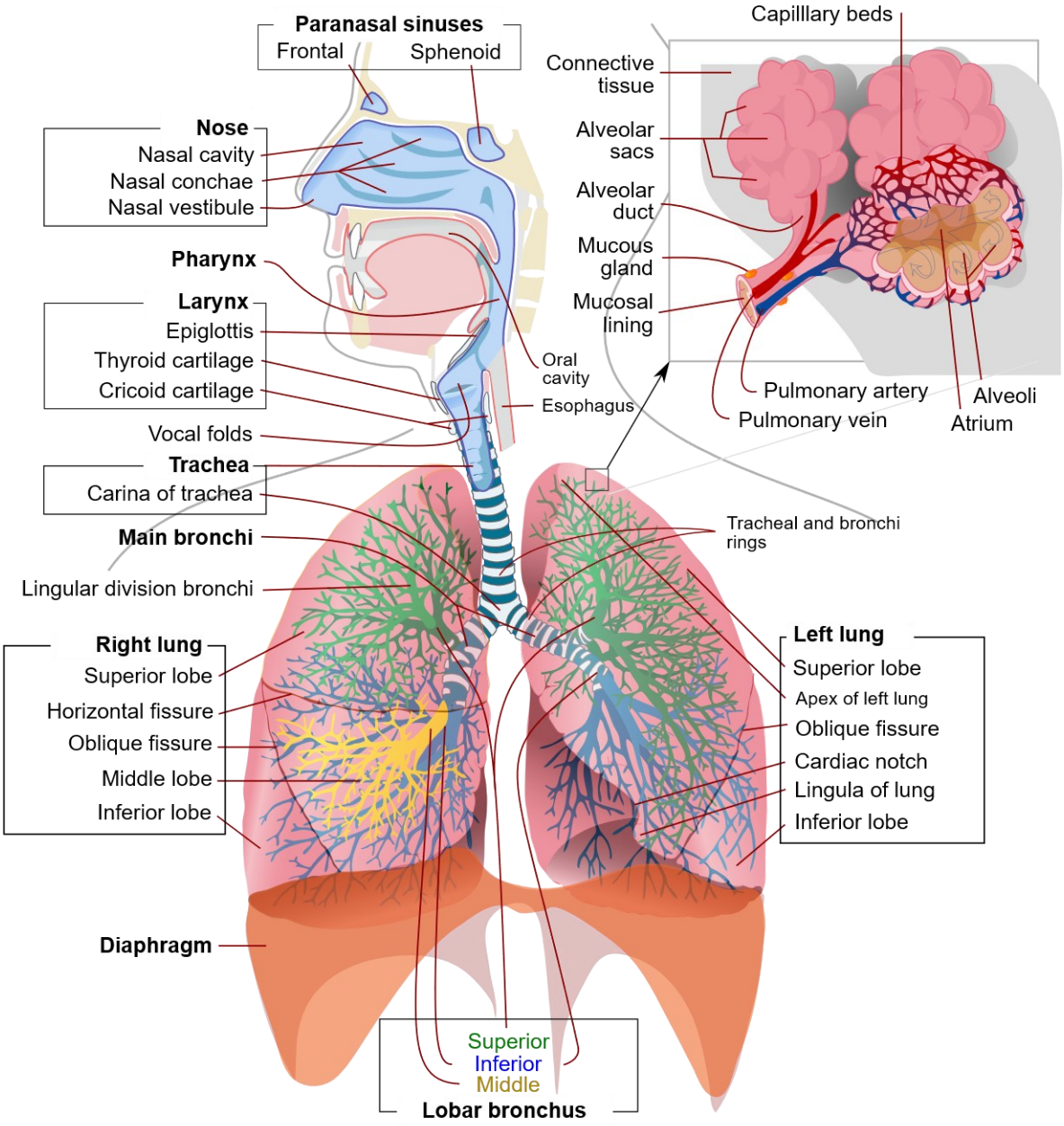


Figure 1– Anatomy of the pulmonary system.

This image was sourced from the website below: https://commons.wikimedia.org/wiki/File:Respiratory_system_complete_en.svg, under creative commons license CCo 1.0: https://creativecommons.org/publicdomain/zero/1.0/. Text available under creative commons license CC BY-SA 4.0: https://creativecommons.org/licenses/by-sa/4.0/.

air flows through to eventually reach the zeroth (Weibel) generation of bifurcations (Weibel and Gomez, 1962) of the tracheobronchial tree – the Trachea, which is followed by the first generation of bifurcations – the two main bronchi as shown in **Figure 1** and **Figure 2**.

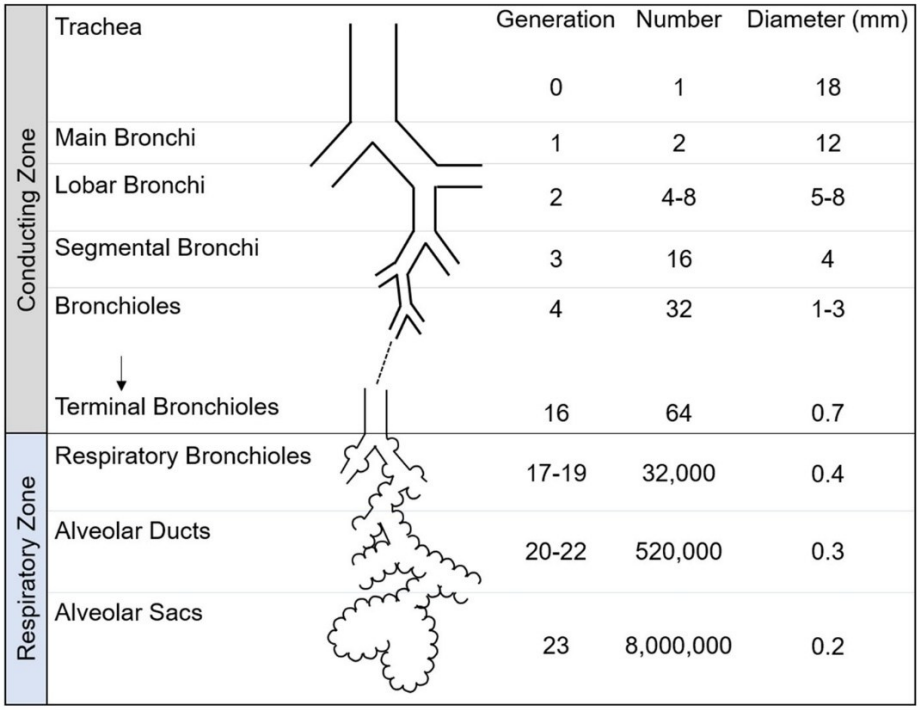


Figure 2– Airway tree schematic of the various zones across Weibel generations of bifurcations.

The figure illustrates the Weibel generations of bifurcations of the human airways and the zones that each set of generations corresponds to. The expected number of branches (bronchi, bronchioles) and alveoli (ducts, sacs) that is included in each generation of bifurcations can be seen in the column "Number". The mean diameter of the branches (bronchi, bronchioles) and alveoli (ducts, sacs) can be seen on the right of the figure for each generation of bifurcations in millimetres. Image reused from (Hofmann et al., 2024), https://www.frontiersin.org/journals/medicine/articles/10.3389/fmed.2024.1285361/full, (Author: Joseph J. Hofmann), under creative commons license CC BY 4.0: https://creativecommons.org/licenses/by/4.0/. Permission to reuse image and table was also obtained from Elsevier, Chapter 1 - Functional Anatomy of the Respiratory Tract, Nunn's Applied Respiratory Physiology (Eighth Edition) (Author: Andrew B Lumb).

Weibel's approach for numbering successive generations of passages, remains the most widely accepted and most useful. This is a model of "regular dichotomy" assuming that each bronchus splits into approximately two equisized daughter bronchi. Starting from the trachea and continuing from 2 main bronchi to 4 lobar bronchi, and thereafter to 16 segmental bronchi, all the way until the end, the model roughly assumes that the number of airways is approximately equal to number 2 raised to the power of the generation of bifurcations as shown in **Figure *2***.

The tracheobronchial tree can be divided into two zones: the conducting zone, starting from the trachea and ending at the terminal bronchioles (generation 14) and the respiratory zone, also known as the acinar zone, starting from the respiratory bronchioles (generation 15) to the alveolar sacs (final generation). Until the smallest bronchiole, the function of the airways is solely humidification and conduction, however beyond this point, starting from the respiratory bronchioles, there is a gradual shift to gas exchange from conduction, including the appearance and increase in the number of alveoli on the walls of respiratory bronchioles. This transition continues until the alveolar ducts are reached, which differ from respiratory bronchioles as they have no walls but only mouths of mural alveoli. Finally, the transition concludes continuing from the alveolar ducts to the alveolar sacs. It is estimated that the number of alveoli arising from each alveolar sac is about 17.

A pulmonary acinus is a lung region which is supplied by a first-order respiratory bronchiole distal to a single terminal bronchiole, including the respiratory bronchioles, and alveolar ducts and sacs. There are approximately 30 000 acini within a human lung, each containing more than 10 000 alveoli. Illustrations of the alveolar ducts, sacs, and alveoli can be seen in **Figure *1***. The figure clearly shows the capillaries covering the alveoli where perfused blood is oxygenated through diffusion of inhaled oxygen through the blood-gas barrier and the red blood cells to eventually bind on haemoglobin. This is the most important function of the lungs as it is responsible for delivering oxygen to all organs and tissue through the systemic capillaries. Simpler illustrations of alveolar ducts and alveolar sacs can be seen in **Figure *2***.

1.3 Pulmonary Function Testing – Current practices

1.3.1 Spirometry

The term spirometry was given to basic tests of lung function that measure inspired and expired air. The related basic three measurements arising from spirometry are time, volume, and flow. It is a non-invasive, objective and reproducible method, sensitive to early change that can be performed anywhere and by anybody with the right training. Spirometry is performed to quantify lung damage, identify the existence or absence of respiratory disease, determine the effects of medications on lung function, and monitor the effects of occupational and environmental exposures (Moore, 2012). More specifically, the measures of spirometry include the forced expiratory volume in 1 second (FEV_1), the forced vital capacity (FVC) which represents the highest amount of air that can be exhaled when a person is exhaling as quickly as possible, the vital capacity (VC), which represents the highest amount of air that can be exhaled when a person is exhaling at a constant rate, the ratio of FEV_1/FVC, the forced expiratory flow (FEF) which is also known as the mid-expiratory flow at 25%, 50%, and 75% of FVC, the inspiratory vital capacity (IVC) which represents the highest air amount that can be inhaled post a full exhalation, and the peak expiratory flow (PEF) representing the maximum flow of exhaled air when exhaling as quickly as possible.

Patient positioning is important during spirometry as it can affect the test results. Patients undergoing spirometry testing need to sit in an upright position, loosen tight-fitting clothing to avoid underestimation of test results due to chest restriction, with their feet placed flat on the floor and with legs uncrossed to minimise the use of abdominal muscles which can also cause restriction (Moore, 2012). A number of criteria have been published for acceptable quality results of spirometry including the guidelines from the ATS/ERS task force (Miller *et al.*, 2005) which suggest that three acceptable manoeuvres should be implemented for a complete test.

Lung function testing obtained results are of no meaning unless a comparison is implemented against predicted or reference values usually calculated using reference equations such as the ones reported by the European Respiratory Society (Pellegrino *et al.*,

2005; Moore, 2012; Quanjer *et al.*, 2012; Hall *et al.*, 2021). In adults, the reference values' key contributing factors for spirometric measurements are race, sex, height, and age. For example, up to approximately 25 years of age the function of the lungs improves and then declines with increasing age. For pre-pubescent individuals (males and females) lung function is generally the same however, post-puberty, the thorax's growth is higher in males resulting in larger lung volumes in males and finally, increased values of height, lead to increased lung volumes.

Reversibility testing is performed usually for asthma diagnosis (Moore, 2012) or reversible airflow limitation (Miller *et al.*, 2005). Asthma can be reversible; therefore, spirometry can yield normal results when someone is not experiencing an asthma attack/ exacerbation (Moore, 2012) while uncontrolled, persistent asthma can result in irreversible airflow obstruction (Barjaktarevic *et al.*, 2018). Therefore, after spirometry is performed, a bronchodilator, that is either a short-acting β-agonist or other agents such as anticholinergics, is administered and spirometry is implemented again. The pre-bronchodilator and post-bronchodilator measurements are then compared to determine whether an individual has reversed however published criteria about what constitutes a significant improvement in lung function differ slightly (Miller *et al.*, 2005). Recommendations from the ATS/ERS task force mention that there needs to be a minimum of 12% or 200ml increase in FEV_1 (Pellegrino *et al.*, 2005). A strongly suggestive indicator of asthma in adults is an increase of more than 400ml in FEV_1 post-bronchodilator, however the absence of reversibility does not rule out asthma (Network, 2008).

Reversibility is a core trait of asthma differentiating it from other causes of airflow obstruction (Moore, 2012) however some studies suggest that reversibility is as common in COPD as it is asthma, making measures of reversibility impractical for distinguishing between COPD and asthma (Janson *et al.*, 2019). Bronchodilator reversibility in asthma however, may be a phenotypic marker indicating type 2 inflammation and IgE sensitisation (Janson *et al.*, 2019).

1.3.2 Multiple Breath Washout

The Multiple Breath Washout (MBW) is a non-invasive, patient-friendly tool which assesses the ventilation distribution uniformity in the lungs and their small airways through monitoring of an inert gas' clearance during tidal breathing (Robinson, Latzin and Gustafsson, 2010). As the lungs have evolved to mix gas efficiently, an inhaled gas should distribute uniformly in the lungs of healthy individuals. With the distribution of gas being typically patchy in the early stages of obstructive lung diseases, less efficient and uneven gas mixing occurs due to the obstruction/narrowing of the peripheral airways. As a result, an increased time for the tracer gas of interest to wash out, is suggestive of decreased efficiency of gas mixing and increased ventilation heterogeneity (Stanojevic, Bowerman and Robinson, 2021). While the MBW was first described by Margaret Becklake in 1952 (Becklake, 1952), widespread interest has only emerged in the past 25 years (Stanojevic, Bowerman and Robinson, 2021). It is reported that the MBW could be used to improve understanding of asthma pathophysiology, specifically bronchial hyperresponsiveness and also act as a tool for the assessment of therapeutic interventions' response (Robinson, Latzin and Gustafsson, 2010). The outcome measure of this test that is most commonly reported is the Lung Clearance Index (LCI), which is a global measure of ventilation heterogeneity. It represents the number of respiration cycles at FRC (also calculated during the test) needed to wash out the tracer gas (Stanojevic, Bowerman and Robinson, 2021). The test also provides outcome measures that distinguish VH arising from different lung regions such as the conducting airways (S_{cond}) and distal airways (S_{acin}) located in the acinar region (respiratory zone) (Stanojevic, Bowerman and Robinson, 2021). Acinar airway ventilation heterogeneity (VH) measure, S_{acin} which represents VH in the most peripheral acinar or pre-acinar airways, was found to mainly reflect severity of asthma in a large asthmatic patient cohort (Postma *et al.*, 2019). Finally, the same study has shown that the measure S_{cond}, which represents persistent disturbance in the conducting airways, was related to asthma exacerbations, airways remodelling and hyperresponsiveness (Postma *et al.*, 2019).

1.3.3 Lung Impedance

The mechanical impedance of the pulmonary system can be measured by oscillometry. This is a non-invasive method during which sound waves are superimposed on normal tidal breathing and requires minimal cooperation, making it ideal for use in individuals who are acutely ill, individuals with coordination difficulties and young children (Ducharme and Chan, 2024). This technique involves the participant typically being connected to a generator of flow which emits, via a mouthpiece, the forced oscillation signal into the airways, requiring and relying on the participant to form a tight seal around the mouthpiece (Alshlowi *et al.*, 2023). While the reason behind this is to avoid a leak, this may prove challenging to some adults and young children therefore a mouth mask may also be provided as a solution in these circumstances (Alshlowi *et al.*, 2023). The mouth mask has also been reported as a potential valid alternative to a mouthpiece in cohorts having difficulties forming the required tight seal which is typically the requirement in oscillometry (Alshlowi *et al.*, 2023). Recently, portable handheld oscillometry devices have been deployed. A study recently demonstrated the feasibility of deployment of a handheld oscillometry device in the acute care setting for the acquisition of information on respiratory mechanics, as it showed significant differences in VH between healthy subjects and patients in the acute care setting (Aliaroof *et al.*, 2025).

Oscillometry has traditionally focused on the frequency dependence of respiratory impedance which is obtained by averaging the impedance spectra across several breathing cycles (Oostveen *et al.*, 2003; Hantos, 2021). Recent advancements in oscillometry have also made possible the monitoring of impedance changes occurring during breathing cycles through intra-breath oscillometry to characterise impedance components dependences on various respiratory disorders (Hantos, 2021). Intra-breath oscillometry was also demonstrated as a technique that reflected asthma control better than spirometry measures and the same study concluded that oscillometry is useful to facilitate severe asthma management (Chiabai *et al.*, 2021). Mechanical impedance represents the forces of reactance (X) and resistance (R) that an oscillating flow signal must overcome to drive itself into the

respiratory system. Resistance and reactance are collectively known as impedance and represent the in and out of phase relationships between airflow and pressure. The forces in the pulmonary system arise from the airways' and tissue's resistance to flow, the stiffness or the elastance of the chest wall and lung parenchyma in response to changes in lung volume and the accelerating gas inertance in the airways (Kaminsky *et al.*, 2022). Reactance represents the lung tissue's energy storage capacity whereas resistance represents the mechanical dissipation properties of the lungs.

Mechanical impedance can be typically measured using two different pulmonary function tests: the Forced Oscillation Technique (FOT) and the Impulse Oscillometry (IOS) (Dubois, Botelho and Comroe, 1956; Smith, Reinhold and Goldman, 2005; Marchal and Hall, 2010). The FOT was first described in 1956 by Dubois et al. (Dubois, Botelho and Comroe, 1956) and forms the basis for the IOS technique (Desiraju and Agrawal, 2016). In principle the two techniques are similar as they both superimpose sound waves, generated with the aid of a loudspeaker on normal tidal breathing, which are transmitted into the lungs. The main difference between the two techniques is that in FOT, different frequency sound waves are sequentially transmitted whereas in IOS an impulse is transmitted which is decomposed mathematically into different frequencies thus reducing the testing time duration (Desiraju and Agrawal, 2016). These sound waves can also be characterised as pressure waves as they cause pressure changes which drive changes in the flow of air. Measurements of the magnitude of these changes in airflow and in the pressure allow to determine various lung mechanical properties (Desiraju and Agrawal, 2016). Lower frequency sound waves, specifically 5Hz, travel to the distal parts of the lungs reflecting the resistance of the entire respiratory system, while higher frequency sound waves, namely 20Hz only reflect the resistance of the larger airways (Desiraju and Agrawal, 2016; Ducharme and Chan, 2024). Subtraction of the resistance measurement at sound frequency of 20Hz from the resistance at 5Hz yields the resistance value R_5-R_{20} which reflects the peripheral airways' resistance (resistance of small-to-mid-sized airways). More specifically, peripheral airway resistance, R_5-R_{20} is thought to be

primarily sensitive to heterogeneous peripheral airways' narrowing, while abnormal values of this measure could also occur due to substantial narrowing heterogeneity of more central airways, upper airway shunt flow, and inhomogeneity of time constants (time required for the lungs to fill/empty – product of compliance and resistance) representing airway or parenchymal disease. Impedance's second component, the reactance, represents the elastic and inertive properties of the lungs, with elevated values of reactance at 5Hz (X_5) and elevated values of AX (the area under the reactance curve between frequency at 5Hz and the resonant frequency – at which impedance is zero) reflecting lung stiffness and VH (Ducharme and Chan, 2024). Specifically, X_5 has been shown to be sensitive to closure of airways and to reflect communicating lung volume, while intra-breath changes in X_5 can be useful in the detection of expiratory flow limitation (Kaminsky *et al.*, 2022). Since the AX is an integrative measure, dominated by the low-frequency components of reactance and predominately determined by elastance, it is more sensitive to variations in the elastic properties of the pulmonary system than reactance at any frequency (Kaminsky *et al.*, 2022). The large asthmatic patient cohort ATLANTIS, has revealed that oscillometry measurements such as peripheral airway resistance R_5-R_{20}, AX, X_5 and R_5 to a certain extent, have been reported to be key indicators of small airways dysfunction (SAD) (Postma *et al.*, 2019; Kaminsky *et al.*, 2022; Ducharme and Chan, 2024). In a recent study, including a large cohort of COPD patients (n=833), SAD, as defined by oscillometry measurements of reactance X_5 and AX, was associated with higher risk of COPD exacerbation and faster lung function decline (Lu *et al.*, 2025).

Measurements of oscillometry are able to differentiate adult asthmatic patients, from healthy subjects (Clément, Làndsér and Van de Woestijne, 1983; Nair, Ward and Lipworth, 2011; Tsuburai *et al.*, 2012; Kaminsky *et al.*, 2022), as well as asthmatics with variant airway obstruction severity (Cavalcanti *et al.*, 2006; Kaminsky *et al.*, 2022), and among adult groups with COPD compared to asthmatics (Clément, Làndsér and Van de Woestijne, 1983; Van Noord *et al.*, 1991; Paredi *et al.*, 2010; Yang and Lin, 2010; Mori *et al.*, 2011; Kaminsky *et al.*, 2022). This technique can be useful especially in the diagnosis of asthma in patients with

preserved spirometry, as an indicator more sensitive to abnormal physiology of the airways (Kim *et al.*, 2020; Kaminsky *et al.*, 2022). Measurements such as AX and peripheral airway resistance R_5-R_{20}, may be useful in aiding asthma diagnosis, monitoring of clinical treatment changes or prediction of future loss of asthma control (Kaminsky *et al.*, 2022). Caution is urged in the strict interpretation of peripheral airway resistance R_5-R20, as a measure which solely relates to small airways disease, particularly when this is measured with devices known to be associated with increased resistance frequency dependence (Tanimura *et al.*, 2014; Soares *et al.*, 2018; Dandurand *et al.*, 2019; Kuo, Jabbal and Lipworth, 2019; Kaminsky *et al.*, 2022). The clinical significance of peripheral airway resistance R_5-R_{20}, continues to be assessed in terms of its prevalence (Anderson, Zajda and Lipworth, 2012), mechanism (Bell *et al.*, 2019; Foy *et al.*, 2019) and correlations with severity and control measures in both adults and children (Shi *et al.*, 2013; Manoharan *et al.*, 2014; Postma *et al.*, 2019; Kaminsky *et al.*, 2022). Furthermore, oscillometry has provided new insights into asthma pathophysiology through lung volume effects on oscillatory mechanics, as well as time-dependent variations (short-term and long-term) in mechanics (Kaminsky *et al.*, 2022). Another use of oscillometry is as an alternative to spirometry for bronchial challenge testing in adults (Rozen, Bracamonte and Sergysels, 1983; Suzuki *et al.*, 1984; Wouters *et al.*, 1988; Van Noord *et al.*, 1989; Wesseling, Vanderhoven-Augustin and Wouters, 1993; Schmekel and Smith, 1997; Bohadana *et al.*, 1999; Broeders *et al.*, 2005; Mansur, Manney and Ayres, 2008; McClean *et al.*, 2011; Naji *et al.*, 2013; Imahashi and Kanazawa, 2014; Tsurikisawa *et al.*, 2015; Kaminsky *et al.*, 2022) and children (Bisgaard and Klug, 1995; Nielsen and Bisgaard, 2000; Malmberg *et al.*, 2008; Hall *et al.*, 2009; Schulze *et al.*, 2012; Alblooshi *et al.*, 2013; Kalliola *et al.*, 2014), providing an advantage of increased sensitivity of bronchoconstriction detection which is able to reduce the testing duration and decrease the cumulative dose of the agent (Kaminsky *et al.*, 2022). Given the bronchoprotective and bronchodilator effect due to deep inhalation in asthma and health, deep breaths with some inhalation agents or during spirometry testing can affect diagnosis of airway hyperresponsiveness (Kaminsky *et al.*, 2022). As a result, oscillometry can be more sensitive than spirometry in the detection of airway

hyperresponsiveness in mild asthmatic patients (Kaminsky *et al.*, 2022). Finally, abnormal oscillometry measurements were found to be significantly associated with an increased risk of exhibiting respiratory diagnoses and respiratory symptoms, with reactance appearing as a more sensitive marker of disease and symptoms compared to resistance (Veneroni *et al.*, 2024). Variations in lung mechanics were also found to be more present in asthmatic patients than in COPD. The mentioned associations were found to be present in a subset of individuals with preserved spirometry measurements (Veneroni *et al.*, 2024). While many gaps in the understanding of oscillometry are closing, in order to ensure a smooth transition of this technique from research to a robust, reliable, clinical tool, many gaps still need to be filled (Kaminsky *et al.*, 2022).

The literature on lung impedance measures shows that they are sensitive to small airway involvement in asthma and COPD and that they can identify changes in lung mechanics in the early stages of respiratory disease as well as during progression and worsening of disease (Veneroni *et al.*, 2024). The vast majority of literature has compared spirometry with oscillometry, however data published suggest that these two techniques have different sensitivities to pulmonary conditions (Veneroni *et al.*, 2024). This sensitivity needs to be precisely understood however, to be clinically useful, which computational modelling could help with (Foy *et al.*, 2019).

1.3.4 Ventilation (V) and Perfusion (Q) matching

The lungs' primary function is gas exchange and its major mechanism for interference in disease is ventilation/perfusion mismatch (Wagner, 1981). Respiratory disease – asthma, ILD, pulmonary hypertension (PH), and COPD are common causes of hypoxemia (decrease of oxygen's partial pressure in blood) due to V/Q mismatch (Petersson and Glenny, 2014; Sarkar, Niranjan and Banyal, 2017). In obstructive lung diseases, the weakened function of the lungs is characterised by an underlying response to inflammation which causes airflow limitation, airway remodelling and increased V/Q mismatch (Burrowes, Doel and Brightling, 2014). V/Q matching is a fundamental lung function, where ventilation facilitates transport of oxygen to

the blood-gas barrier where, blood is transported via perfusion to pulmonary capillaries enabling gas exchange. This intricate interplay of V and Q is crucial for efficient gas exchange, and essential for respiratory health. Furthermore, ventilation is the delivery mechanism of inhaled therapies and therefore its assessment is crucial for targeted aerosol deposition in specific lung regions (Abdelrahim *et al.*, 2021). The V/Q ratio is not uniform in the human lungs. Gravity and variable sub-atmospheric intrapleural pressure make V/Q matching regionally heterogeneous. Ventilation and perfusion are lower at the apex and higher at the base of the lungs, whereas the V/Q ratio is lower at the base and higher at the apex. Lower V/Q at the base is caused by an increase in perfusion much larger than the increase in ventilation. Higher V/Q at the apex occurs due to a larger decrease in perfusion than the decrease in ventilation (Sarkar, Niranjan and Banyal, 2017). A vital compensatory mechanism of the respiratory system due to hypoxemia, is hypoxic pulmonary vasoconstriction (HPV) which restricts perfusion in areas of the lungs where ventilation is reduced, resulting to the diversion of blood to well-ventilated lung regions thus maintaining the V/Q matching (West, Dollery and Naimark, 1964; Orchard, Sanchez de Leon and Sykes, 1983; Sarkar, Niranjan and Banyal, 2017). Diffusion limitation can cause development or worsening of hypoxemia during exercise because of shortened capillary transit time. It is defined as the impairment of oxygen transport across the alveolar-capillary membrane and may be caused by decreased surface area of the lungs for diffusion, fibrosis of the alveolar-capillary membrane, inflammation, extremely small capillary transit time and low alveolar oxygen. Rise in alveolar oxygen and recruitment or distension of capillaries prevents hypoxemia from developing, however patients with pulmonary fibrosis develop exercise-induced or exercise-exaggerated hypoxemia. Emphysema and ILD are important causes of diffusion limitation (Sarkar, Niranjan and Banyal, 2017). Physiological techniques such as the multiple inert gas elimination technique (MIGET), and the carbon monoxide (CO) gas-transfer test have been traditionally employed to assess V/Q. The MIGET, based on mass conservation principles (Lumb and Thomas, 2021a), measures gas-exchange of intravenously infused dissolved gases to compute V/Q distribution. The CO gas-transfer test (Graham *et al.*, 2017) is based on a method developed

by Marie Krogh (Krogh, 1915), to measure uptake of CO in the lungs utilising fundamentals of gas diffusion (Fick's law) (Modi and Cascella, 2024). Its output, DLCO is a predictor of exacerbations in COPD and a risk factor for all-cause mortality (Li *et al.*, 2023; Park *et al.*, 2024). This test is a composite of V and Q hence it does not dissect the two, making results hard to interpret. While both tests provide insights into gas-exchange efficiency, they fail to offer a comprehensive understanding of mechanisms underlying blood-gas barrier dysfunction as their outputs are not localising blood-gas barrier pathology and are non-spatial – whereas lung disease is highly spatial.

1.3.5 Blood-gas barrier function

The alveolar-capillary membrane, also known as the blood-gas barrier, is the fundamental functional component of the lung, acting as the place where oxygen and carbon dioxide are exchanged between the pulmonary capillaries and the distal airspaces (alveoli). The average number of alveoli that a healthy pair of adult human lungs is composed of is estimated to be around 480 million each with an approximate mean diameter of 200 μm (Ochs *et al.*, 2004). To achieve the lung's primary functions which are blood oxygenation and removal of carbon dioxide from systemic circulation, the lung must spread blood into a thin layer of capillaries which are intermeshed within the alveolar walls to allow very close proximity between inspired air and perfused blood. The blood-gas barrier consists of several layers that oxygen must pass through to reach a red blood cell (RBC), including the alveolar lining layer (ALL), epithelium, extracellular matrix, endothelium, blood plasma and the RBC membrane. The thickness of the blood-gas barrier varies between some maximal and minimal thickness and thus it is not uniform along the membrane (Leiby, Raredon and Niklason, 2020). The thinnest part of the alveolar-capillary membrane in humans is estimated to range between 0.2 and 0.4 μm thickness (Gehr, Bachofen and Weibel, 1978).

The mean arithmetic thickness provides information about the mass of the tissue composing the barrier and consuming oxygen in the lung, however the characteristic blood-gas barrier thickness relevant to gas diffusion is the harmonic mean thickness which provides emphasis

on smaller values / thinner regions of the membrane which allow higher gas diffusion, as opposed to the arithmetic mean which considers all varying thickness values along the membrane equally (Weibel and Knight, 1964). The mean harmonic blood-gas barrier thickness in humans was estimated to be 0.62 μm (Gehr, Bachofen and Weibel, 1978). The harmonic mean thickness is particularly relevant to the diffusion capacity. It measures the gases' ability to be transported across the membrane from air to RBC, and is inversely proportional to the membrane's thickness as governed by Fick's law for diffusion (Leiby, Raredon and Niklason, 2020).

A method introduced by (Driehuys *et al.*, 2006), utilised hyperpolarised ^{129}Xe to image its transfer differentially from the air spaces of the alveoli, through the blood-gas barrier and the RBCs in the gas exchange lung regions. By imaging ^{129}Xe separately in these compartments, this method allowed the image of blood-gas barrier gas transfer which is the fundamental function of the lungs. The ratio of RBC/barrier (obtained with pixel counts) was proposed as a method of gas-transfer efficiency quantification. More recently, hyperpolarised ^{129}Xe MRI which allows imaging of the airspace, blood-gas barrier, and RBC as shown in **Figure *3***, was utilised to examine the relationship of exercise limitation and persistent symptoms of COVID-19 (Matheson *et al.*, 2022). This study showed that there was a statistically significant relationship with the DLCO % predicted result and the RBC:Barrier ratio (obtained from the area under the receiver operating characteristic curve of the separated peaks) in patients with post-acute COVID-19 syndrome indicating the importance of these ratios in the assessment of blood-gas barrier function and the gas-exchange efficiency.

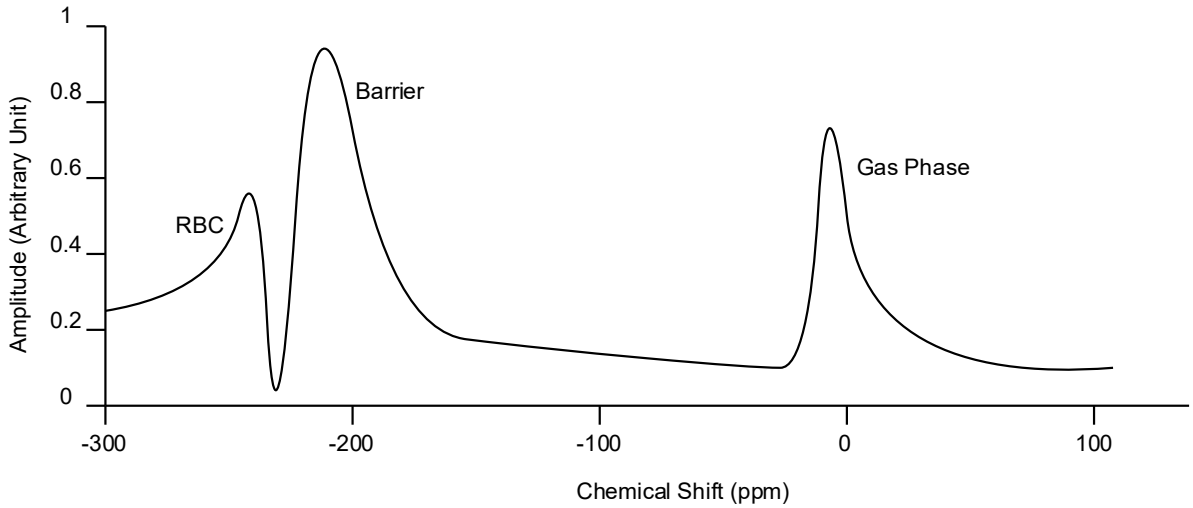


Figure 3 – Illustration of ^{129}Xe Magnetic resonance spectrum graph

The figure was drawn for illustrative purposes of the peaks acquired from ^{129}Xe MRI and do not reflect typical values for individuals.

1.3.6 Questionnaires

Various questionnaires have been designed and validated for the assessment of symptoms and lung function impairment severity (Jones *et al.*, 1992; Trinick, Southern and McNamara, 2012; Cassidy, Roberts and Colby, 2015; Stanojevic *et al.*, 2022). Questionnaires have also been designed and utilised for the assessment of asthma control (Juniper *et al.*, 1999; Soler *et al.*, 2018), as well as the assessment of Quality of Life (QoL) of patients (The EuroQol Group, 1990; Devlin and Brooks, 2017; Hernandez *et al.*, 2019). The Asthma Control Test (ACT) is a tool allowing physicians to quickly estimate the asthma symptoms' control (Crimi *et al.*, 2020) and has also been proven to be reliable for use among smoking asthmatics, who have more asthma exacerbations and symptoms and respond worse to asthma therapies (Soler *et al.*, 2018). Furthermore, this questionnaire is a valid instrument for the identification of uncontrolled asthma patients and also shows potential for deployment in the identification of asthma patients who are at risk of death or hospitalisation (Sundbaum *et al.*, 2024). Asthma control has been assessed using another questionnaire – the Asthma Control Questionnaire (ACQ) (Juniper *et al.*, 1999) which is a validated tool used commonly in clinical trials for the assessment of therapeutic efficacy, due to its responsiveness to asthma control (Singh *et al.*,

2023). This questionnaire is originally composed of seven items which are scored on a seven-point scale. The first six items involve patient's scores on symptoms on walking, shortness of breath, night-time awakening due to asthma, limitation of activities, the mean number of puffs taken of short-acting beta-agonist bronchodilator used daily, and wheezing. The final point is the spirometry result FEV_1 which is combined with the other six items and averaged to provide the final score. Shortened versions of the test exist, including the ACQ-6 questionnaire, which does not take into account FEV_1, and the ACQ-5 questionnaire, which does not take into account both the FEV_1 and bronchodilator use (Juniper *et al.*, 2005; Wyrwich *et al.*, 2011; Sundbaum *et al.*, 2024). The two questionnaires, the ACT and the ACQ together with asthma exacerbation history in the past year have also been shown to have potential to provide useful information for future risk of asthma exacerbations predictions (Uematsu *et al.*, 2018).

The principal goal of the group known as "EuroQol Group", was the testing of the feasibility of the joint development of a non-disease-specific standardised instrument to value and describe health-related quality of life (The EuroQol Group, 1990; Brooks, 1996, 2013). The EuroQol instrument, developed by a five-country multidisciplinary group (fields included mathematics, philosophy, sociology, psychology, medicine, nursing and economics) (The EuroQol Group, 1990) providing a five-dimensional three-level measure, hence 5Q-5D, and designed to assess and quantify health status, was initially termed "EQ-5D" (Devlin and Brooks, 2017). Following acquisition of experience in the development of the EQ-5D, two further instruments were developed, the EQ-5D-5L and the youth version EQ-5D-Y (Devlin and Brooks, 2017). The EuroQol-5D-5L has been shown to have high/good reliability (Hernandez *et al.*, 2019; Szentes *et al.*, 2019, 2020), thus supporting its adequacy for the assessment of health-related quality of life in asthmatic patients (Hernandez *et al.*, 2019). The questionnaire has also appeared to respond unsatisfactorily to changes in asthma control (Szentes *et al.*, 2019) which is supported by another study where the questionnaire's reaction was not very sensitive to small asthma control changes (Szentes *et al.*, 2020). The study authors suggest that in addition to the EuroQol-5D-5L questionnaire, the use of

supplementary measures is advised to evaluate more comprehensively asthma-specific interventions (Szentes *et al.*, 2020).

1.3.7 Differential Cell Counts

1.3.7.1 Complete Blood Count (CBC)

The complete blood count is the most frequently ordered laboratory test worldwide (Marin *et al.*, 2024) and is performed to determine the cellular composition of blood. Samples of blood are collected through the insertion of a needle into an arm's vein followed by drainage of a small blood volume inside a sample tube. CBC can be measured manually with a microscope or with an automated haematology analyser which is responsible for counting the number of different blood cells (platelets, RBCs, and white blood cells) in a given blood volume (Ke *et al.*, 2023). Asthma is a chronic airways inflammatory disease which involves various cells including neutrophils, macrophages, lymphocytes and eosinophils (Alobaidi, Alsamarai and Alsamarai, 2021; Ke *et al.*, 2023). Blood counts may be useful in facilitating monitoring of uncontrolled asthma and blood eosinophil counts were found capable in predicting eosinophilic asthma accurately in patients with uncontrolled, persistent asthma, regardless of treatment (Zhang *et al.*, 2014). CBC has also been used to provide evidence of eosinophilia and neutrophilia prevalence in asthma patients deeming haematological abnormalities important to be taken into account for management and proper monitoring of asthmatic patients (Solomon *et al.*, 2022). Furthermore, monocytes have also been shown to be important in asthma as studies have shown that inflammatory process is promoted by monocytes differentiating into dendritic cells or macrophages which can promote asthma by impairing lung function (Rastogi *et al.*, 2015; Paplinska-Goryca *et al.*, 2020; Zhang *et al.*, 2021; Han *et al.*, 2022; Ke *et al.*, 2023). Finally, lymphocytes also play an important role in asthma, by releasing cytokines which promote bronchoconstriction, mucus production, and inflammation of the airways (Huang *et al.*, 2020; Ke *et al.*, 2023).

1.3.7.2 Sputum Cytology

Induced sputum cell counts are the gold standard test, used in characterising inflammatory phenotypes (Zhang *et al.*, 2014). Airway inflammation phenotypes can be assessed with the non-invasive biomarker, cell count induced in sputum (Gao *et al.*, 2017; Gilbey *et al.*, 2024). The cell counts of sputum are widely used in the treatment of COPD and asthma (Gao *et al.*, 2017). There is also evidence that as an inflammatory biomarker, sputum cell counts could carry some information to distinguish among asthma, COPD and their overlap condition (Gao *et al.*, 2017). In a study involving a large cohort of asthmatic patients (n=833) and healthy volunteers (n=194), the existence of significant eosinophilic inflammation was demonstrated with the use of sputum cell counts, across all asthma categories included in the study (Demarche *et al.*, 2016).

1.4 Spatial tests and medical imaging

Imaging techniques are fundamental to diagnose and detect respiratory diseases, identify possible complications and monitor their treatment (Tárnoki *et al.*, 2024). Studies involving lung imaging are important in assessing and following up respiratory diseases. X-rays were accidentally discovered by Wilhelm Conrad Rontgen in 1895 and have been used in the development of chest radiography (CXR) which is still the first imaging method performed in patients with symptoms affecting their respiratory system (Tárnoki *et al.*, 2024). This method is low radiation and cost, it is widely available and provides 2 dimensional x-ray images rapidly however it is limited by its low sensitivity and specificity (Tárnoki *et al.*, 2024). Thoracic computed tomography (CT) is a method with higher sensitivity and the ability of constructing real-time three-dimensional images. High-resolution CT (HRCT) is able to detect arterioles with 0.2mm in diameter allowing for the detection of interstitial inflammation and idiopathic interstitial pneumonitis (Tárnoki *et al.*, 2024). Another highly sensitive CT technique is multi-detector CT (MDCT) which is capable of capturing air trapping, (Litmanovich *et al.*, 2014; Usmani *et al.*, 2021) a major determinant of airway obstruction in asthma (Park *et al.*, 2012). Endobronchial optical coherence tomography (OCT), is a minimally invasive technique which allows the assessment of microstructural remodelling in the small airways (Chen *et al.*, 2015;

Usmani *et al.*, 2021). Single photon emission CT (SPECT) combines emissions from inspired radiotracer with CT imaging. A SPECT of the airways can provide unique information as it allows for the measurement of regional defects in ventilation (Farrow and King, 2019; Usmani *et al.*, 2021). More detailed structure-function relationships can also be identified using micro-CT (Pennati *et al.*, 2023). Micro-CT cannot be used on living humans however, due to high radiation doses.

Lung CT methods have been widely deployed to study lung structure-function relationships in asthma (Gupta *et al.*, 2014; Shim *et al.*, 2018; Bell *et al.*, 2019). The application of image registration to expiratory and inspiratory CT imaging has more recently been used for the derivation of functional small airways disease indices (fSAD) (Galbán *et al.*, 2012; Choi *et al.*, 2013; Boes *et al.*, 2015). A specific approach that is widely utilised is parametric response mapping (PRM) (Galbán *et al.*, 2012; Boes *et al.*, 2015). This approach was first applied to CT pulmonary imaging data in a 2012 study published in Nature Medicine (Galbán *et al.*, 2012). PRM is different from other methods – which compile CT imaging-derived information throughout the lungs into a single outcome, thus forfeiting the inherent spatial information of the CT images – as it allows the capture of the unique signature, specific to an individual patient's disease state through the classification process imposed on individual voxels (Galbán *et al.*, 2012). The PRM approach allows the characterisation of voxel-wise spatial deformation between acquired whole-lung CT images at different lung volumes, namely total lung capacity (TLC) and functional residual capacity (FRC), providing the potential to detect spatial mechanisms ventilation heterogeneity (VH) markers which are derived from Impulse Oscillometry, and the Multiple Breath Washout test (Bell *et al.*, 2019). Mean whole-lung PRM indices were found to be associated with airflow obstruction which was measured with spirometry (Bell *et al.*, 2019). Stratified axial analysis (SAA) has been used for the evaluation of regional change in tissue density gradients in a given direction, using voxel-wise FRC to TLC change in tissue density, eventually providing markers of regionalised airway closure such as the $\overline{\Delta HU}^{AP}$ where AP denotes the direction of regional density change Anterior to Posterior and $\overline{\Delta HU}^{IS}$, which represents specifically regionalised airway closure in the lower lobes of the

lungs, where IS denotes the direction of regional density change Inferior to Superior (Bell *et al.*, 2019).

Spatial tests utilising advanced imaging techniques such as MRI coupled with inhaled gases such as hyperpolarised ^{129}Xenon (Cleveland *et al.*, 2014; Matheson *et al.*, 2022; O'Sullivan-Murphy, Driehuys and Mammarappallil, 2022), offer more localised V/Q dynamics. Hyperpolarised ^{129}Xenon has also been used in the identification of ventilation defects in asthma and has provided a way of quantification of ventilation heterogeneity as ventilation defect percent (VDP) (Fain *et al.*, 2007; McIntosh *et al.*, 2023). Hyperpolarised ^{129}Xe MRI data have also been used in the training of advanced regression models for the prediction of regional transfer factor (DLCO) in a recent study providing a tool for regional visualisation of DLCO (Pilgrim-Morris *et al.*, 2025). However, these advanced imaging techniques cannot provide measurements in hypothetical or unseen scenarios involving changes to the lungs' structure to understand how such changes may drive alterations to lung function – something that computational modelling allows. Difficulty in validating imaging measurements can also deem in-silico models valuable.

1.5 Mathematical modelling of pulmonary function

The development of a framework for modelling the functions of the entire human body was the aim of the physiome project which started in 1997 (Burrowes, Doel and Brightling, 2014). This was followed by the virtual physiological human (VPH) initiative, a European initiative with roots to the international Physiome initiative, (Gavaghan, Coveney and Kohl, 2009; Hunter *et al.*, 2010; Viceconti and Hunter, 2016; Van Sint Jan and Geris, 2019) which set the foundation for recent advancements in regional V/Q assessment which have been driven by models utilising imaging-derived structural information and have been employed (Montesantos *et al.*, 2013; Tawhai and Bates, 2015; Foy and Kay, 2017, 2019; Bell *et al.*, 2019; Choi *et al.*, 2019; Foy *et al.*, 2019) to enhance understanding of normal and abnormal patho(physiologies). By allowing structure perturbation, models offer a pathway to infer mechanistic insights that conventional techniques may overlook. Moreover, models are

unaffected by ethical or technical constraints encountered in experimental studies (Clark, Burrowes and Tawhai, 2021) making their use in the implementation of experiments more time efficient. Pulmonary diseases are entering the era of precision medicine (Porsbjerg *et al.*, 2023), an evolving strategy for tailored treatment and disease prevention, incorporating a gradually widening spectrum of biological, environmental and lifestyle data (Antman and Loscalzo, 2016). Optimal patient-tailored therapy would benefit from a detailed mechanistic understanding of the lungs combining tissue, organ-level data, and pathophysiology. Precision medicine would benefit from development of a 'complete pulmonary digital-twin' through not only acquisition of more detailed patient data, but also exploitation, integration, and analysis of the data (Corral-Acero *et al.*, 2020). Its development would require underlying PFT models and information of the lung's tissue, as well as its response to disease and drug administration. Knowledge of the physics as well as the physiology, encapsulated in mechanistic models, able to integrate clinical data, would enable outcome prediction and/or the identification of disease mechanisms even under hypothetical unseen conditions (Corral-Acero *et al.*, 2020).

1.5.1 Digital Twins in Healthcare

A virtual and digital depiction of any physical entity can be characterised as a digital twin (DT) when its foundation is made of a mathematical model and it utilises the physical entity's data to update the digital counterpart (Zhang *et al.*, 2024). Originally, the description of a DT is described by the physical and virtual components and the connection between the two, where information is exchanged in real time (Katsoulakis *et al.*, 2024). The initial concept of DTs was initially adopted by the space program of the National Aeronautics and Space Administration (NASA) in the 1960s, for the simulation of spacecraft that allowed real-time debugging of flight issues as they arose (Katsoulakis *et al.*, 2024). This concept emerged again when it was later introduced during a Product Lifecycle Management (PLM) course at the University of Michigan in 2002 as "Conceptual Ideal for PLM" by Michael Grieves (Grieves and Vickers, 2017; Gonsard, Genet and Drummond, 2024). The conceptual model term became the "Mirrored Spaces Model" as it was referenced in a 2005 journal article (Grieves, 2005; Grieves

and Vickers, 2017). NASA and John Vickers around 2010, utilised the DT as a physical system's virtual model (Piascik, B *et al.*, 2010; Glaessgen and Stargel, 2012; Katsoulakis *et al.*, 2024), with the actual term "Digital Twin" being firstly published in the NASA report of 2012 (Glaessgen and Stargel, 2012; Gonsard, Genet and Drummond, 2024).

The DT was termed as an integrated multiscale, multi-physics, probabilistic simulation of a system which makes use of the best sensor updates, physical models, etc., to mirror its corresponding flying twin's life. The concept introduced by Michael Grieves, emphasises the three system's elements which are the digital twin, the physical twin, and the bidirectional flow between the two (Gonsard, Genet and Drummond, 2024), however, NASA considers the digital twin as a "highly advanced simulation system" itself. These two different approaches are associated with the fact that the DTs' concept combines advances in two fields; simulation, and the cyber-physical systems (Gonsard, Genet and Drummond, 2024). An example of a cyber-physical system is an autonomous car, utilising numerous sensors allowing real-time representation of its state, machine-learning techniques enabling data processing, actuators implementing insight-based changes to the physical system and networks combining data from multiple machines and sensors (Gonsard, Genet and Drummond, 2024). The DT concept evolved partially from the evolution of physical simulations, which with the digital revolution, were transformed into virtual simulations and modelling of virtual replicas of, for example, aircraft (Gonsard, Genet and Drummond, 2024).

DTs have been used in the manufacturing and engineering industries for process monitoring and modelling as well as for efficiency optimisation, such as in the evaluation of jet engines' performance (Zhang *et al.*, 2024). As a result of advances in modelling and cyber-physical systems, the application of digital twins has multiplied across numerous industries and disciplines, and has recently surged within the healthcare sector (Katsoulakis *et al.*, 2024). Digital twins for health (DT4H) is a concept that holds immense promise to transform the healthcare system entirely, including disease prevention and treatment, and well-being maintenance, ultimately aiming for the improvement of human life (Katsoulakis *et al.*, 2024). Continuous advancements in data science and the fast growth of big data and artificial

intelligence have the potential to advance research in the development of digital twins through provision of robust cybertechnology infrastructure, essential data, and scientific expertise (Katsoulakis *et al.*, 2024).

Compared to digital twins of engineered systems, there are several difficulties in the development of patient digital twins. Unlike an aircraft which is created with materials whose physical properties are known, the biological and physical processes governing the functions of human body parts remain poorly understood (National Academies of Sciences, Engineering, and Medicine, 2023; Gonsard, Genet and Drummond, 2024). Moreover, humans being the creators of man-made engineered products such as aircraft, have a multi-scale view of them, from the smallest electrical unit to the entire product. The same cannot be said however about organ-organ, tissue-organ, or tissue-cell interactions in the human body as they are incompletely understood. Furthermore, another reason of why the DT development of patients is difficult lies in the fact that engineered systems are developed with increasing numbers of sensors for the collection of trustworthy data allowing the representation of the system as a digital replica, while obtaining such data from the human body would require wearing or implantation of sensors with ethical, technical, and medical problems occurring as a result (Drummond and Coulet, 2022; Gonsard, Genet and Drummond, 2024).

Digital twins in healthcare can be split into two categories based on the origins of the modern digital twin coming from, the cyber-physical systems, called “monitoring patient digital twins”, and the simulation, called “simulation patient digital twins” (Gonsard, Genet and Drummond, 2024). The former are dynamic systems, based on a data-driven approach, allowing live tracking of the patient’s state, including visualisations of their organs from data collected through sensors and informing decision-making based on machine-learning techniques (Gonsard, Genet and Drummond, 2024). The latter is based on a mechanistic approach, primarily focused on physics in the respiratory care context, which allows the depiction of the patients’ three-dimensional anatomy entirely or partially as well as modelling of the physiology of their organ(s) or biological system therefore allowing the simulation of hypothetical scenarios to assess the effectiveness of various therapeutic approaches or predict

disease progression (Gonsard, Genet and Drummond, 2024). Due to the need to acquire three-dimensional in-clinic structural information of the organs through medical imaging (CT - Computed Tomography or MRI - Magnetic Resonance Imaging), simulation patient digital twins are characterised as static systems useful for one-time assessments (Gonsard, Genet and Drummond, 2024).

In the past few decades, various models have been proposed for simulation of lung function and significant progress has been made for the development of physics-based modelling of the pulmonary system that can be used in the development of multi-scale, multi-physics patient digital twins of the lungs. These models include, reduced respiratory models, refined air-flow models, refined gas-exchange models, refined tissue motion/deformation models, and finally tissue remodelling models (Gonsard, Genet and Drummond, 2024). Respiratory models of global lung function are usually termed as "lumped" or "reduced" and model relationships among global variables instead of representing explicitly each mechanism with an aim to represent the main functions of the lungs which are ventilation and gas exchange. Such models that are the simplest in nature are characterised as “single-compartment” and represent the global pressure-volume relationship along with diffusion models for oxygen and carbon dioxide (Keener and Sneyd, 2009; Morton *et al.*, 2018; Gonsard, Genet and Drummond, 2024). Models of high complexity, however, can be composed of hundreds of compartments each capable of diffusing oxygen and carbon dioxide as well as exchanging gas (Hardman *et al.*, 1998; Roth, Ismail, *et al.*, 2017; Bou Jawde *et al.*, 2020; Gonsard, Genet and Drummond, 2024) with some models accounting for hemodynamics by including blood compartments (Das *et al.*, 2013, 2017; Gonsard, Genet and Drummond, 2024). Such models combine air/blood composition and breathing data namely partial pressure of oxygen and/or carbon dioxide in the blood, pH, cardiac output and expired/inspired oxygen fraction (Gonsard, Genet and Drummond, 2024). Numerous clinically relevant questions have been addressed through application of these models such as the effect of various manoeuvres on recruitment of alveoli (Das *et al.*, 2015; Geitner *et al.*, 2023), the effect of COVID-19 (Weaver *et al.*, 2021) and COPD (Wang *et al.*, 2014) on breathing, the positive expiratory pressure’s role in patients

with acute respiratory distress syndrome (Chikhani *et al.*, 2016). While the reduced respiratory models may provide a good representation of global lung function, a need arises for more refined, specific-phenomena-simulating models, due to the reduced respiratory models' limitation in representing more complex, or finer phenomena (Gonsard, Genet and Drummond, 2024). These refined models can be autonomously designed or can be designed to interact with a reduced model representing the remaining parts of functions of the system (Burrowes *et al.*, 2008; Ismail, Comerford and Wall, 2013; Lam *et al.*, 2025).

For the achievement of more realistic simulations, better representing the complex nature of airflow in the human airways, models of three-dimensional Computational Fluid Dynamics (CFD) have been developed solving the Navier-Stokes equations with reasonable computational cost which simulate the airflow into the large airways (Luo *et al.*, 2004; Wall and Rabczuk, 2008; Tawhai, Hoffman and Lin, 2009; Kleinstreuer and Zhang, 2010; Boudin *et al.*, 2015; Rahimi-Gorji *et al.*, 2015; Guha and Pradhan, 2017). As the resolution of medical imaging is limited to larger airways and the computational cost is higher for the implementation of CFD simulations of airflow in the smaller airways, coupling the small-airways, represented in a lumped manner, with larger airway models is an important area which needs to be addressed (Yin *et al.*, 2010; Roth, Yoshihara, *et al.*, 2017). Dynamic breathing motion can be represented with static (Oakes *et al.*, 2014; Rahimi-Gorji *et al.*, 2015) or moving airway walls (Wall and Rabczuk, 2008; Pozin *et al.*, 2017), which is another distinction among modelling approaches. The geometries used in these models can either be personalised (Bordas *et al.*, 2015) or idealised (Baffico, Grandmont and Maury, 2010). A recent study investigated asthma phenotypes and their association with particle deposition and VH using qCT markers, SPECT imaging and a subject-specific whole-lung computational fluid and particle dynamics (CFPD) model (Zhang *et al.*, 2025). The study showed that the combination of imaging and computational modelling approaches can provide insights into VH and particle deposition in asthma (Zhang *et al.*, 2025).

Being the most important function of the lungs, gas-exchange has had a lot of attention and has been the subject of a vast body of research, nonetheless, models, even well-established,

are subject to debate. Detailed three-dimensional models of gas-exchange and perfusion have been published (Frank, Chuong and Johnson, 1997; Zurita and Hurtado, 2022), however, these have not yet been integrated with respiratory models of global lung function (Gonsard, Genet and Drummond, 2024).

The solid mechanics community has focused on another well-researched area which is the lung parenchyma, with recent work utilizing realistic microstructures of acini segmented from micro-CT medical images (Kumar *et al.*, 2013; Xiao *et al.*, 2013), to investigate the structures' complex patterns of deformation (Koshiyama and Wada, 2015; Álvarez-Barrientos, Hurtado and Genet, 2021). The lung has also been modelled at organ scale, as a poroelastic solid - a mixture of deformable solid and fluid flowing inside, outside and within the structure (Berger *et al.*, 2016; Patte, Genet and Chapelle, 2022; Hurtado, Avilés-Rojas and Concha, 2023) - and as a compressible solid (Tawhai and Lin, 2010). Parenchymal deformity has also been studied in the context of fractional-order modelling combined with a simple forced oscillation technique model (which does not make use of anatomical airway lung structures) in asthma (Tuza *et al.*, 2020) using equations derived by Jason Bates (Jason H.T. Bates, 2009) by assessment of constant phase model of impedance tissue parameters, damping (G), elastance (H), and hysteresivity (η).

Large-scale application of DTs in healthcare encounters multiple obstacles including interoperability, i.e. the ability of digital twin systems to interact with each other and learn from each other, ethical and regulatory considerations, data integration – the need for development of computational methods able to combine diverse data types into digital twins, prioritisation – the identification and prioritisation of therapeutic targets and disease mechanisms, global scaling – global expansion of the DT technology to ensure equitable access to healthcare, biological complexity – characterisation of dynamic molecular changes across different scales, and user interface – the design of interfaces needs to be intuitive for clinicians and patients (Li *et al.*, 2025). According to the famous aphorism, "all models are wrong, but some are useful", therefore models should not be assessed based on their ability to best describe the lungs but instead on their ability to answer the investigated questions (Gonsard,

Genet and Drummond, 2024). Reliable digital twins require high data accuracy and high data quality, as incomplete or inaccurate data can result in unreliable insights and flawed representations.

1.6 Application of modelling in Asthma

Around 300 million people are affected by asthma worldwide (Stern, Pier and Litonjua, 2020; Porsbjerg *et al.*, 2023). It is an airways disease defined by irregular contraction of the muscular coat of the bronchi (bronchospasm) characterised by airway hyper-responsiveness (AHR) - excessive narrowing of the airways/ bronchoconstriction in response to stimuli which would have no or little effect in healthy individuals (Bradding *et al.*, 2024), airway inflammation, mucus hypersecretion, all contributing to variable airflow obstruction, but with inhomogeneous underlying inflammatory mechanisms causing symptoms such as tightness of chest, dyspnoea, cough, phlegm and wheezing (Porsbjerg *et al.*, 2023). Symptoms occur in response to triggers such as cold air, exercise, allergens, viral infections, occupational exposures, smoking, pollution and emissions or occur spontaneously (Porsbjerg *et al.*, 2023). Some patients experience asthma attacks (exacerbations) with more persistent and noticeable symptoms. Asthma diagnosis is essentially based on a combination of the patient's history (family history and symptoms) and demonstration of variable airflow limitation which can be identified through spirometry with reversibility testing and bronchial challenge testing. Asthma is also characterised by ventilation heterogeneity (VH) (Downie *et al.*, 2007; Svenningsen *et al.*, 2016; Cottini *et al.*, 2023) which can be captured clinically using physiologic tidal breathing techniques measuring inhomogeneities in ventilation such as the multiple breath washout (MBW) (Subbarao *et al.*, 2015; Stanojevic, Bowerman and Robinson, 2021), and mechanical behaviour such as the forced oscillation technique (FOT) – both helpful in assessing asthma patients with preserved spirometry and potential small airways disease (SAD) (Kim *et al.*, 2020).

During an FOT test (Kaminsky *et al.*, 2022), sound waves are superimposed on normal tidal breathing and lung resistance and reactance (real and imaginary parts of impedance) are

calculated. An established CT-imaging-informed FOT model demonstrated that peripheral airway resistance R_5-R_{20} is a direct measure of anatomical small airway narrowing (Foy *et al.*, 2019) through the assessment of the impact of airway branch radii perturbation on R_5-R_{20}. The results however demonstrated only modest concordance with measurements, suggesting that there was room for simulation improvement of this concordance (Foy *et al.*, 2019) through model optimisation. This FOT model utilises imaging-extracted airways to calculate impedance (Foy *et al.*, 2019) by summation of branch impedances assuming branches are cylinders functioning under acoustic impedance theory (Daniels, 1950; Thurston, 1952) connected to terminal bronchioles, subtended by the constant-phase model (CPM) (Bates *et al.*, 2011). The CPM is derived from power-law stress relaxation – the response of lung's tissue under lung volume increase over time (i.e., inspiration). Fourier transform of this law, transforms time space to frequency space resulting to the CPM equation composed of tissue parameters damping (G) and elastance (H) (Bates *et al.*, 2011). Impedance is then added to chest-wall, and glottal contributions to impedance and to cheek and upper airway shunting (Strohl, Butler and Malhotra, 2012; Bhatawadekar, Leary and Maksym, 2015). Simulations are sensitive to CPM parameters therefore personalising them can improve simulations' concordance with measurements. As no method is available to infer these viscoelastic tissue parameters from imaging, prediction of patient-specific CPM parameters can therefore be useful for optimisation of the FOT mathematical model.

This study holds promise for providing insights into the localised nature of VH and blood-gas barrier dysfunction, facilitating more targeted interventions in respiratory disease management. The development of a CO gas-transfer digital-twin and optimisation of the FOT model show potential and are aimed to contribute to the development of the complete pulmonary "monitoring patient digital twin" with the addition of these new and optimised "simulation patient digital twins".

2. Forced Oscillation Technique – model optimisation

2.1 Rationale

As discussed in the first chapter of this thesis, connecting the structure to the function of the lungs is the basis of medical diagnosis and supports our understanding of the mechanisms of the respiratory system. Current challenges faced in respiratory disease include early diagnosis to allow early intervention before organ damage becomes irreversible. Various tools have been developed in the diagnosis and assessment of chronic respiratory diseases including the MBW, and FOT which are both useful in the assessment of VH, a characteristic feature of asthma. Advancements in technology have allowed the development of advanced imaging techniques for the assessment of the localised nature of VH however, these are limited in their ability to simulate unseen hypothetical scenarios to provide insight into potential underlying mechanisms. The combination therefore of imaging techniques with computational models has emerged as an advanced method which utilises the structural information of the lungs extracted from medical imaging as well as the physics governing the function of pulmonary function test of VH (MBW,FOT) and the respiratory system. Similar models representing different pulmonary functions, characterised as "simulation patient digital twins" can be combined together, along with advanced monitoring equipment and machine learning techniques to form the desired "monitoring patient digital twin". The development of this however will require optimised, near-perfect "simulation patient digital twins" making optimisation of existing models vital. As explored in the literature, the results simulated by a published FOT mathematical model (Foy *et al.*, 2019) infer that there is room for improvement in the simulation accuracy of this model. In this chapter, we utilised clinical and imaging-extracted data from the large cohort ATLANTIS (Assessment of Small Airways Involvement in Asthma) which included asthmatic patients and healthy volunteers, to optimise the FOT mathematical model by the development and addition of two linear regression models which predicted subject-specific CPM viscoelastic parameters, tissue damping (G) and elastance (H).

2.2 Materials and methods

2.2.1 Data Collection

The ATLANTIS dataset consisted of 872 individuals who were enrolled in the cohort, out of which 773 were asthmatic patients and 99 were healthy volunteers. Out of the 872 individuals who were enrolled and contributed to baseline data, 349 individuals had a CT scan taken. Medical imaging CT scans (n=349) were acquired at Residual Volume (RV) and Total Lung Capacity (TLC) in the ATLANTIS study out of which 71 individuals' scans failed segmentation. Quantitative CT (qCT) markers were derived from these scans for 278 individuals using the Michigan Topographic Analysis Pipeline (Mi-TAP). Centrelines of the upper airways were extracted following segmentation of the upper airways of the CT scans using YACTA (Yet Another CT Analyzer). The segmentations were patient-specific to generations 6-10, and the trees were then algorithmically generated to the terminal bronchioles' depth. Following the segmentation of the upper airways for 278 individuals, as seen in the consort diagram **Figure *4***, the diameter and length of each branch were calculated, and assigned to centrelines of the segmented airways. The airway trees were then algorithmically grown from the upper airway centrelines to complete conducting zone airway trees using previously reported patient-based algorithms in MATLAB (Mathworks) (Bordas *et al.*, 2015; Bell *et al.*, 2019; Foy *et al.*, 2019). This work was completed by Alexander Bell at Michigan Medicine who provided the full conducting airway lung structures as well as the qCT markers. At Imperial College, the complete conducting airway tree structures underwent quality control which led to the initial exclusion of 29 individuals due to the generation of branch radii with a value of zero. Further 33 individuals were excluded from this study due to lack of data for impulse oscillometry (IOS) test outputs R5, R20, R5-R20, and X5, which are statistically significant in the asthmatic cohort as compared to the healthy controls **Table 1**. Finally, 56 individuals were excluded from the study due to identified spurious distal, tracheal, and bronchial branch growths in their segmented airway tree structures - leading to the final study population number of 160 individuals out of which 135 were asthmatic patients, and 25 were healthy controls.

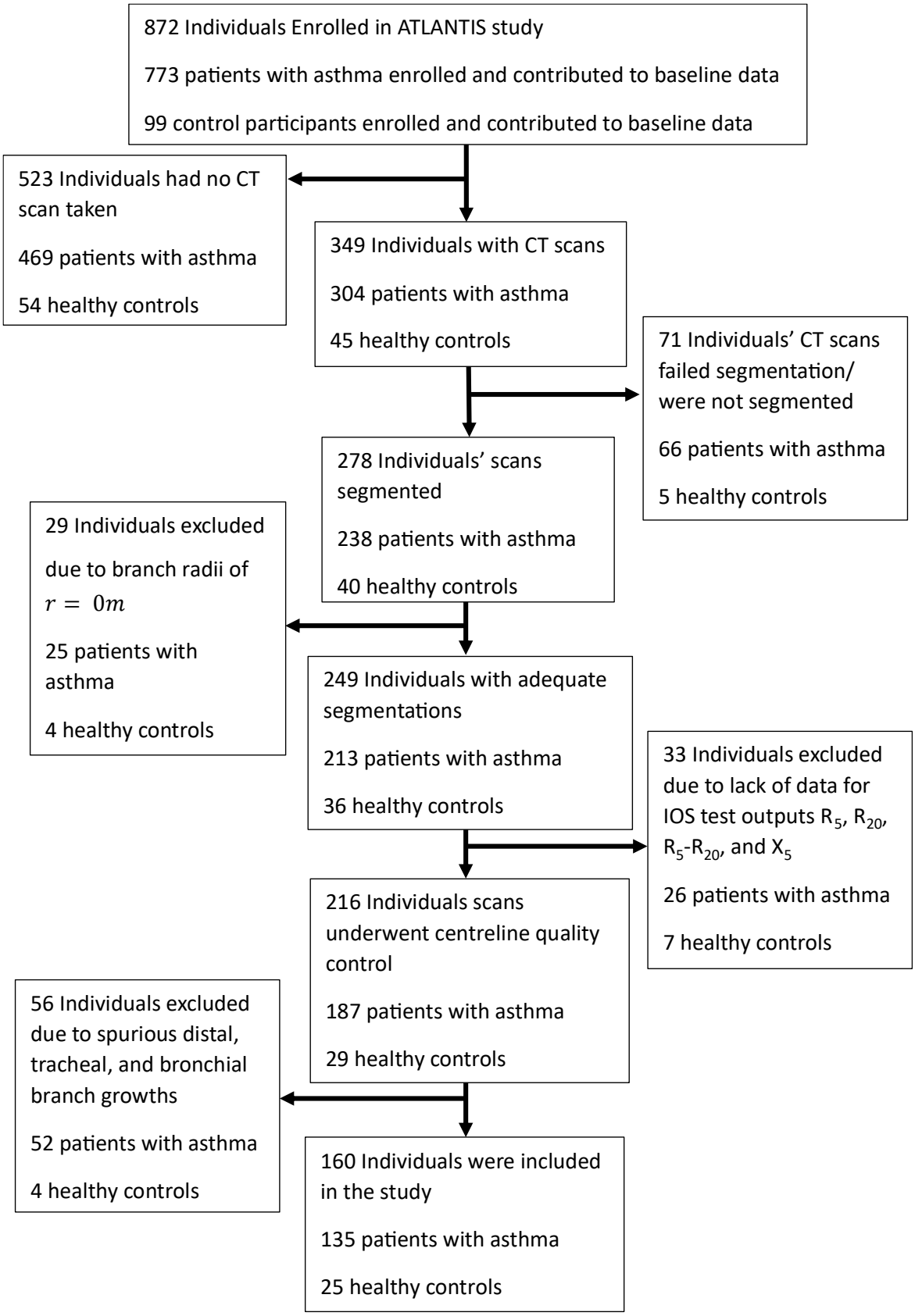


Figure 4 – ATLANTIS Consort Diagram.

The diagram presents the initial number of individuals enrolled in the ATLANTIS study (n=872) at the top. Following inclusion and exclusion criteria as shown on the right and left of the diagram, a group of individuals (n=160) were finally selected to participate in this FOT model optimisation study.

2.2.2 Scaling of lung structures

The complete conducting airway trees were segmented from CT scans taken at total lung capacity (TLC), therefore the resulting algorithmically grown complete conducting airway trees, as received from Michigan Medicine, reflected lungs at full inspiration. In order to make the FOT simulations as realistic as possible, the complete conducting zone centreline structures underwent scaling to reflect the typical volume of the lungs during the test. To approximate this volume, it is important to understand how the test is implemented in a clinical setting. Finally, for clarity and to facilitate a more comprehensive understanding of this subsection, an illustration of the lung volumes arising from spirometry was included which can be seen in **Figure *5***.

According to the European Respiratory Society's (ERS) technical standards for respiratory oscillometry (FOT), measurements of the test are taken during quiet tidal breathing (King *et al.*, 2020). Another publication, (Oostveen *et al.*, 2003) stated that the test is implemented during normal breathing, however this was considered to be the functional residual capacity (FRC) in this case. Since FRC is the volume of air remaining after normal exhalation, also termed resting expiration (Lutfi, 2017), it does not account for the tidal volume during breathing, i.e., the resting inspiration - which is the volume of the lungs after a full inspiration at rest, during normal breathing - making FRC an underestimation of the lungs' volume during the test. The typical contribution of FRC to TLC in normal adult lungs was found to be about 50% and the typical contribution of tidal volume (VT) to TLC around 15% in Fig. 2.8 "Static lung volumes of Dr Nunn in 1990" (Lumb and Thomas, 2021b) which broadly agrees with static lung volume values in (Bhakta *et al.*, 2023) where the FRC to TLC contribution is around 49%, and the VT to TLC contribution around 11%. Assuming therefore that VT, ranging

between 11% and 15% of TLC can have a mean value of 13% and that FRC is 50% of TLC, the resting inspiratory volume (FRC+VT) can be estimated to be 63%. Since the FOT test takes measurements at both resting expiration (FRC) and resting inspiration (FRC + VT), to account for both states that the lungs oscillate between during the test, in this study it was deemed appropriate to assume that the test is implemented at FRC + VT/2, therefore at approximately 56.5% of TLC, reflecting a snapshot halfway through normal tidal breathing or VT in healthy individuals. In asthma, FRC was found to change similarly in direction and magnitude with RV (Woolcock and Read, 1966). Due to air-trapping the RV contribution to TLC tends to be elevated compared to the general population. This RV/TLC increase tends to range from 11% (Schiffers *et al.*, 2022), to 24% in severe asthma (Sorkness *et al.*, 2019). Taking into account this elevation of RV in asthma which corresponds to FRC changes, and given that the majority of this study's population is asthmatic, FRC was assumed to be 50% + 11% = 61%, which after addition of the half VT leads to an approximate volume representing the volume contribution to TLC of the lungs during the FOT test of 67.5% which was rounded up to 70% to account for the 37% of the study's population who are severe asthmatics.

The scaling of the complete conducting zone airway structures is not homogeneous across the airways of a bronchial tree structure. Airway mechanics change along the bronchial tree, with central airways being less compliant than the peripheral airways as described by the relationship between transmural pressure and airway area (Lambert *et al.*, 1982). In a study for the development of a computational model for expiratory flow, Lambert and colleagues reported the relationship of between airway fractional cross-sectional area (as compared to maximal airway area at full inflation) for 16 Weibel (Weibel and Gomez, 1962) generations of bifurcations (Lambert *et al.*, 1982). While this method addressed the heterogeneity of airway mechanics, it only provided scaling for 16 (Weibel) generations of bifurcations, while many of the complete conducting zone airway trees were composed of more generations of bifurcations.

Carl Whitfield from the University of Manchester, suggested that extension of the scaling to airway generations lager than 16, was addressed by (Hedges and Tawhai, 2016) where model coefficients were interpolated from Weibel generations to Horsfield orders to generalise the model to an asymmetric tree. Highest order coefficients were set equal to values for Weibel generation zero, for Horsfield order of one were set equal to values for Weibel generation 15 and for orders in between, a linear logarithmic decrease was followed with order. In this study, the same method was used for the scaling of the lung structures.

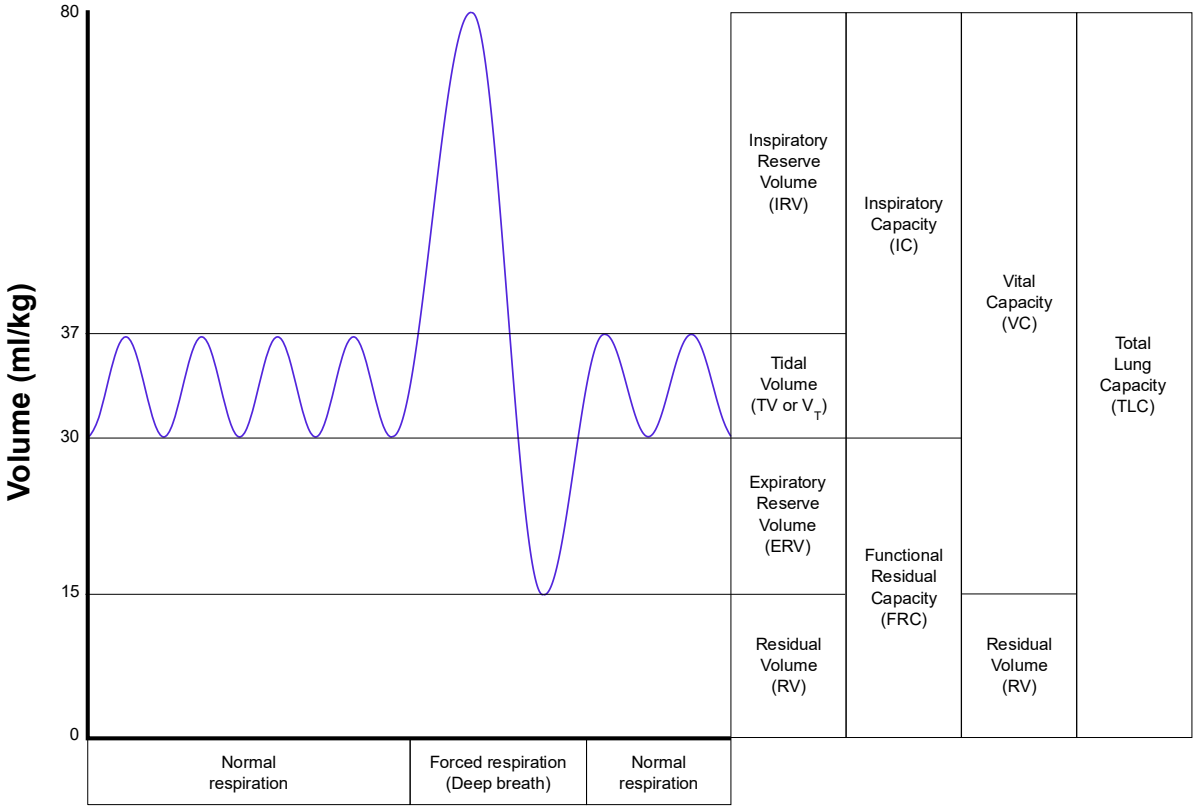


Figure 5 – Illustration of lung volumes resulting from spirometry.

The unit of measurement ml/kg denotes the amount of air inside the lungs in millilitres per unit of bodyweight as used for example in (Myrianthefs and Baltopoulos, 2013; Chan et al., 2019). The image represents the volume of air inside the lungs throughout normal breathing and forced breathing. Image reused from https://commons.wikimedia.org/wiki/File:Lungvolumes.svg, under creative commons license CC BY-SA 3.0: https://creativecommons.org/licenses/by-sa/3.0/deed.en

Specifically, values per generation for the model parameters a_0, a_0', and n_2 of bronchial mechanical properties where sourced from (Lambert *et al.*, 1982) Table 1, however the parameter α_0' - the slope of area-pressure curve at transpulmonary pressure difference of zero normalized on total maximal cross-sectional area that is available to flow in a generation – was corrected through its multiplication by 1000, as used correctly in a later study conducted by Lambert (Lambert and Beck, 2004). For an individual lung structure, the below parameters denoted in the equations below represent arrays of numbers, each representing a generation of bifurcations.

$$P_2 = -n_2 * \frac{a_0}{a_0'}$$

$$a = 1 - (1 - a_0)\left(1 - \frac{P}{P_2}\right)(-n_2)$$

In the above equation, P represents the transmural pressure which was approximated based on the lung volume percentage contribution to TLC. As mentioned previously, the scaling chosen was 70% of TLC corresponding to a transpulmonary pressure of approximately $P{\sim}7\ cmH_2O$ according to (Lambert *et al.*, 1982) Figure 2. To scale the radii of the branches, their geometry was taken into account having a cross-sectional area (A) equal to πr^2. In the equation below, A represents the cross-sectional area after scaling, and A_0 represents the cross-sectional area before scaling. Therefore, r represents the radius of the cross-sectional area before scaling and r_0 represents the cross-sectional area after scaling.

$$a = \frac{A}{A_0} = \frac{\pi r^2}{\pi r_0^2} \Rightarrow a = \frac{r^2}{r_0^2} \Rightarrow r^2 = a r_0^2$$

$$\therefore r = \sqrt{a}\sqrt{r_0^2} \Rightarrow r = r_0\sqrt{a}$$

The scaling factor for the radii here is therefore $\sqrt{a}$.

$$\therefore rscale = \frac{r}{r_0} = \sqrt{a}$$

The maximum Horsfield generation (trachea – Weibel generation 0) was mapped to the equivalent Weibel generation as below and alpha values were interpolated on a linear scale.

$$W = 16\left(1 - \frac{H}{H_{max}}\right)$$

The above was used to construct an array of numbers – with a size equal to the number H_{max} which is the maximum Horsfield generation (the trachea) – starting from 16 and ending at 0. The array of the scaling factor $rscale$ was then linearly interpolated with y being the interpolated scaling factor based on Horsfield generations $rscale_H$.

$$W1 = rounded\ to\ the\ nearest\ integer\ towards\ negative\ infinity$$

$$W2 = normally\ rounded\ to\ the\ nearest\ integer\ towards\ infinity$$

$$Linear\ Interpolation\ equation \Rightarrow y = y_1 + (x - x_1)\frac{(y_2 - y_1)}{(x_2 - x_1)}$$

$$y = rscale_{Horsfield}$$

$$y_1 = rscale\ at\ generation\ number\ W_1 = rscale(W_1)$$

$$y_2 = rscale\ at\ generation\ number\ W_2 = rscale(W_2)$$

$$x = W$$

$$x_1 = W_1$$

$$x_2 = W_2$$

$$\therefore rscale_H = rscale(W_1) + (W - W_1)\frac{(rscale(W_2) - rscale(W_1))}{(W_2 - W_1)}$$

Since the spacing is normalised and $W_2 - W_1 = 1$, therefore by multiplying each term by 1 gives

$$rscale_H = rscale(W_1)(W_2 - W_1) + (W - W_1)\frac{(rscale(W_2) - rscale(W_1))}{(W_2 - W_1)}(W_2 - W_1)$$

$$rscale_H = rscale(W_1)(W_2 - W_1) + (W - W_1)(rscale(W_2) - rscale(W_1))$$

$$rscale_H = W_2 rscale(W_1) - W_1 rscale(W_1) + W rscale(W_2) - W rscale(W_1) - W_1 rscale(W_2) + W_1 rscale(W_1)$$

$$rscale_H = rscale(W_1)(W_2 - W_1 - W + W_1) + rscale(W_2)(W - W_1)$$

$$\therefore rscale_H = rscale(W_1)(W_2 - W) + rscale(W_2)(W - W_1)$$

The above equation provides an array of length H_{max} composed of interpolated scaling factors for all the Horsfield generations. The radii of the structures were then scaled by the corresponding scaling factor interpolated for each Horsfield generation. The lengths of the branches of the complete conducting airway trees were scaled homogeneously with the cube root of the lungs' volume contribution to TLC (during the test) as implemented by Lambert (Lambert *et al.*, 1982). In this case, as the lung volume scaling was chosen to be 70%, this translates to a scaling of $0.7^{1/3}$ for all branch lengths.

While applying personalised scaling to the individuals' complete conducting airway structures based on their FRC and TLC values, could potentially lead to more accurate simulation results, this would require personalised VT values to accurately estimate a personalised structure scaling which were not available for use within the dataset. Investigation of the effect of personalised scaling based on patient-specific FRC, TLC and VT values remained outside of the scope of this study. This study therefore focused on the differences in asthma severity across the study cohort caused by the structural differences occurring from the CT scans, with structural differences emerging only from the patient-specific segmentations of the upper airways and no further personalised modifications applied.

2.2.3 Clinical Characteristics and Structure Morphology

The clinical characteristics of the asthma patients (n=135) and healthy individuals (n=25) included in the study can be seen in **Table 1** while the morphometric properties of the digital complete conducting airway tree structures of these individuals can be seen in **Table 2**. The morphology of the structures was assessed by comparison of the morphometric properties shown in **Table 2** with previously reported morphometric parameters of full conducting airway centreline structures (Bordas *et al.*, 2015). The radii of branches per generation were also assessed by comparison with reported radii per generation of bifurcations (Weibel and Gomez, 1962) as shown in **Figure 6A**.

Table 1 - Clinical Characteristics of individuals included in the study

	Healthy Participants (N = 25)	Participants with asthma (N = 135)	p-value
Baseline demographics			
Age, years	33 (28 - 52)	46 (29 - 55)	0.1271
Age at first diagnosis, years	-	18.57 (6.94 - 40.57)	
Duration of disease, years	-	19.24 (8.06 - 28.13)	
Sex, n (%)			0.9258
Male	11 (44%)	58 (43%)	-
Female	14 (56%)	77 (56%)	-
BMI (kg/m²)	24.14 (22.28 - 27.47)	26.37 (23.90 - 30.68)#	**0.0426**
Race			
Asian	-	5 (4%)	-
Black or African American	-	3 (2%)	-
More than one race	-	2 (1%)	-
Other	2 (8%)	4 (3%)	-
White/Caucasian	23 (92%)	121 (90%)	-
Smoking Status, n (%)			
Non-smoker	18 (72%)	99 (73.3%)	-
Ex-smoker	6 (24%)	28 (20.7%)	-
Current smoker	1 (4%)	8 (6.0%)	-
GINA treatment intensity			
1	-	27 (20%)	-
2	-	20 (15%)	-
3	-	38 (28%)	-
4	-	45 (33%)	-
5	-	5 (4%)	-
Any inhaled corticosteroids (ICS)	-	48 (35.6%)	-
Mean ICS dose (µg/24 hours)	-	320 (200 - 400)	-
Systemic Corticosteroids, n (%)	-	4 (3.0%)	-
Number of exacerbations (within 12 months prior to study entry)			
0	-	118 (87.4%)	-
1	-	8 (6.0%)	-
2	-	6 (4.4%)	-
3	-	0 (0%)	-
4	-	2 (1.5%)	-
5	-	0 (0%)	-
6	-	1 (0.7%)	-
Baseline Questionnaires			
ACQ-6 score	-	1 (0.50 - 1.67)	-
ACT score	-	21 (19 - 23)	-
EuroQoL score-5D-5L	-	85 (72.5 - 90)	-
Blood differential cell counts			
Eosinophils (10^9/L)	0.20 (0.10 - 0.27)	0.22 (0.12 - 0.39)#	**0.0341**

	Healthy Participants (N = 25)	Participants with asthma (N = 135)	p-value
Neutrophils (10^9/L)	3.70 (2.95 - 4.41)	3.47 (2.79 - 4.41)	0.6913
Lymphocytes (10^9/L)	1.87 (0.54)	1.90 (0.53)	0.7873
Monocytes (10^9/L)	0.40 (0.36 - 0.59)	0.48 (0.38 - 0.58)	0.2823
Sputum differential cell counts			
Eosinophils (% of non-squamous cells)	0.30 (0.30 - 0.45)	1.65 (0.35 – 5.30)	0.2383
Neutrophils (% of non-squamous cells)	60.50 (45.75 - 76.30)	40.35 (20.60 - 60.25)	0.2821
Macrophages (% of non-squamous cells)	36.60 (21.25 - 48.75)	46.95 (23.40 - 65.15)	0.9590
Lymphocytes (% of non-squamous cells)	0.80 (0.43 - 1.30)	0.70 (0.38 - 1.23)	0.6103
Lung physiology			
Body Box TLC (L)	5.96 (0.90)	5.92 (1.34)	0.5326
Body Box RV/TLC	0.30 (0.08)	0.34 (0.10)	0.1412
FeNO at 50ml/s	14 (9.75 - 25)	27.5 (17.5 - 37)##	**0.0028**
R_5 [kPa/L/s]	0.37 (0.10)	0.50 (0.17)###	**<0.001**
R_{20} [kPa/L/s]	0.32 (0.06)	0.38 (0.10)##	**0.0024**
$R_5 - R_{20}$ [kPa/L/s]	0.03 (0.02 - 0.06)	0.10 (0.05 - 0.18)###	**<0.001**
X_5 [kPa/L/s]	-0.11 (-0.12 to -0.08)	-0.14 (-0.21 to -0.11)##	**0.0072**
AX [Hz*kPa/L/s]	0.25 (0.17 - 0.63)	0.75 (0.33 – 2.00)##	**0.0015**
S_{acin}*VT(L)	0.10 (0.07 - 0.13)	0.11 (0.08 - 0.17)	1.00
S_{cond}*VT(L)	0.02 (0.01 - 0.03)	0.04 (0.02 - 0.06)	0.3021
FEV_1 % of predicted normal value (%)	98.94 (12.48)	81.81 (18.76)###	**<0.001**
FVC % of predicted normal value (%)	103.33 (13.70)	97.51 (15.56)	0.0829
FEF_{25-75} units	3.14 (1.05)	1.97 (1.11)###	**<0.001**
FEF_{50} units	3.79 (0.94)	2.43 (1.17)###	**<0.001**
FEV_1/FVC	0.79 (0.06)	0.68 (0.11)###	**<0.001**

Data presented as n (%), median(IQR) for non-parametric data, and μ(σ) for normally distributed parametric data. Normality of the datasets was assessed using a Kolmogorov-Smirnov test, after normalisation of data (normalised data = (x-μ)/σ) followed by the calculation of p-values using a Mann-Whitney U-test for parametric data and a two-sample t-test for non-parametric data.

#p < 0.05 compared to healthy control group

##p < 0.01 compared to healthy control group

###p < 0.001 compared to healthy control group

Table 2 - Morphometric properties calculated from bifurcations of the lung structures

	All (n=160)	*Healthy (n=25)*	*Mild Asthma (n=27)*	*Moderate Asthma (n=58)*	*Severe Asthma (n=50)*
θ	21.23 (21.10 – 22.35)	21.27 (21.17 – 42.78)	21.19 (21.13 – 21.53)	21.19 (21.06 – 21.40)	21.23 (21.10 – 45.97)
θ $(D_{parent}>4mm)$	58.21 ± 8.80	59.15 ± 7.05	57.39 ± 7.60	58.76 ± 9.34	57.54 ± 9.67
θ $(4mm>D_{parent}>3mm)$	31.77 (14.88 – 62.34)	49.85 ± 40.76	37.74 ± 34.15	40.05 ± 30. 64	39.77 ± 30.75
θ $(3mm>D_{parent}>2mm)$	26.28 (15.42 – 47.33)	35.95 ± 24.43	40.33 ± 37.44	34.14 ± 23.50	32.19 ± 21.67
θ $(2mm>D_{parent}>1mm)$	21.53 (12.49 – 39.50)	32.17 ± 28.29	30.16 ± 18.55	19.90 (12.22 – 36.87)	20.65 (12.29 – 29.71)
φ	102.57 (102.10 – 102.87)	102.71 (102.37 – 103.03)	102.58 (102.03 – 102.99)	102.63 (102.23 – 102.84)	102.34 (99.29 – 102.80)
L/D	4.61 ± 0.53	4.39 ± 0.42	4.59 ± 0.57	4.57 ± 0.47	4.79 ± 0.59#
L/D_{minor}	5.13 ± 0.591	4.88 ± 0.46	5.11 ± 0.63	5.08 ± 0.52	5.32 ± 0.65#
L/D_{major}	4.92 ± 0.57	4.68 ± 0.45	4.90 ± 0.61	4.88 ± 0.50	5.10 ± 0.63#
D_{minor}/D_{major}	0.97 ± 0.00033	0.97 ± 0.00032	0.97 ± 0.00035	0.97 ± 0.00033	0.97 ± 0.00031
D/D_{parent}	0.42 ± 0.00014	0.42 ± 0.00014	0.42 ± 0.00016	0.42 ± 0.00014	0.42 ± 0.00013
D_{minor}/D_{parent}	0.91 ± 0.00023	0.91 ± 0.00022	0.91 ± 0.00026	0.91 ± 0.00023	0.91 ± 0.00020
D_{major}/D_{parent}	0.94 ± 0.00018	0.94 ± 0.00011	0.94 ± 0.00016	0.94 ± 0.00019	0.94 ± 0.00020
L/L_{parent}	0.47 ± 0.014	0.47 ± 0.0014	0.47 ± 0.0015	0.47 ± 0.0014	0.47 ± 0.0014
$L1/L2$	0.50 ± 0.0042	0.50 ± 0.0044	0.50 ± 0.0043	0.50 ± 0.0040	0.50 ± 0.0041

Morphometric properties of the scaled complete conducting airway trees accounting for bifurcations. Data presented as median(IQR) for non-parametric data, and μ±σ for normally distributed parametric data. Normality of the datasets was assessed using a Kolmogorov-Smirnov test, after normalisation of data (normalised data = (x-μ)/σ) followed by the calculation of p-values using a one-way Analysis of Variance (ANOVA) test for parametric data and a Kruskal-Wallis test for non-parametric data.

#p < 0.02 compared to healthy control group

Table 3 - Description of morphometric markers – For each individual, these markers represent the mean value obtained by averaging measurements across the full conducting airway tree.

Marker	*Description*
θ	Branching angle – the angle between a parent airway and each of its daughter airways
$\theta(D_{parent}>4mm)$	Branching angle – the angle between a parent airway with a diameter larger than 4mm and each of its daughter branches
$\theta\ (4mm>D_{parent}>3mm)$	Branching angle – the angle between a parent airway with a diameter between 3mm and 4mm and each of its daughter airways
$\theta\ (3mm>D_{parent}>2mm)$	Branching angle – the angle between a parent airway with a diameter between 2mm and 3mm and each of its daughter airways
$\theta\ (2mm>D_{parent}>1mm)$	Branching angle – the angle between a parent airway with a diameter between 1mm and 2mm and each of its daughter airways
φ	Rotation angle – the angle between the plane formed by the parent airway and its sibling branch and the plane formed by the daughter airways.
L/D	Dimensionless marker describing the ratio of airway length to airway diameter
L/D_{minor}	Dimensionless marker representing the ratio of airway length to the diameter of the daughter airway with the smaller diameter
L/D_{major}	Dimensionless marker representing the ratio of airway length to the diameter of the daughter airway with the larger diameter
D_{minor}/D_{major}	Dimensionless marker representing the ratio of the diameters of the smaller and larger daughter airways

Marker	*Description*
D/D_{parent}	Dimensionless marker representing the ratio of each daughter airway diameter to the diameter of its parent airway
D_{minor}/D_{parent}	Dimensionless marker representing the ratio of the diameter of the smaller daughter airway to the diameter of its parent airway
D_{major}/D_{parent}	Dimensionless marker representing the ratio of the diameter of the larger daughter airway to the diameter of its parent airway
L/L_{parent}	Dimensionless marker representing the ratio of the length of each daughter airway to the length of its parent airway
L1/L2	Dimensionless marker representing the ratio of the lengths of the two daughter airways

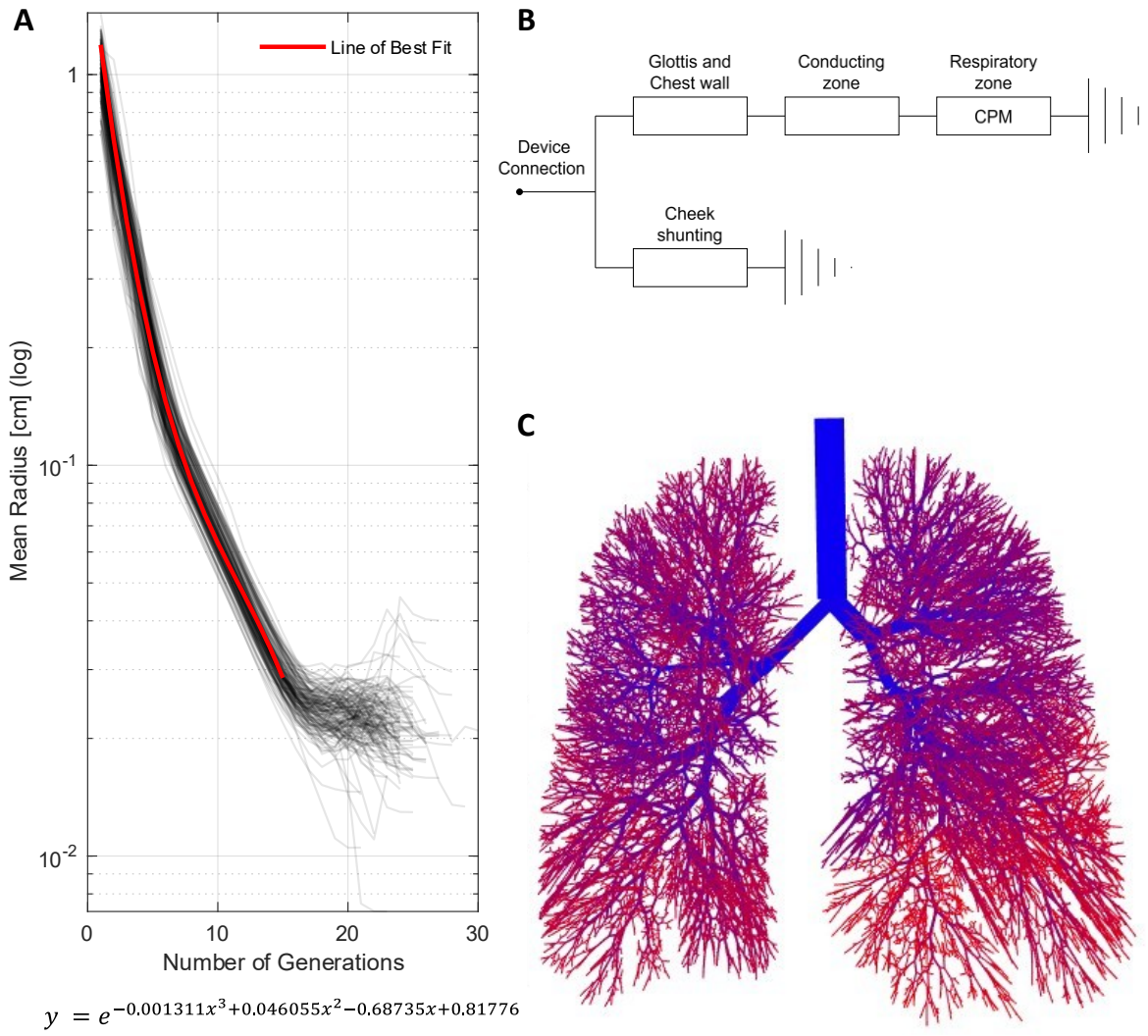


Figure 6 – Overview of the FOT Mathematical model and the full conducting zone airway lung structures

(A) Complete conducting airway structures (n=160) and the mean radius of their branches per generation of bifurcations. (B) Forced Oscillation Technique (FOT) model and its components for which the conducting cone is represented in (C) and the respiratory zone by the constant-phase model (CPM). (C) Complete conducting airway 3D structure of a 64-year-old female patient with severe asthma (GINA 5). Blue branches represent larger radii while red branches represent smaller radii.

2.2.4 Imaging biomarkers

Inspiratory and expiratory CT scans from the ATLANTIS cohort were analysed at Michigan University. Imaging biomarkers that were derived from the CT scans and were utilised in this study can be seen along with their units and descriptions in **Table 4**. The importance of these markers in asthma was assessed through their separation across asthma severity groups.

Table 4 –Imaging Biomarkers and their description

Imaging Biomarker	Unit	Description
Delta_HU (ΔHU)	HU	Difference between Exp_HU and Ins_HU (Exp_HU – Ins_HU)
Exp_Vol	liters	Whole lung volume (segmented VOI) at expiration (exp).
Exp_HU	HU	Mean HU (Hounsfield unit) of segmented lungs at exp.
Ins_Vol	liters	Whole lung volume (segmented VOI) at inspiration (ins).
Ins_HU	HU	Mean HU of segmented lungs at ins.
Exp_856	%	% of segmented lung < -856 HU at exp (gas trapping)
Ins_950	%	% of segmented lung < -950 HU at ins (emphysema)
Ins_810	%	% of segmented lung ≥ -810 HU at ins and < -250 HU
Ins_810low	%	% of segmented lung ≥ -810 HU at ins and < -500 HU
Ins_500	%	% of segmented lung ≥ -500 HU at ins and < 0 HU
Ins_GGOI	%	% of segmented lung ≥ -810 HU at ins and < -700 HU
Ins_FIBI	%	% of segmented lung ≥ -810 HU at ins and < -250 HU
scatnetAT_pct	%	% of segmented lung classified by ScatterNet as Air Trapping on Exp
scatnetAT_mean	HU	Mean HU of ScatterNet Air Trapping segmentation
scatnetEmph_pct	%	% of segmented lung classified by ScatterNet as Emphysema on Ins
scatnetEmph_mean	HU	Mean HU of ScatterNet Emphysema segmentation
NUM_VESSELS	N/A	Number of blood vessel voxels
NUM_COMPONENTS	N/A	Number of blood vessels identified
NUM_ENDPOINTS	N/A	Number of terminal vessels in vessel tree(s)
WallPct_3_8_1	%	Average area of the airway wall % for airway generations 3 to 8
WallPct_3_8_2	%	Number of points used for calculation of mean (above)
Wall_pct_1	%	Area of airway wall % for the entire segmented tree
Wall_pct_2	%	Number of points used for calculation of mean (above)
Pi10	mm	Mean wall thickness of airways normalized to a 'theoretical' airway lumen of 10-mm inner perimeter
Pi15	mm	Mean wall thickness of airways normalized to a 'theoretical' airway lumen of 15-mm inner perimeter
BEI	N/A	Bronchiectasis index
BEI_gen	N/A	Number of generations used for calculation of BEI (above)
WT_seg	mm	Average wall thickness of the segmental airways
WT_subseg	mm	Average wall thickness of the subsegmental airways
xPFavg (ΔHU^{AP})	HU	Lung spatial deformation gradient in the anterior-posterior axis
zPFavg (ΔHU^{IS})	HU	Lung spatial deformation gradient in the inferior-superior axis
ellArea	HU^2	Area of ellipse perceived in the joint density histogram (JDH)
ellAngle	rad	Angle between major and horizontal axes, of ellipse perceived in the joint density histogram (JDH)
Jac_mean	N/A	Mean value of the spatial Jacobian determinant resulting from image registration
Jac_var	N/A	Variance of the spatial Jacobian determinant – change in volume
dBlood_mean	HU	Change in HU between Ins and Exp attributed to differences in blood volume
dBlood_var	HU	Variance of dBlood

Imaging Biomarker	Unit	Description
PRM_1	%	Normal (sub-region)
PRM_2	%	Normal (sub-region)
PRM_3	%	Functional small airways disease
PRM_4	%	Emphysema (sub-region)
PRM_5	%	Emphysema (sub-region)
PRM_6	%	'Emptying emphysema'
PRM_8	%	Parenchymal disease (PD) (sub-region)
PRM_9	%	HAA (High Attenuation Area)/PD (sub-region)
PRM_10	%	HAA (High Attenuation Area)/PD (sub-region)
PRM_Norm	%	PRM_1+PRM_2 (normal lung) / PRM of Normal lung
PRM_fSAD	%	PRM_3 (functional small airways disease)
PRM_Emph	%	PRM_4+PRM_5 (emphysema)
PRM_PD	%	PRM_8+PRM_9+PRM_10 (parenchymal disease)
tPRM_norm_V	N/A	Average topological PRM (tPRM) relative to volume of Normal
tPRM_norm_S	mm^{-1}	Mean tPRM relative surface area of Normal lung
tPRM_norm_B	mm^{-2}	Mean relative mean breadth of Normal lung
tPRM_norm_X	N/A	Mean Euler characteristic (homology) of Normal lung
tPRM_fsad_V	N/A	Mean relative volume of fSAD regions
tPRM_fsad_S	mm^{-1}	Mean relative surface area of fSAD regions
tPRM_fsad_B	mm^{-2}	Mean relative mean breadth of fSAD regions
tPRM_fsad_X	N/A	Euler characteristic of fSAD regions
tPRM_emph_V	N/A	Mean relative volume of Emph regions
tPRM_emph_S	mm^{-1}	Mean relative surface area of Emph regions
tPRM_emph_B	mm^{-2}	Mean relative mean breadth of Emph regions
tPRM_emph_X	N/A	Mean Euler characteristic of Emph regions
tPRM_pd_V	N/A	Mean relative volume of PD regions
tPRM_pd_S	mm^{-1}	Mean relative surface area of PD regions
tPRM_pd_B	mm^{-2}	Mean relative mean breadth of PD regions
tPRM_pd_X	N/A	Mean Euler characteristic of PD regions

2.2.5 Mathematical assumptions for the FOT model

The mathematical FOT model uses the earlier derived analytical solution of the acoustic impedance equation (Daniels, 1950; Thurston, 1952) to estimate the impedance Z_j of a branch j, responding to a frequency f,

$$Z_j = \left(\frac{\omega \rho l_j}{\pi r_j^2}\right)\left(1 - \frac{2}{r_v\sqrt{-i}}\frac{J_1\left(r_v\sqrt{-i}\right)}{J_0\left(r_v\sqrt{-i}\right)}\right)^{-1} \qquad r_v = \left(\frac{\omega\rho}{\mu}\right)^{\frac{1}{2}} r_j$$

where μ and ρ are the dynamic viscosity and density of air respectively, angular frequency is represented by $\omega = 2\pi f$, r_j and l_j are radius and length of each branch, $i = \sqrt{-1}$ and J_1 and J_0 are the first and zeroth solutions to the Bessel equations. The constant-phase viscoelastic model is represented by Z_{acin} which is approximated at the end of each final bronchiole, given by the equation

$$Z_{acin} = \frac{N(G - iH)}{\omega^{\alpha}} \qquad \alpha = \frac{2}{\pi}\tan^{-1}\left(\frac{H}{G}\right)$$

where G represents the Tissue Damping and H represents the Elastance of the lung tissue (Kaczka *et al.*, 1997), and N is the number of total bronchioles. The model used in this study also accounted for chest wall, and glottal resistances taken from the literature as 0.5 cm $H_2O.s.L^{-1}$ each (Bhatawadekar, Leary and Maksym, 2015) as well as chest wall elastance taken as 10.6 cm $H_2O.s.L^{-1}$ (Bhatawadekar, Leary and Maksym, 2015) and added in series to airway tree impedance. Furthermore, cheek shunting was also taken into consideration and was therefore added in parallel to the rest of the airway tree model. Data for the shunting were taken from (Strohl, Butler and Malhotra, 2012) and interpolated through utilisation of least-squares method with models

$$R = \frac{a}{b + f}$$

$$X = c\log(f) + d$$

where the data-fitting parameters are a, b, c, and d calculated as follows,

if Shunt resistance at frequencies (f=5Hz, f=20Hz) is

shunt_res_5Hz = 1.7*10.197 cm $H_2O.s.L^{-1}$

shunt_res_20Hz = 1.3*10.197 cm $H_2O.s.L^{-1}$

$$aR = shunt_res_{5Hz} * bR + 5 * shunt_res_{5Hz}$$

$$bR = \frac{20 * shunt_res_{20Hz} - 5 * shunt_res_{5Hz}}{shunt_res_{5Hz} - shunt_res_{20Hz}}$$

$$shunt_{resistance} = \frac{aR}{bR + f}$$

and Shunt elastance at frequencies (f=5Hz, f=20Hz) is

shunt_elast_5Hz = -4.5*10.197 cm $H_2O.s.L^{-1}$

shunt_elast_20Hz = -1.15*10.197 cm $H_2O.s.L^{-1}$

$$aX = \frac{shunt_elast_{5Hz} - shunt_elast_{20Hz}}{\log(5) - \log(20)}$$

$$bX = shunt_elast_{5Hz} - aX * log(5)$$

$$shunt_elastance = aX * log(f) + bX$$

2.2.5 Simulation of the FOT in study cohort

The FOT test was initially simulated across the entire study cohort, as in the published literature, with constant CPM viscoelastic parameters tissue damping (G) and elastance (H) across the study participants. The results of the simulations, acted as validation of the observation from the literature review of chapter 1, which states that there is room for improvement in the FOT simulations, since the correlation between simulated and measured oscillometry outputs was poor as shown below.

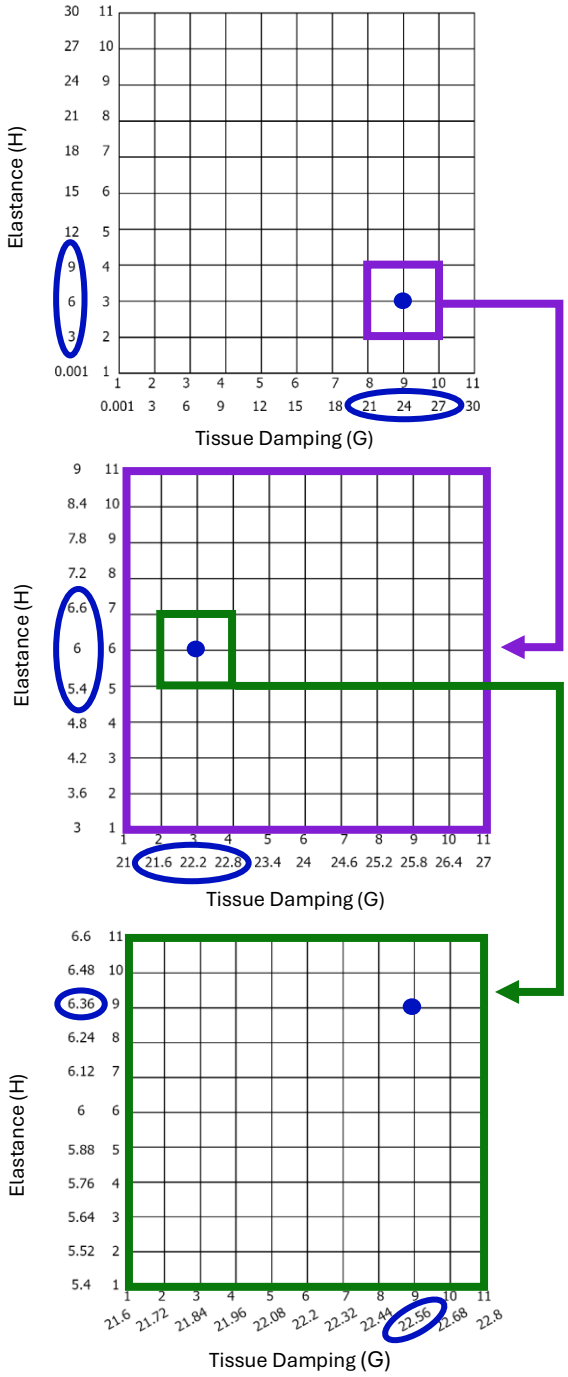
R^2(AX)=0 (ns), R^2(X_5)=0 (ns), R^2(R_5-R_{20})=0 (ns), R^2 (R_{20})=0.08 (p<0.001), R^2 (R_5)=0.12 (p<0.00001) (using previously reported (Foy *et al.*, 2019) G=0.12 kPa.L^{-1} = 1.22 cm$H_2O.L^{-1}$ .s^{-1} and H=0.57 kPa.L^{-1} = 5.81 cm$H_2O.L^{-1}$ .s^{-1} across all study participants

2.2.6 Tissue Parameter Identification through grid-search

To increase the concordance between simulated and measured FOT outputs, an adaptive grid search was implemented using the previously reported FOT model (Foy *et al.*, 2019). The grid search is described with visual aids in **Figure *7*** and was used to identify patient-specific viscoelastic CPM parameters G and H that mostly minimised the root mean squared error (RMSE) between measured and simulated oscillometry outputs R_5, R_{20}, R_5-R_{20}, X_5, and AX.

- Choice of a range for 11 equally spaced values G & H of 0.001 to 30 cmH2O/L/s
- Calculation of RMSE
- Identification of combination of G & H for which RMSE is lowest
- Construction of New Grid based on one point before and after the previously identified G and H points
- Repeating steps 1,2,3 to reach a more refined grid

- Calculation of RMSE
- Identification of Final G and H values i.e.,
- G = 22.56 cmH2O/L/s
- H = 6.36 cmH2O/L/s



$$RMSE = \sqrt{\frac{\left(\frac{|R5_S - R5_M|}{IQR(R5_M)}\right)^2 + \left(\frac{|R20_S - R20_M|}{IQR(R20_M)}\right)^2 + \left(\frac{|(R5_S - R20_S) - (R5_M - R20_M)|}{IQR(R5_M - R20_M)}\right)^2 + \left(\frac{|X5_S - X5_M|}{IQR(X5_M)}\right)^2 + \left(\frac{|AX_S - AX_M|}{IQR(AX_M)}\right)^2}{5}}$$

Figure 7 – Personalised viscoelastic CPM parameter identification through grid-search for FOT model optimisation

The grid search demonstrated in the figure was implemented over a range between 0.001 to 30 using an 11 x 11 evenly spaced grid. This was repeated three times, each time zooming in on

a narrower, 11 x 11 evenly spaced grid around the best values found in the previous iteration to eventually lead to the values of tissue damping (G) and elastance (H) that mostly minimised the RMSE between measured and simulated oscillometry outputs. Because only AX measurements were missing from the dataset for 9 asthmatic patients, the RMSE for these patients was calculated using the equation below, which excluded the AX component showed in **Figure** *7*.

$$RMSE = \sqrt{\frac{\left(\frac{|R5_S - R5_M|}{IQR(R5_M)}\right)^2 + \left(\frac{|R20_S - R20_M|}{IQR(R20_M)}\right)^2 + \left(\frac{|(R5 - R20_S) - (R5 - R20_M)|}{IQR(R5 - R20_M)}\right)^2 + \left(\frac{|X5_S - X5_M|}{IQR(X5_M)}\right)^2}{4}}$$

2.2.6 Validation of grid-search-obtained G and H

Clinical validity of the grid-search-obtained CPM parameters was assessed through their comparison with asthma severity, spirometry, questionnaire results, lung physiology, sputum differential cell counts, demographics as well as CT-derived imaging markers of regionalised airway closure.

2.2.7 Assessment of markers in across asthma severity

The CT-derived imaging biomarkers, and the morphometric markers calculated from the full conducting airway trees were assessed through their separation across asthma severity.

2.2.8 Prediction of G and H using imaging biomarkers

Following clinical validation of the grid-search-obtained CPM parameters, and assessment of the imaging biomarkers and morphometric markers to identify important markers, two multiple linear regression models were trained to predict G and H, acting as optimising components that when added to the FOT digital twin, could provide more accurate simulated FOT outputs.

To create the multiple linear regression models, the spearman correlation coefficient of each biomarker was plotted as a heatmap along with G and H to identify important markers. Statistically significant qCT markers were selected for the training of the models with high

spearman correlation coefficients for G and H. The markers chosen for the training of the linear regression models had the highest correlation coefficients with G and H while allowing for a similar number of biomarkers to be included in each model. The markers were statistically significant ($p<0.05$) and their spearman correlation coefficient was higher than 0.4 and lower than -0.4 for G (WallPct_3_8_1, Wall_Pct_1, Pi10, Pi15, jac_var) and higher than 0.3 and lower than -0.3 for H (PRM_Norm, tPRM_norm_V, PRM_1). All imaging biomarkers selected for G apart from "jac_var" belong in the same cluster as shown in the dendrogram in **Figure *12*** which demonstrates clusters of imaging biomarkers constructed using hierarchical clustering, an unsupervised machine learning method. All imaging biomarkers selected for G appear to significantly separate across asthma severity groups as shown in **Table *6***. For H, all selected imaging biomarkers belong in the same cluster as shown in the dendrogram in **Figure *12*** and also separate significantly across asthma severity groups as shown in **Table *6***. Description of each qCT marker can be found in **Table 4**. Following the training of the model using the entire dataset (n=160), the parameters were predicted using the models described below.

$$G = c_0 + c_1 WallPct_{3_{8_1}} + c_2 Wall_{Pct_1} + c_3 Pi10 + c_4 Pi15 + c_5 jac_{var}$$

$$c_0 = 1.58791674087206$$

$$c_1 = 0.16016521139192$$

$$c_2 = 0.112505087698083$$

$$c_3 = -3.31781299339777$$

$$c_4 = -8.57544065814801$$

$$c_5 = -1.84590206828466$$

The imaging biomarker "jac_var" was statistically significant in this model with a p-value of 0.02.

$$H = d_0 + d_1 PRM_{Norm} + d_2 tPRM_{norm_V} + d_3 PRM_1$$

$$d_0 = 5.50601231154348$$

$$d_1 = -2.14542659092669$$

$$d_2 = 209.935852510656$$

$$d_3 = -0.0138187202604582$$

The imaging biomarkers “PRM_Norm” and “tPRM_norm_V” were statistically significant in this model with p-values equal to 0.006.

Following training of the linear regression models, these were utilised in the prediction of CPM parameters G & H which were then used to simulate of the FOT outputs for the entire study cohort (n=160). The simulated oscillometry results which were obtained with the linear regression predicted CPM G & H parameters, were then compared with the measured FOT outputs to assess the models’ performance and whether model optimisation was achieved.

2.2.9 Validation of predicted G and H

Clinical validity of the predicted CPM parameters was assessed through their comparison with asthma severity, spirometry, questionnaire results, lung physiology, sputum differential cell counts, demographics as well as markers of regionalised airway closure.

2.3 Results

This section includes the results in three separate sections. The first two sections are similar in the structure as they only differ in the data used for the illustration of the results, apart from the qCT and morphometric markers used throughout. The first section includes results simulated with the grid-search-obtained CPM parameters, while the second section includes results obtained with the imaging biomarker-regressed CPM parameters. Finally, a results' summary relevant to the aim of this chapter is included in the third section of this subsection. The first results obtained demonstrating the correlation of simulated and measured outputs are shown below. The results show that there is room for improvement in the FOT simulations whether the simulations are implemented accounting for branch-level impedance only or implemented accounting for cheek shunting, glottal and chest wall resistance.

R^2(AX)=0 (ns), R^2(X_5)=0 (ns), R^2 (R_5-R_{20})=0 (ns), R^2 (R_{20})=0.08 (p<0.001), R^2 (R_5)=0.12 (p<0.00001) (using previously reported (Foy *et al.*, 2019) G = 0.12 kPa.L^{-1} = 1.22 $cmH_2O.L^{-1}.s^{-1}$ and H = 0.57 kPa.L^{-1} = 5.81 $cmH_2O.L^{-1}.s^{-1}$ across all study participants)

R^2(AX)=0.02 (ns), R^2(X_5)=0 (ns), R^2 (R_5-R_{20})=0.04 (p=0.007), R^2 (R_{20})=0.10 (p<0.001), R^2 (R_5)=0.12 (p<0.001) (using previously reported (Foy *et al.*, 2019) G = 0.12 kPa.L^{-1} = 1.22 $cmH_2O.L^{-1}.s^{-1}$ and H = 0.57 kPa.L^{-1} = 5.81 $cmH_2O.L^{-1}.s^{-1}$ across all study participants – Only accounting for branch impedance)

2.3.1 Grid-search for personalised G & H identification

Simulated oscillometry results using the grid-search obtained, personalised CPM parameters G and H, significantly increased the correlation between simulated and measured outputs as shown below and on **Figure *8***, indicating the importance of personalisation.

R^2(AX)=0.61, R^2(X_5)=0.70, R^2 (R_5-R_{20})=0.44, R^2 (R_{20})=0.34, R^2 (R_5)=0.60 p<0.001 (using personalised grid-search-obtained G and H)

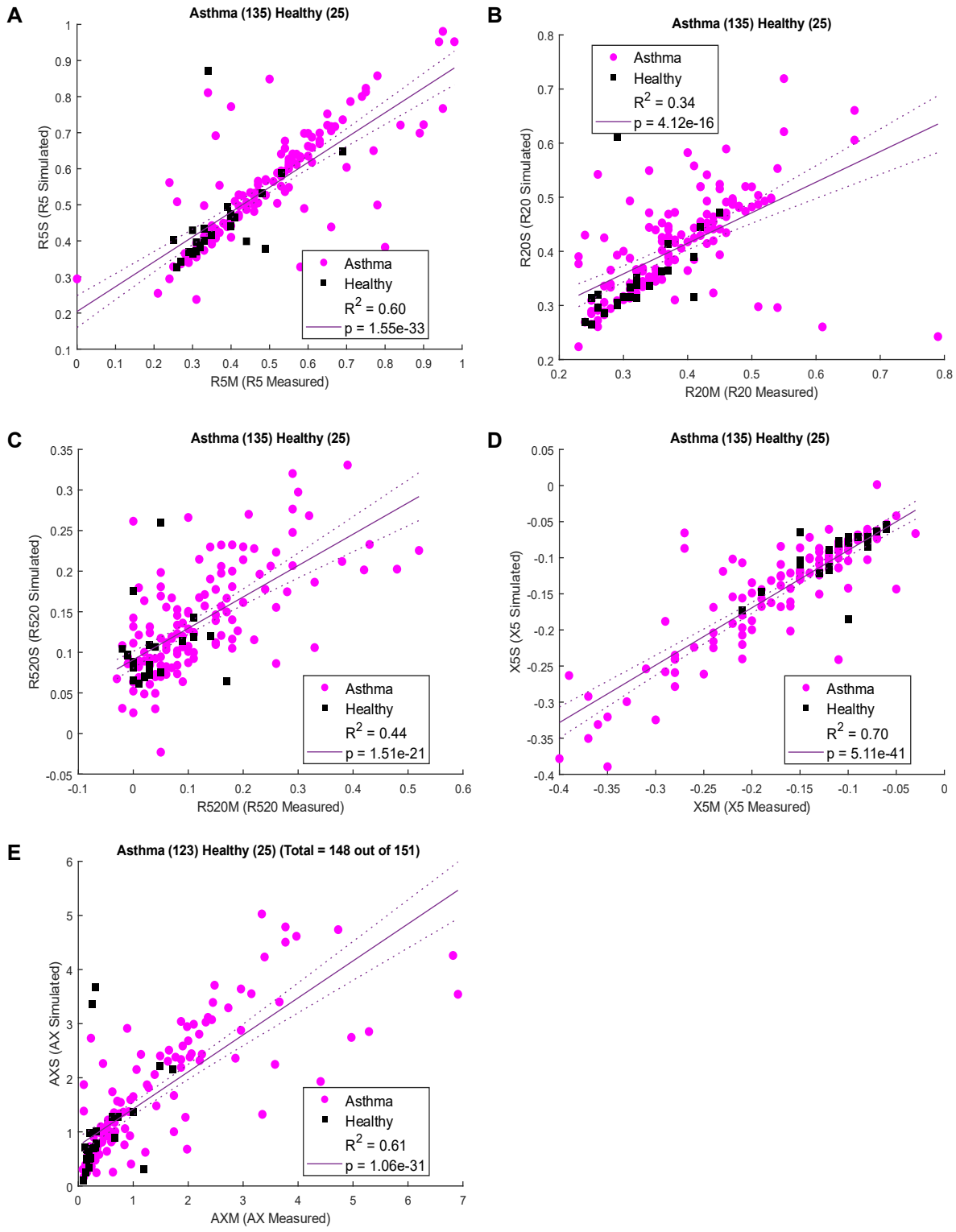


Figure 8 – FOT outputs R_5, R_{20}, R_5-R_{20}, X_5, and AX simulated with personalised viscoelastic CPM parameters G and H post grid-search, against their in-clinic measured corresponding values

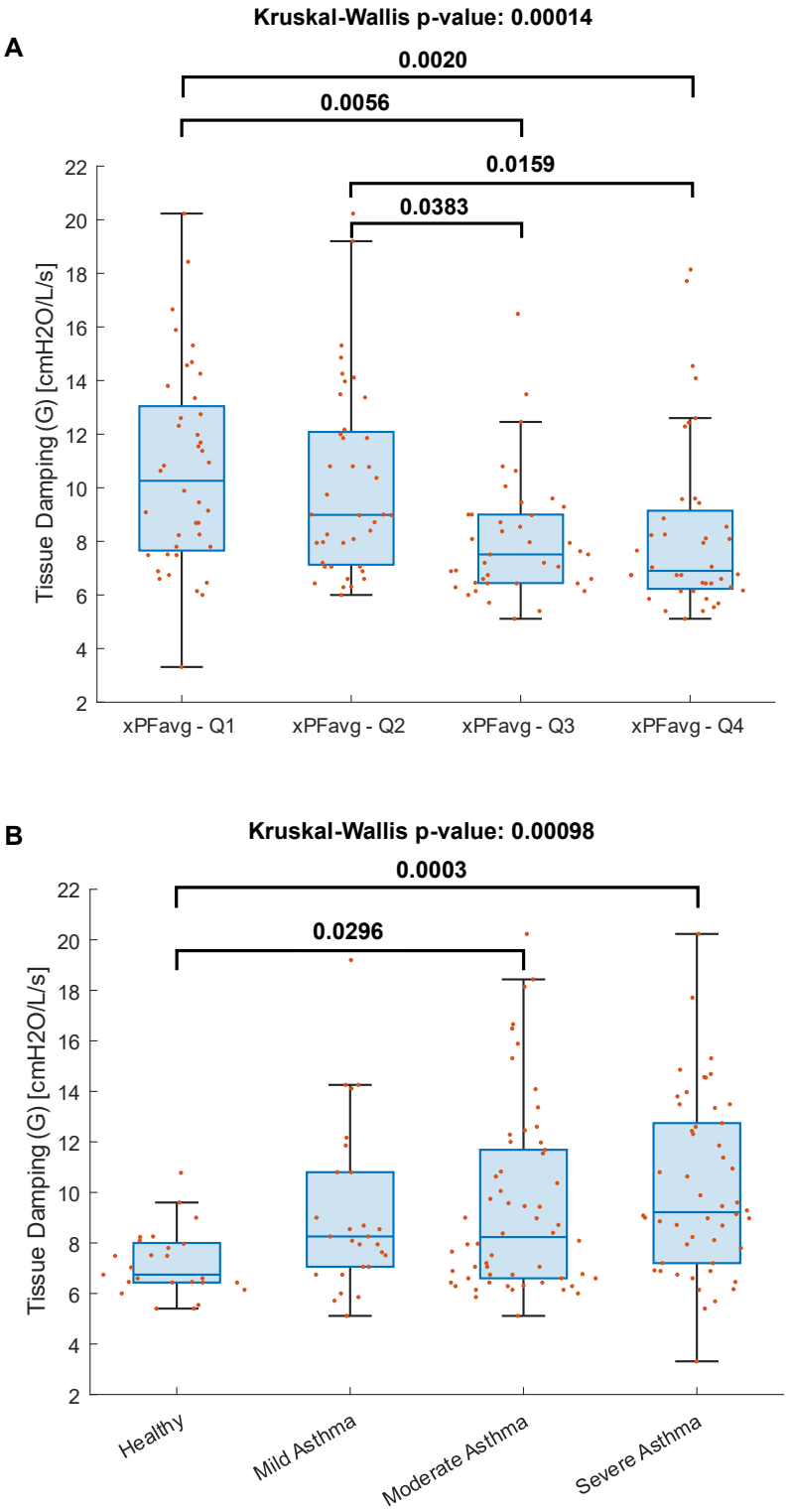


Figure 9 – Personalised grid-search-obtained Tissue Damping (G) separation across (A) xPFavg or ΔHU^{AP} quartiles – which represents lung spatial deformation gradient in the anterior-posterior axis and (B) asthma severity groups.

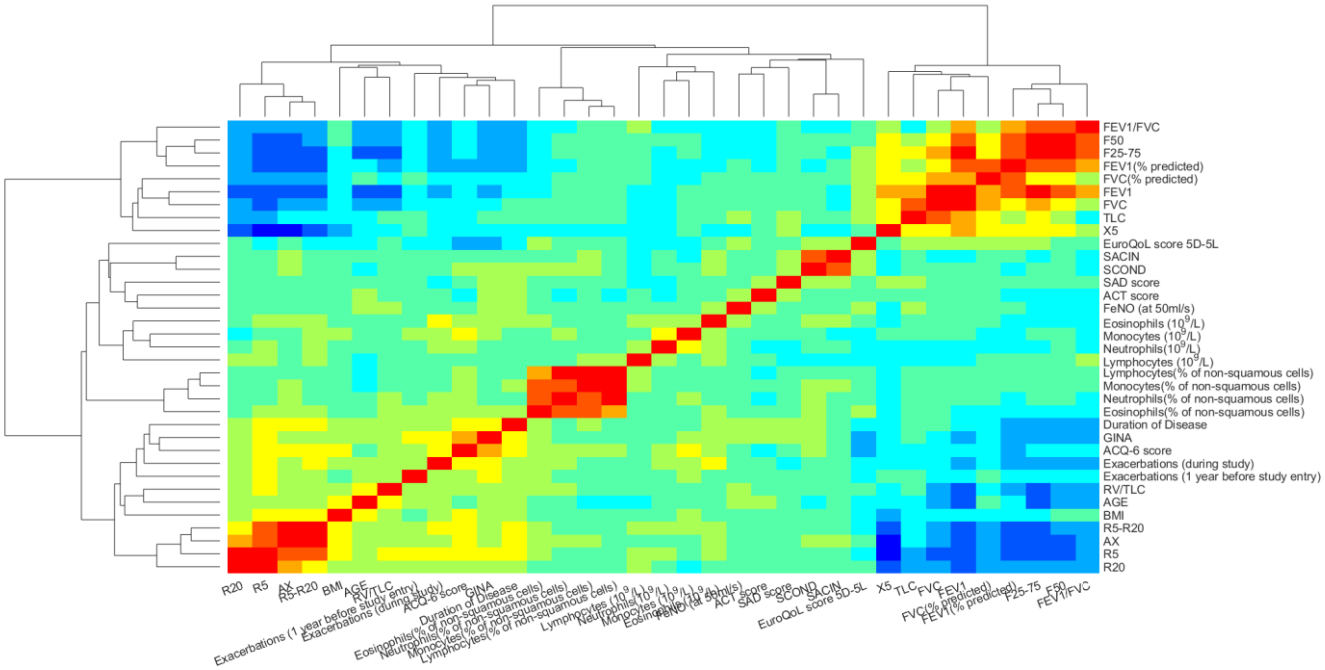


Figure 10 – Spearman correlation coefficients dendrogram of clinical characteristics

Singificant separation of tissue damping G was found across asthma severity, namely between healthy and moderate asthma (p=0.0296) as well as between healthy and severe asthma (p=0.0003) as shown in **Figure 9**.

Tissue damping was also significantly separated across quartiles of the imaging biomarker xPFavg or ΔHU^{AP}, which represents lung spatial deformation gradient across the anterior-posterior axis. Significant separation is observed between the first quartile and the third, the first quartile and the fourth, as well as between the second quartile and the third, and the second quartile and the fourth as shown in **Figure 9**.

The clinical characteristic features used in **Table 1**, were hierarchically clustered using unsupervised machine learning to identify similarity patterns in the data as shown in the dendrogram in **Figure 10**. The spearman correlation coefficients of these features and the CPM parameters, G, H and η were plotted in a heatmap to facilitate comparison and between the clinical characteristics and the CPM markers as shown in **Figure *11***.

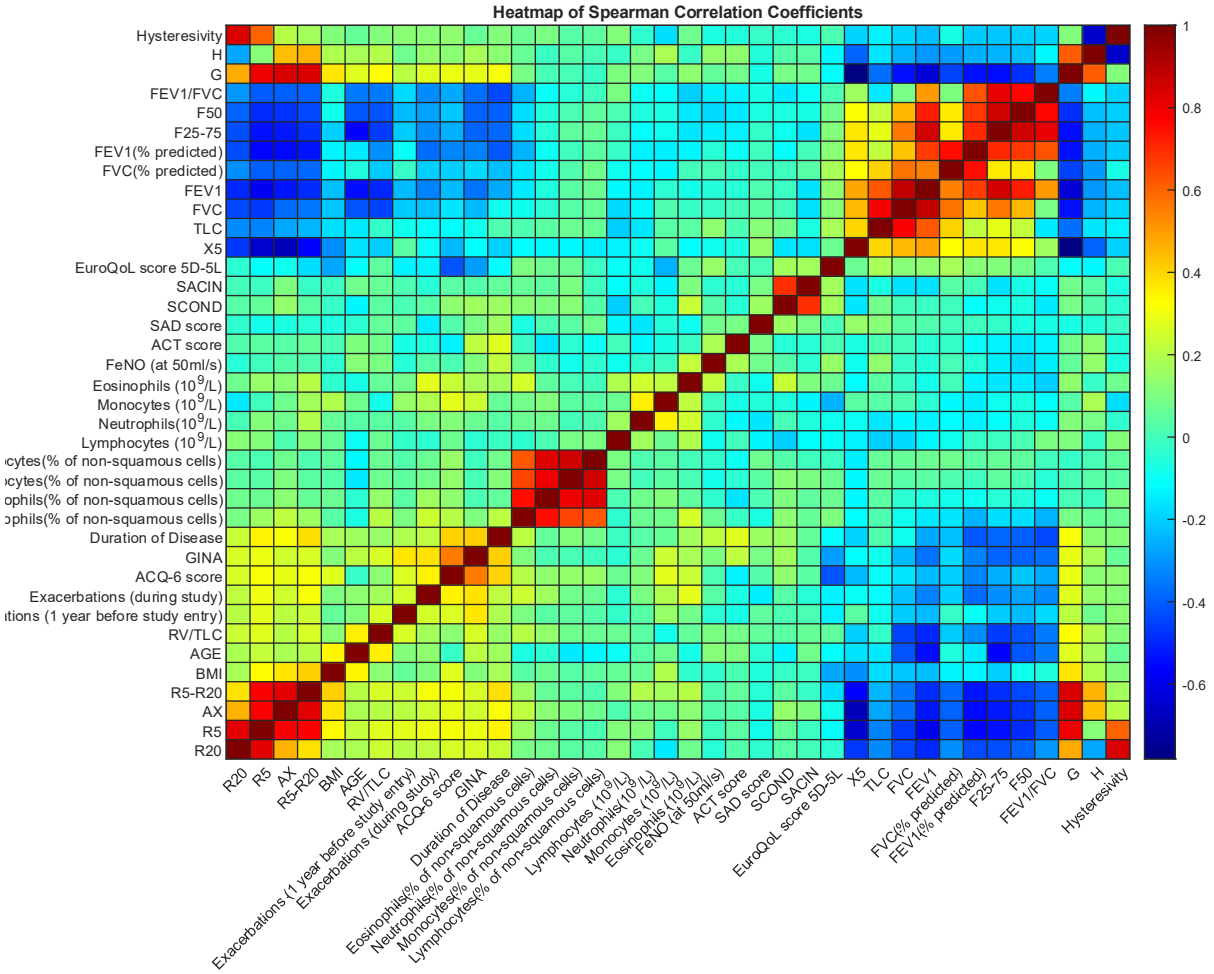


Figure 11 – Spearman correlation coefficients heatmap of clinical characteristics and viscoelastic CPM parameters (top 3 rows and first 3 columns from the right)

The following clinical characteristics were significant for **Tissue Damping G**, **p-value < 0.001** – R_5-R_{20} ($p=1.238*10^{-42}$), [$\rho=0.8339$], AX ($p=1.565*10^{-43}$) , [$\rho=0.8386$], R_5 ($p=1.277*10^{-36}$), [$\rho=0.7983$], R_{20} ($p=2.142*10^{-10}$), [$\rho=0.4753$], RV/TLC ($p=2.007*10^{-5}$), [$\rho=0.3302$], AGE ($p=0.000408$), [$\rho=0.2761$], BMI ($p=1.754*10^{-6}$), [$\rho=0.3675$], Exacerbations (during study) ($p=0.00049$), [$\rho=0.2724$], ACQ-6 score ($p=0.000194$), [$\rho=0.2905$], GINA ($p=0.000261$), [$\rho=0.2849$], Duration of Disease ($p=4.46*10^{-5}$), [$\rho=0.3169$], X_5 ($p=3.163*10^{-34}$), [$\rho=-0.7818$], TLC ($p=2.124*10^{-6}$), [$\rho=-0.3647$], FVC ($p=3.501*10^{-13}$), [$\rho=-0.5341$], FEV_1 ($p=3.166*10^{-19}$), [$\rho=-0.6320$], FVC(% predicted) ($p=2.98*10^{-9}$), [$\rho=-0.4475$], FEV_1(% predicted) ($p=4.813*10^{-12}$), [$\rho=-0.5315$], F25-75 ($p=1.071*10^{-13}$), [$\rho=-0.5438$], F50 ($p=1.62*10^{-10}$), [$\rho=-0.4781$], and FEV_1/FVC ($p=1.215*10^{-5}$), [$\rho=-0.3383$].

p-value < 0.01 – Exacerbations (1 year before study entry) (p=0.00841), [ρ=0.2077]

The following clinical characteristics were significant for **Elastance H**

p-value < 0.001 – R_5-R_{20} (p1.177*10^{-09}), [ρ=0.4576], AX (p=5.544*10^{-9}), [ρ=0.4406], R_{20} (p=0.00056), [ρ=-0.2698], BMI (p<0.0015), [ρ=0.1907], X_5 (p=3.828*10^{-7}), [ρ=-0.3886], FEV_1 (p=0.000136), [ρ=-0.2971], FVC(% predicted) (p=0.0002), [ρ=-0.2899]

p-value < 0.01 – FVC (p=0.0015), [ρ=-0.2487], FEV_1(% predicted) (p=0.00125), [ρ=-0.2529], F25-75 (p=0.00128), [ρ=-0.2525], and F50 (p=0.0033), [ρ=-0.1256]

p-value < 0.05 – AGE (p=0.028), [ρ=0.1741], RV/TLC (p=0.012), [ρ=0.1974], GINA (p=0.026), [ρ=0.1758], Monocytes (10^9/L) (p=0.0187), [ρ=0.1857], and TLC (p=0.046), [ρ=-0.1578]

The following clinical characteristics were significant for **Hysteresivity (heterogeneity) η**,

p-value < 0.001 – R_5 (p=5.973*10^{-17}), [ρ=0.5989], and R_{20} (p=2.017*10^{-43}), [ρ=0.8380]

p-value < 0.01 – FEV_1 (p=0.00375), [ρ=-0.2279], FEV_1(% predicted) (p=0.00869), [ρ=-0.2068], and F25-75 (p=0.00659), [ρ=-0.2140]

p-value < 0.05 – AX (p=0.0102), [ρ=0.2025], R_5-R_{20} (p=0.0361) , [ρ=0.1658], Monocytes (10^9/L) (p=0.0295), [ρ=-0.1721], X_5 (p=0.0132), [ρ=-0.1957], FVC (p=0.0176), [ρ=0.1875], F50 (p=0.0109), [ρ=-0.2008], and FEV_1/FVC (p=0.0151), [ρ=0.1918]

The figure illustrates that the CPM parameters are highly correlated with the oscillometry outputs. This is reasonable since the RMSE of the grid search was minimised using the same oscillometry outputs. The CPM parameters also appear to be correlated with spirometry measures, shown clearly in **Table *5***. The spearman correlation coefficients of the spirometry measures shown in **Table *5*** align very well with the correlations reported in the literature, with G and H having been obtained from a different FOT model (Tuza *et al.*, 2020).

Similarly, hierarchical clustering using unsupervised machine learning, was used to cluster the imaging biomarkers using the "clustergram" MATLAB function, as shown in the dendrogram in **Figure *12*** to identify similarities in the biomarker groups. A heatmap of the spearman correlation coefficients of the imaging biomarkers and the CPM parameters G, H and η, was created to facilitate comparison between the imaging biomarkers and the CPM parameters. The heatmap, shown in **Figure 13**, was used to guide the choice of imaging biomarkers which were used in the training of the linear regression models for the prediction of G and H. The figure illustrates clearly that the parameters G, H, and η are poorly correlated with all the imaging biomarkers.

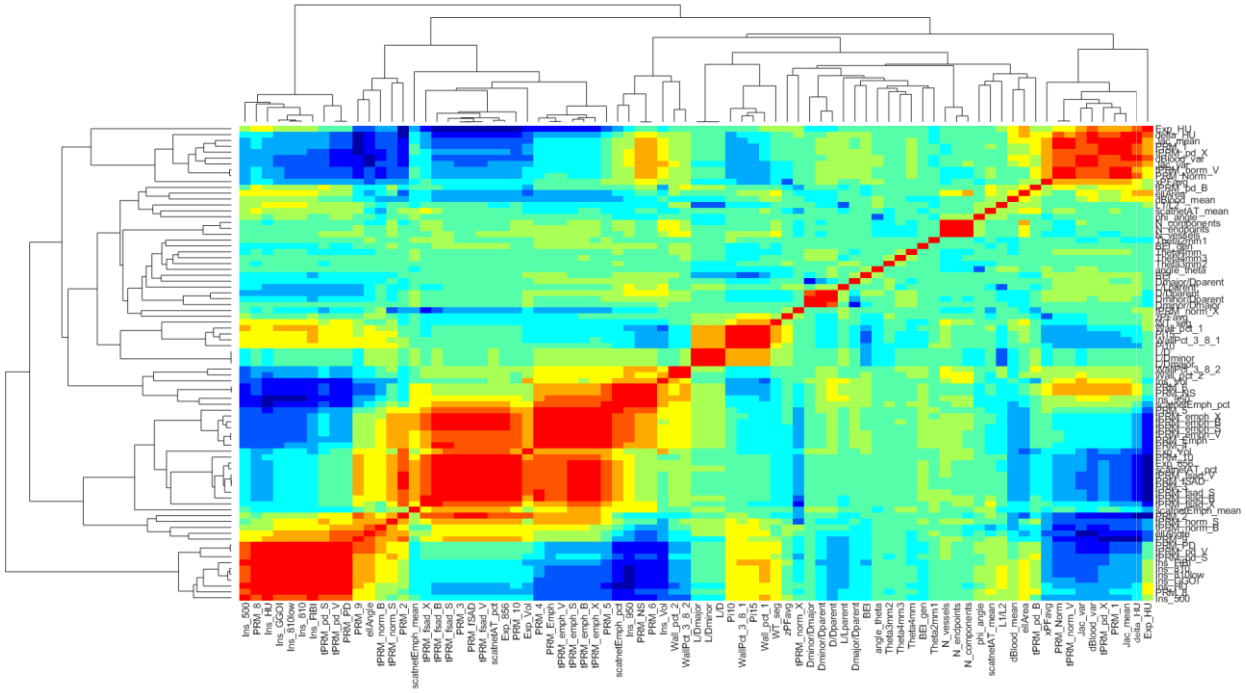


Figure 12 – Spearman correlation coefficients dendrogram of imaging biomarkers

Table 5 - Spearman correlation coefficients of spirometry compared to CPM parameters.

	FEV_1 (L)	*FEV_1 (%)*	*FVC (L)*	*FVC (%)*	*FEV_1/FVC*	*FEF25-75 (%)*
G	-0.632	-0.532	-0.534	-0.448	-0.338	-0.544
	p=3.166*10^{-19}	p=4.813*10^{-13}	p=3.501*10^{-13}	p=2.98*10^{-9}	p=1.215*10^{-5}	p=1.071*10^{-13}
H	-0.297	-0.253	-0.249	-0.290	-0.126	-0.253
	p=0.000136	p=0.00125	p=0.00151	p=0.00020	ns	p=0.00128
η	-0.228	-0.207	-0.188	-0.075	-0.191	-0.214
	p=0.00357	p=0.00869	p=0.0176	ns	p=0.0151	p=0.00659

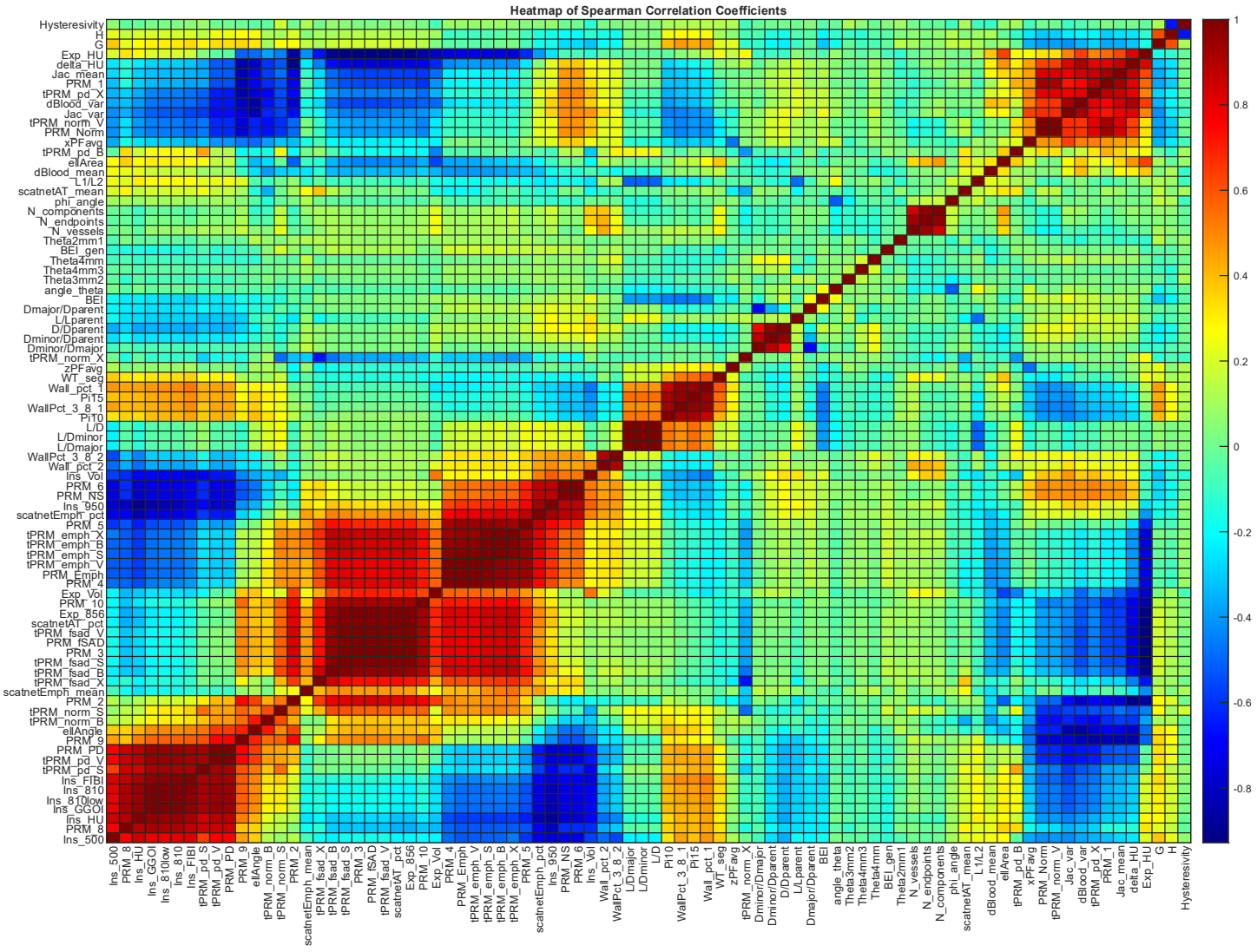


Figure 13 – Spearman correlation coefficients heatmap and viscoelastic CPM parameters (top 3 rows and first 3 columns from the right)

2.3.2 Prediction of G & H using imaging biomarkers

The importance of the statistically significant imaging biomarkers in asthma was reported in **Table *6*** which demonstrates the separation of statistically significant imaging biomarkers across GINA, asthma severity scales. The table also includes the statistically significant morphometric markers sourced from **Table 2**. The morphometric markers' (L/D and L/D_{minor}) significance between the healthy and the severe asthma groups, aligns with the significance reported in the literature between healthy and GINA 3-5 groups (Bordas *et al.*,

2015). It is noteworthy that our results also demonstrate significant separation of the marker L/D_{major} between the healthy and severe asthma groups which was not found in the literature.

Table 6 – Comparison of statistically significant imaging biomarkers and morphometric markers across asthma severity groups

	All (n=160)	***Healthy (n=25)***	***Mild Asthma (n=27)***	***Moderate Asthma (n=58)***	***Severe Asthma (n=50)***
delta_HU	159.40 ± 63.39	179.24 ± 59.50	188.44 ± 62.40	155.15 ± 59.49	138.74 ± 63.24$^{\#\dagger\dagger}$
Exp_Vol	2.72 (2.28 – 3.20)	2.64 ± 0.64	2.52 ± 0.74	2.94 ± 0.74	3.081 ± 1.21
Exp_HU	-616.09 ± 64.74	-601.53 ± 68.35	-588.30 ± 58.42	-613.98 ± 53.74	-640.82 ± 70.56††
Exp_856	1.37 (0.40 – 6.91)	4.03 ± 5.21	0.49 (0.22 – 1.06)	1.26 (0.45 – 5.00)	3.78 (1.18 – 12.90)†††
scatnetAT_pct	3.46 (0.93 – 15.69)	8.13 ± 9.77	1.23 (0.60 – 2.73)	3.02 (0.95 – 11.11)	8.41 (2.82 – 24.32)†††
WallPct_3_8_1	44.23 ± 8.41	37.07 ± 5.68	42.12 ± 5.75	45.40 ± 8.29$^{\#\#\#}$	47.58 ± 8.66$^{\#\#\#\dagger}$
WallPct_3_8_2	277.72 ± 124.94	264.88 ± 83.27	338.74 ± 146.89	257.69 ± 121.42†	274.42 ± 126.62
Wall_pct_1	45.15 ± 5.40	40.67 ± 4.83	44.50 ± 4.51$^{\#}$	45.41 ± 4.90$^{\#\#\#}$	47.43 ± 5.36$^{\#\#\#}$
Pi10	0.19 ± 0.073	0.13 ± 0.051	0.17 ± 0.046	0.20 ± 0.072$^{\#\#\#}$	0.22 ± 0.08$^{\#\#\#\dagger}$
Pi15	0.37 ± 0.071	0.31 ± 0.052	0.35 ± 0.049	0.37 ± 0.071$^{\#\#\#}$	0.39 ± 0.074$^{\#\#\#}$
BEI	0.78 ± 0.41	0.97 ± 0.39	0.80 ± 0.32	0.78 ± 0.40	0.69 ± 0.46$^{\#}$
WT_seg	1.68 ± 0.29	1.52 ± 0.23	1.71 ± 0.27	1.71 ± 0.29$^{\#}$	1.72 ± 0.30$^{\#}$
WT_subseg	0.92 (0.81 – 1.10)	0.86 ± 0.18	0.93 ± 0.18	0.98 ± 0.22	1.057 ± 0.27$^{\#\#}$
Jac_mean	1.98 ± 0.47	2.18 ± 0.46	2.08 ± 0.52	1.97 ± 0.43	1.83 ± 0.47$^{\#}$
Jac_var	0.30 (0.15 – 0.44)	0.47 ± 0.34	0.40 ± 0.30	0.30 (0.17 – 0.43)	0.27 ± 0.25$^{\#}$
dBlood_mean	30.85 (14.67 – 44.58)	33.02 ± 21.64	33.60 (14.01 – 47.92)	32.32 ± 19.65	21.74 (6.41 – 36.01)

	All (n=160)	Healthy (n=25)	Mild Asthma (n=27)	Moderate Asthma (n=58)	Severe Asthma (n=50)
dBlood_var	55961.50 (35846.10 – 93525.12)	85805.99 ± 54595.09	59483.45 (44384.76 – 113604.76)	58225.42 (37892.82 – 82025.69)	41951.70 (25828.76 – 79180.20)#†
PRM_1	50.89 ± 22.74	58.64 ± 19.56	55.34 ± 22.44	52.43 ± 20.81	42.81 ± 24.70#
PRM_2	11.90 (4.18 – 22.19)	12.53 ± 12.13	10.25 ± 9.86	14.20 ± 10.92	17.48 ± 12.41
PRM_3	1.25 (0.32 – 6.57)	3.77 ± 4.91	0.414 (0.24 – 1.02)	1.18 (0.42 – 4.36)	3.032 (0.87 – 12.04)†††
PRM_4	0.091 (0.04 – 0.29)	0.1047 (0.04 – 0.26)	0.066 (0.044 – 0.096)	0.08 (0.043 – 0.18)	0.25 (0.062 – 0.85)††
PRM_5	0.030 (0.01 – 0.08)	0.051 ± 0.06	0.018 (0.0095 – 0.034)	0.03 (0.011 – 0.056)	0.096 ± 0.098†
PRM_9	3.77 (2.24 – 6.05)	3.41 ± 2.49	3.87 ±2.43	3.98 (2.34 – 6.32)	6.14 ± 5.59#
PRM_10	0.042 (0.02 – 0.15)	0.036 (0.01 – 0.16)	0.023 (0.014 – 0.038)	0.05 (0.018 – 0.14)	0.076 (0.035 – 0.21)††
PRM_Norm	69.83 (61.71 – 76.61)	71.17 ± 12.57	65.60 ± 21.12	69.44 (63.84 – 75.43)	60.29 ± 19.35#
PRM_fSAD	1.25 (0.32 – 6.57)	3.77 ± 4.91	0.41 (0.24 – 1.02)	1.18 (0.42 – 4.36)	3.032 (0.87 – 12.04)†††
PRM_Emph	0.12 (0.06 – 0.37)	0.1465 (0.06 – 0.32)	0.08 (0.05 – 0.13)	0.12 (0.052 – 0.24)	0.33 (0.078 – 1.01)††
tPRM_norm_V	0.71 (0.63 – 0.78)	0.73 ± 0.13	0.67 ± 0.22	0.71 (0.65 – 0.77)	0.62 ± 0.20#
tPRM_fsad_V	0.013 (0.0034 – 0.07)	0.039 ± 0.05	0.0043 (0.0025 – 0.011)	0.01 (0.0043 – 0.045)	0.031 (0.01 – 0.12)†††
tPRM_fsad_S	0.035 (0.0087 – 0.12)	0.061 ± 0.071	0.013 (0.0057 – 0.025)	0.02 (0.0081 – 0.085)	0.066 (0.023 – 0.17)††
tPRM_fsad_B	0.0038 (0.014 – 0.012)	0.0061 ± 0.006	0.0022 (0.00092 – 0.0042)	0.0029 (0.0013 – 0.0092)	0.0093 ± 0.0073†
tPRM_emph_V	0.0012 (0.00059 – 0.0037)	0.0014 (0.00058 – 0.0078)	0.00078 (0.00050 – 0.0013)	0.0011 (0.00054 – 0.0024)	0.0034 (0.00078 – 0.010)††
tPRM_emph_S	0.0028 (0.0012 – 0.010)	0.0032	0.0017 (0.00099 – 0.0028)	0.0023 (0.0011 – 0.0065)	0.0099 (0.0013 – 0.026)††*
tPRM_emph_B	0.00049 (0.00016 – 0.0019)	0.0012 ± 0.0017	0.00029 (0.00014 – 0.00053)	0.00035 (0.00015 – 0.0012)	0.0018 (0.00024 – 0.0046)††*
tPRM_emph_X	0.0000805287 (0.000027 – 0.00033)	0.00009931 (0.000020 – 0.00026)	0.000053 (0.000015 – 0.000082)	0.000074 (0.000022 – 0.00020)	0.00044 ± 0.00043††

	All (n=160)	Healthy (n=25)	Mild Asthma (n=27)	Moderate Asthma (n=58)	Severe Asthma (n=50)
zPFavg	-0.70 ± 3.32	-1.50 ± 3.22	-1.25 ± 1.95	-1.21 ± 3.60	0.58 ± 3.31*
L/D	4.61 ± 0.53	4.39 ± 0.42	4.59 ± 0.57	4.57 ± 0.47	4.79 ± 0.59#
L/D_{minor}	5.13 ± 0.591	4.88 ± 0.46	5.11 ± 0.63	5.08 ± 0.52	5.32 ± 0.65#
L/D_{major}	4.92 ± 0.57	4.68 ± 0.45	4.90 ± 0.61	4.88 ± 0.50	5.10 ± 0.63#

Statistically Significant Imaging biomarkers and morphometric markers ($p<0.05$). Data presented as median(IQR) for non-parametric data, and $\mu\pm\sigma$ for normally distributed parametric data. Normality of the datasets was assessed using a Kolmogorov-Smirnov test, after normalisation of data (normalised data = $(x-\mu)/\sigma$) followed by the calculation of p-values using a one-way Analysis of Variance (ANOVA) test for parametric data and a Kruskal-Wallis test for non-parametric data. Healthy – GINA 0, Mild Asthma – GINA 1, Moderate Asthma – GINA 2 & 3, Severe Asthma – GINA 4 & 5

#p < 0.05 compared to healthy control group

##p < 0.01 compared to healthy control group

###p < 0.001 compared to healthy control group

†p < 0.05 compared to Mild Asthma group

††p < 0.01 compared to Mild Asthma group

†††p < 0.001 compared to Mild Asthma group

*p < 0.05 compared to Moderate Asthma group

**p < 0.01 compared to Moderate Asthma group

***p < 0.001 compared to Moderate Asthma group

Following training of the linear regression models with the selected imaging biomarkers described in the methods section, the oscillometry outputs were simulated again using the personalised, predicted CPM parameters. The results demonstrate that optimisation of the FOT model can be achieved through prediction of personalised CPM parameters using

imaging biomarkers as the concordance between simulated and measured outputs is much higher (shown below and on **Figure *14***) across all FOT outputs compared to the concordance obtained with constant G and H across study participants.

$R^2(AX)=0.28$, $R^2(X_5)=0.17$, R^2 $(R_5-R_{20})=0.17$, R^2 $(R_{20})=0.13$, R^2 $(R_5)=0.16$ $p<0.001$ (with G and H predicted from linear regression models with qCT markers)

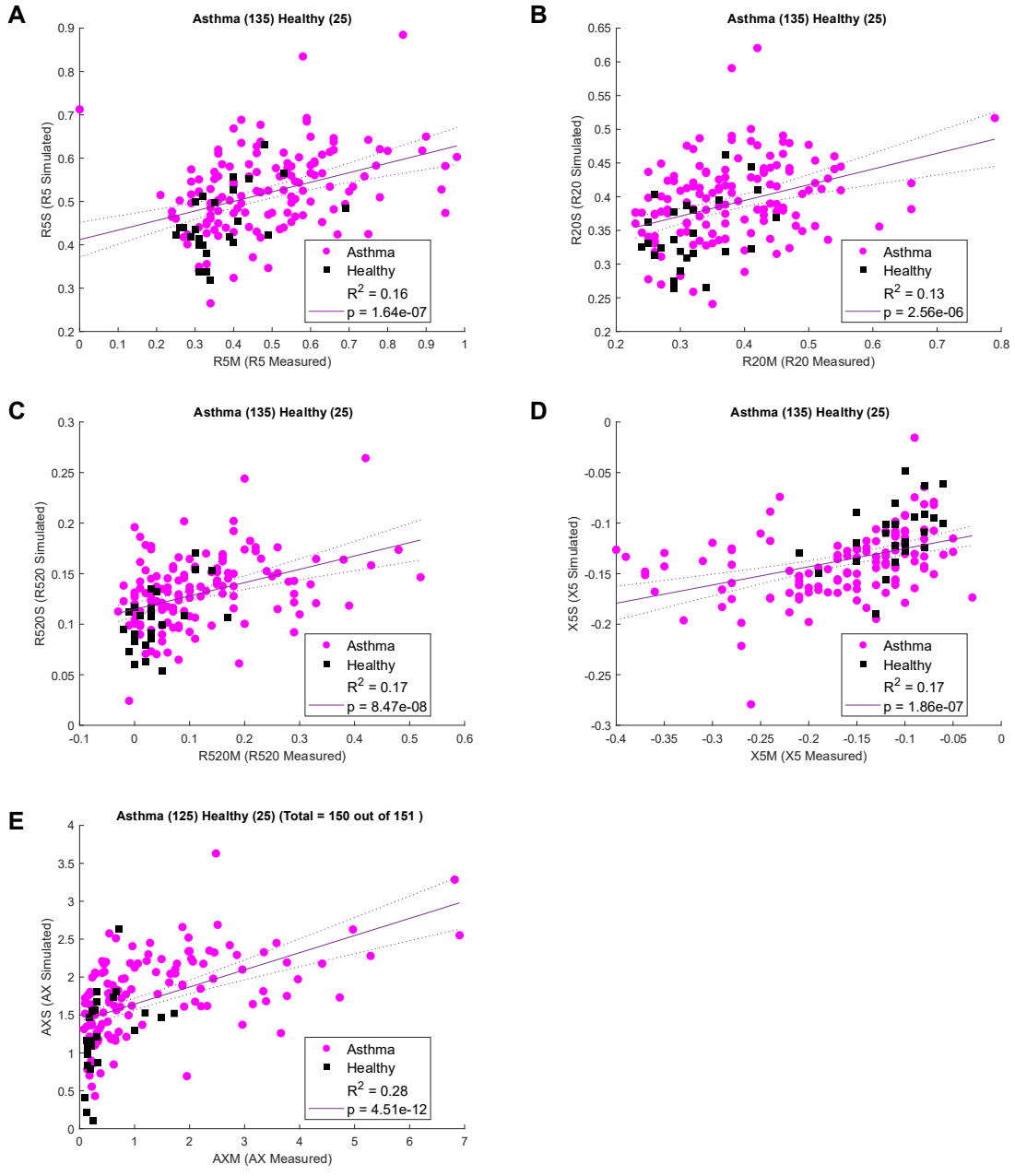


Figure 14 - FOT measurements compared to simulations obtained with predicted Tissue Damping (G) and Elastance (H)

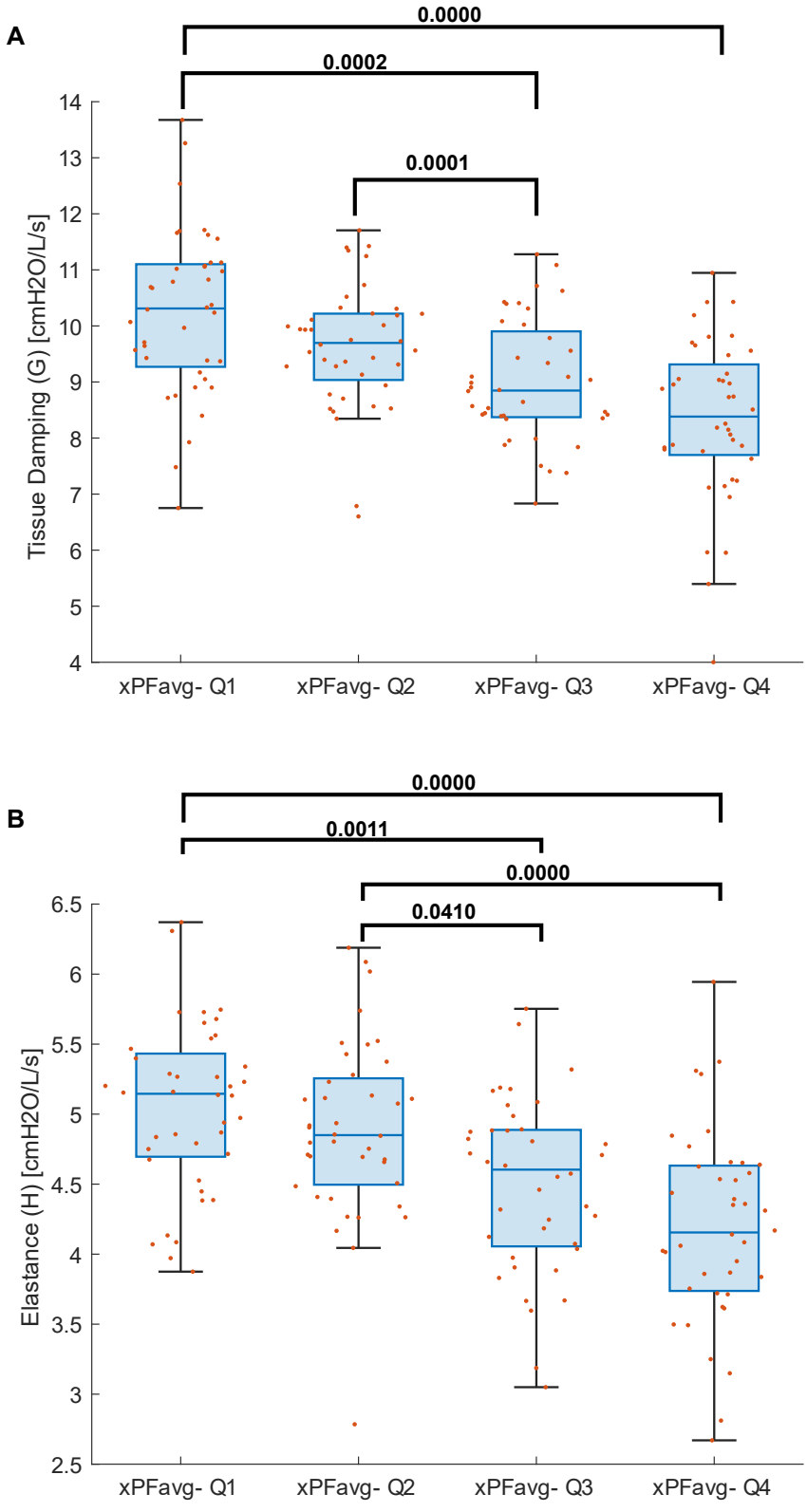


Figure 15 – Separation of predicted (A) Tissue Damping, G and (B) Elastance, H across quartiles of xPFavg or ΔHU^{AP} quartiles – which represents lung spatial deformation gradient in the anterior-posterior axis

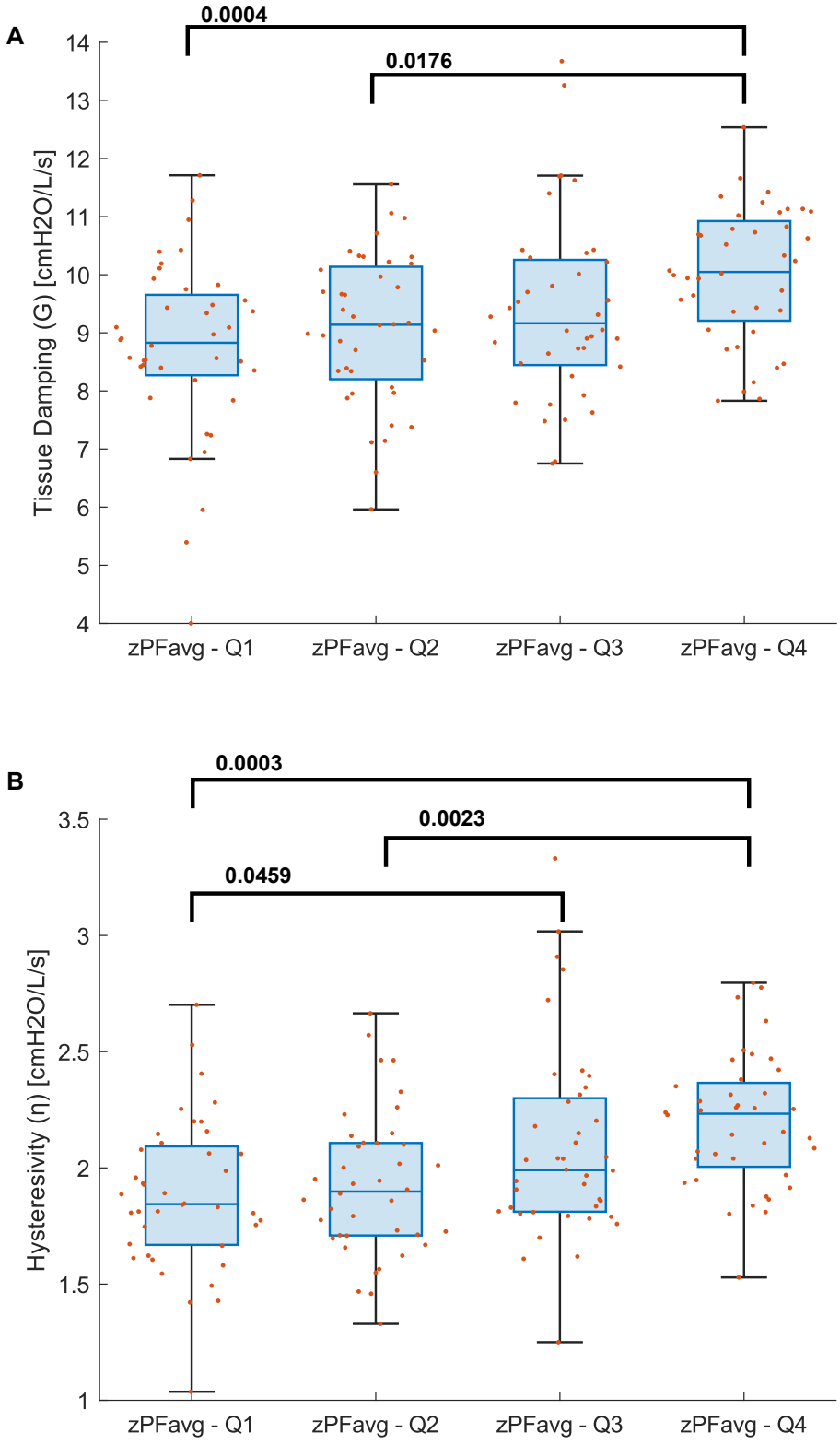


Figure 16 - Separation of predicted (A) Tissue Damping, G and (B) Hysteresivity, η across quartiles of zPFavg or ΔHU^{IS} quartiles – which represents lung spatial deformation gradient in the inferior-superior axis

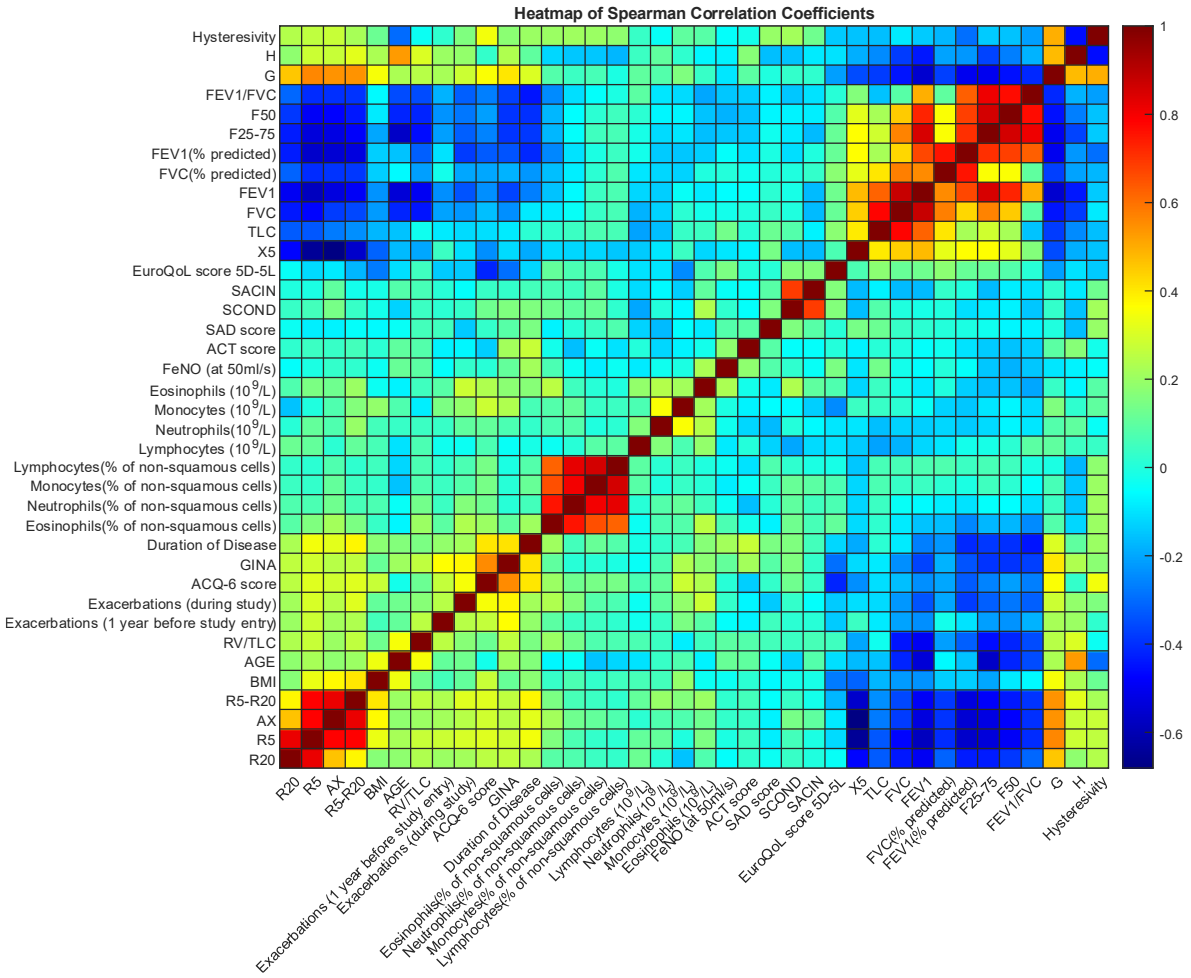


Figure 17 – Spearman correlation coefficients heatmap of clinical characteristics and predicted viscoelastic CPM parameters (top 3 rows and 3 first columns from the right)

Singificant separation of tissue damping G was found across quartiles of the imaging biomarker xPFavg or ΔHU^{AP}, which represents lung spatial deformation gradient across the anterior-posterior axis, namely between the first and fourth quartiles, the first and third quartiles, the second and third quartiles and the second and fourth quartiles which can be seen in **Figure 15 (A)**. Significant separation of elastance H was also identified across quartiles of the imaging biomarker xPFavg, which can be seen in **Figure 15 (B)**. Statistical significance was identified between the first and third quartiles, the first and fourth quartiles, the second and third quartiles and the second and fourth quartiles.

Tissue damping was also significantly separated across quartiles of the imaging biomarker zPFavg or ΔHU^{IS}, which represents lung spatial deformation gradient across the inferior-superior axis. Significant separation is observed between the first and fourth quartiles, and the second and fourth quartiles, which can be seen in **Figure *16* (A)**. The ratio of G/H, hysteresivity, η, was also found to significantly separate across quartiles of the zPFavg marker. Namely, significant separation is observed between the first and third quartiles, the first and fourth quartiles, and the second and fourth quartiles, which can be seen in **Figure *16* (B)**.

The clinical characteristic features used in **Table 1**, which were hierarchically clustered using unsupervised machine learning to identify similarity patterns in the data and shown in the dendrogram in **Figure 10**, were used again for comparison of spearman correlation coefficients of these features and the CPM parameters', G, H and η. The coefficients were plotted in a heatmap to facilitate comparison between the clinical characteristics which is presented in **Figure *17***.

The following clinical characteristics were significant for **Tissue Damping G (predicted)**

p-value < 0.001 – R_5-R_{20} ($p=9.211*10^{-14}$), [$\rho=0.5451$], AX ($p=8.693*10^{-14}$), [$\rho=0.5455$], R_5 ($p=6.067*10^{-15}$), [$\rho=0.5662$], R_{20} ($p=1.172*10^{-9}$), [$\rho=0.4576$], BMI ($p=5.62*10^{-6}$), [$\rho=0.3502$], Exacerbations (during study) ($p=0.000291$), [$\rho=0.2828$], ACQ-6 score ($p=3.633*10^{-6}$), [$\rho=0.3568$], GINA ($p=1.262*10^{-7}$), [$\rho=0.4031$], Duration of Disease ($p=8.762*10^{-5}$), [$\rho=0.3051$], X_5 ($p=5.39*10^{-6}$), [$\rho=-0.3509$], TLC ($p=1.101*10^{-6}$), [$\rho=-0.3741$], FVC ($p=5.249*10^{-9}$), [$\rho=-0.4412$], FEV_1 ($p=3.047*10^{-14}$), [$\rho=-0.5538$], FVC(% predicted) ($p=1.378*10^{-6}$), [$\rho=-0.3709$], FEV_1(% predicted) ($p=1.862*10^{-11}$), [$\rho=-0.4990$], F25-75 ($p=1.415*10^{-11}$), [$\rho=-0.5016$], F50 ($p=3.849*10^{-9}$), [$\rho=-0.4447$], and FEV_1/FVC ($p=1.039*10^{-7}$), [$\rho=-0.4055$].

p-value < 0.01 – AGE (p=0.00323), [ρ=0.2315], RV/TLC (p=0.00176), [ρ=0.2455], Exacerbations (1 year before study entry) (p=0.00458), [ρ=0.2231], Quality of Life 5D-5L (p=0.0066), [ρ=-0.2139]

p-value < 0.05 – Monocytes (10^9/L) (p=0.0498), [ρ=0.1553]

The following clinical characteristics were significant for **Elastance H (predicted)**

p-value < 0.001 – R_5-R_{20} ($p=4.278*10^{-5}$), [ρ=0.3176], AX (p=0.000515), [ρ=0.2715], BMI (p=0.00361), [ρ=0.2288], R_5 (p=0.000371), [ρ=0.2780], AGE ($p=7.809*10^{-13}$), [ρ=0.5274], RV/TLC ($p=8.874*10^{-5}$), [ρ=0.3048], FVC ($p=1.052*10^{-6}$), [ρ=-0.3747], FEV_1 ($p=9.023*10^{-9}$) , [ρ=-0.4350], F25-75 ($p=2.098*10^6$), [ρ=-0.3649], F50 (p=0.00086), [ρ=-0.2609].

p-value < 0.01 – TLC (p=0.00197), [ρ=-0.2429], FEV_1(% predicted) (p=0.00481), [ρ=-0.2219], Exacerbations (1 year before study entry) (p=0.00969), [ρ=0.2039], GINA (p=0.00275), [ρ=0.2352], FVC(% predicted) (p=0.00831), [ρ=-0.2080].

p-value < 0.05 – R_{20} (p=0.0193), [ρ=-0.1848], Exacerbations (during study) (p=0.0182), [ρ=0.1865], Lymphocytes (% of non-squamous cells) (p=0.0278), [ρ=-0.1739], ACT score (p=0.0351), [ρ=0.1667], SAD Score (p=0.0465), [ρ=-0.1576], X_5 (p=0.0176), [ρ=-0.1875], FEV_1/FVC (p=0.0234), [ρ=-0.1792]

The following clinical characteristics were significant for **Hysteresivity (heterogeneity) η, (predicted)**

p-value < 0.001 – R_5 (p=0.000837), [ρ=0.2615], AX (p=0.000475), [ρ=0.2731], AGE (p=0.000147), [ρ=-0.2957], ACQ-6 Score ($p=8.382*10^6$), [ρ=0.3441], FEV_1(% predicted) (p=0.000225), [ρ=-0.2877]

p-value < 0.01 – R_{20} (p=0.00214), [ρ=0.2410], R_5-R_{20} (p=0.00473), [ρ=0.2223], Duration of Disease (p=0.00969), [ρ=0.2040], Neutrophils (% of non-squamous cells) (p=0.00806) , [ρ=0.2088], Scond (p=0.00574), [ρ=0.2174], FEV_1/FVC (p=0.00684), [ρ=-0.2130]

p-value < 0.05 – Exacerbations (during study) (p=0.0453), [ρ=0.1585], GINA (p=0.0246), [ρ=0.1777], Eosinophils (% of non-squamous cells) (p=0.0112), [ρ=0.2002], Monocytes (10^9/L) (p=0.0102), [ρ=0.1064], Neutrophils (% of non-squamous cells) (p=0.0197), [ρ=0.2088], SAD score (p=0.0143), [ρ=0.1934], TLC (p=0.0408), [ρ=-0.1619], FVC (% predicted) (p=0.0305), [ρ=-0.1711]

Figure *17*, illustrates that the CPM parameters are highly correlated with the oscillometry outputs. This is reasonable since the RMSE of the grid search which provided the personalised G and H on which the linear regression models were trained, was minimised using the same oscillometry outputs. The CPM parameters also appear to be correlated with spirometry measures, shown clearly in **Table *7*** which indicates that the properties of G and H that led to the correlation of **Table *5***, have been preserved. The spearman correlation coefficients of the spirometry measures shown in **Table *7*** also align well with the correlations reported in the literature (Tuza *et al.*, 2020).

Similarly, as in the previous section, hierarchical clustering using unsupervised machine learning, was used to cluster the imaging biomarkers using the "clustergram" MATLAB function, as shown in the dendrogram in **Figure *12*** to identify similarities in the biomarker groups. A heatmap of the spearman correlation coefficients of the imaging biomarkers and the predicted CPM parameters, was created to facilitate comparison between the imaging biomarkers and the CPM parameters. The heatmap, shown in **Figure 18**, appears to be broadly similar to the heatmap presented in **Figure 13**. While most imaging biomarkers demonstrate relatively weak correlations with the CPM parameters, several markers show stronger associations with G and H. In particular, strong negative correlations are observed between the predicted CPM parameters and the biomarkers Exp_HU, delta_HU, Jac_mean, PRM_1, tPRM_pd_X, dBlood_var, Jac_var, tPRM_norm_V, PRM_Norm and xPFavg. As delta_HU represents the difference in lung density between inspiratory and expiratory scans and Jac_var reflects the spatial variance of the Jacobian determinant, representing variability in regional volume change within the lung, it is plausible that the CPM parameters may capture some information related to ventilation behaviour in the lungs. In addition, the biomarker tPRM_pd_B shows a strong negative correlation with the predicted parameter H, which was not observed in the heatmap of the grid-search-obtained parameters shown in **Figure 13**. Strong positive correlations with G are also preserved for several airway wall area- and airway wall thickness-related biomarkers, including Wall_pct_1, Pi15, Wall_pct_3_8_1 and Pi10.

These findings suggest that structural information contained in biomarkers reflecting airway wall area and thickness may be associated with tissue damping G, which represents energy dissipation within the respiratory system (Tuza *et al.*, 2020). These biomarkers, as shown in **Table 5**, appear to be sensitive to differences in asthma severity. Inflammation of the airways and mucus hypersecretion in asthma, arising from airway hyper-responsiveness can affect airway wall area and wall thickness and it is therefore plausible that these structural changes influence the dissipation of energy within the respiratory system. Elastance, H, reflects the potential elastic energy accumulation of the lung tissue (Tuza *et al.*, 2020) and appears to

show weaker and less consistent associations with the imaging biomarkers compared to G, with several correlations differing between the predicted and grid-search-obtained CPM parameters. Finally, hysteresivity η, which has been reported to be proportional to the heterogeneity of ventilation in the lung (Tuza *et al.*, 2020), does not appear to show strong associations with the imaging biomarkers in this study.

Table 7 - Spearman correlation coefficients of spirometry compared to predicted CPM parameters.

	FEV_1 (L)	*FEV_1 (%)*	*FVC (L)*	*FVC (%)*	*FEV_1/FVC*	*FEF25-75 (%)*
G	-0.554	-0.50	-0.441	-0.371	-0.406	-0.502
	$p=3.047*10^{-14}$	$p=1.862*10^{-11}$	$p=5.249*10^{-9}$	$p=1.378*10^{-6}$	$p=1.039*10^{-7}$	$p=1.415*10^{-11}$
H	-0.435	-0.221	-0.375	-0.208	-0.179	-0.365
	$p=9.023*10^{-9}$	p=0.00481	$p=1.052*10^{-6}$	p=0.00831	p=0.0233	$p=2.098*10^{-6}$
η	-0.137	-0.288	-0.089	-0.171	-0.213	-0.365
	ns	p=0.000225	ns	p=0.0305	p=0.00684	ns

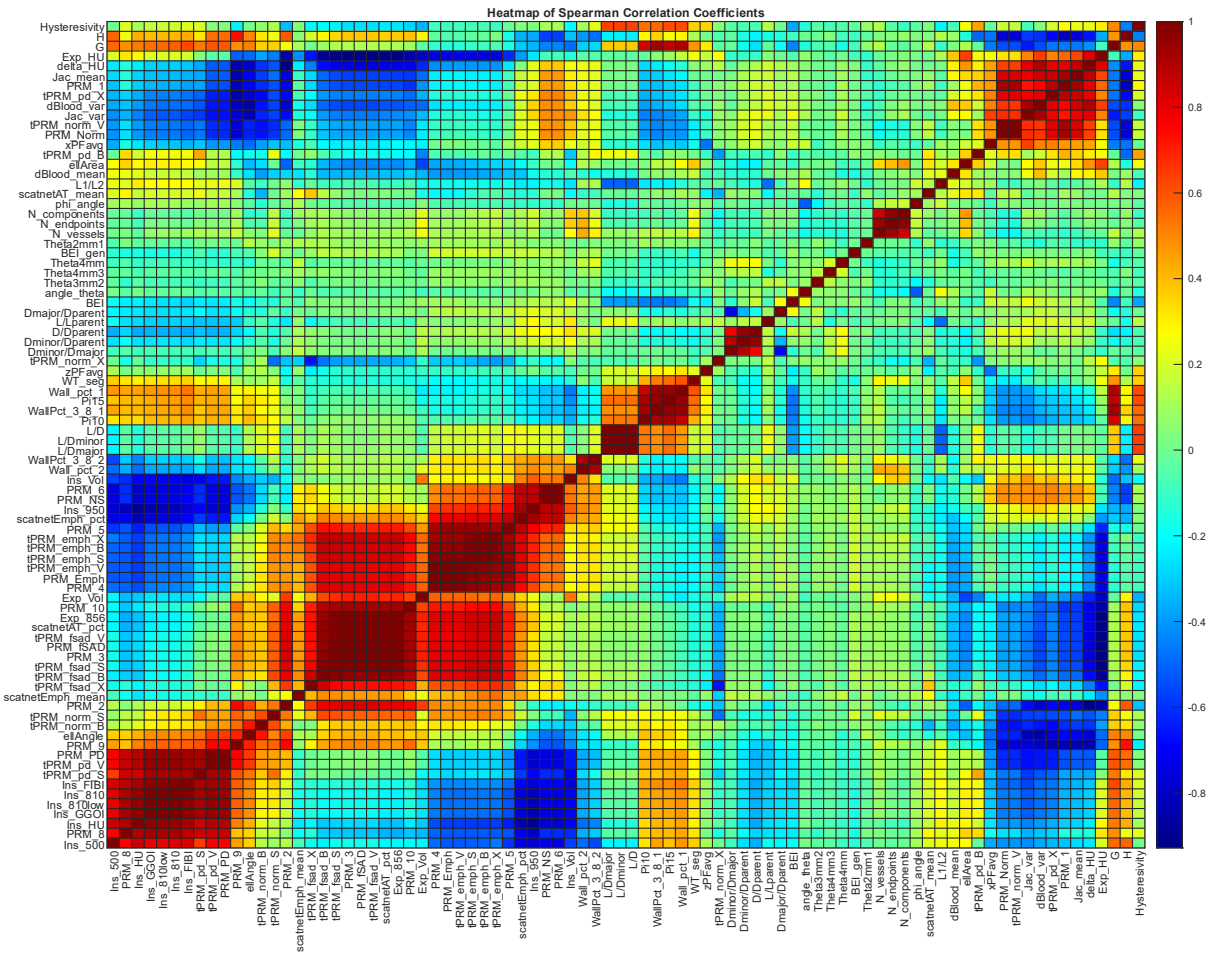


Figure 18 – Spearman correlation coefficients heatmap of imaging biomarkers and predicted viscoelastic CPM parameters (top 3 rows and 3 first columns from the right of heatmap)

2.3.3 Summary of results

In this chapter, a series of simulations were implemented and the results from each simulation cycle are reported below for comparison. The results include the results obtained from the initial simulations with constant G and H across the study participants, the simulations implemented using grid-search obtained, personalised G and H, and the simulations implemented using imaging-biomarker regressed, personalised G and H**.** The results are summarised in the next page to facilitate comparison. The personalised viscoelastic parameters G, H and η, obtained from the grid search and predicted using the imaging-biomarker-trained linear regression

models are reported in **Table *8*** which demonstrates their separation across asthma severity groups. While in the grid-search obtained parameters, statistical significance is only present in tissue damping (G), interestingly, the predicted CPM parameters appear to all be statistically significant with the predicted hysteresivity η, significantly separating between healthy and severe asthma groups.

R^2(AX)=0 (ns), R^2(X_5)=0 (ns), R^2 (R_5-R_{20})=0 (ns), R^2 (R_{20})=0.08 (p<0.001), R^2 (R_5)=0.12 (p<0.00001) (using previously reported (Foy *et al.*, 2019) G = 0.12 kPa.L^{-1} = 1.22 $cmH_2O.L^{-1}.s^{-1}$ and H = 0.57 kPa.L^{-1} = 5.81 $cmH_2O.L^{-1}.s^{-1}$ across all study participants)

R^2(AX)=0.02 (ns), R^2(X_5)=0 (ns), R^2 (R_5-R_{20})=0.04 (p=0.007), R^2 (R_{20})=0.10 (p<0.001), R^2 (R_5)=0.12 (p<0.001) (using previously reported(Foy *et al.*, 2019) G = 0.12 kPa.L^{-1} = 1.22 $cmH_2O.L^{-1}.s^{-1}$ and H = 0.57 kPa.L^{-1} = 5.81 $cmH_2O.L^{-1}.s^{-1}$ across all cases – Accounting only for impedance of branches, no shunting applied)

R^2(AX)=0.61, R^2(X_5)=0.70, R^2 (R_5-R_{20})=0.44, R^2 (R_{20})=0.34, R^2 (R_5)=0.60 p<0.001 (using personalised grid-search-obtained G and H)

R^2(AX)=0.28, R^2(X_5)=0.17, R^2 (R_5-R_{20})=0.17, R^2 (R_{20})=0.13, R^2 (R_5)=0.16 p<0.001 (with G and H predicted from linear regression models with qCT markers)

Table 8 - Comparison of grid-search obtained and predicted CPM parameters across asthma severity groups

	All (n=160)	***Healthy (n=25)***	***Mild Asthma (n=27)***	***Moderate Asthma (n=58)***	***Severe Asthma (n=50)***
G	8.24 (6.74 – 11.16)	7.20 ± 1.32	9.19 ± 3.28	9.50 ± 3.69$^{\#}$	10.18 ± 3.49$^{\#\#\#}$
H (ns)	4.42 (3.29 – 5.86)	3.95 ± 1.53	4.80 ± 2.95	4.67 ± 2.19	4.92 ± 2.30
η (ns)	2.04 (1.68 – 2.71)	2.00 ± 0.61	2.38 ± 1.22	2.04 (1.74 – 2.77)	2.08 (1.62 – 2.77)
G (predicted)	9.30 ± 1.46	8.14 ± 1.19	9.00 ± 1.17	9.39 ± 1.47$^{\#\#}$	9.94 ± 1.36$^{\#\#\#\dagger}$
H (predicted)	4.66 ± 0.71	4.42 ± 0.54	4.43 ± 0.73	4.77 ± 0.75	4.78 ± 0.70
η (predicted)	2.03 ± 0.36	1.85 ± 0.27	2.08 ± 0.35	2.00 ± 0.39	2.11 ± 0.34$^{\#}$

Data presented as median(IQR) for non-parametric data, and μ±σ for normally distributed parametric data. Normality of the datasets was assessed using a Kolmogorov-Smirnov test, after normalisation of data (normalised data = (x-μ)/σ) followed by the calculation of p-values using a one-way Analysis of Variance (ANOVA) test for parametric data and a Kruskal-Wallis test for non-parametric data. Healthy – GINA 0, Mild Asthma – GINA 1, Moderate Asthma – GINA 2 & 3, Severe Asthma – GINA 4 & 5. Hysteresivity, the ratio of G/H is represented by the Greek letter η.

#p < 0.05 compared to healthy control group

##p < 0.01 compared to healthy control group

###p < 0.001 compared to healthy control group

†p < 0.05 compared to Mild Asthma group

††p < 0.01 compared to Mild Asthma group

†††p < 0.001 compared to Mild Asthma group

2.4 Discussion

The study presented in this chapter aimed to examine whether prediction of personalised CPM parameters of tissue damping, G and elastance, H, using CT imaging biomarkers would increase the concordance between simulated and measured oscillometry outputs in the ATLANTIS dataset (Postma *et al.*, 2019; Kraft *et al.*, 2022). Medical imaging CT scans acquired at RV and TLC were used in the derivation of imaging biomarkers while segmentations of airways to Weibel generations 6-10 were used to algorithmically grow the rest of the conducting zone airways, using previously reported patient-based algorithms (Bordas *et al.*, 2015; Bell *et al.*, 2019; Foy *et al.*, 2019). Following extensive quality control of the complete conducting airway tree structures which were provided by Alex Bell, the final study population amounted to 160 individuals whose airway structures underwent scaling to reflect the structural state of the airways during an FOT test, using Lamberts' scaling (Lambert *et al.*, 1982).

Simulations were implemented using the airway centreline structures of the selected study participants with the same FOT mathematical model as published previously (Bell *et al.*, 2019; Foy *et al.*, 2019), which, as explored in the literature review, and validated in the results' section allowed room for improvement in its simulations' concordance with measurements when a constant value of G and H was used throughout the study population. A grid search was implemented for the identification of personalised G and H for each participant as it was hypothesised that this would lead to higher concordance between simulated and measured oscillometry outputs. Simulations obtained using grid-search obtained, personalised CPM parameters significantly increased the concordance between simulated and measured oscillometry outputs, highlighting the importance of personalisation of these parameters.

For the optimisation of the FOT mathematical model, a tool that would allow the calculation or prediction of these personalised CPM parameters was required. It was therefore explored whether prediction of these CPM parameters was possible with the use of imaging biomarkers.

The imaging biomarkers were hierarchically clustered using unsupervised machine learning and their spearman correlation coefficients were plotted along with the grid-search obtained, personalised CPM markers' spearman correlation coefficients. This facilitated the selection of imaging biomarkers used in the training of the linear regression models and aided the comparison between CPM parameters and imaging biomarkers.

Following training of the linear regression models, the CPM parameters were predicted and used to simulate the FOT test again, for all study participants. The results proved that the imaging-informed linear regression models can be used to optimise the FOT model, as the predicted, personalised CPM parameters led to simulation results whose concordance with measured data was much higher than the results obtained with constant G and H used throughout the study participants.

2.4.1 Grid search

The simulation results obtained from the study cohort with constant G and H across all study participants showed poor correlation with measured oscillometry outputs as shown below. While the correlations reported below appear lower than those previously reported by (Foy *et al.*, 2019), this may reflect differences in the software frameworks used for airway segmentation and algorithmic construction of the complete conducting airway trees. In the present study, airway trees were generated using YACTA (Yet Another CT Analyzer) segmentation software in combination with MATLAB (Mathworks), whereas the previous study utilised Materialise Mimics segmentation software together with the CHASTE (Cancer Heart and Soft Tissue Environment) open-source software package (Bordas *et al.*, 2015). Although the underlying methodological approach used to generate the airway trees was similar, differences in the segmentation capabilities of the software and associated workflow, including manual inspection and correction of anomalous branches, may introduce variability in the resulting airway geometries and therefore influence the strength of the correlations obtained. It is also possible that the smaller cohort size in the previous study allowed more

extensive manual inspection and refinement of the airway segmentations, which could further contribute to differences in the resulting correlations.

$R^2(AX)=0$ (ns), $R^2(X_5)=0$ (ns), $R^2(R_5-R_{20})=0$ (ns), R^2 $(R_{20})=0.08$ $(p<0.001)$, R^2 $(R_5)=0.12$ $(p<0.00001)$ (constant G and H across cohort)

The use of acquired, personalised, G and H parameters through the adaptive grid search, led to simulations which demonstrated significantly higher concordance with measured oscillometry outputs which are shown below.

$R^2(AX)=0.61$, $R^2(X_5)=0.70$, R^2 $(R_5-R_{20})=0.44$, R^2 $(R_{20})=0.34$, R^2 $(R_5)=0.60$ $p<0.001$ (personalised grid-search-obtained G and H)

The first observation when comparing the two sets of results, is that the reactive components of impedance simulations AX and X_5, have seen a vast improvement in their concordance with their measured counterparts. This potentially occurs because the lung stiffness represented by reactance, is captured by the viscoelastic CPM parameters damping (G) and elastance (H) of the lung's tissue. Another observation is that the resistive components of impedance appear to show lower concordance improvement between simulations and measurements than the reactive components. This may be attributed to the simplifying mathematical assumptions of the study. As described in the introduction and methods of this chapter, the FOT test takes place over time, and reflects impedance measured across one or more breathing cycles, during which airways contract and expand dynamically. Within this study, impedance was simulated using a static airway geometry and modelling framework, that do not account for the cyclic contraction and expansion occurring during breathing. As a result, the model cannot capture the dynamic effects of breathing on airway resistance, which may contribute to the smaller improvement in concordance observed for the resistive components of impedance.

Overall, there are many reasons contributing to the fact that the improvements in concordance are not perfect. Inconsistencies can be attributed to the static nature of the FOT model, the limited resolution of the medical imaging used in the study which affects the ability of the segmentation software to accurately capture the morphology of smaller airways, as well as the simplifying assumptions used for the development of the complete conducting airway trees, the algorithmic generation of the trees, and the simplifying assumptions involved in the scaling of the trees. For example, the transmural pressure, used in the scaling of the airways' radii of the lung structures, could be personalised based on the subjects' percentage contribution of their lung volume during normal tidal breathing to TLC based on their static lung volumes (FRC, TLC, and VT) for a more accurate scaling. Many pressure-volume (P-V) curves are reported in the literature such as in (Oliveira *et al.*, 2016), therefore the choice of P-V curve used will also have an effect on the transmural pressure. Another source of inconsistencies is the 1D nature of the model. This essentially means that the model is not able to account for ridging along the airways, and similar phenomena inherent in a 3D structure which may cause turbulent airflow effects and therefore affecting the simulation outputs. Another limitation that may contribute to the lower concordance observed for R_{20} arises from the extent of airway personalisation in the model. Personalised airway geometry was available only up to approximately generations 6–10, depending on the individual, while the remaining distal airways of the conducting airway tree were generated algorithmically. A previous study has suggested that small airways (≤2 mm in diameter) and upper airway/cheek shunting may contribute substantially to airway resistance, whereas larger airways may have a smaller influence on resistance (Foy *et al.*, 2019). As a result, the personalised larger airways may contribute less to the simulated resistance than the smaller airways generated algorithmically, meaning that a substantial portion of the simulated resistance may

arise from airway geometry that is not personalised. Finally, the main limitation of the model is the use of non-personalised chest wall, glottal and shunting contributions to impedance. Non-personalised model components have been utilised as personalised information, which could inform the model parameters, was unavailable. The model's limitations do not however represent limitations of the study itself, as the aim of the study is to assess whether optimisation of the model is possible through prediction of personalised CPM parameters using imaging as a physiological anchor.

Finally, the tissue damping obtained from the grid search, appeared to be statistically significant, and demonstrated significant separation between the healthy and moderate asthma groups as well as the healthy and severe asthma groups which indicates its importance in moderate and severe asthma.

2.4.2 Imaging Biomarkers and morphometric markers

Many imaging biomarkers demonstrate significant statistical separation across asthma severity groups as shown in **Table 6**. Overall, the biomarkers appeared to be poorly correlated with the viscoelastic parameters G and H, in both the grid-search-obtained and the predicted set of values as shown in the spearman correlation coefficients heatmaps. The biomarkers "jac_var", "PRM_Norm" and "tPRM_norm_V" appeared to be statistically significant in the liner regression models. For the linear regression model of G, "jac_var" which represents the change in volume, could reflect a potential relationship between tissue damping and ventilation since, the predicted tissue damping values also appeared to significantly separate between quartiles of the biomarker "zPFavg" which is a marker of regionalised airway closure in the lower lobes (Bell *et al.*, 2019). Elastance H appears to be related to the imaging biomarkers representing normal parts of the lung rather than impaired, as the biomarkers which were statistically significant in its predictive model were "PRM_Norm" and "tPRM_norm_V ". While providing a plausible explanation of imaging biomarkers in asthma remains outside the scope of this study, it is notable that the morphometric markers' (L/D and

L/D_{minor}) significance between the healthy and the severe asthma groups aligns with the significance reported in the literature between healthy and GINA 3-4 groups (Bordas *et al.*, 2015). It is also noteworthy that the results demonstrate significant separation of the marker L/D_{major} between the healthy and severe asthma groups which was not found in the literature. All three morphometric markers are higher in severe asthma than in the healthy group which indicates a smaller diameter compared to the length of the branch that is present in severe asthma, compared to a larger diameter compared to the length of the branch found in the healthy group which reflects overall airways' constriction in the severe asthma group.

2.4.3 Prediction of G and H

Following training of the linear regression models to predict the CPM parameters G and H, simulations were implemented with personalised, predicted G and H for the entire study population. The concordance between simulated and measured oscillometry outputs, which can be seen below, appeared to be higher than the concordance obtained between simulated results using constant values of G and H across the study population.

$R^2(AX)=0.28$, $R^2(X_5)=0.17$, R^2 (R_5-R_{20})$=0.17$, R^2 (R_{20})$=0.13$, R^2 (R_5)$=0.16$ $p<0.001$ (with G and H predicted from linear regression models with qCT markers)

While the concordance between the results using predicted G and H and measurements appears to be lower than the concordance observed between results obtained with grid-search-obtained G and H and measurements, this can be attributed to the simplified selection of imaging biomarkers, the imaging resolution not being able to fully capture the structural properties of the acini, which are therefore being poorly represented by the imaging biomarkers and finally the simple linear regression models used. The imaging biomarkers used to train the regression models were selected based on the strength of their Spearman correlation coefficients with the CPM parameters G and H, while maintaining a comparable number of predictors in each model. Only biomarkers showing statistically significant correlations with the CPM parameters and the strongest positive or negative associations were included. While this approach allowed identification of imaging biomarkers most strongly

associated with the CPM parameters within the dataset, it represents a simplified feature-selection strategy and may not identify the optimal combination of predictors. A more advanced method, such as an elastic net regression, or any other machine learning method could potentially yield more accurate predictions of the CPM parameters, leading to better concordance between simulated and measured oscillometry outputs. Furthermore, the predictive models were developed and evaluated within the same cohort, and no independent validation cohort was used. The inclusion of a separate validation cohort would allow the predictive performance of the regression models to be assessed on independent data and would provide greater confidence in their robustness and generalisability.

The predicted CPM parameters appeared to be more statistically significant in asthma than their grid-search-obtained counterparts. Predicted G demonstrated significant separation between healthy and moderate asthma, healthy and severe asthma, and between mild asthma and severe asthma groups. The ratio of predicted G and H, η, hysteresivity was also significantly separated between healthy and severe asthma groups, which may mostly be driven by G. Nevertheless, the predicted parameters appear to retain the properties of the grid-search-obtained parameters and therefore show potential for the linear regression models to be used for their prediction as optimising additional components to the FOT model. Another indication that the properties of the predicted CPM parameters are preserved, is the correlations between the CPM parameters and the spirometry measurements presented in **Table *5***, relevant to the grid search, and **Table *7***, relevant to the predicted measurements, which appear to be broadly similar. With the improvement in concordance arising from the use of predicted, personalised G and H, predicted using the optimising imaging-informed regression models, the aim of the study was successfully achieved proving that prediction of personalised CPM parameters G and H can increase concordance between simulated and measured oscillometry outputs.

2.5 Summary

An established FOT mathematical model demonstrated that there was room for improvement in the concordance of its simulations and measured oscillometry outputs. In this study, data were collected from a large cohort (ATLANTIS) which included asthmatic patients (n=135) and healthy individuals (n=25), to assess whether the prediction of personalised CPM parameters using imaging biomarkers derived from CT imaging, can improve the concordance between FOT simulations in this cohort, and their measured oscillometry counterparts. The concordance obtained between results arising from simulations utilising grid-search-obtained, personalised CPM parameters, and measurements was significantly improved compared to the concordance obtained with results arising from simulations using constant CPM parameters across the study cohort. The grid-search-obtained tissue damping G also showed statistically significant separation between the healthy and moderate asthma groups as well as healthy and severe asthma groups suggesting that this parameter is sensitive to differences in asthma severity. The concordance obtained between results arising from - simulations utilising predicted, personalised CPM parameters predicted with imaging-informed linear regression models - and measurements, was also improved, compared to the concordance obtained with results arising from simulations using constant CPM parameters across the cohort, however with a lower concordance than the one obtained with the grid-search-obtained CPM parameters. This can be attributed to imaging resolution limitations and the simplicity of the methods used for training and prediction of the CPM parameters. The predicted CPM parameters appear to be similarly correlated with spirometry measurements and imaging biomarkers as the grid-search-obtained CPM parameters which are both aligned with the literature, indicating that the regression models can be used as optimising components to the FOT model. Additionally, the predicted tissue damping G values appeared to significantly separate across asthma severity scales in a similar manner to the grid-search-obtained values demonstrating that the markers' sensitivity to differences in asthma severity is preserved. Finally, the aim of the study to assess whether prediction of personalised CPM parameters using imaging biomarkers would increase the concordance between FOT

simulated outputs and measurements, was successfully achieved showing the potential of future use of the regression models and the imaging biomarkers in the optimisation of the FOT model.

3. V/Q model Development

3.1 Rationale

In the introduction, the importance of structure function relationships was highlighted as they facilitate our understanding of the mechanisms of the respiratory system and form the basis of medical diagnosis. Various tests have been developed to diagnose and assess chronic respiratory diseases including the single-breath CO gas-transfer test (Graham *et al.*, 2017) which is based on a method developed in 1915 by Marie Krogh (Krogh, 1915). This test measures the uptake of CO in the lungs utilising fundamentals of gas diffusion (Fick's law) (Modi and Cascella, 2024). Its output, DLCO is a predictor of exacerbations in COPD and a risk factor for all-cause mortality (Li *et al.*, 2023; Park *et al.*, 2024). The results of this test are not easy to interpret as they are composites of V and Q and do not dissect the two. While this test provides insights into gas-exchange efficiency, it fails to provide a comprehensive understanding of mechanisms underlying blood-gas barrier dysfunction. This is because the test's outputs do not localise blood-gas barrier pathology and are non-spatial. Lung disease however is highly spatial and therefore the test outputs are limited in their ability to capture the localised nature of lung disease. Advancements in technology have made the development of advanced imaging techniques possible leading to spatial tests such as MRI coupled with inhaled gases such as hyperpolarised ^{129}Xenon (Cleveland *et al.*, 2014; Matheson *et al.*, 2022; O'Sullivan-Murphy, Driehuys and Mammarappallil, 2022). Such techniques offer more localised V/Q dynamics. Hyperpolarised ^{129}Xenon has been used in the identification of ventilation defects in asthma and has provided a way to quantify VH as ventilation defect percent (VDP) (Fain *et al.*, 2007; McIntosh *et al.*, 2023). Advanced imaging techniques such as this, however, are limited in their ability to provide measurements in hypothetical or unseen scenarios involving changes to the lungs' structure. An advantage of computational modelling is that it allows simulation of hypothetical or unseen scenarios to understand the effect of structural alterations on lung function.

The combination of imaging techniques with computational modelling has shown promise in providing insights into the structural and functional relationships of the respiratory system. Various models representing different pulmonary functions, and allowing the exploration of structure-function relationships, characterised as “simulation patient digital twins” can form the desired “monitoring patient digital twin” when joined together, and in combination with advanced monitoring equipment and machine learning techniques. The development of this “monitoring patient digital twin” however requires the development and validation of smaller “simulation patient digital twins”, therefore the development and validation of an imaging-informed digital twin of the CO gas transfer test is a vital and necessary step forward.

3.1.1 Single-breath CO gas-transfer test in clinical practice

Gas exchange between the atmosphere and the pulmonary circulation is the primary function of the lungs (Sylvester *et al.*, 2020). The lungs’ ability to exchange gas through the alveolar-capillary membrane is determined by functional and structural characteristics. Structural characteristics include the membrane’s thickness, lung volume, capillary blood volume and surface area of the lungs participating in gas exchange. Functional characteristics of the ability of the lung’s to exchange gas through the alveolar-capillary membrane include V/Q matching, membrane characteristics, and haemoglobin (Hb) levels among others (Sylvester *et al.*, 2020).

As discussed in the introduction, gas exchange is governed by Fick’s law of diffusion. This law states that “the rate of transfer of a gas through a membrane of constant thickness is proportional to its surface area and the difference in gas partial pressure between the two sides (P_1-P_2), and inversely proportional to the membrane thickness” (Sylvester *et al.*, 2020). For the single-breath CO gas transfer test, the membrane refers to the alveolar-capillary membrane, its thickness and surface area, and the partial pressure of CO and blood on the other side of the membrane.

The test requires the participant to fully exhale effortlessly to RV and then inhale maximally to TLC a mixture of gas which is typically composed of 21% oxygen, 0.3% carbon monoxide, a tracer gas, which is usually either helium or methane and a balance of nitrogen (Graham *et al.*,

2017; Sylvester *et al.*, 2020). The utility of the tracer gas is to determine the initial alveolar CO concentration and alveolar volume (volume of air participating in gas exchange) from which uptake of CO is occurring (Graham *et al.*, 2017). This is followed by a breath-holding time (BHT) of approximately 10 seconds, during which the CO diffuses into the blood, followed by a complete exhalation. Following the breath hold, during exhalation, the initial portion of the exhaled air is discarded from the collected sample as it includes gas from the instrumental and anatomical dead spaces. To estimate the alveolar volume, the collected sample is scaled down by the mass balance ratio of the tracer gas' (helium or methane) concentration at the start and end of the test. The concentration of carbon monoxide at the end of the test C_o and the concentration of carbon monoxide at the end of the test C_t, along with the alveolar volume (volume of ventilated alveoli), and the partial pressure of CO in the alveoli Pb^* (difference between atmospheric/barometric pressure at sea level – 760 mmHg and water vapour pressure at 37°C – 47 mmHg), are used in the calculation of the two test outputs, the diffusing capacity of the lungs for CO – DLCO (total diffusing capacity of the lung), and the transfer coefficient of the lungs for CO - KCO (gas transfer efficiency per unit lung). The directly measured quantities from the test are the alveolar volume (Va) and KCO, while DLCO is a derived quantity arising from the product of KCO and Va as shown below.

$$kCO = \frac{ln\left(\frac{C_0}{C_t}\right)}{BHT}$$

$$DLCO = \frac{kCO * V_A}{Pb^*}$$

$$KCO = \frac{DLCO}{V_A} = \frac{kCO * V_A}{Pb^* * V_A} = \frac{kCO}{Pb^*}$$

$$DLCO = \frac{kCO}{Pb^*} * V_A = KCO * V_A$$

The outputs of the single-breath CO gas transfer test can be influenced by multiple factors including anthropological, such as height, sex, age and ethnicity or race as well as kinetics and location, i.e., exercise and altitude (Yamamoto and Shimizu, 2025). The former affects the

pulmonary blood flow which subsequently affects both test outputs, known to be elevated during exercise, and the latter affects the barometric/atmospheric pressure which is used in the calculation of both test outputs (Yamamoto and Shimizu, 2025). Increased capillary blood volume is known to raise KCO values due to increased efficacy of CO absorption (Yamamoto and Shimizu, 2025). The calculation of DLCO is based on the assumption that the tracer gas (helium) and CO mixture, is evenly and quickly diluted into the alveoli. The assessment's validity therefore is highly affected by pathophysiologies such as V/Q mismatch and VH (Yamamoto and Shimizu, 2025). Underestimation of DLCO, for example, can result from VH preventing access of the mixture of CO and helium to the alveoli and thus not allowing the mixture to dilute evenly within the alveoli (Yamamoto and Shimizu, 2025).

3.2 Materials and Methods

A mechanistic mathematical model was developed, serving as a spatially localised physiological digital twin of the single-breath carbon monoxide (CO) gas-transfer test (Graham *et al.*, 2017), with DLCO and KCO as test outputs **Figure *33***. The model input parameters are based on physiologic inputs **Figure *19*A** related to lung morphology, that can be obtained from medical images such as CT or MRI lung scans. The current physiologic inputs can be calculated for an individual of a selected age, height and gender using the (Global Lung Function Initiative) GLI reference equations (Stanojevic *et al.*, 2017; Hall *et al.*, 2021). The model consists of four compartments (reflecting the four primary lung lobes), each with its own blood supply as shown in **Figure *19*B**. Given CO has a high affinity for haemoglobin, the model assumes that gas exchange is diffusion-limited (*Diffusion-Limited and Perfusion-Limited Gas Exchange - Respiratory - Medbullets Step 1*, 2024). Capillary blood was modelled as an infinite sink, with CO uptake being limited by the diffusion rate, and not affected by capillary blood flow. This means that for a given capillary length, CO partial pressure does not equilibrate (i.e., gas diffusion does not stop) by the end of the capillary, regardless of the volume of blood that can flow along that length, (regardless of capillary blood flow or capillary volume)(*Diffusion-Limited and Perfusion-Limited Gas Exchange - Respiratory - Medbullets Step 1*, 2024). The CO diffusion rate is the driving mechanism of the model and is scaled as described in the *Methods* section (3.2.1*)* for each lung chamber. The baseline diffusion rate is calculated using a healthy DLCO value for an individual of a selected age, height and gender using the GLI reference equations (Stanojevic *et al.*, 2017). The scaling of the healthy DLCO accounts for changes in blood volume from a two-lung healthy respiratory system's CO diffusion rate to a compartmental CO diffusion rate. The healthy DLCO is also scaled by the mean harmonic alveolar-capillary membrane thickness and surface area which are the major determinants of gas transfer across the membrane according to Fick's law (Hsia, 2006). Finally, the scaling takes into account the alveolar expansion and more specifically the changes in radius of an alveolus (McGrath and Thomson, 1959) which is represented by changes in the ratio of alveolar volume (VA) to total lung capacity TLC. The model was used to simulate a 10-

second breath-hold in small time increments (using a timestep of 0.001s), from an initial CO concentration of 0.3%, according to the standard practise for performing a single breath CO gas-transfer test. The model uses simple principles of dilution to calculate the concentration in the volume of air in the lungs participating in gas exchange and the dead space, from the initial 0.3% concentration of CO in the mouth. The final concentration that is used to calculate the outputs DLCO and KCO, is the concentration of CO that is present within the volume of the lungs that participates in gas exchange (i.e., not at the mouth). The calculation of the outputs is implemented using the concentration of CO in that area of the lungs, which mimics the dismissal of exhaled anatomical and instrumental dead space volumes of air for the calculation of the test outputs during the real-world test. The DLCO and KCO were estimated from the simulated exhalation curves after the 10s breath bold **Figure *19*C.**

3.2.1 Mathematical assumptions for V/Q model development

The 'digital twin' of the CO gas-transfer test is split into 4 compartments, to allow for symmetry among the compartments and simplify data acquisition for validation of the model outputs. Each compartment as seen in **Figure *19***, consists of its own blood supply, volume, mean harmonic alveolar-capillary membrane thickness and subsequently its own diffusion scaling equation, and thus its own diffusion rate. The diffusion rate is approximated using a healthy DLCO predicted value for the individual, and it is scaled for each compartment using the diffusion scaling equation.

To approximate the rate of diffusion of CO from an alveolus to the bloodstream, a baseline Diffusing Capacity (DLCO) value of a healthy subject can be utilised as it is the only indication of the rate at which CO diffuses into the blood, across the alveolar-capillary membrane. In the model, a healthy DLCO is calculated using the reference Global Lung Function Initiative (GLI) equation (Stanojevic *et al.*, 2017) using a subject's age, height, and gender. A healthy value of i.e., an adult male, as follows, transformed as below, can then be used as the baseline rate of diffusion. To account for regional changes in the structure, the baseline diffusion rate needs

to be scaled and calculated for each region of the structure, based on relative changes to a two-lung structure.

$$DLCO_h = 28\ [mL/min/mmHg] = \frac{28}{1000 \times 60}\ [L/s/mmHg]$$

The model here is split into 4 regions, each with its own blood supply. Since the amount of blood and surface area participating in gas-exchange are vital elements in the gas-exchange process, the diffusion rate is scaled based on relative changes between the regional compartment and the two-lung structure. Assuming the diffusion rate is directly proportional to the surface area (SA) participating in gas-exchange,

$$D \propto SA_{gas\ exchange}$$

and assuming that the diffusion rate is also proportional to the Capillary Blood Volume (V_C), the equations for volume and surface area (participating in gas exchange) can be used to derive the effect that a blood volume change will have on the surface area participating in gas-exchange and thus the diffusion rate. In this study it was therefore assumed that the surface area participating in gas exchange is half the curved surface area of a cylinder (SA_1) and the volume where capillary blood is contained is half the volume of a cylinder (V_1) which both represent half the surface area and half a volume of a pulmonary capillary.

$$SA_1 = \pi r_1 h \tag{1}$$

$$V_1 = \frac{1}{2}\pi r_1^2 h \tag{2}$$

Solving for r_1 in (2) and substituting to (1),

$$r_1 = \left(2\frac{V_1}{\pi h}\right)^{\frac{1}{2}}$$

$$\therefore\ SA_1 = \pi\left(2\frac{V_1}{\pi h}\right)^{\frac{1}{2}} h \tag{3}$$

Considering therefore a change in blood volume ΔV_C, the new volume V_2 can be expressed as:

$$V_2 = V_1\ \Delta V_C$$

The change is expressed in equation 4 as the percentage of the compartment's half capillary blood volume as compared to half of the total capillary blood volume of a two-lung structure.

This is due to the assumption that half of the curved surface area of the cylinder (capillary) participates in gas-exchange.

$$\Delta V_C = \frac{\frac{V_{CS}}{2}\frac{P_C}{2}}{\frac{V_{CH}}{2}} = \frac{V_{CS}\,P_C}{4}\,\frac{2}{V_{CH}} = \frac{V_{CS}\,P_C}{2V_{CH}} \tag{4}$$

Where, V_{CS} is the total capillary blood volume of the subject, P_C is the compartmental capillary blood volume percentage contribution to the total and V_{CH} is the healthy capillary blood volume of a two-lung structure. The resulting change in surface area can be obtained by applying the change in blood volume to the surface area as follows,

$$SA_2 = \pi\left(2\frac{V_2}{\pi h}\right)^{\frac{1}{2}} h = \pi\left(2\frac{V_1\,\Delta V_C}{\pi h}\right)^{\frac{1}{2}} h$$

$$\Rightarrow SA_2 = \pi\left(2\frac{V_1}{\pi h}\right)^{\frac{1}{2}} h\,\Delta V_C{}^{\frac{1}{2}}$$

$$\Rightarrow SA_2 = SA_1\,\Delta V_C{}^{\frac{1}{2}} \tag{5}$$

Substituting equation (4) to (5) results to equation (6) below which shows the relationship between SA_2 and SA_1 following a change in blood volume. The relationship is illustrated in equations 7 and 8.

$$\Rightarrow SA_2 = SA_1\left(\frac{V_{CS}\,P_C}{2V_{CH}}\right)^{\frac{1}{2}} \tag{6}$$

$$SA_2 \propto \Delta V_C{}^{\frac{1}{2}} \Rightarrow SA_2 \propto \sqrt{\Delta V_C} \tag{7}$$

$$\therefore SA_2 \propto \sqrt{\frac{V_{CS}\,P_C}{2V_{CH}}} \tag{8}$$

This yields the first scaling of the diffusion rate due to changes in capillary blood volume for each of the compartments of the model as shown in equation 9.

$$D = DLCO_h\,\Delta V_C{}^{\frac{1}{2}} \;\Rightarrow D = DLCO_h\sqrt{\frac{V_{CS}\,P_C}{2V_{CH}}} \tag{9}$$

To account for changes in the alveolar volume as compared to the alveolar volume at TLC, the same approach is used to derive the effect of volume change to the radius of an alveolus

(sphere). Assuming that the radius of an alveolus is proportional to the diffusion rate (permeability)(McGrath and Thomson, 1959) as,

$$D \propto r$$

The volume of an alveolus is given by:

$$V_{alv1} = \frac{4}{3}\pi r_1^3$$

Solving for the radius,

$$r_{alv1} = \left(\frac{3}{4}\frac{V_{alv1}}{\pi}\right)^{\frac{1}{3}}$$

Considering therefore a change in alveolar volume as compared to TLC - ΔV_A, the effect on the radius can be obtained as follows and is presented in equations 10 and 11.

$$r_{alv2} = \left(\frac{3}{4}\frac{V_{alv1}\,\Delta V_A}{\pi}\right)^{\frac{1}{3}}$$

$$r_{alv2} = \left(\frac{3}{4}\frac{V_{alv1}}{\pi}\right)^{\frac{1}{3}} {\Delta V_A}^{\frac{1}{3}}$$

$$r_{alv2} = r_{alv1}\,{\Delta V_A}^{\frac{1}{3}} \tag{10}$$

$$\therefore \quad D \propto {\Delta V_A}^{\frac{1}{3}} \Rightarrow \quad D \propto \sqrt[3]{\Delta V_A} \Rightarrow D \propto \sqrt[3]{\frac{VA}{TLC}} \tag{11}$$

This yields the second scaling of the diffusion rate due to changes in alveolar volume as compared to TLC as shown below in equation 12.

$$D = DLCO_h \sqrt{\Delta V_C}\ \sqrt[3]{\Delta V_A}$$

$$\Rightarrow D = DLCO_h \sqrt{\frac{V_{CS}\,P_C}{2V_{CH}}}\ \sqrt[3]{\frac{VA}{TLC}} \tag{12}$$

$$or\ D = DLCO_h \left(\frac{V_{CS}\,P_C}{2V_{CH}}\right)^{\frac{1}{2}} \left(\frac{VA}{TLC}\right)^{\frac{1}{3}}$$

To account for changes in the alveolar-capillary membrane (ACM) thickness as compared to a healthy membrane thickness, the following approach was used. I assumed that the mean harmonic alveolar-capillary membrane thickness of an alveolus is inversely proportional to

the diffusion rate (Hsia, 2006; Leiby, Raredon and Niklason, 2020). The mean harmonic alveolar-capillary membrane thickness was assumed to consist of the tissue barrier ($\tau_{acm_{tissue}} = 0.62\mu m$)(Gehr, Bachofen and Weibel, 1978) and the plasma barrier ($\tau_{acm_{plasma}} = 0.15\mu m$)(Gehr, Bachofen and Weibel, 1978).

$$D \propto \frac{1}{\tau_{acm}}$$

Therefore, the diffusivity was assumed to be inversely proportional to the change in mean harmonic alveolar-capillary membrane thickness $\Delta_{\tau_{acm}}$.

$$D \propto \frac{1}{\Delta_{\tau_{acm}}}$$

Where the change can be expressed as,

$$\Delta_{\tau_{acm}} = \frac{\tau_{acm}}{\tau_{acm_{Healthy}}} \tag{13}$$

The baseline diffusion rate scaling – accounting for a change in blood volume from a two-lung structure to a structure of a single compartment, a change in alveolar volume as compared to TLC, as well as a change in mean harmonic alveolar-capillary membrane thickness – can be implemented for each lung compartment as shown below with equation 15.

$$D = DLCO_h \left(\frac{V_{CS}\, P_C}{2V_{CH}}\right)^{\frac{1}{2}} \left(\frac{VA}{TLC}\right)^{\frac{1}{3}} \frac{\tau_{acm_{Healthy}}}{\tau_{acm_{compartment}}} \tag{14}$$

$$D = DLCO_h \left(\frac{V_{CS}\, P_C}{2V_{CH}}\right)^{\frac{1}{2}} \left(\frac{VA}{TLC}\right)^{\frac{1}{3}} \frac{\tau_{h_H}}{\tau_{h_C}} \tag{15}$$

To account for changes in the Red Blood Cell (RBC) membrane thickness as compared to a healthy RBC membrane thickness, a similar approach can be used. The mean harmonic alveolar-capillary membrane thickness of an RBC can be assumed to be inversely proportional to the diffusion rate (Hsia, 2006; Leiby, Raredon and Niklason, 2020) and the RBC membrane can be assumed to have a mean value of $\tau_{RBC} = 0.45nm$ (Heinrich *et al.*, 2001).

$$D \propto \frac{1}{\tau_{RBC}}$$

Therefore, the diffusivity can be assumed to be inversely proportional to the change in mean RBC membrane thickness $\Delta_{\tau_{RBC}}$.

$$D \propto \frac{1}{\Delta_{\tau_{RBC}}}$$

Where the change can be expressed as,

$$\Delta_{\tau_{RBC}} = \frac{\tau_{RBC}}{\tau_{RBC_{Healthy}}} \tag{16}$$

Finally, the mean harmonic thickness (τ_h) of the entire blood-gas barrier including all the membranes (RBC and the alveolar-capillary membranes) can be expressed as follows (Leiby, Raredon and Niklason, 2020):

$$\frac{1}{\tau_h} = \frac{1}{n}\sum_{i=1}^{n}\frac{1}{\tau_i}$$

$$\therefore \quad \frac{1}{\tau_h} = \frac{1}{2}\left(\frac{1}{\tau_{acm}} + \frac{1}{\tau_{RBC}}\right) \tag{17}$$

Since the diffusion capacity is inversely proportional to the total harmonic mean barrier thickness (Leiby, Raredon and Niklason, 2020), it can be assumed that the diffusion rate is also inversely proportional to the total harmonic mean barrier thickness.

$$D \propto \frac{1}{\tau_h}$$

By substituting the change in alveolar-capillary membrane thickness and the change in RBC membrane thickness in the above equation (17), the following relationship can be obtained, expressed in equation 18.

$$D \propto \frac{1}{\tau_h} = \frac{1}{n}\sum_{i=1}^{n}\frac{1}{\tau_i}$$

$$D \propto \frac{1}{n}\sum_{i=1}^{n}\frac{1}{\tau_i}$$

$$D \propto \frac{1}{2}\left(\frac{1}{\Delta_{\tau_{acm}}} + \frac{1}{\Delta_{\tau_{RBC}}}\right)$$

$$D \propto \frac{1}{2}\left(\frac{1}{\frac{\tau_{acm_{cmp}}}{\tau_{acm_{Healthy}}}} + \frac{1}{\frac{\tau_{RBC_{cmp}}}{\tau_{RBC_{Healthy}}}}\right)$$

$$D \propto \frac{1}{2}\left(\frac{\tau_{acm_{Healthy}}}{\tau_{acm_{cmp}}} + \frac{\tau_{RBC_{Healthy}}}{\tau_{RBC_{cmp}}}\right) \quad (18)$$

The baseline diffusion rate scaling – accounting for a change in blood volume from a two-lung structure to a structure of a single compartment, a change in alveolar volume as compared to TLC, a change in mean harmonic alveolar-capillary membrane thickness as well as a change in RBC membrane thickness – can be implemented for each lung compartment as shown below with equation 19.

$$D = DLCO_h\left(\frac{V_{CS}\,P_C}{2V_{CH}}\right)^{\frac{1}{2}}\left(\frac{VA}{TLC}\right)^{\frac{1}{3}}\frac{1}{2}\left(\frac{\tau_{acm_H}}{\tau_{acm_c}} + \frac{\tau_{RBC_H}}{\tau_{RBC_c}}\right) \quad (19)$$

The new amount of CO within each compartment is calculated in small time increments of time until the breath-holding time of 10 seconds is reached. This is achieved with the equation 20 below where N_{CO} is the new CO amount in the compartment, E_{CO} is the existing amount of CO in the compartment, D is the scaled diffusion rate, dt is the small time increment of 0.001 seconds, P_{blood} is the partial pressure of blood and is assumed to be zero since blood is modelled as an infinite sink due to the nature of the diffusion limited gas exchange and finally P_{acin} is the alveolar CO partial pressure of the compartment which has a fixed value of 713 mmHg which is calculated by subtracting the water vapour pressure at body temperature (37°C) of 47 mmHg from the alveolar gas pressure taken as 760 mmHg. The new amount of CO remaining in the compartment is calculated in litres and updated every time increment and is then used to calculate the final concentration of CO in the volume of air that participates in gas-exchange, i.e., the alveolar volume, considering the removal of anatomical and instrumental dead-space that takes place during the test in the real world.

$$N_{CO} = E_{CO} + dt\,D\,(P_{blood} - P_{acin}) \quad (20)$$

3.2.2 Personalisation of structural lung information

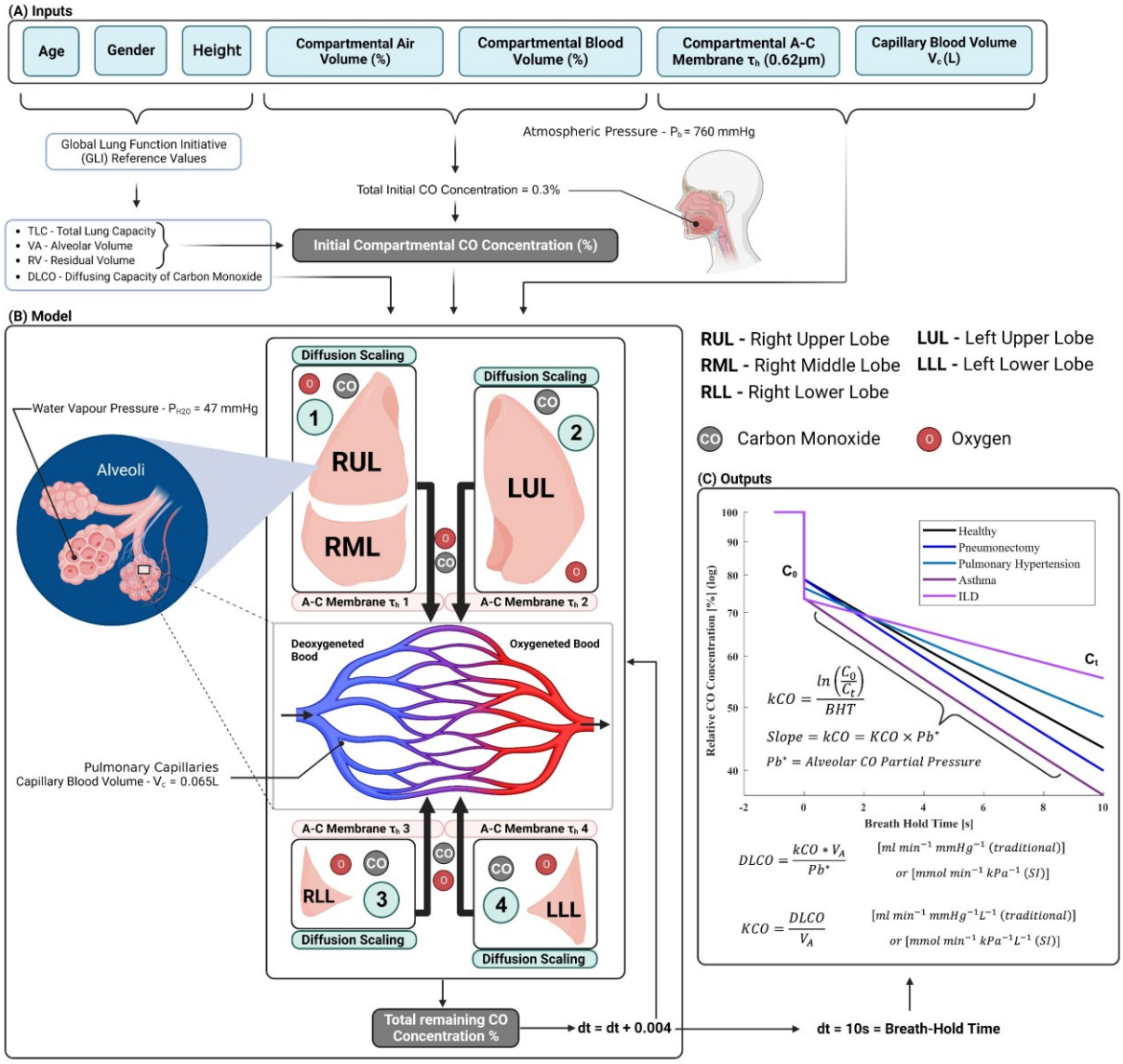


Figure 19 – V/Q Model Overview

Inputs (A), Conceptualisation (B) and Outputs (C) – (A) Model Inputs where Lobar percentage contributions to TLC (Yamada et al., 2020) as LUL 23%, LLL 23.7%, RUL + RML 26.4%, RLL 26.9%, and GLI reference equations (Stanojevic et al., 2017; Hall et al., 2021). GLI equations are used for the calculation of patient-specific predicted lung volumes TLC, RV, VA, as well as the predicted DLCO as an indication of the rate of diffusion of CO across the alveolar-capillary membrane. **(B) Internal Model Operation** – The remaining CO concentration is calculated iteratively in small increments of time (dt) until the Breath-Hold Time (BHT) is

reached. The healthy diffusion is scaled based upon the changes occurring in the structural inputs from a two-lung system to a compartmental system. This leads to each compartment having its own diffusion rate which is used to calculate the remaining CO concentration. Each compartmental calculation of the remaining CO concentration contributes 0.001s to the BHT. Finally, the pulmonary capillary blood volume was taken as V_C=65 mL (Lewis et al., 1958). **(C) Model Outputs** – DLCO and KCO are calculated based on the rate of decrease of the relative CO concentration over the 10-second breath hold. Created with BioRender.com.

3.2.3 Simulations of hypothetical disease

The model was validated by comparing estimated changes in KCO and DLCO (from healthy simulated baseline values) to clinically reported changes in hypothetical disease states. These disease states included Pulmonary Hypertension, by changing the capillary blood volume, VA and RV, Asthma, by changing the ratio of VA/TLC to simulate gas-trapping, as well as changing the distribution of capillary blood from poorly-ventilated regions to well-ventilated regions due to HPV and TLC, Pneumonectomy by the removal of the right lung which subsequently causes reduction of TLC and RV, and an increase in the Capillary Blood Volume of the remaining lung, and Interstitial Lung Disease by changing the mean harmonic alveolar-capillary membrane thickness of the two lungs, the capillary blood volume and TLC as shown in **Table 9**. The healthy mean harmonic alveolar-capillary membrane thickness was taken as $\tau_{h_{tissue}} + \tau_{h_{plasma}} = 0.77\mu m$ and the application of changes in thickness is described in **Table 9**. The minimum and maximum changes were calculated based on changes to the mean reported ratio of thickness between τ_h_ILD = 1.464 (0.187)μm and healthy subjects τ_h_healthy = 0.829 μm. The ratio of mean thickness change was taken as Mean: 1.464/0.829 = 1.77 and therefore the minimum and maximum change was calculated as follows taking into account 2 standard deviations from the mean. Change: minimum = (1.464 - 2*0.187)/0.829 = 1.31 maximum = (1.464 + 2*0.187)/0.829 = 2.22. The expected input vectors used in the simulations were generated as 51 equally spaced increments for each input range plotted are shown in **Table 9**.

3.2.4 Validation with healthy behaviour in Va reduction

Firstly, the 'single-breath CO gas-transfer digital twin' was validated through an examination of the dependence of the DLCO and KCO on alveolar volume as a percentage of fully expanded volume at TLC, to understand how alveolar volume, and thus alveolar surface area tracks with the DLCO and KCO. This was implemented by simulating DLCO and KCO while changing the Va input relative to a fixed TLC. I then compared the model results to previously reported data (Johnson, 2000; Hughes and Pride, 2012) from 24 healthy volunteers that had been derived using statistical regression methods.

3.2.5 Validation with structural alterations in disease

I assessed the model's performance by comparison of its outputs in three prototypical cardio-respiratory disease cases and right-lung post-surgical pneumonectomy – all characterised by different intrinsic drivers for abnormal DLCO and/or KCO test results in clinical practise. The four cases were asthma – which is characterised by an elevated KCO, a reduced DLCO and the main mechanism of its gas exchange abnormality is V/Q mismatch (Sarkar, Niranjan and Banyal, 2017), post-operative right lung pneumonectomy – where changes in the KCO and DLCO would be expected to be driven by changes in lung volumes primarily, Interstitial Lung Disease (ILD) – characterised by alveolar basement membrane thickening and reduced CO gas transfer due to fibrosis and Pulmonary Hypertension (PH) – characterised by pulmonary vascular remodelling and reduced CO gas transfer. For each case, the comparison of changes to physiological model inputs was implemented against a baseline 'healthy lung simulation' of the test outputs (DLCO and KCO), for an individual of the selected age, height, and gender. Starting from the simulation of a baseline healthy simulation, the healthy lung structure and function was then modified based on expected changes to the physiology, according to each disease case. Comparison of disease simulations with the 'healthy baseline simulation for the subject of selected age, height and gender was implemented in all simulations presented in this study leading to the results being presented as % of the healthy simulated test outputs DLCO and KCO.

Table 9 - Investigative physiologic input data. Input Alterations for 4 hypothetical disease cases and simulated DLCO and KCO results.

Where, V_C – Capillary Blood Volume, TLC – Total Lung Capacity, VA – Alveolar Volume, Th – mean harmonic alveolar-capillary membrane thickness, PPH – Primary Pulmonary Hypertension, CTPH – Chronic Thromboembolic Pulmonary Hypertension, CHD-PAH – Congenital Heart Disease associated Pulmonary Arterial Hypertension

Disease	Input Alterations (% of baseline)		DLCO	KCO
Pulmonary Hypertension (PH)	PH Systemic Sclerosis Female majority, mean Height 1.6m, mean Age 68	(Sivova *et al.*, 2013)	44 (27-56)	59 (34-110)
	PPH – Female majority, mean Height 1.64m mean Age 44	(D'Alonzo, Bower and Dantzker, 1984; Sun *et al.*, 2003)	68 (51-85) 59 (15-103)	81 (62-100)
	CTPH	(D'Alonzo, Bower and Dantzker, 1984)	60 (22-98)	-
	CHD-PAH – mean Height 1.63 mean Age 32	(Jing *et al.*, 2009; Broberg *et al.*, 2014)	71.21 (66.81-75.61), 62 (34-108)	- 75 (45-111) (Broberg *et al.*, 2014)
	V_c – 60(34-89) (Sivova *et al.*, 2013)			
	TLC – 90(82-110) (Sivova *et al.*, 2013), 87 (63-111) (D'Alonzo, Bower and Dantzker, 1984), 98 (74-122) (Meyer *et al.*, 2002)			
	RV – 118 (70-166) (Meyer *et al.*, 2002)			
	VA – 83 (55-111) (Sun *et al.*, 2003), 89 (59-119) (Broberg *et al.*, 2014)			
	Female Mean Age 48, Height 1.62m (simulation with no TLC change)			
	Mean of means and maximum range	**Literature**	**60.70 (15-108)**	**71.67 (34-111)**
Pneumonectomy	Male, Height 1.7m, Age 67 (Deslauriers *et al.*, 2011)	(Corris *et al.*, 1987; Deslauriers *et al.*, 2011)	57.6 (31-64) 55(33-77)	111.3 (38-172)
	TLC – 58(32-84)			
	RV – 56(30-82)			
	Right Lung Size – 0% Left Lung Size – 46.7%			
	V_c – (46.7%*77%*V_{CH} - 46.7%*239%*V_{CH}) Table 5 (Ravikumar *et al.*, 2013) Normal - 1.31(0.19) ml/kg INF2 - 2.07(0.53) ml/kg DEF – 2.39(0.37) ml/kg Range INF2 – 2.07/1.31 = 1.58 Minimum INF2 – (2.07-2*0.53)/1.31 = 0.77 Maximum INF2 – (2.07+2*0.53)/1.31 = 2.39			

	Range DEF – 2.39/1.31 = 1.82 Minimum DEF – (2.39-2*0.37)/1.31 = 1.26 Maximum DEF – (2.39+2*0.37)/1.31 = 2.39 Maximum range – (0.77-2.39)			
	Male, Height – 1.7m, Age – 67			
	Mean of means and maximum range	**Literature**	**56.3 (31-77)**	**111.3 (38-172)**
Asthma	Female (54% of 74 individuals), Height 1.62m, Age 55.5 years	(Gonem *et al.*, 2014)	91.2 (86.2-96.2) mild 89.5 (83.7 – 95.3) severe	107.4 (102-112.8) 104.6 (98.6 – 110.6)
	VA/TLC –82(78.8-85.2) mild, 80.8(78-83.6) 2SD severe			
	TLC –104.9(99.9-109.9) mild, 107.8(101.4-114.2) severe			
	Distribution of blood from lower lobes, specifically LLL & RLL from 100% (healthy) to 25% - Blood re-distributed to upper lobes – RUL + RML and LUL			
	Mean of means and maximum range	**Literature**	**90.35 (83.7-96.2)**	**106 (98.6-112.8)**
Interstitial Lung Disease (ILD)	Female, Height 1.65m, Age 52	(Sivova *et al.*, 2013)	52 (34-87)	76 (50-102)
		(Ventura *et al.*, 2023)	72.2 (63.3-81)	
	Female majority	(Pugashetti *et al.*, 2023)	41.4 (8.6-74.8) 36.8 (12-61.6)	-
	Th - 177(131 - 222) (Cassan, Divertie and Brown, 1974; Gehr, Bachofen and Weibel, 1978)			
	TLC – 80(65-123) (Sivova *et al.*, 2013), 73.5 (66.5-80.5) (Ventura *et al.*, 2023)			
	V_c – 53(27-142) (Sivova *et al.*, 2013)			
	Female, Height 1.65m, Age 52			
	Mean of means and maximum range	**Literature**	**50.6 (8.6-87)**	**76 (50-102)**

3.3 Results

3.3.1 Healthy behaviour in alveolar volume reduction

The results can be seen in **Figure *20*** where the simulated outputs were plotted along with the regressed model outputs (Johnson, 2000). This is a verification of the model's functionality as a structure-function model and validation of its simulated results with published literature. The primary observation from **Figure *20*** for both DLCO and KCO is that the simulated outputs are almost identical to the regression predicted output DLCO ($R^2 =$

0.99), KCO ($R^2 = 0.99$). There are subtle differences however, the most evident one being that the DLCO follows an exponential function rather than a linear one with respect to VA/VA_{TLC} in the simulated output.

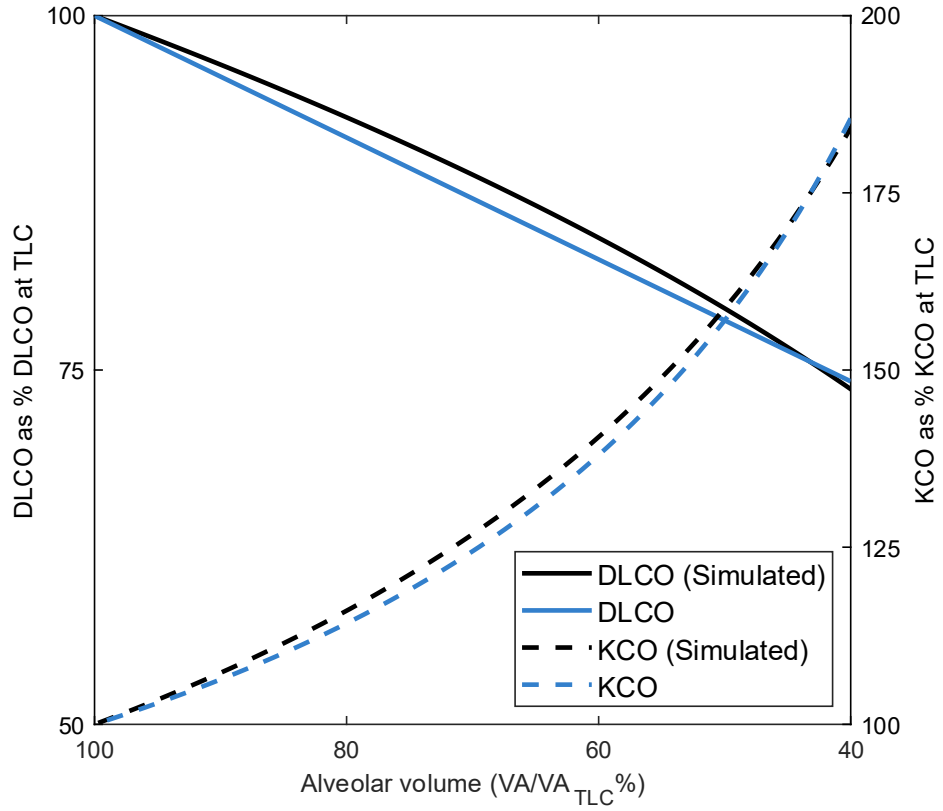


Figure 20 – Validation of the Digital Twin in reduction of alveolar volume.

Model simulated (black) effect of reduction in alveolar volume (Va) on DLCO ($R^2 = 0.99$) and KCO ($R^2 = 0.99$) is concordant with expected output behaviour reported in the literature (blue). The effects of Va reduction on DLCO and KCO test outputs were simulated using the 'digital twin' of the CO gas-transfer **(black)** and compared against a regression model **(blue)**, derived from healthy volunteers as a validation of the model. The high concordance between the simulated and regressed outputs shows the ability of the mechanistic model to capture the expected regressed behaviour of DLCO and KCO upon reduction of Va. Re-created with MATLAB using the reference equations from literature **(blue)** where KCO/KCO_{TLC} was calculated for various values of V_A/V_{ATLC} using the equation

$KCO/KCO_{TLC} = 0.43 + 0.57 / (V_A/V_{ATLC})$ and $DLCO/DLCO_{TLC}$ was calculated as the product of KCO/KCO_{TLC} and V_A/V_{ATLC}. These reference equations were derived from a regressed model for 24 normal subjects.

3.3.2 Sensitivity to a blend of structural alterations in disease

The results of structural alterations in disease are summarised in **Figure *21***. The figure represents the means ±2σ for each of the plots shown in **Figure *22*** and **Figure *23***. The sensitivity of DLCO and KCO to structural and functional changes at the blood-gas barrier was further evaluated in the disease context (**Figure 22 and Figure 23**)**.** Initial investigation (**Figure 23**) focussed on disease associated with lung volume changes – pneumonectomy (reduced lung volume and compensatory lung hyperinflation) and asthma (elevated lung volume and gas trapping due to distal airways closure and obstruction) as well as blood re-distribution from poorly ventilated areas to well-ventilated areas due to Hypoxic Pulmonary Vasoconstriction (HPV) which is the compensatory mechanism as a result of hypoxemia (Sarkar, Niranjan and Banyal, 2017). Notably our mechanistic model suggests that capillary blood volume (V_C) is a major driver of the DLCO post pneumonectomy, but not the KCO – which is predominantly driven by residual volume of the native remaining lung (**Figure *23*A**). In contrast in asthma **Figure *23*B**, the DLCO was primarily driven by blood re-distribution and lung size (TLC) with the KCO being primarily dependant on the degree of blood re-distribution, and gas trapping. Thus, in the context of the disease, the DLCO and KCO values could be used to dissect the pathophysiological drivers of blood-gas barrier function. Next, we evaluated diseases with primary abnormalities at the blood-gas interface related to alveolar membrane thickening (ILD) and pulmonary vascular remodelling (PH) respectively **Figure *22***. In ILD the capillary blood volume was the primary determinant of DLCO, and the alveolar membrane thickness the primary determinant of the KCO (**Figure *22*A**). In PH both the DLCO and KCO appeared to be primarily sensitive to changes in alveolar volume and to a lesser extent capillary volume (but with opposite directional effect) (**Figure *22*B).**

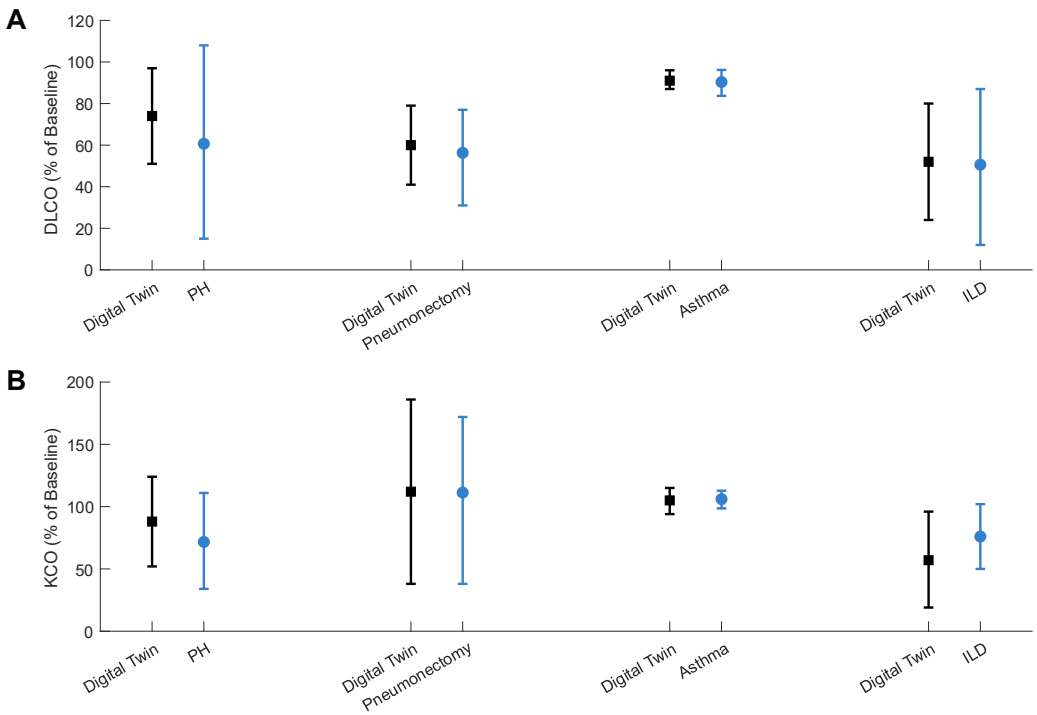


Figure 21 - Comparison of reported real-world test outputs (blue) with digital-twin-simulated outputs as a percentage of a healthy baseline simulation (black) following application of expected physiologic changes for 4 disease cases.

Model outputs capture the expected range of DLCO and KCO in disease following expected changes to physiologic inputs for each disease. Comparison of model simulated results with expected **DLCO (A)** and **KCO (B) % of healthy simulation** test outputs following expected changes to the physiology in Pulmonary Hypertension (PH), Pneumonectomy, Asthma, and Interstitial Lung Disease (ILD). The values presented in blue represent the mean (circle in the middle) ± 2σ (bars) of values that have been reported in the literature as shown in **Table 9** – PH (D'Alonzo, Bower and Dantzker, 1984; Sun et al., 2003; Jing et al., 2009; Sivova et al., 2013; Broberg et al., 2014), pneumonectomy (Corris et al., 1987; Deslauriers et al., 2011), asthma (Gonem et al., 2014), and ILD (Sivova et al., 2013; Pugashetti et al., 2023; Ventura et al., 2023) – while values presented in black represent the mean (square in the middle) ± 2σ (bars) of simulated outputs included in each of the cubic plots of **Figure 22** and **Figure 23**. The mean values of the simulated results appear to be close to the mean of the expected outputs, and the range of the simulated results largely overlaps with the

expected outputs sourced from the literature. Details of the changes applied to the inputs and the source from which they were taken for each case can be seen in **Table 9**.

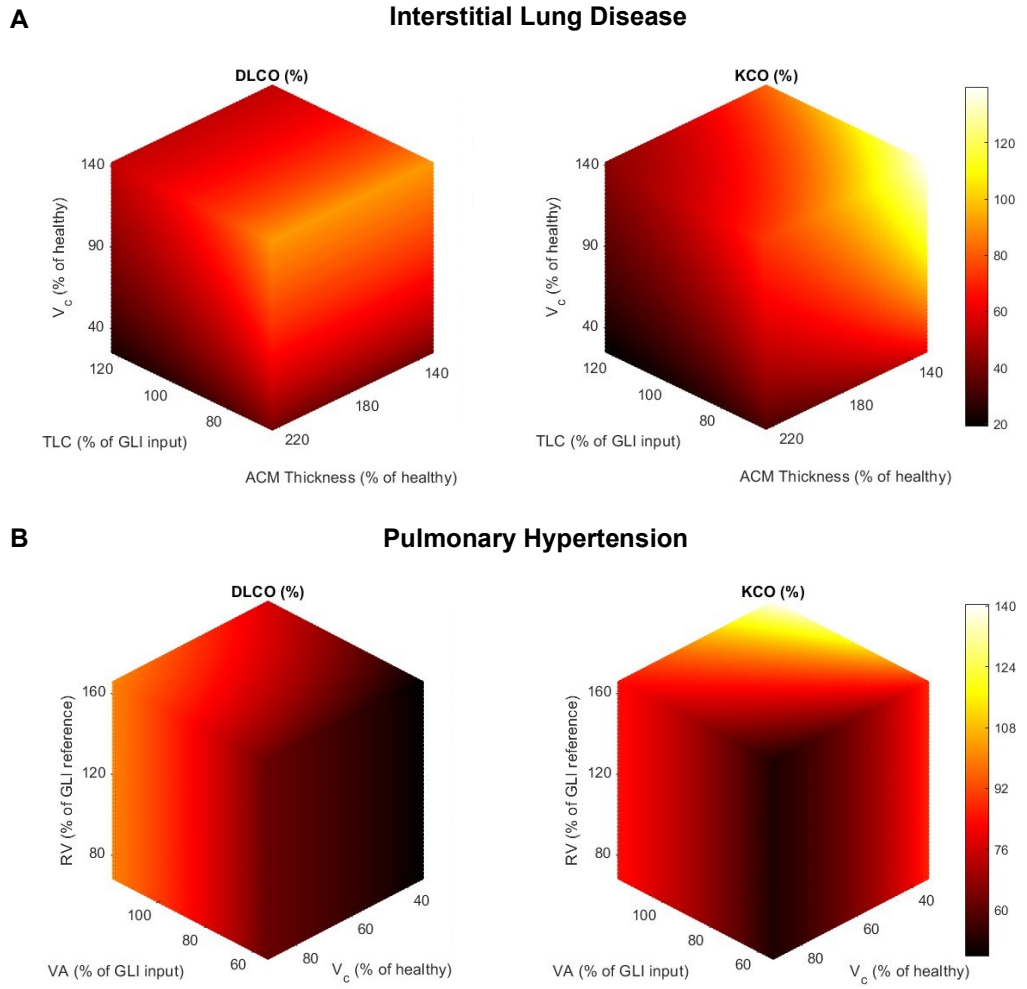


Figure 22 - Visualisation of the model's sensitivity to input alterations for ILD (A) and PH (B).

Alveolar Capillary Membrane (ACM) thickness has significant impact on KCO % of healthy simulation and a lesser effect on DLCO in ILD (Interstitial Lung Disease) while Capillary Blood Volume (V_C) has significant impact on KCO % of healthy simulation and a lesser effect on DLCO % of healthy simulation in PH (Pulmonary Hypertension). (A) Effect of changes in ACM thickness (in all compartments/ lung lobes), TLC, and V_C on DLCO and KCO in Interstitial Lung Disease (ILD). DLCO % of healthy simulation appears to be similarly sensitive to V_C, and

TLC however not as sensitive to ACM thickness. Conversely, KCO % of healthy simulation appears to be equally sensitive to ACM thickness, V_C and TLC changes. Range magnitudes of input changes and sources can be seen in **Table 9**. **(B) Effect of V_C, TLC and Alveolar Volume (VA) changes, on DLCO and KCO in PH.** DLCO % of healthy simulation appears to be very sensitive to gas trapping (VA) and V_C changes while less sensitive to RV and changes. KCO % of healthy simulation appears to be equally sensitive to V_C, and gas trapping, while less sensitive to RV. Range magnitudes of input changes and sources can be seen in **Table 9**.

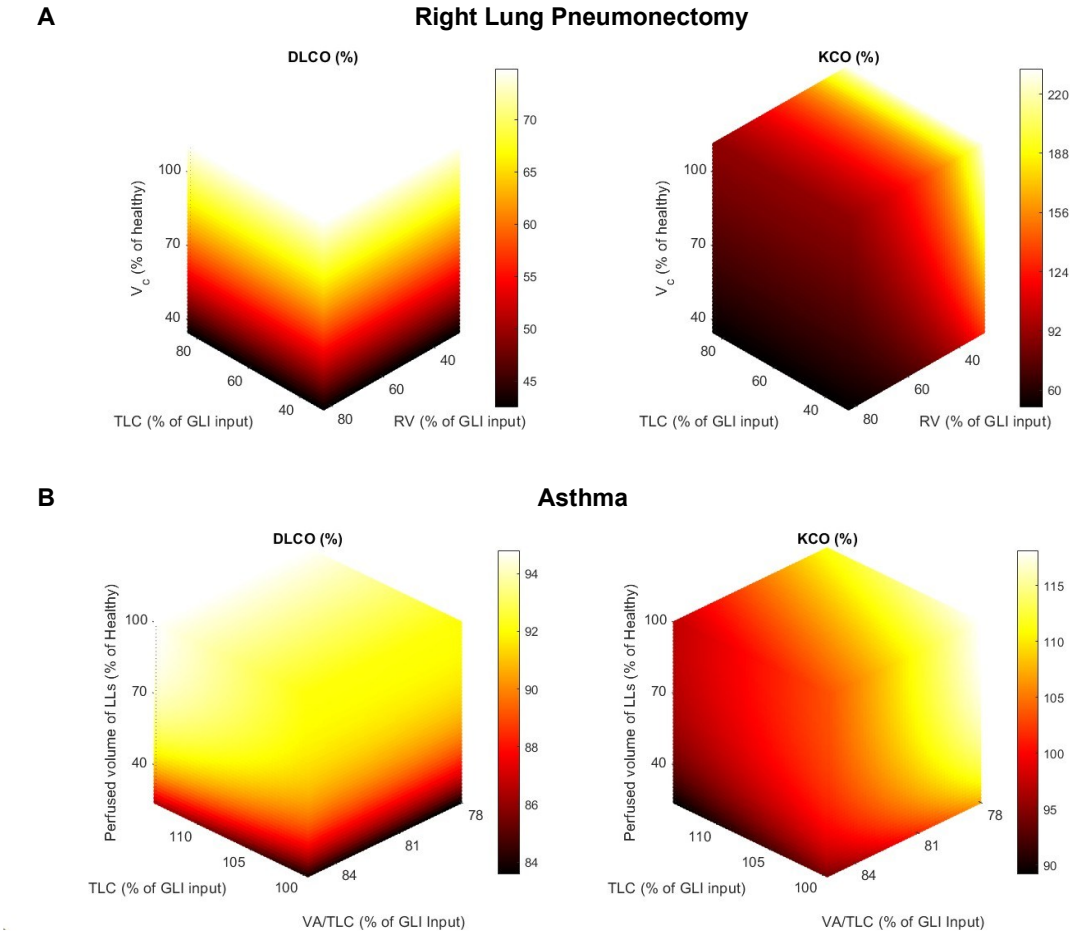


Figure 23 - Visualisation of the model's sensitivity to input alterations for Right Lung (RL) Pneumonectomy (A) and Asthma (B).

RV has significant impact on KCO % of healthy simulation and lesser effect on DLCO % of healthy simulation post pneumonectomy while blood re-distribution

is the key driver in changes to DLCO in asthma and gas trapping in KCO. (A) Effect of TLC, RV and Capillary Blood Volume changes post removal of the right lung on DLCO % of healthy simulation (left) and KCO % of healthy simulation (right). DLCO % of healthy simulation appears to be highly sensitive to V_C changes however not as sensitive to TLC and RV changes. Conversely, KCO appears to be less sensitive to V_C more sensitive to TLC and RV changes. **(B) Effect of changes in Blood Distribution between the lower and upper lobes due to Hypoxic Pulmonary Vasoconstriction (HPV), Alveolar Volume representing gas trapping, and TLC on DLCO % of healthy simulation (left) and KCO % of healthy simulation (right) in Asthma.** DLCO % of healthy simulation appears to be highly sensitive to blood re-distribution and TLC however, not very sensitive to gas trapping (VA/TLC) changes. KCO % of healthy simulation appears to be equally affected by blood re-distribution, gas trapping and TLC changes. Range magnitudes of input changes and sources can be seen in **Table 9.**

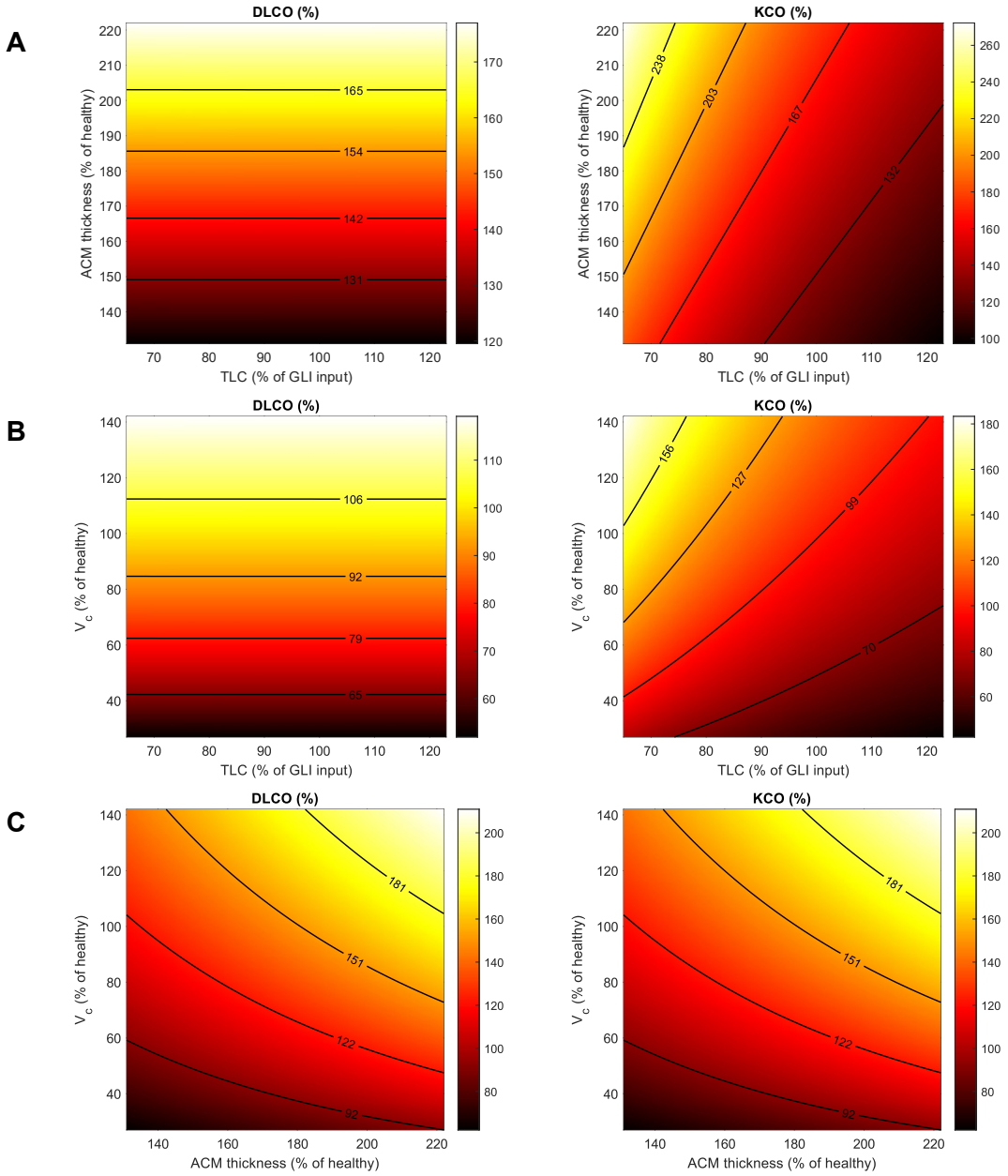


Figure 24 – 2D visualisation of the model's sensitivity to alterations of 2 inputs simultaneously for Interstitial Lung Disease (ILD).

The figure involves changes to (A) Alveolar Capillary Membrane (ACM) thickness and TLC, to (B) Capillary Blood Volume (Vc) and TLC, and to (C) Capillary Blood Volume (Vc) and Alveolar Capillary Membrane (ACM) thickness. TLC appears to have no impact on DLCO, while it affects KCO as shown in panels A and B, with DLCO being mostly driven by ACM thickness and Vc.

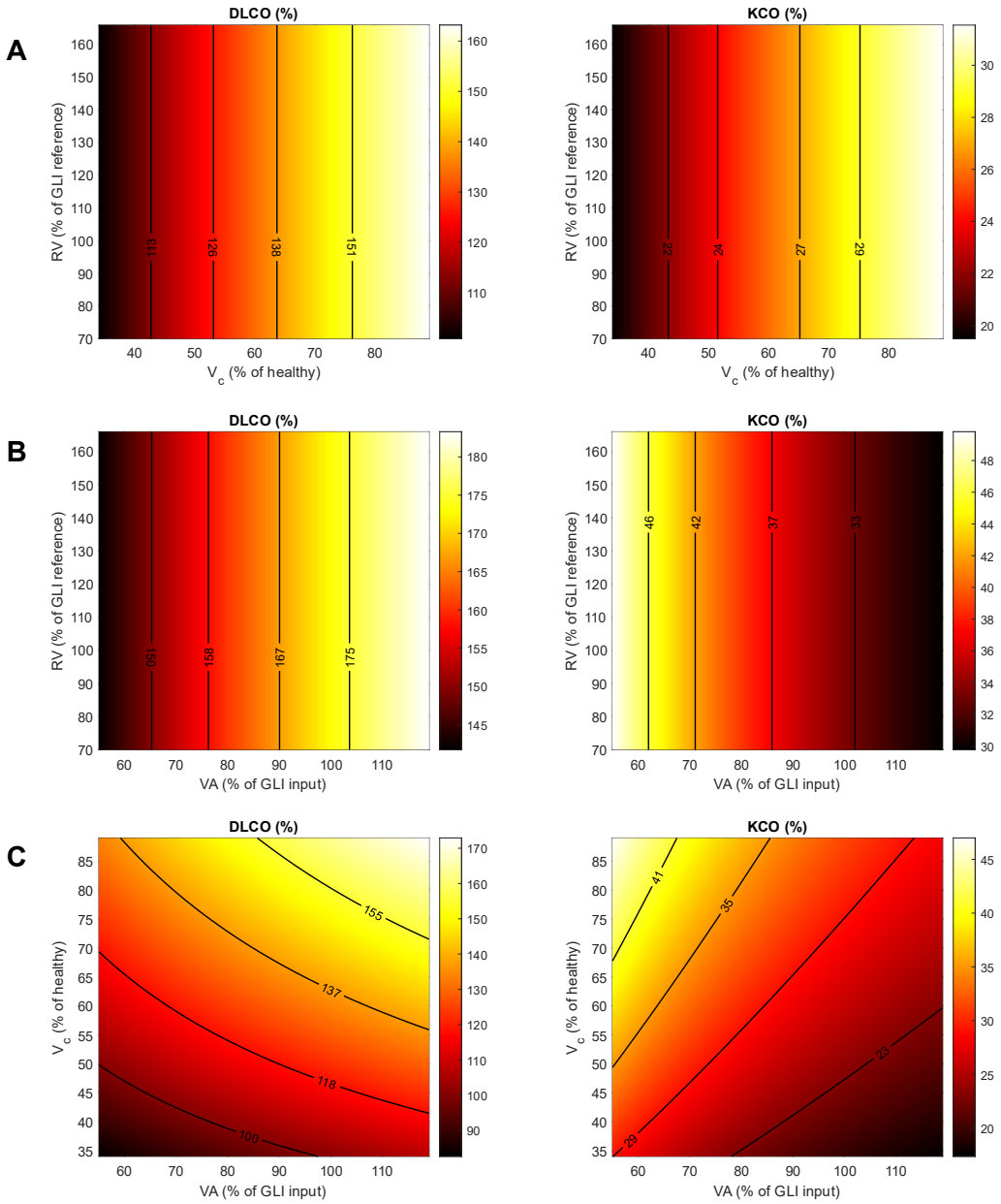


Figure 25 – 2D visualisation of the model's sensitivity to alterations of 2 inputs simultaneously for Pulmonary Hypertension (PH).

The figure involves changes to (A) Residual Volume (RV) and Capillary Blood Volume (Vc), to (B) Residual Volume (RV) and Alveolar Volume (Va), and to (C) Capillary Blood Volume (Vc) and Alveolar Volume (Va). RV appears to have no effect on DLCO and KCO as shown in panels A and B, with DLCO and KCO values being mainly driven by Capillary Blood Volume (Vc) and Alveolar Volume (Va).

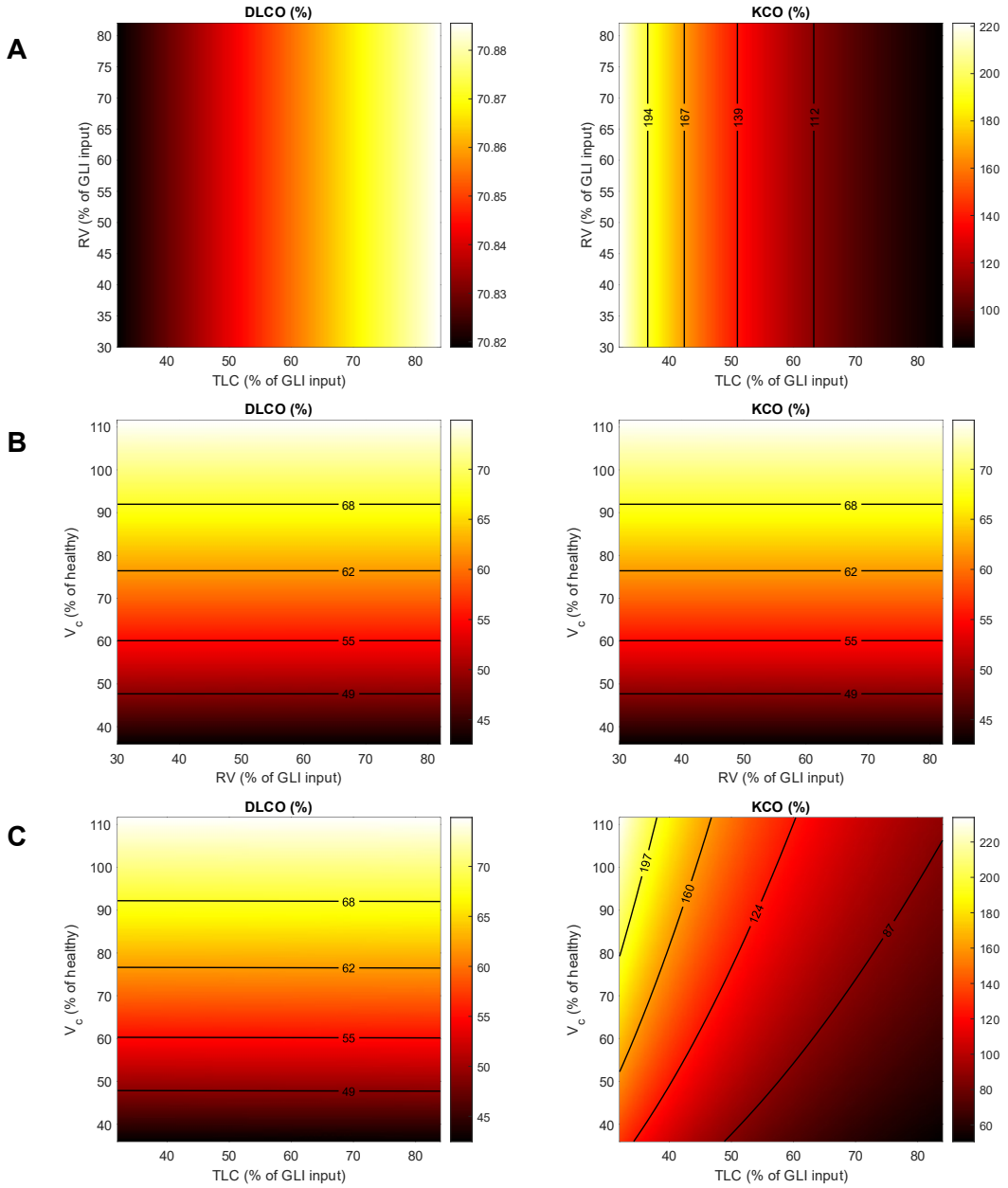


Figure 26 – 2D visualisation of the model's sensitivity to alterations of 2 inputs simultaneously for Right Lung Pneumonectomy.

The figure involves changes to (A) RV and TLC, to (B) Capillary Blood Volume (Vc) and RV, and to (C) Capillary Blood Volume (Vc) and TLC. RV appears to have no effect on DLCO and KCO as shown in panels A and B, while TLC appears to have little but negligible effect on DLCO as shown in panel A. DLCO and KCO appear to be mostly driven by changes in Capillary Blood Volume (Vc) as shown in panels B and C, with TLC having an impact on KCO as opposed to DLCO on which it has no impact.

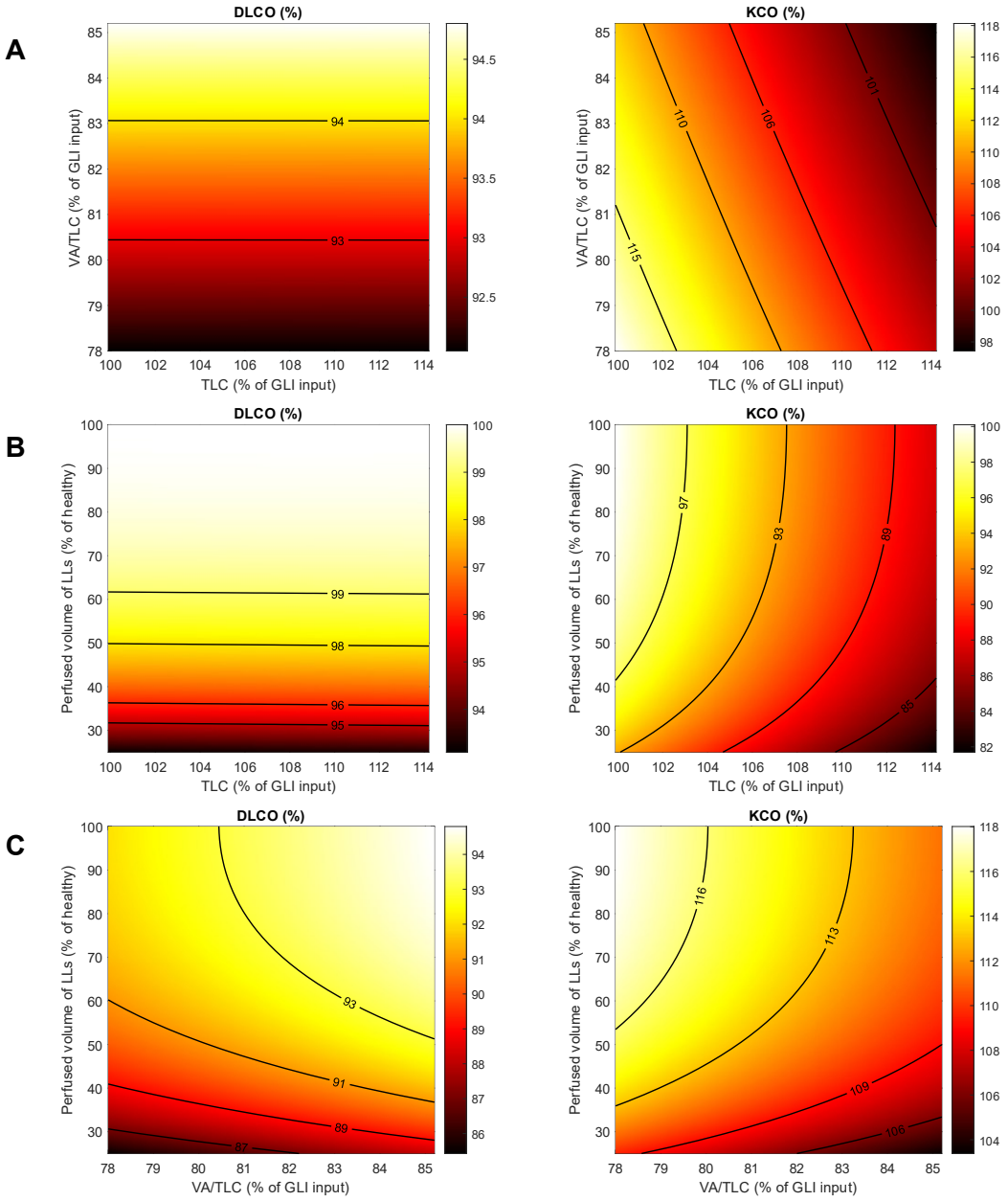


Figure 27 – 2D visualisation of the model's sensitivity to alterations of 2 inputs simultaneously for Asthma.

The figure involves changes to (A) VA/TLC ratio and TLC, to (B) Blood Distribution between the lower and upper lobes due to Hypoxic Pulmonary Vasoconstriction (HPV) and TLC, and to (C) Blood Distribution between the lower and upper lobes due to HPV and Gas Trapping represented by the VA/TLC ratio. TLC appears to have no effect on DLCO, while it appears to affect KCO as shown in A

and B, with DLCO mostly being driven by gas trapping and blood redistribution as shown in C.

3.3.4 Results expressed relative to GLI healthy reference values

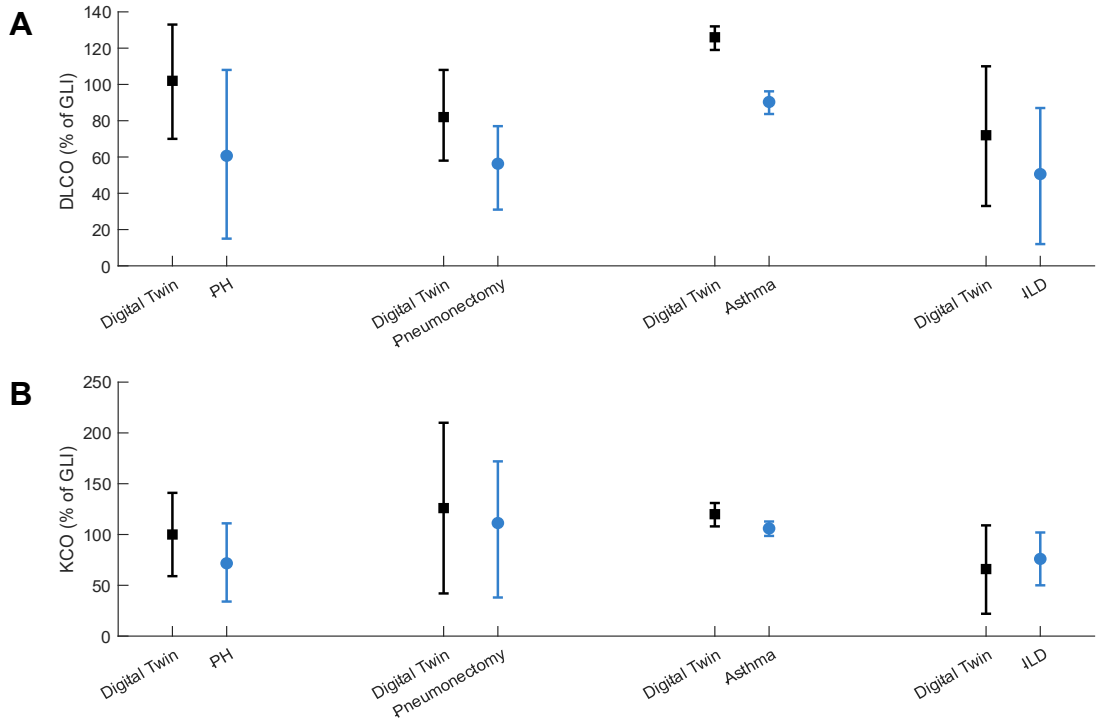


Figure 28 – Results of simulated disease cases as compared to their GLI predicted DLCO and KCO.

Comparison of reported real-world test outputs (blue) with digital-twin-simulated outputs as a percentage of the GLI healthy predicted output (black) following application of expected physiologic changes for 4 disease cases. Model outputs capture the expected range of DLCO and KCO in disease following expected changes to physiologic inputs for each disease for KCO however, the results are not as concordant for DLCO. Comparison of model simulated results with expected **DLCO (A)** and **KCO (B)** test outputs following expected changes to the physiology in Pulmonary Hypertension (PH), Pneumonectomy, Asthma, and Interstitial Lung Disease

(ILD). The values presented in blue represent the mean (circle in the middle) ± 2σ (bars) of values that have been reported in the literature as shown in **Table 9** – PH (D'Alonzo, Bower and Dantzker, 1984; Sun et al., 2003; Jing et al., 2009; Sivova et al., 2013; Broberg et al., 2014), pneumonectomy (Corris et al., 1987; Deslauriers et al., 2011), asthma (Gonem et al., 2014), and ILD (Sivova et al., 2013; Pugashetti et al., 2023; Ventura et al., 2023) –, while values presented in black represent the mean (square in the middle) ± 2σ (bars) of simulated outputs included in each of the cubic plots of **Figure 29, Figure 30, Figure 31,** and **Figure 32**. The mean values of the simulated results appear to be close to the mean of the expected outputs for KCO (panel B), and the range of the simulated results largely overlaps with the expected outputs sourced from the literature. This does not appear however to be the case for DLCO outputs as seen in panel A. Details of the changes applied to the inputs and the source from which they were taken for each case can be seen in **Table 9.**

The results for DLCO in panel A appear to be slightly elevated as compared to **Figure 21**. This does not appear to be the case for KCO. The reason for this is that the model simulates KCO more accurately than DLCO as compared to their predicted GLI values. Both DLCO and KCO healthy simulations appear to be lower than their actual GLI predicted values, however DLCO is much lower than its predicted value than KCO is to its predicted value.

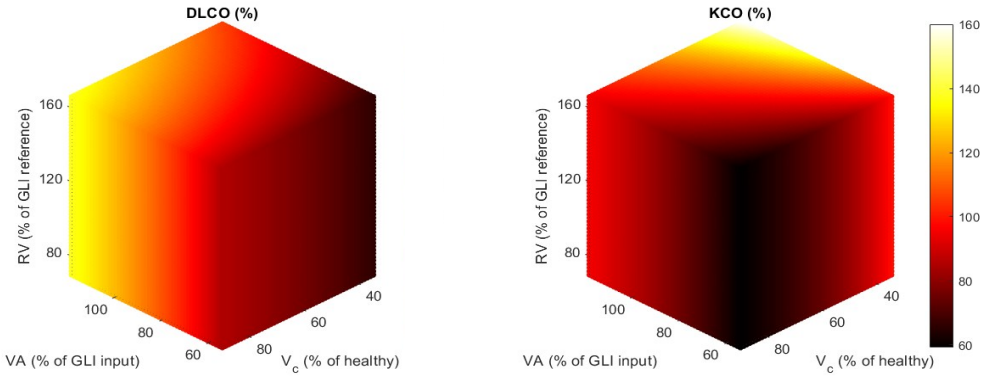


Figure 29 – PAH simulation of DLCO and KCO % predicted

Results presented as DLCO and KCO as a percentage of their GLI predicted value μ(min - max) DLCO 102 (66-138), KCO 100 (59-160) Effect of V_C, TLC and Alveolar Volume (VA) changes, on DLCO and KCO in PH. DLCO appears to be very sensitive to gas trapping (VA/TLC) while less sensitive to RV and V_C changes. KCO appears to be equally sensitive to V_C, and gas trapping, while less sensitive to RV. Range magnitudes of input changes and sources can be seen in **Table 9**.

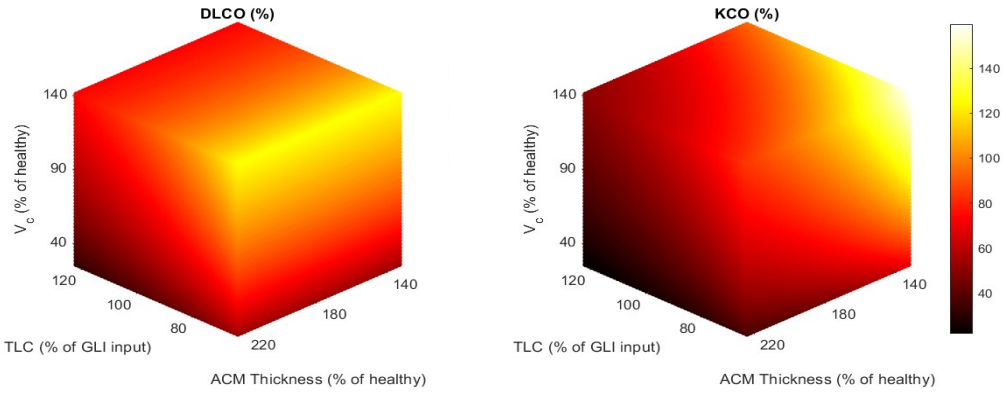


Figure 30 – ILD simulation of DLCO and KCO % predicted

Results presented as DLCO and KCO as a percentage of their GLI predicted value μ(min - max) DLCO 72 (32-125), KCO 66 (22-160) Effect of changes in ACM thickness (in all compartments/ lung lobes), TLC, and V_C on DLCO and KCO in Interstitial Lung Disease (ILD). DLCO appears to be more sensitive to V_C, less sensitive to TLC not as sensitive to ACM thickness. Conversely, KCO appears to be very sensitive to ACM

thickness, less sensitive to V_C and not as sensitive to TLC. Range magnitudes of input changes and sources can be seen in **Table 9**.

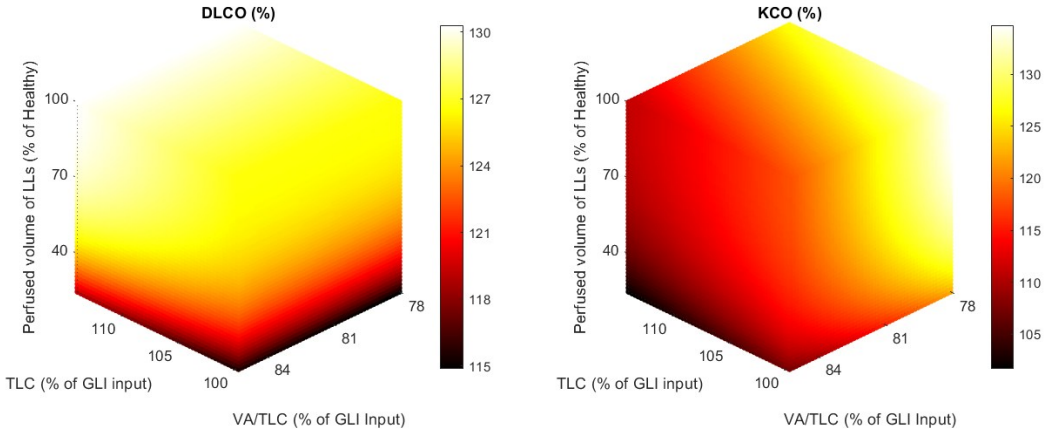


Figure 31 – Asthma simulation of DLCO and KCO % predicted

Results presented as DLCO and KCO as a percentage of their GLI predicted value μ(min - max) DLCO 91 (84-95), KCO 105 (89-118). Effect of changes in Blood Distribution between the lower and upper lobes due to Hypoxic Pulmonary Vasoconstriction (HPV), Alveolar Volume representing gas trapping, and TLC on DLCO (left) and KCO (right) in Asthma. DLCO appears to be highly sensitive to blood re-distribution and TLC however, not very sensitive to gas trapping (VA/TLC) changes. KCO appears to be sensitive blood re-distribution and gas trapping however less sensitive to TLC changes. Range magnitudes of input changes and sources can be seen in **Table 9**.

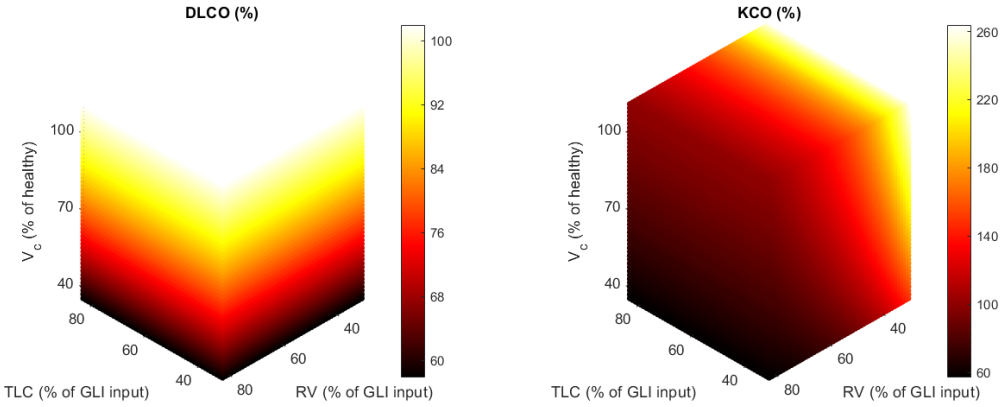


Figure 32 – Pneumonectomy simulation of DLCO and KCO % predicted

Results presented as DLCO and KCO as a percentage of their GLI predicted value μ(min - max) DLCO 82 (58-102), KCO 126 (57-264). Effect of TLC, RV and Capillary Blood Volume changes post removal of the right lung on DLCO (left) and KCO (right). DLCO appears to be highly sensitive to TLC and RV changes however not as sensitive to V_C. Conversely, KCO appears to be highly sensitive to V_C and less sensitive to TLC and RV changes. Range magnitudes of input changes and sources can be seen in **Table 9**.

3.4 Discussion

In this study, I presented the development and validation of a new 'digital twin' of the CO gas transfer test which functions under simplifying assumptions using Fick's law and utilises structural information of the lungs which can potentially be obtained by CT or MRI medical images to provide patient specific/ personalised estimates of model parameters. In the present study, I tested the performance of this 'simulation patient digital twin' by applying expected changes to the physiology thus simulating four diverse cardio-respiratory disease cases characterised by differential lung volumes and/or blood-gas barrier pathologies.

This model's nature is mechanistic, which means its inputs can be altered to assess the effect of changes on its outputs. The model was developed to operate with personalised physiological inputs, including lung volumetric measurements expressed in litres or volume units. These inputs may be estimated from demographic data using the GLI reference equations or derived from measured lung volumes obtained using techniques such as body plethysmography, CT, or MRI. The model is composed of 4 compartments, for symmetry and simplification of data acquisition for validation. Each of these compartments has its own blood supply, mean harmonic alveolar-capillary membrane thickness, volume, and consequently its own diffusion scaling equation leading to its own diffusion rate. This rate is estimated with an individual's healthy predicted DLCO and is scaled for each compartment using the diffusion scaling equation. The equation changes subject to structural alterations that the lung compartment has undergone to classify as being in a "diseased" state.

The results showed that the model captures the physiologic effects on the test outputs since the expected range of outputs largely overlapped with the simulated range of DLCO and KCO in each disease. Although not perfect, the results can act as a strong validation of the model's performance. Inconsistencies between the simulated and expected output changes were expected as the model functions under simplifying mathematical assumptions to approximate the structural geometry and its effect on DLCO and KCO. The simplifying assumption of the surface area participating in gas exchange being only the curved area of a cylinder (capillary) is the key example of why some inconsistencies were expected since it affects the key

determinant of gas diffusion which according to Fick's law is the surface area. While the model takes into account that CO has high affinity for haemoglobin, and simulates gas-exchange as diffusion-limited by assigning a value of zero to the partial pressure of blood, the model does not account for haemoglobin binding. Furthermore, in this study I assumed uniform changes in the capillary blood volume across the four compartments (pneuomonectomy, two compartments), which means no blood redistribution was modelled in this study. In addition, thinning of the alveolar-capillary membrane was not modelled for pneumonectomy, which might occur due to redistribution of blood to the remaining lung as post operation there is an increased amount of capillary blood which leads to stretching of the capillaries since no compesatory lung growth occurs after lung resection (Glénet *et al.*, 2017). The model's simple four-compartment nature might also be the source of inconsistencies between simulated outputs and expected DLCO and KCO changes in disease, as considering the physiology; smaller-scale sub-regions of each compartment could lead to more detailed diffusion scaling across the two lungs since each sub-region would have information about its own diffusion scaling equation and therefore its own diffusion rate. Sensitivity plots in **Figure *22*** have shown that the ACM thickness has a significant impact on the simulated KCO and less effect on simulated DLCO in ILD while V_C was shown to have high impact on KCO and less effect on DLCO in PH. More detailed 2 dimensional plots presenting changes to 2 physiologic inputs however, have shown that in ILD, shown in **Figure *24***, - TLC appears to have no impact on DLCO while it affects KCO, with DLCO and KCO being mostly driven my ACM thickness and Vc - while in PH, shown in **Figure *25***, - RV appears to have no effect on DLCO and KCO with the DLCO and KCO outputs being mainly driven by Vc and Va. Sensitivity plots in **Figure 23** also showed that V_C has a high impact on KCO and a lesser effect on DLCO post pneumonectomy while blood re-distribution and TLC are the key drivers in changes to DLCO and TLC and gas trapping are the key drivers of changes in KCO in asthma. More detailed 2 dimensional plots presenting changes to 2 physiologic inputs however, have shown that post pneumonectomy, shown in **Figure *26***, - RV and TLC appear to have no/negligible effect on DLCO and KCO which appear to be mostly driven by changes in Vc with TLC having an impact

on KCO as opposed to DLCO on which it has no impact - while in Asthma, shown in **Figure *27***, - TLC appears to have no effect on DLCO while it appears to affect KCO, with DLCO being mosly driven by gas trapping and blood redistribution.

The results in **Figure *20*** act as strong validation of the digital twin and show that it can successfully capture the expected changes to the test outputs under reduction of Va. Some inconsistencies between the simulated changes are expected in this comparison and can be attributed to the model's limitations which lie in the model's simplifying assumptions – the foundation of the diffusion-scaling equation.

All in all, the model has accurately captured expected changes subject to physiologic changes in hypothetical disease despite of its simplifing assumptions' constraints, which demonstrated the model's potential in further development. Finally, compartments can be increased allowing use of localised ventilated volume – useful in obstructive diseases where VH is present. Longer-term options for development include incorporating oxygen binding to haemoglobin using altitude-dependent partial pressure of oxygen in the capillary blood to study for example, the impact of high altitude on blood-gas barrier function with personalised modelling in mountaineers (Peacock, 1998). The model not only shows promise for its application in research but as shown in the proposed concept of the model's utility highlighted in **Figure *33***, it can also prove useful in a clinical setting in the future, subject to further development and optimisation.

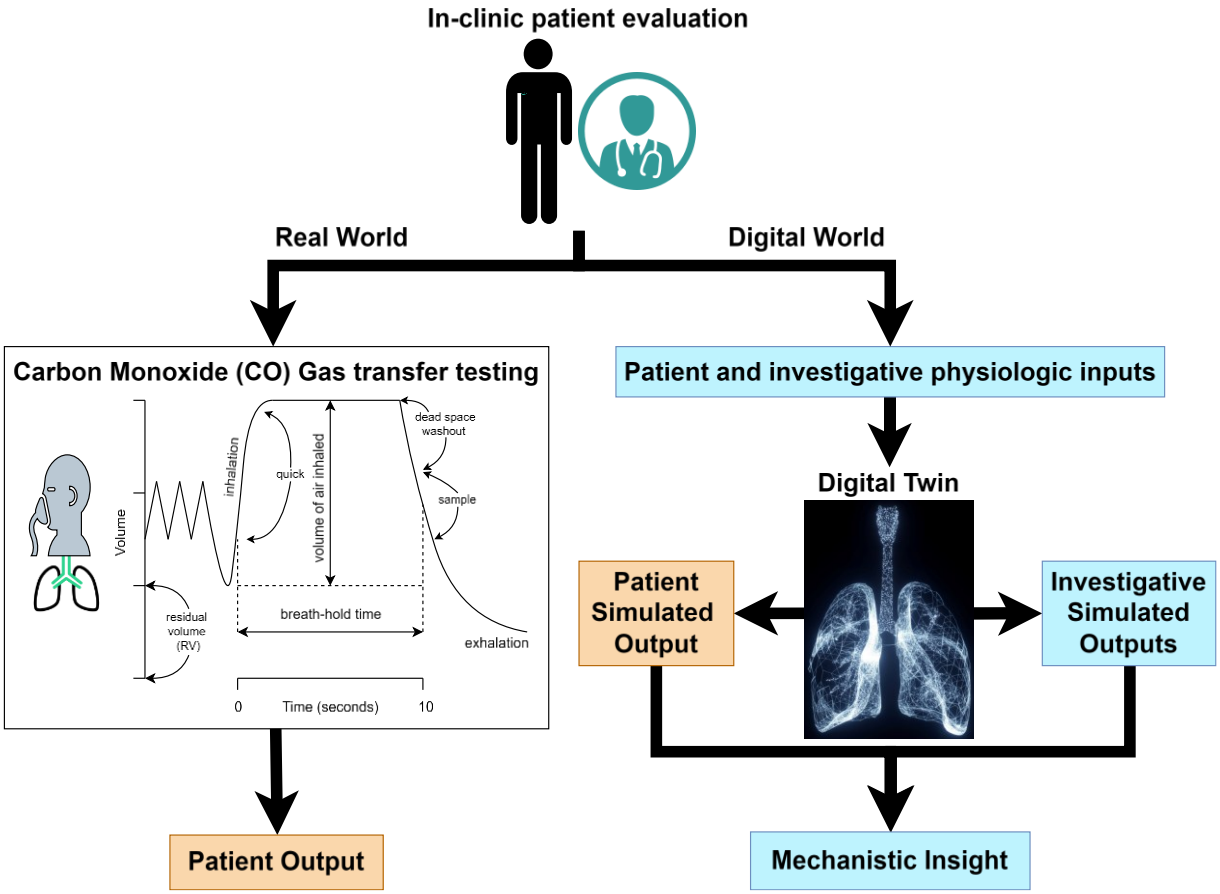


Figure 33 – Schematic of proposed use of the V/Q model in a clinical setting

The Digital Twin presents the advantage of providing mechanistic insight to the blood-gas barrier function in contrast to the current real-world pulmonary function CO gas-transfer test. Comparison of real (left) and digital (right) worlds. In the real world, after in clinic evaluation, the patient performs the test which firstly involves normal breathing in the device, followed by a complete exhalation, and after inhalation of an air mixture consisting of Oxygen, Helium and Carbon Monoxide (CO), a 10-second breath-hold before the patient finally exhales allowing for the output to be calculated. In the digital world, the clinician would collect the patient's physiologic information which would then input to the digital twin of the test. The Patient Simulated Output would be a very close approximation to the real-world patient output. The clinician can implement multiple investigative simulations with the digital twin by varying the values of the patient's physiologic inputs. The investigative outputs obtained from the investigative inputs can therefore provide insight into the effect

that each investigative parameter has alone or in combination with other parameters on the output. The patient simulated output would be used as a guide, allowing for the inputs to be varied accordingly so that the investigative outputs are varied within a small range from the patient simulated output.

3.5 Summary

Motivated by the need for a V/Q "simulation patient digital twin" of blood-gas barrier function that represents regional gas-transfer processes underlying the CO gas transfer test, this chapter outlined its development and validation in hypothetical disease scenarios and post-operative right lung pneumonectomy. This mechanistic model was built to function with personalised physiologic inputs which can be calculated either based on an individual's demographics using the GLI reference equations or can be obtained via CT or MRI medical imaging. The model is split into 4 compartments, to account for symmetry and simplify data acquisition for validation of the model outputs. Each compartment consists of its own blood supply, volume, mean harmonic alveolar-capillary membrane thickness and subsequently its own diffusion scaling equation, and thus its own diffusion rate. This rate is approximated using a healthy DLCO predicted value for an individual and is scaled for each compartment using the diffusion scaling equation, which changes based on structural changes the compartment has undergone to enter a "diseased" state. While the model is limited by simplifying mathematical assumptions, it was capable to accurately capture expected relative (percentage increase or decrease compared to healthy) changes of the DLCO and KCO outputs in both hypothetical disease scenarios and post-operative right lung pneumonectomy accurately.

4. V/Q model, hyperpolarised Xe^{129} MRI coupling

4.1 Rationale

In the previous chapter and introduction, the importance of the single-breath CO gas transfer test was discussed along with the importance of the development of computational modelling techniques coupled with imaging to address the localised nature of lung disease and provide insights into structural and functional relationships. This is due to the limitation of advanced imaging techniques, which, while able to assess more localised V/Q dynamics, cannot provide measurements in hypothetical or unseen scenarios, involving changes to the lungs' structure.

Computational modelling provides the advantage of allowing simulation of various scenarios involving structural modifications to provide insights into their effect on lung function. Development, validation and ultimately utilisation of such models could aid in understanding blood-gas barrier dysfunction and facilitate more targeted interventions in respiratory disease management. As discussed the previous chapter, the development of a "monitoring patient digital twin" requires development and validation of smaller "simulation patient digital twins". The development and validation of a "simulation patient digital twin" of the CO gas transfer test was presented in the previous chapter which included its validation under hypothetical disease scenarios and post-surgical pneumonectomy.

Building on the previous chapter, this chapter aims to incorporate hyperpolarised ^{129}Xe MRI into the modelling framework, thereby establishing an imaging-informed model. The coupled model's simulated results are aimed to be compared with measurements in a small cohort including asthmatic patients and healthy volunteers for the validation of the model's functionality and utility.

4.1.1 Hyperpolarised Xenon 129 and Blood-gas barrier

The alveolar-capillary membrane, also known as the blood-gas barrier comprises a number of layers including the alveolar lining layer, epithelium, extracellular matrix, endothelium, blood plasma and the RBC membrane. These are the layers that oxygen must pass through in order

to reach a red blood cell. A method introduced in 2006 (Driehuys *et al.*, 2006), allowed imaging of the differential transfer of hyperpolarised ^{129}Xe from the air spaces of the alveoli, through the alveolar-capillary membrane and RBC membranes in the gas exchange regions of the lungs. The area under the receiver characteristic curve (AUC) of the distinct peaks acquired from hyperpolarised ^{129}Xe MRI, provides information of the diffusion of hyperpolarised ^{129}Xe through the blood-gas barrier and the RBC membrane.

A study has shown a statistically significant relationship between DLCO (% predicted) and the ratio of RBC AUC and Barrier AUC, denoted as RBC:Barrier, in patients with post-acute COVID-19 syndrome (Matheson *et al.*, 2022). This finding indicates the relationship between hyperpolarised ^{129}Xe MRI measurements and the single-breath CO gas transfer test – a relationship which seems natural as both assessments examine the diffusion of gases through the blood-gas barrier and RBC membranes. RBC AUC and Barrier AUC represent the signals arising from hyperpolarised ^{129}Xe MRI from xenon dissolved in the RBC and barrier compartments respectively. Provided its reported association with DLCO, the ratio of these metrics RBC:Barrier, is assumed to be an analogous measure of gas-exchange efficiency. This relationship was the basis of other studies which linked the two assessments together. Another recent study utilised hyperpolarised ^{129}Xe MRI to train advanced regression models and predict whole-lung, spatially localised/ regional DLCO, also addressing the need for spatially localising the CO gas transfer (Pilgrim-Morris *et al.*, 2025). While this method addresses the need for spatial localisation of the single-breath CO gas transfer test, the method is limited in its ability to provide regional DLCO predictions in hypothetical or unseen scenarios which involve alterations to the lungs' structure to assess their effect on lung function.

4.2 Materials and methods

The coupling of the V/Q model with hyperpolarised ^{129}Xe MRI data involved the addition of simplifying mathematical assumptions to realistically approximate the efficiency of gas exchange through the use of hyperpolarised ^{129}Xe MRI gas exchange analogues. In this chapter, the foundation of the model remains the same as in the previous chapter, unless

otherwise specified. No changes were implemented on the model's reported methods in section 3.2, apart from the coupling method of the model with hyperpolarised ^{129}Xe MRI.

4.2.1 Data Collection

Table 10 – Participant Demographics for V/Q model validation with hyperpolarised ^{129}Xe data

Characteristic	Asthma (N=10)	Healthy (N=5)	p-value
Age (years)	53.8 (15.64)	31.8 (13.94)	**<0.05**
Sex			1.00
Male	3 (30%)	2 (40%)	
Female	7 (70%)	3 (60%)	
Height	170.6 (12.65)	171.4 (10.92)	0.91
RV (%$_{predicted}$)	117 (95 - 170)	100 (100 - 101)	0.29
TLC (%$_{predicted}$)	103.2 (15.11)	101 (12.86)	0.79
VDP (%)	11.2 (8.31)#	1 (0)	**<0.05**
FEV1	2.26 (0.86)	3.30 (1.00)	0.06
FEV1 (%$_{predicted}$)	71.4 (15.71)	86.2 (12.87)	0.09
FVC	3.46 (1.31)	4.14 (1.34)	0.37
FVC (%$_{predicted}$)	85.2 (9.30)	89.6 (13.69)	0.47
RBC:Barrier	0.39 (0.10)	0.46 (0.10)	0.20
Barrier:Gas	0.90 (0.28)	0.99 (0.18)	0.49
RBC:Gas	0.34 (0.10)	0.47 (0.17)	0.08
RBC	76 (31 - 108)#	238 (124 - 910.8)	**<0.05**
Barrier	178 (73 - 295)#	540 (367.5 - 1743.8)	**<0.05**
Gas	252.6 (243.63)	1209.4 (1607.62)	0.08
DLCO (mL/min/mmHg)	23.08 (7.47)	29.18 (8.45)	0.18
KCO (mL/min/mmHg/L)	4.33 (0.94)	5.41 (0.98)	0.06
DLCO (%$_{predicted}$)	96.99 (20.63)	108.96 (19.82)	0.30
KCO (%$_{predicted}$)	100.51 (18.86)	114.28 (16.16)	0.19

Data presented as n (%), and μ(σ) for normally distributed parametric data. Normality of the datasets was assessed using a Kolmogorov-Smirnov test, after normalisation of data (normalised data = (x-μ)/σ) followed by the calculation of p-values using a Mann-Whitney U-test for parametric data and a two-sample t-test for non-parametric data. Percentage difference values to the predicted, obtained using the adjusted observed value to account for haemoglobin are shown as "% predicted, Hb". VDP stands for Ventilation Defect Percent, RV for Residual Volume, TLC for Total Lung Capacity, FEV1 for Forced Expiratory Volume in 1 second, FVC for Forced Vital Capacity and AUC for Area Under the receiver operating characteristic Curve.

#p < 0.05 compared to healthy control group

4.2.2 Coupling of V/Q model with Xenon 129 MRI

As information about the change in membrane thickness cannot be inferred easily from CT scans which are limited by resolution, the formulation used in the previous chapter about ACM and RBC membrane thicknesses was modified. Instead of explicitly modelling membrane thickness, I assumed that the diffusion rate is proportional to a permeation coefficient for oxygen in the material composing the membrane, denoted as K (Leiby, Raredon and Niklason, 2020). I further assumed that the RBC:barrier ratio obtained by the integrated area under the two out of three receiver operating characteristic curves (AUCs) with distinct resonance peaks of the ^{129}Xe MRI spectrum for the RBC and Barrier compartments (Matheson *et al.*, 2022; O'Sullivan-Murphy, Driehuys and Mammarappallil, 2022) reflects gas exchange efficiency. As this ratio RBC:Barrier, has been shown to be related to DLCO (Matheson *et al.*, 2022) and therefore was assumed to reflect gas-exchange efficiency, it was used in the model as an analogue linked to the permeation coefficient. These assumptions led to the final relationship between the diffusion rate and the changes in the permeation coefficient analogue as below.

$$D \propto \Delta_{\text{RBC:barrier}}$$

$$\Delta_{\text{RBC:Barrier}} = \frac{RBC:barrier}{RBC:barrier_{Healthy}}$$

Finally, accounting for all the relative changes, the final diffusion scaling equation for the calculation of the scaled diffusion rate is presented in equation 21.

$$D = DLCO_h \left(\frac{V_{CS}\, P_C}{2V_{CH}}\right)^{\frac{1}{2}} \left(\frac{VA}{TLC}\right)^{\frac{1}{3}} \Delta_{\text{RBC:barrier}} \tag{21}$$

4.2.3 Scaling of permeation analogue RBC:barrier ratio

Assuming a positive correlation between DLCO and RBC:barrier ratio, where doubling of the ratio RBC:barrier from results in a 35% increase of DLCO (Matheson *et al.*, 2022), the following equations can be obtained.

$$ax + b = 1 \tag{22}$$

$$2ax + b = 1.35 \quad (23)$$

Where, x represents the RBC:barrier change (RBC:barrier / RBC:barrier (healthy)), solving for α and b allows for the scaling of x within the model, so that the doubling effect of the RBC:barrier ratio results in a 35% increase in DLCO.

$$ax + b = 1 \Rightarrow a = \frac{1 - b}{x}$$

$$2ax + b = 1.35$$

$$\Rightarrow 2x\left(\frac{1 - b}{x}\right) + b = 1.35 \Rightarrow \frac{2x - 2xb}{x} + b = 1.35 \Rightarrow \frac{2x}{x} - \frac{2xb}{x} + b = 1.35 \Rightarrow 2 - 2b + b = 1.35$$

$$\Rightarrow 2 - b = 1.35$$

$$\Rightarrow 2 - 1.35 = b$$

$$\Rightarrow b = 0.65$$

$$a = \frac{1 - 0.65}{x}$$

In the model validation, x was taken as the interquartile range of RBC:barrier / RBC:barrier (healthy) value for the entire participant cohort.

4.2.4 Simulations with patient and healthy volunteer data

Ventilation Defect Percent (VDP) was used to approximate the volume of air participating in gas exchange. VDP(%) is obtained as shown in equation 24, where VDV is the Ventilation Defect Volume [L] and FRC the Functional Residual Capacity. The unventilated volume (VDV) was therefore calculated with equation 25, using age, sex and height to approximate the healthy FRC using GLI reference equations (Hall *et al.*, 2021). To estimate the volume of air participating in gas exchange (ventilated volume - VV), the anatomical dead space (Vd) – which was approximated using the height of each study participant (Hart, Orzalesi and Cook, 1963) and the unventilated volume – were subtracted from the FRC+1L as shown in equation

26. FRC + 1 represents the total lung volume (TLV) at which the proton MRI measurements were acquired, under breath-hold of FRC + 1L of N_2 (nitrogen).

$$VDP = \frac{VDV}{FRC + 1} \tag{24}$$

$$VDV = VDP * (FRC + 1) \tag{25}$$

$$VV = FRC + 1 - Vd - VDV \tag{26}$$

The residual volume for 4 out of the 5 healthy individuals was approximated using the GLI reference equations, as measurements of RV were not available for these study participants. Finally, the permeation analogue RBC:barrier ratio was scaled as described in section 4.2.3.

4.3 Results

4.3.1 Simulations in Asthma and Health

Simulations of the CO gas transfer test were implemented for 10 asthmatic and 5 healthy individuals, whose characteristics can be seen in **Table *10***. For the implementation of the simulations, the model was coupled with hyperpolarised ^{129}Xenon results and utilised the Ventilation Defect Percent (VDP) as described in the methods to approximate the volume of air participating in gas exchange. The results can be seen in **Figure *34*** which clearly presents that the digital-twin-simulated range of DLCO and KCO outputs, largely overlaps with the measured range of DLCO and KCO in asthma. Furthermore, the mean simulated values closely match the mean of the measured DLCO and KCO in both asthma and health. The results however show that the model simulated DLCO and KCO values are not correlated with the measured corresponding values as shown in **Figure *35***.

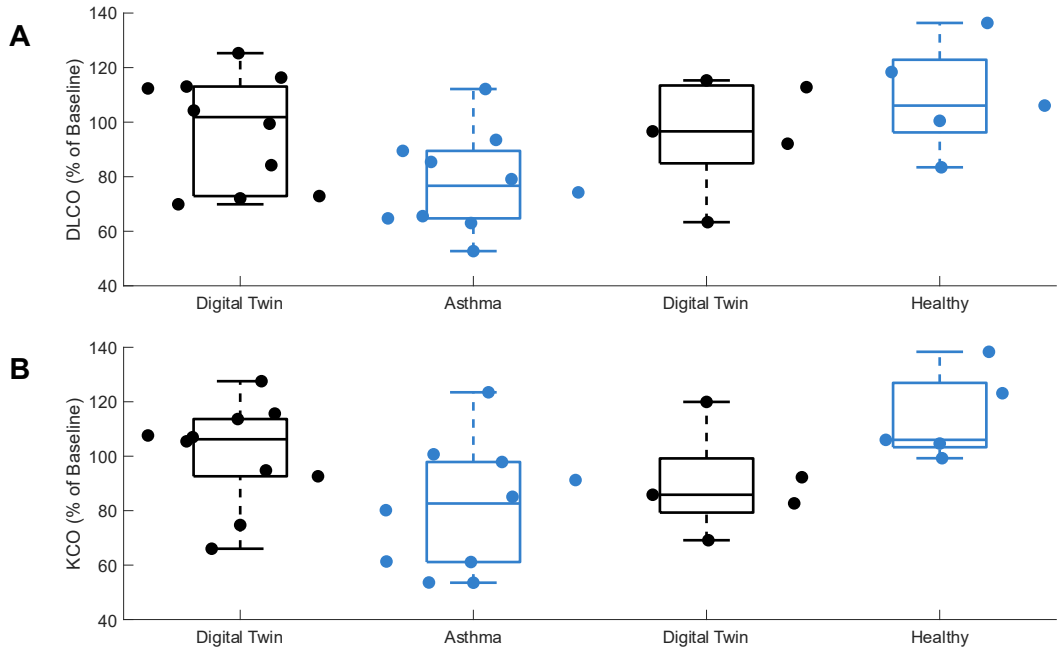


Figure 34 – Box plots of DLCO and KCO simulation results in asthma (n=10) and health (n=5).

Simulated outputs (black) capture the observed range of DLCO % of healthy simulation (A) and KCO % of healthy simulation (B) of 10 patients with asthma and 5 healthy control individuals (blue) following personalised changes to inputs. Comparison of observed DLCO % of predicted and KCO % of predicted outputs (blue) for 10 patients with asthma, and 5 healthy control individuals, whose clinical characteristics can be seen in **Table 10**, with digital-twin-simulated DLCO % of healthy simulation and KCO % of healthy simulation (black) following application of personalised input changes sourced from hyperpolarised xenon MRI spectroscopy and proton imaging (described in the methods). The values presented in blue represent the mean (circle in the middle) ± 2σ (bars) of the observed outputs, while values presented in black represent the mean (square in the middle) ± 2σ (bars) of simulated outputs.

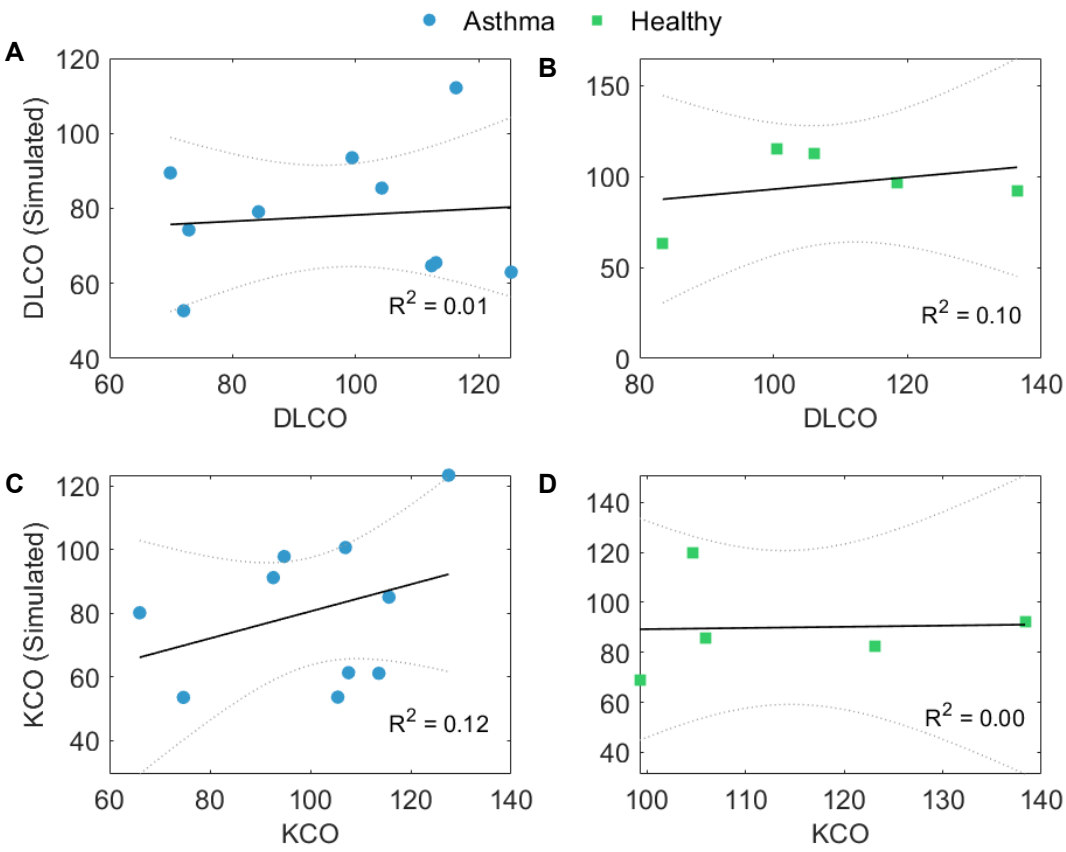


Figure 35 – Correlation plots of simulated outputs against measured DLCO and KCO in asthma (n=10) and health (n=5) using hyperpolarised Xenon^{129} MRI gas exchange analogues.

There appears to be a generally low correlation between simulated and measured outputs with R^2 values being less than 0.12, suggesting that more patient-specificity is required for the V/Q model to be able to accurately simulate the CO gas-transfer test using hyperpolarised Xenon^{129} MRI data.

4.4 Discussion

Simulations using real huuman data, shown in **Figure *34*** as mean ± 2 standard deviations increase the conficence in the functionality of the model, as they show that the simulated range of values largely overlaps with the measured range and the means closely match. The same results shown in **Figure *35*** as correlation plots however, indicate that the model cannot accurately simulate the test outputs, neither in asthma nor in health, since the results demonstrate poor correlation between simulated and measured DLCO and KCO of less than R^2=0.12. While higher correlation values would increase the confidence in the model's accuracy it is important to note that low correlation values were expected due to the model's limitations which lie in the model's own simplifying mathematical assumptions and approximations of personalised parameters.

The model functions under simplifying mathematical assumptions which is the main source of error for the simulations, as the assumptions only partially reflect the reality of the physics and the physiology. Gas exchange efficiency analogues were used to approximate the efficiency of gas exchange across the RBC membrane and blood-gas barrier. These values were taken as global values for each inividuals' pair of lungs. As the diffusion scaling equation and therefore the scaled diffusion rate differ across model compartments based on the individual's compartment's structural properties – including capillary blood volume, alveolar volume (estimated based on global VDP), and total lung capacity – compartment-specific hyperpolarised Xenon-129 MRI gas-exchange analogues should have been used for the calculation of more accurate compartment-specific diffusion rates which could have potentially led to more accurate sumulations. The use of global hyperpolarised Xenon-129 MRI gas-exchange analogues for each pair of lungs therefore does not perfectly reflect the real diffusion rate in each compartment and as a result, leads to less accurate simulation results.

The model demonstrates strong potential for its future application in research and clinical usage despite the low correlations obtained in a small study cohort. Firstly, the model can act as a very good tool for prognosis of post-operative lung resection. Secondly, the model can be further compartmentalised, thus increasing its patient-specificity while at the same time

potentially increasing the concordance between its simulated outputs with measured test output values. Smaller compartments, especially with compartment-specific ventilation information approximated by regionalised VDP would increase the model's accuracy.

While the model is not a "simulation patient digital twin" that provides regional outputs of the CO gas transfer test, it addresses the need for a "simulation patient digital twin" that represents regional gas-transfer processes underlying the CO gas transfer test in a 2-dimensional, 4-compartment respiratory system and allows simulations of hypothetical unseen scenarios involving structural changes to give insight into their effect on lung function. The model also shows promise in providing regional, 3-dimensional CO gas transfer outputs, subject to further development of the model (i.e., increasing the amount of compartments in all 3 dimensions) and the use of regional three-dimensional hyperpolarised ^{129}Xe MRI gas exchange analogues RBC and Barrier ratios as well as regional three-dimensional VDP as inputs. Additional future development options for the model include incorporation of oxygen binding to haemoglobin using altitude-dependent oxygen partial pressure in the capillary blood to investigate the impact of high altitude on blood-gas barrier function through personalised modelling in mountaineers (Peacock, 1998), including regionalised VDP and hyperpolarised Xenon-129 gas exchange analogues. Finally, the results act as a strong indication that this explanatory model of blood-gas barrier function may aid the clinical interpretation of the CO gas-transfer test if further developed.

4.5 Summary

In the previous chapter, the development and validation of a "simulation patient digital twin" was presented, that spatially localised the CO gas transfer test. While the model was validated in the previous chapter, the validation did not include real human data. Building on the previous chapter, the validation of the model with real human data, namely a cohort including 10 asthmatic patients and 5 healthy volunteers, was presented in this chapter. The model coupling was improved in this chapter, using the published gas-exchange efficiency analogue RBC:Barrier ratio, while the rest of the model remained the same as in the previous chapter.

Simulations implemented using personalised VPD and hyperpolarised ^{129}Xe MRI RBC:Barrier ratio, as well as patient demographics to estimate the rest of the model inputs using the GLI reference equations, appeared to largely overlap with the measured CO gas transfer outputs in both the asthmatic and healthy groups. The same simulation results however, appeared to be poorly correlated with the measured CO gas transfer outputs, in both the asthmatic and healthy groups. While the results indicate that the correlation between simulated and measured DLCO and KCO is low, this can be attributed to the model's limitations which lie in its own simplifying mathematical assumptions and are expected to negatively affect the simulation results. It is hypothesized that regional data of hyperpolarised ^{129}Xe MRI and VDP can lead to more accurate simulations. While the simplifying mathematical assumptions represent limitations of the model, it is not believed that they represent limitations of the study as the results represent the model's ability to capture the reasonable range of expected outputs in both the asthmatic and healthy groups. Opportunities for future development include an increase in the compartments of the model in all 3 dimensions to enhance the model's regionalisation, and allow investigation of VH effects on simulations, as well as the addition of an oxygen-dependent partial pressure of blood to investigate the impact of altitude on blood-gas barrier function.

5. Conclusion

Motivated by the need for the development of "monitoring patient digital twins" – systems enabling live tracking of a patient's state, including organ visualisations from sensor-collected data and allowing the guidance of decision-making using machine learning and mechanistic methods – this thesis focused on the optimisation and validation of two "simulation patient digital twins" as essential components of such monitoring digital twins. Simulation digital twins are not only useful as elements of monitoring digital twins but are also valuable in research for facilitating understanding of lung structure-function relationships by allowing simulation of hypothetical unseen scenarios involving changes to the lungs' structure to assess their impact on the lungs' function. Advanced computational modelling techniques combined with imaging, provide this advantage over other established methods which address the spatialised nature of lung disease such as hyperpolarised ^{129}Xe MRI, which does not allow simulation of hypothetical scenarios. Optimisation of an established imaging-informed FOT mathematical model was implemented as the first aim of this thesis, relevant to Chapter 2, through the assessment of whether imaging-regressed, personalised viscoelastic lung tissue parameters would increase concordance between simulations and measurements in asthma and health. The optimisation utilised CT medical imaging to aid in the approximation of the participants' lung structures and to predict optimising lung tissue viscoelastic parameters using imaging-biomarker-trained regression models. In the third chapter of this thesis, the second aim involved the development and validation of an imaging-informed, V/Q mechanistic, mathematical model that spatially localised the CO gas-transfer test in a 2-dimensional respiratory system, to enable investigation that would provide insight into blood-gas barrier dysfunction. Finally, in Chapter 4 of this thesis, the V/Q model, developed and validated in Chapter 3, was optimised through its coupling with hyperpolarised ^{129}Xe MRI gas-exchange efficiency analogues, as part of the third and final aim of this thesis, and the simulation results were compared with measured DLCO and KCO values for its validation.

5.1 Clinical Importance

The work in this thesis has focused on development, optimisation and validation of mechanistic, mathematical models spatially localising pulmonary function tests relevant to VH – FOT test, V/Q mismatch, and blood-gas barrier dysfunction – CO gas transfer test. The results arising from the optimisation process provide important insights into the study's clinical importance.

In the second chapter, the optimisation of the FOT model was achieved through prediction of personalised viscoelastic lung tissue parameters through imaging-informed regression models which shows promise in the utilisation of imaging biomarkers to personalise FOT mathematical model parameters reflecting tissue viscoelasticity. This study has anchored the inference of CPM parameters G and H to the physiology by allowing their prediction from imaging biomarkers – providing a pathway towards regional prediction of CPM parameters using imaging biomarkers at bronchiole level. The predicted CPM parameters were the result of trained regression models with imaging biomarkers and grid-search-obtained personalised parameters G and H. Out of these parameters, both sets of values for G (grid-search-obtained and predicted) were found to significantly separate across asthma severity groups which reflects the sensitivity of this parameter to differences in asthma severity, while at the same time being in agreement with the sensitivity of this parameter to differences in asthma severity, arising from a different, imaging-uninformed mathematical impedance model (Tuza *et al.*, 2020).

The development and validation of the digital twin that represents regional gas-transfer processes underlying the single-breath CO gas transfer test, relevant to chapters 3 and 4, has provided valuable insights into the clinical significance of the model. The simulation results in Chapter 3, not only validate the model's functionality and ability to accurately simulate hypothetical disease scenarios and post-operative pneumonectomy but also show the model's potential in being used in a clinical setting, acting as a tool for prognosis of post-operative lung resection. While the model performed well in simulating hypothetical scenarios in Chapter 3,

its performance was not as consistent in Chapter 4. This can be attributed to the model's simplifying mathematical assumptions for coupling with hyperpolarised ^{129}Xe MRI, lack of compartment-specific VDP data, as well as lack of compartment-specific hyperpolarised ^{129}Xe MRI gas exchange analogues. The model's potential in being further developed was highlighted, with a focus on further development of its coupling with hyperpolarised ^{129}Xe MRI gas exchange analogues which could allow in-depth investigation of blood-gas barrier dysfunction.

5.2 Future work and recommendations

As explored in the literature review in the introduction of this thesis, computational modelling and the development of digital twins have a long history. Recent computational models have built upon a vast amount of prior knowledge from published literature, and so have the models presented within this thesis. The mathematical models contained within this work count as an improvement in our capabilities to simulate the functions of the respiratory system accurately and in a personalised manner. While optimisation and validation of the models within this thesis have been achieved, the results raise further questions regarding potential improvements of the simulations in the future for the application of these models in research as well as in a clinical setting.

5.2.1 Impedance Model

The impedance model simulating the FOT test is inherently limited by the imaging resolution of the scans from which the personalised airways are segmented. Simulations within this thesis were implemented on complete conducting zone airway lung structures which were only personalised to (Weibel) generations 6-10 and algorithmically grown to form the full conducting zone. Naturally, better personalisation of the airways would lead to more accurate simulations. This could be achieved with the use of more advanced imaging techniques capable of capturing smaller airways which may enable the development of lung structures that are personalised to higher (Weibel) generations and therefore more distal depths. Currently, micro-CT (Pennati *et al.*, 2023, 2024; Zaw Thin *et al.*, 2023) is unsuitable for use on living

humans due to its high radiation burden; however should comparable techniques with an acceptable risk profile for living humans become available in the future, they would present a viable and valuable alternative. Higher or more detailed imaging resolution would also enable the generation of higher quality imaging biomarkers that would more accurately capture the viscoelastic properties of the acini, leading to better training and more accurate prediction of the CPM parameters using the imaging biomarkers.

Scaling of the complete conducting zone airway structures was implemented as described in the methods section of Chapter 2, which included the estimation of transmural pressure. In this work, the transmural pressure used was the same across the study population and was not personalised. The personalisation of transmural pressure i.e., from published pressure-volume relationships, and by using the participants' lung volume measurements to estimate the percentage contribution of the volume of their lungs during normal quiet breathing to TLC could lead to more accurate impedance simulations. Simulating personalised impedance more accurately would itself lead to more realistic estimation of personalised lung tissue viscoelastic CPM parameters tissue damping (G) and elastance (H). Finally, the use of more realistic CPM parameters would allow the training of better predictive models, which can act as optimising components to the impedance model.

Furthermore, the robustness and generalisability of the regression models could be assessed in an independent study cohort which could provide confidence in the future use of these models. The regression models and the FOT model can be used to assess the response of the CPM parameters to bronchial challenge, pre-and-post- administration of, for example, a short-acting β-agonist or other agents such as anticholinergics. Knowing the effects of the response of these parameters to various medications could aid prognosis of the function of the lungs post-administration of medication with the use of the FOT model following application of expected regional changes to the CPM parameters.

Within Chapter 2, linear regression models were trained to predict personalised CPM parameters. While this method was effective in the prediction of personalised viscoelastic

parameters and therefore in the optimisation of the entire impedance model, more sophisticated methods could be used which may provide more accurate personalised predictions. Different approaches may include machine learning methods or more advanced regression models such as elastic net regression.

Future work could therefore focus on the development of highly personalised impedance digital twins in which the distal airway structure (Weibel generations greater than 10) is captured using higher-resolution imaging, while the lung tissue viscoelastic CPM parameters are inferred regionally from regional quantitative imaging biomarkers at bronchiole level. Such models would enable investigation of regional lung mechanics by allowing estimation of CPM parameters at bronchiole level, providing insight into how energy dissipation (G) and elastic energy storage (H) vary across lung regions in health and asthma.

For example, the framework developed in this thesis could be extended to investigate how energy dissipation (G) and elastic energy storage (H) vary across asthma severity groups, providing insight into how lung tissue mechanics change as disease progresses. In addition, the model could be used to examine regional variations in these parameters following bronchial challenge or pharmacological interventions such as bronchodilators or anti-inflammatory therapies. Such simulations could provide insight into both treatment response and regional drug delivery mechanisms by evaluating changes in the magnitude of regional CPM parameters following therapeutic intervention. This would open the possibility of using the FOT digital twin framework to simulate treatment responses and support the development of personalised therapeutic strategies.

5.2.2 V/Q Model

The V/Q model is limited by its mathematical simplifying assumptions; however, these can be progressively refined to better represent the physiological complexity of the respiratory system. In the current implementation, the model represents regional gas-transfer processes underlying the single-breath CO gas transfer test within four compartments, arranged in a two-dimensional representation of the respiratory system. A natural extension of this

framework would involve increasing the number of compartments and extending the framework into three dimensions to increase the spatial resolution of the model. Such developments would allow the model to better capture the highly spatial nature of lung disease, particularly in obstructive diseases where VH is present. The suggested framework could be used to assess how well the model captures VH in an asthmatic cohort by comparison of simulated and measured DLCO and KCO outputs.

Further validation of the model in another patient cohort could also be useful in increasing the confidence in the functionality of the coupling of the model with hyperpolarised ^{129}Xe MRI. Specifically, a cohort composed of healthy individuals and ILD patients would be valuable, as the RBC:Barrier ratio is expected to be more strongly affected by blood-gas barrier dysfunction arising from fibrosis. Any future validation would also benefit from incorporation of regional VDP measurements to be used as model inputs rather than global measurements. Regional VDP would also be useful in the assessment of how well the model can capture VH in asthma. A longer-term optimisation option includes the addition of oxygen binding to haemoglobin using an altitude-dependent partial pressure of oxygen in the capillary blood. This would enable the examination of the impact of high altitude on blood-gas barrier function in mountaineers (Peacock, 1998).

6. References

Aaron, S.D. *et al.* (2024) 'Early Diagnosis and Treatment of COPD and Asthma - A Randomized, Controlled Trial', *The New England Journal of Medicine*, 390(22), pp. 2061–2073. Available at: https://doi.org/10.1056/NEJMoa2401389.

Abdelrahim, M.E.A. *et al.* (2021) *Essentials of Aerosol Therapy in Critically ill Patients*. Cham: Springer International Publishing. Available at: https://doi.org/10.1007/978-3-030-85026-5.

Alblooshi, A.S. *et al.* (2013) 'The safety and feasibility of the inhaled mannitol challenge test in young children', *The European Respiratory Journal*, 42(5), pp. 1420–1423. Available at: https://doi.org/10.1183/09031936.00041713.

Aliaroof, M. *et al.* (2025) 'Oscillometry to assess ventilation heterogeneity during hospital admission for acute cardiorespiratory illness', *ERJ Open Research*, 11(3), pp. 00351–02024. Available at: https://doi.org/10.1183/23120541.00351-2024.

Alobaidi, A.H., Alsamarai, A.M. and Alsamarai, M.A. (2021) 'Inflammation in Asthma Pathogenesis: Role of T Cells, Macrophages, Epithelial Cells and Type 2 Inflammation', *Anti-Inflammatory & Anti-Allergy Agents in Medicinal Chemistry*, 20(4), pp. 317–332. Available at: https://doi.org/10.2174/1871523020666210920100707.

Alshlowi, M. *et al.* (2023) 'Differences in respiratory oscillometry measurements using mouthpiece, mouth, and nasal mask in healthy adults', *Journal of Applied Physiology*, 134(1), pp. 142–146. Available at: https://doi.org/10.1152/japplphysiol.00491.2022.

Álvarez-Barrientos, F., Hurtado, D.E. and Genet, M. (2021) 'Pressure-driven micro-poro-mechanics: A variational framework for modeling the response of porous materials', *International Journal of Engineering Science*, 169, p. 103586. Available at: https://doi.org/10.1016/j.ijengsci.2021.103586.

Anderson, W.J., Zajda, E. and Lipworth, B.J. (2012) 'Are we overlooking persistent small airways dysfunction in community-managed asthma?', *Annals of Allergy, Asthma & Immunology: Official Publication of the American College of Allergy, Asthma, & Immunology*, 109(3), pp. 185-189.e2. Available at: https://doi.org/10.1016/j.anai.2012.06.022.

Antman, E.M. and Loscalzo, J. (2016) 'Precision medicine in cardiology', *Nature Reviews Cardiology*, 13(10), pp. 591–602. Available at: https://doi.org/10.1038/nrcardio.2016.101.

Arshad, S.H. *et al.* (2020) 'Assessing small airway function for early detection of lung function impairment', *European Respiratory Journal*, 56(1). Available at: https://doi.org/10.1183/13993003.01946-2020.

Baffico, L., Grandmont, C. and Maury, B. (2010) 'Multiscale modeling of the respiratory tract', *Mathematical Models and Methods in Applied Sciences*, 20(01), pp. 59–93. Available at: https://doi.org/10.1142/S0218202510004155.

Barjaktarevic, I. *et al.* (2018) 'Bronchodilator responsiveness or reversibility in asthma and COPD – a need for clarity', *International Journal of Chronic Obstructive Pulmonary Disease*, 13, pp. 3511–3513. Available at: https://doi.org/10.2147/COPD.S183736.

Bates, J.H.T. *et al.* (2011) 'Oscillation Mechanics of the Respiratory System', *Comprehensive Physiology*. John Wiley & Sons, Ltd, pp. 1233–1272. Available at: https://doi.org/10.1002/cphy.c100058.

Becklake, M.R. (1952) 'A New Index of the Intrapulmonary Mixture of Inspired Air', *Thorax*, 7(1), pp. 111–116. Available at: https://doi.org/10.1136/thx.7.1.111.

Bell, A.J. *et al.* (2019) 'Functional CT imaging for identification of the spatial determinants of small-airways disease in adults with asthma', *Journal of Allergy and Clinical Immunology*, 144(1), pp. 83–93. Available at: https://doi.org/10.1016/j.jaci.2019.01.014.

Berger, L. *et al.* (2016) 'A poroelastic model coupled to a fluid network with applications in lung modelling', *International Journal for Numerical Methods in Biomedical Engineering*, 32(1), p. e02731. Available at: https://doi.org/10.1002/cnm.2731.

Bhakta, N.R. *et al.* (2023) 'European Respiratory Society/American Thoracic Society technical statement: standardisation of the measurement of'lung volumes, 2023 update', *EUROPEAN RESPIRATORY JOURNAL* [Preprint].

Bhatawadekar, S.A., Leary, D. and Maksym, G.N. (2015) 'Modelling resistance and reactance with heterogeneous airway narrowing in mild to severe asthma', *Canadian Journal of Physiology and Pharmacology*, 93(3), pp. 207–214. Available at: https://doi.org/10.1139/cjpp-2014-0436.

Bisgaard, H. and Klug, B. (1995) 'Lung function measurement in awake young children', *The European Respiratory Journal*, 8(12), pp. 2067–2075. Available at: https://doi.org/10.1183/09031936.95.08122067.

Boes, J.L. *et al.* (2015) 'Parametric Response Mapping Monitors Temporal Changes on Lung CT Scans in the Subpopulations and Intermediate Outcome Measures in COPD Study (SPIROMICS)', *Academic Radiology*, 22(2), pp. 186–194. Available at: https://doi.org/10.1016/j.acra.2014.08.015.

Bohadana, A.B. *et al.* (1999) 'Dose-response slope of forced oscillation and forced expiratory parameters in bronchial challenge testing', *The European Respiratory Journal*, 13(2), pp. 295–300. Available at: https://doi.org/10.1034/j.1399-3003.1999.13b13.x.

Bordas, R. *et al.* (2015) 'Development and Analysis of Patient-Based Complete Conducting Airways Models', *PLOS ONE*, 10(12), p. e0144105. Available at: https://doi.org/10.1371/journal.pone.0144105.

Bou Jawde, S. *et al.* (2020) 'Tracking respiratory mechanics around natural breathing rates via variable ventilation', *Scientific Reports*, 10(1), p. 6722. Available at: https://doi.org/10.1038/s41598-020-63663-8.

Boudin, L. *et al.* (2015) 'Modelling and Numerics for Respiratory Aerosols', *Communications in Computational Physics*, 18(3), pp. 723–756. Available at: https://doi.org/10.4208/cicp.180714.200415a.

Bradding, P. *et al.* (2024) 'Airway hyperresponsiveness in asthma: The role of the epithelium', *Journal of Allergy and Clinical Immunology*, 153(5), pp. 1181–1193. Available at: https://doi.org/10.1016/j.jaci.2024.02.011.

Brereton, C.J. *et al.* (2020) 'Time taken from primary care referral to a specialist centre diagnosis of idiopathic pulmonary fibrosis: an opportunity to improve patient outcomes?', *ERJ Open Research*, 6(2). Available at: https://doi.org/10.1183/23120541.00120-2020.

Broberg, C.S. *et al.* (2014) 'Lung function and gas exchange in Eisenmenger syndrome and their impact on exercise capacity and survival', *International Journal of Cardiology*, 171(1), pp. 73–77. Available at: https://doi.org/10.1016/j.ijcard.2013.11.047.

Broeders, M.E.A.C. *et al.* (2005) 'Bronchial challenge, assessed with forced expiratory manoeuvres and airway impedance', *Respiratory Medicine*, 99(8), pp. 1046–1052. Available at: https://doi.org/10.1016/j.rmed.2005.01.006.

Brooks, R. (1996) 'EuroQol: the current state of play', *Health Policy*, 37(1), pp. 53–72. Available at: https://doi.org/10.1016/0168-8510(96)00822-6.

Brooks, R. (2013) *The EuroQol Group after 25 years*. Dordrecht: Springer Netherlands. Available at: https://doi.org/10.1007/978-94-007-5158-3.

Burrowes, K.S. *et al.* (2008) 'Towards a virtual lung: multi-scale, multi-physics modelling of the pulmonary system', *Philosophical Transactions. Series A, Mathematical, Physical, and Engineering Sciences*, 366(1879), pp. 3247–3263. Available at: https://doi.org/10.1098/rsta.2008.0073.

Burrowes, K.S., Doel, T. and Brightling, C. (2014) 'Computational modeling of the obstructive lung diseases asthma and COPD', *Journal of Translational Medicine*, 12(2), p. S5. Available at: https://doi.org/10.1186/1479-5876-12-S2-S5.

Cassan, S.M., Divertie, M.B. and Brown, A.L. (1974) 'Fine structural morphometry on biopsy specimens of human lung. 2. Diffuse idiopathic pulmonary fibrosis', *Chest*, 65(3), pp. 275–278. Available at: https://doi.org/10.1378/chest.65.3.275.

Cassidy, R.N., Roberts, M.E. and Colby, S.M. (2015) 'Validation of a Respiratory Symptom Questionnaire in Adolescent Smokers', *Tobacco Regulatory Science*, 1(2), pp. 121–128. Available at: https://doi.org/10.18001/TRS.1.2.2.

Cavalcanti, J.V. *et al.* (2006) 'Detection of changes in respiratory mechanics due to increasing degrees of airway obstruction in asthma by the forced oscillation technique', *Respiratory Medicine*, 100(12), pp. 2207–2219. Available at: https://doi.org/10.1016/j.rmed.2006.03.009.

Chan, M.-C. *et al.* (2019) 'First tidal volume greater than 8 mL/kg is associated with increased mortality in complicated influenza infection with acute respiratory distress syndrome', *Journal of the Formosan Medical Association = Taiwan Yi Zhi*, 118(1 Pt 2), pp. 378–385. Available at: https://doi.org/10.1016/j.jfma.2018.06.010.

Chen, Y. *et al.* (2015) 'Validation of human small airway measurements using endobronchial optical coherence tomography', *Respiratory Medicine*, 109(11), pp. 1446–1453. Available at: https://doi.org/10.1016/j.rmed.2015.09.006.

Chiabai, J. *et al.* (2021) 'Intrabreath oscillometry is a sensitive test for assessing disease control in adults with severe asthma', *Annals of Allergy, Asthma & Immunology: Official*

Publication of the American College of Allergy, Asthma, & Immunology, 127(3), pp. 372–377. Available at: https://doi.org/10.1016/j.anai.2021.06.005.

Chikhani, M. *et al.* (2016) 'High PEEP in acute respiratory distress syndrome: quantitative evaluation between improved arterial oxygenation and decreased oxygen delivery', *British Journal of Anaesthesia*, 117(5), pp. 650–658. Available at: https://doi.org/10.1093/bja/aew314.

Choi, S. *et al.* (2013) 'Registration-based assessment of regional lung function via volumetric CT images of normal subjects vs. severe asthmatics', *Journal of Applied Physiology*, 115(5), pp. 730–742. Available at: https://doi.org/10.1152/japplphysiol.00113.2013.

Choi, S. *et al.* (2019) '1D network simulations for evaluating regional flow and pressure distributions in healthy and asthmatic human lungs', *Journal of Applied Physiology*, 127(1), pp. 122–133. Available at: https://doi.org/10.1152/japplphysiol.00016.2019.

Clark, A.R., Burrowes, K.S. and Tawhai, M.H. (2021) 'Integrative Computational Models of Lung Structure-Function Interactions', *Comprehensive Physiology*. John Wiley & Sons, Ltd, pp. 1501–1530. Available at: https://doi.org/10.1002/cphy.c200011.

Clément, J., Làndsér, F.J. and Van de Woestijne, K.P. (1983) 'Total resistance and reactance in patients with respiratory complaints with and without airways obstruction', *Chest*, 83(2), pp. 215–220. Available at: https://doi.org/10.1378/chest.83.2.215.

Cleveland, Z.I. *et al.* (2014) '3D MR Imaging of Impaired Hyperpolarized 129Xe Uptake in a Rat Model of Pulmonary Fibrosis', *NMR in biomedicine*, 27(12), pp. 1502–1514. Available at: https://doi.org/10.1002/nbm.3127.

Corral-Acero, J. *et al.* (2020) 'The "Digital Twin" to enable the vision of precision cardiology', *European Heart Journal*, 41(48), pp. 4556–4564. Available at: https://doi.org/10.1093/eurheartj/ehaa159.

Corris, P.A. *et al.* (1987) 'Use of radionuclide scanning in the preoperative estimation of pulmonary function after pneumonectomy.', *Thorax*, 42(4), pp. 285–291.

Cottini, M. *et al.* (2023) 'Impulse oscillometry defined small airway dysfunction in asthmatic patients with normal spirometry: Prevalence, clinical associations, and impact on asthma control', *Respiratory Medicine*, 218. Available at: https://doi.org/10.1016/j.rmed.2023.107391.

Covar, R.A. *et al.* (2012) 'The Childhood Asthma Management Program (CAMP): Contributions to the Understanding of Therapy and the Natural History of Childhood Asthma', *Current Respiratory Care Reports*, 1(4), pp. 243–250. Available at: https://doi.org/10.1007/s13665-012-0026-9.

Crimi, C. *et al.* (2020) 'Comparability of asthma control test scores between self and physician-administered test', *Respiratory Medicine*, 170, p. 106015. Available at: https://doi.org/10.1016/j.rmed.2020.106015.

Crisafulli, E. *et al.* (2017) 'Prevalence of Small-Airway Dysfunction among COPD Patients with Different GOLD Stages and Its Role in the Impact of Disease', *Respiration; International Review of Thoracic Diseases*, 93(1), pp. 32–41. Available at: https://doi.org/10.1159/000452479.

D'Alonzo, G.E., Bower, J.S. and Dantzker, D.R. (1984) 'Differentiation of Patients with Primary and Thromboembolic Pulmonary Hypertension', *Chest*, 85(4), pp. 457–461. Available at: https://doi.org/10.1378/chest.85.4.457.

Dandurand, R.J. *et al.* (2019) 'Comparison of oscillometry devices using active mechanical test loads', *ERJ Open Research*, 5(4). Available at: https://doi.org/10.1183/23120541.00160-2019.

Daniels, F.B. (1950) 'On the Propagation of Sound Waves in a Cylindrical Conduit', *The Journal of the Acoustical Society of America*, 22(5), pp. 563–564. Available at: https://doi.org/10.1121/1.1906650.

Das, A. *et al.* (2013) 'Optimization of mechanical ventilator settings for pulmonary disease states', *IEEE transactions on bio-medical engineering*, 60(6), pp. 1599–1607. Available at: https://doi.org/10.1109/TBME.2013.2239645.

Das, A. *et al.* (2015) 'Evaluation of lung recruitment maneuvers in acute respiratory distress syndrome using computer simulation', *Critical Care (London, England)*, 19(1), p. 8. Available at: https://doi.org/10.1186/s13054-014-0723-6.

Das, A. *et al.* (2017) 'Hemodynamic effects of lung recruitment maneuvers in acute respiratory distress syndrome', *BMC Pulmonary Medicine*, 17(1), p. 34. Available at: https://doi.org/10.1186/s12890-017-0369-7.

Deepak, D. *et al.* (2017) 'Recognition of Small Airways Obstruction in Asthma and COPD - The Road Less Travelled', *Journal of Clinical and Diagnostic Research : JCDR*, 11(3), pp. TE01–TE05. Available at: https://doi.org/10.7860/JCDR/2017/19920.9478.

Demarche, S. *et al.* (2016) 'Detailed analysis of sputum and systemic inflammation in asthma phenotypes: are paucigranulocytic asthmatics really non-inflammatory?', *BMC Pulmonary Medicine*, 16(1), p. 46. Available at: https://doi.org/10.1186/s12890-016-0208-2.

Desiraju, K. and Agrawal, A. (2016) 'Impulse oscillometry: The state-of-art for lung function testing', *Lung India : Official Organ of Indian Chest Society*, 33(4), pp. 410–416. Available at: https://doi.org/10.4103/0970-2113.184875.

Deslauriers, J. *et al.* (2011) 'Adjustments in cardiorespiratory function after pneumonectomy: results of the pneumonectomy project', *The Journal of Thoracic and Cardiovascular Surgery*, 141(1), pp. 7–15. Available at: https://doi.org/10.1016/j.jtcvs.2010.09.010.

Devlin, N.J. and Brooks, R. (2017) 'EQ-5D and the EuroQol Group: Past, Present and Future', *Applied Health Economics and Health Policy*, 15(2), pp. 127–137. Available at: https://doi.org/10.1007/s40258-017-0310-5.

Diffusion-Limited and Perfusion-Limited Gas Exchange - Respiratory - Medbullets Step 1 (2024). Available at: https://step1.medbullets.com/respiratory/117015/diffusion-limited-and-perfusion-limited-gas-exchange (Accessed: 22 March 2024).

Downie, S.R. *et al.* (2007) 'Ventilation heterogeneity is a major determinant of airway hyperresponsiveness in asthma, independent of airway inflammation', *Thorax*, 62(8), pp. 684–689. Available at: https://doi.org/10.1136/thx.2006.069682.

Driehuys, B. *et al.* (2006) 'Imaging alveolar–capillary gas transfer using hyperpolarized 129Xe MRI', *Proceedings of the National Academy of Sciences of the United States of America*, 103(48), pp. 18278–18283. Available at: https://doi.org/10.1073/pnas.0608458103.

Drummond, D. and Coulet, A. (2022) 'Technical, Ethical, Legal, and Societal Challenges With Digital Twin Systems for the Management of Chronic Diseases in Children and Young People', *Journal of Medical Internet Research*, 24(10), p. e39698. Available at: https://doi.org/10.2196/39698.

Dubois, A.B., Botelho, S.Y. and Comroe, J.H. (1956) 'A new method for measuring airway resistance in man using a body plethysmograph: values in normal subjects and in patients

with respiratory disease', *The Journal of Clinical Investigation*, 35(3), pp. 327–335. Available at: https://doi.org/10.1172/JCI103282.

Ducharme, F.M. and Chan, R. (2024) 'Oscillometry in the diagnosis, assessment, and monitoring of asthma in children and adults', *Annals of Allergy, Asthma & Immunology*, 134(2), pp. 135–143. Available at: https://doi.org/10.1016/j.anai.2024.11.013.

Fain, S.B. *et al.* (2007) 'Functional lung imaging using hyperpolarized gas MRI', *Journal of Magnetic Resonance Imaging*, 25(5), pp. 910–923. Available at: https://doi.org/10.1002/jmri.20876.

Farrow, C. and King, G. (2019) 'SPECT Ventilation Imaging in Asthma', *Seminars in Nuclear Medicine*, 49(1), pp. 11–15. Available at: https://doi.org/10.1053/j.semnuclmed.2018.10.007.

Foy, B.H. *et al.* (2019) 'Lung Computational Models and the Role of the Small Airways in Asthma', *American Journal of Respiratory and Critical Care Medicine*, 200(8), pp. 982–991. Available at: https://doi.org/10.1164/rccm.201812-2322OC.

Foy, B.H. and Kay, D. (2017) 'A computational comparison of the multiple-breath washout and forced oscillation technique as markers of bronchoconstriction', *Respiratory Physiology & Neurobiology*, 240, pp. 61–69. Available at: https://doi.org/10.1016/j.resp.2017.02.016.

Foy, B.H. and Kay, D. (2019) 'A computationally tractable scheme for simulation of the human pulmonary system', *Journal of Computational Physics*, 388, pp. 371–393. Available at: https://doi.org/10.1016/j.jcp.2019.03.014.

Frank, A.O., Chuong, C.J.C. and Johnson, R.L. (1997) 'A finite-element model of oxygen diffusion in the pulmonary capillaries', *Journal of Applied Physiology*, 82(6), pp. 2036–2044. Available at: https://doi.org/10.1152/jappl.1997.82.6.2036.

Galbán, C.J. *et al.* (2012) 'Computed tomography–based biomarker provides unique signature for diagnosis of COPD phenotypes and disease progression', *Nature Medicine*, 18(11), pp. 1711–1715. Available at: https://doi.org/10.1038/nm.2971.

Gao, J. *et al.* (2017) 'Sputum cell count: biomarkers in the differentiation of asthma, COPD and asthma–COPD overlap', *International Journal of Chronic Obstructive Pulmonary Disease*, 12, pp. 2703–2710. Available at: https://doi.org/10.2147/COPD.S142466.

Gavaghan, D., Coveney, P.V. and Kohl, P. (2009) 'The virtual physiological human: tools and applications I', *Philosophical Transactions of the Royal Society A: Mathematical, Physical and Engineering Sciences* [Preprint]. Available at: https://doi.org/10.1098/rsta.2009.0070.

Gehr, P., Bachofen, M. and Weibel, E.R. (1978) 'The normal human lung: ultrastructure and morphometric estimation of diffusion capacity', *Respiration Physiology*, 32(2), pp. 121–140. Available at: https://doi.org/10.1016/0034-5687(78)90104-4.

Geitner, C.M. *et al.* (2023) 'An approach to study recruitment/derecruitment dynamics in a patient-specific computational model of an injured human lung', *International Journal for Numerical Methods in Biomedical Engineering*, 39(9), p. e3745. Available at: https://doi.org/10.1002/cnm.3745.

Gilbey, S. *et al.* (2024) 'Clinical utility of sputum cell count in severe asthma', *European Respiratory Journal*, 64(suppl 68). Available at: https://doi.org/10.1183/13993003.congress-2024.PA3522.

Glaessgen, E. and Stargel, D. (2012) 'The Digital Twin Paradigm for Future NASA and U.S. Air Force Vehicles', *53rd AIAA/ASME/ASCE/AHS/ASC Structures, Structural Dynamics and Materials Conference
20th AIAA/ASME/AHS Adaptive Structures Conference
14th AIAA. 53rd AIAA/ASME/ASCE/AHS/ASC Structures, Structural Dynamics and Materials Conference
20th AIAA/ASME/AHS Adaptive Structures Conference
14th AIAA*, Honolulu, Hawaii: American Institute of Aeronautics and Astronautics. Available at: https://doi.org/10.2514/6.2012-1818.

Glénet, S. *et al.* (2017) 'No compensatory lung growth after resection in a one-year follow-up cohort of patients with lung cancer', *Journal of Thoracic Disease*, 9(10), pp. 3938–3945. Available at: https://doi.org/10.21037/jtd.2017.08.135.

Gonem, S. *et al.* (2014) 'Clinical significance of small airway obstruction markers in patients with asthma', *Clinical & Experimental Allergy*, 44(4), pp. 499–507. Available at: https://doi.org/10.1111/cea.12257.

Gonsard, A., Genet, M. and Drummond, D. (2024) 'Digital twins for chronic lung diseases', *European Respiratory Review*, 33(174). Available at: https://doi.org/10.1183/16000617.0159-2024.

Graham, B.L. *et al.* (2017) '2017 ERS/ATS standards for single-breath carbon monoxide uptake in the lung', *European Respiratory Journal*, 49(1). Available at: https://doi.org/10.1183/13993003.00016-2016.

Grieves, M. and Vickers, J. (2017) 'Digital Twin: Mitigating Unpredictable, Undesirable Emergent Behavior in Complex Systems', in F.-J. Kahlen, S. Flumerfelt, and A. Alves (eds) *Transdisciplinary Perspectives on Complex Systems*. Cham: Springer International Publishing, pp. 85–113. Available at: https://doi.org/10.1007/978-3-319-38756-7_4.

Grieves, M.W. (2005) 'Product lifecycle management: the new paradigm for enterprises', *International Journal of Product Development*, 2(1–2), pp. 71–84. Available at: https://doi.org/10.1504/IJPD.2005.006669.

Guha, A. and Pradhan, K. (2017) 'Secondary motion in three-dimensional branching networks', *Physics of Fluids*, 29(6), p. 063602. Available at: https://doi.org/10.1063/1.4984919.

Gupta, S. *et al.* (2014) 'Quantitative computed tomography–derived clusters: Redefining airway remodeling in asthmatic patients', *Journal of Allergy and Clinical Immunology*, 133(3), pp. 729-738.e18. Available at: https://doi.org/10.1016/j.jaci.2013.09.039.

Hall, G.L. *et al.* (2009) 'Application of a shortened inhaled adenosine-5'-monophosphate challenge in young children using the forced oscillation technique', *Chest*, 136(1), pp. 184–189. Available at: https://doi.org/10.1378/chest.08-2848.

Hall, G.L. *et al.* (2021) 'Official ERS technical standard: Global Lung Function Initiative reference values for static lung volumes in individuals of European ancestry', *European Respiratory Journal*, 57(3), p. 2000289. Available at: https://doi.org/10.1183/13993003.00289-2020.

Han, P. *et al.* (2022) 'Upregulated expression of substance P and NK1R in blood monocytes and B cells of patients with allergic rhinitis and asthma', *Clinical and Experimental Immunology*, 210(1), pp. 39–52. Available at: https://doi.org/10.1093/cei/uxac074.

Hantos, Z. (2021) 'Intra-breath oscillometry for assessing respiratory outcomes', *Current Opinion in Physiology*, 22, p. 100441. Available at: https://doi.org/10.1016/j.cophys.2021.05.004.

Hardman, J.G. *et al.* (1998) 'A physiology simulator: validation of its respiratory components and its ability to predict the patient's response to changes in mechanical ventilation', *British*

Journal of Anaesthesia, 81(3), pp. 327–332. Available at: https://doi.org/10.1093/bja/81.3.327.

Hart, M.C., Orzalesi, M.M. and Cook, C.D. (1963) 'Relation between anatomic respiratory dead space and body size and lung volume', *Journal of Applied Physiology* [Preprint]. Available at: https://doi.org/10.1152/jappl.1963.18.3.519.

Hedges, K.L. and Tawhai, M.H. (2016) 'Simulation of Forced Expiration in a Biophysical Model, With Homogeneous and Clustered Bronchoconstriction', *Journal of Biomechanical Engineering*, 138(6). Available at: https://doi.org/10.1115/1.4033475.

Heinrich, V. *et al.* (2001) 'Elastic thickness compressibilty of the red cell membrane.', *Biophysical Journal*, 81(3), pp. 1452–1463.

Hernandez, G. *et al.* (2019) 'EuroQol (EQ-5D-5L) Validity in Assessing the Quality of Life in Adults With Asthma: Cross-Sectional Study', *Journal of Medical Internet Research*, 21(1), p. e10178. Available at: https://doi.org/10.2196/10178.

Hofmann, J.J. *et al.* (2024) 'Review of quantitative and functional lung imaging evidence of vaping-related lung injury', *Frontiers in Medicine*, 11. Available at: https://doi.org/10.3389/fmed.2024.1285361.

Hogg, J.C., Macklem, P.T. and Thurlbeck, W.M. (1968) 'Site and nature of airway obstruction in chronic obstructive lung disease', *The New England Journal of Medicine*, 278(25), pp. 1355–1360. Available at: https://doi.org/10.1056/NEJM196806202782501.

Hsia, C.C.W. (2006) 'Quantitative morphology of compensatory lung growth', *European Respiratory Review*, 15(101), pp. 148–156. Available at: https://doi.org/10.1183/09059180.00010105.

Hsia, C.C.W., Hyde, D.M. and Weibel, E.R. (2016) 'Lung Structure and the Intrinsic Challenges of Gas Exchange', *Comprehensive Physiology*, 6(2), pp. 827–895. Available at: https://doi.org/10.1002/cphy.c150028.

Huang, C. *et al.* (2020) 'Innate-like Lymphocytes and Innate Lymphoid Cells in Asthma', *Clinical Reviews in Allergy & Immunology*, 59(3), pp. 359–370. Available at: https://doi.org/10.1007/s12016-019-08773-6.

Hughes, J.M.B. and Pride, N.B. (2012) 'Examination of the Carbon Monoxide Diffusing Capacity (DlCO) in Relation to Its Kco and Va Components', *American Journal of*

Respiratory and Critical Care Medicine, 186(2), pp. 132–139. Available at: https://doi.org/10.1164/rccm.201112-2160CI.

Hunter, P. *et al.* (2010) 'A vision and strategy for the virtual physiological human in 2010 and beyond', *Philosophical Transactions of the Royal Society A: Mathematical, Physical and Engineering Sciences* [Preprint]. Available at: https://doi.org/10.1098/rsta.2010.0048.

Hurtado, D.E., Avilés-Rojas, N. and Concha, F. (2023) 'Multiscale modeling of lung mechanics: From alveolar microstructure to pulmonary function', *Journal of the Mechanics and Physics of Solids*, 179, p. 105364. Available at: https://doi.org/10.1016/j.jmps.2023.105364.

Imahashi, Y. and Kanazawa, H. (2014) 'Analysis of the Contributing Factors to Airway Hyperresponsiveness by a Forced Oscillation Technique in Patients with Asthma'.

Ismail, M., Comerford, A. and Wall, W.A. (2013) 'Coupled and reduced dimensional modeling of respiratory mechanics during spontaneous breathing', *International Journal for Numerical Methods in Biomedical Engineering*, 29(11), pp. 1285–1305. Available at: https://doi.org/10.1002/cnm.2577.

Janson, C. *et al.* (2019) 'Bronchodilator reversibility in asthma and COPD: findings from three large population studies', *European Respiratory Journal*, 54(3). Available at: https://doi.org/10.1183/13993003.00561-2019.

Jason H.T. Bates (2009) *Lung Mechanics*. Available at: https://www.cambridge.org/core/books/lung-mechanics/D95220907DAF0A264FA80925AE5E1127 (Accessed: 12 August 2025).

Jing, Z.-C. *et al.* (2009) 'Pulmonary function testing in patients with pulmonary arterial hypertension', *Respiratory Medicine*, 103(8), pp. 1136–1142. Available at: https://doi.org/10.1016/j.rmed.2009.03.009.

Johnson, D.C. (2000) 'Importance of adjusting carbon monoxide diffusing capacity (DLCO) and carbon monoxide transfer coefficient (K CO) for alveolar volume', *Respiratory Medicine*, 94(1), pp. 28–37. Available at: https://doi.org/10.1053/rmed.1999.0740.

Jones, P.W. *et al.* (1992) 'A self-complete measure of health status for chronic airflow limitation. The St. George's Respiratory Questionnaire', *The American Review of Respiratory Disease*, 145(6), pp. 1321–1327. Available at: https://doi.org/10.1164/ajrccm/145.6.1321.

Juniper, E.F. *et al.* (1999) 'Development and validation of a questionnaire to measure asthma control', *European Respiratory Journal*, 14(4), pp. 902–907. Available at: https://doi.org/10.1034/j.1399-3003.1999.14d29.x.

Juniper, E.F. *et al.* (2005) 'Measurement properties and interpretation of three shortened versions of the asthma control questionnaire', *Respiratory Medicine*, 99(5), pp. 553–558. Available at: https://doi.org/10.1016/j.rmed.2004.10.008.

Kaczka, D.W. *et al.* (1997) 'Partitioning airway and lung tissue resistances in humans: effects of bronchoconstriction', *Journal of Applied Physiology (Bethesda, Md.: 1985)*, 82(5), pp. 1531–1541. Available at: https://doi.org/10.1152/jappl.1997.82.5.1531.

Kalliola, S. *et al.* (2014) 'Assessing direct and indirect airway hyperresponsiveness in children using impulse oscillometry', *Annals of Allergy, Asthma & Immunology: Official Publication of the American College of Allergy, Asthma, & Immunology*, 113(2), pp. 166–172. Available at: https://doi.org/10.1016/j.anai.2014.04.026.

Kaminsky, D.A. *et al.* (2022) 'Clinical significance and applications of oscillometry', *European Respiratory Review*, 31(163). Available at: https://doi.org/10.1183/16000617.0208-2021.

Katsoulakis, E. *et al.* (2024) 'Digital twins for health: a scoping review', *npj Digital Medicine*, 7(1), p. 77. Available at: https://doi.org/10.1038/s41746-024-01073-0.

Ke, J. *et al.* (2023) 'Associations of complete blood cell count-derived inflammatory biomarkers with asthma and mortality in adults: a population-based study', *Frontiers in Immunology*, 14, p. 1205687. Available at: https://doi.org/10.3389/fimmu.2023.1205687.

Keener, J. and Sneyd, J. (eds) (2009) *Mathematical Physiology*. New York, NY: Springer (Interdisciplinary Applied Mathematics). Available at: https://doi.org/10.1007/978-0-387-75847-3.

Kim, S.R. *et al.* (2020) 'Application of Impulse Oscillometry in Adult Asthmatic Patients With Preserved Lung Function', *Allergy, Asthma & Immunology Research*, 12(5), pp. 832–843. Available at: https://doi.org/10.4168/aair.2020.12.5.832.

King, G.G. *et al.* (2020) 'Technical standards for respiratory oscillometry', *European Respiratory Journal*, 55(2). Available at: https://doi.org/10.1183/13993003.00753-2019.

Kleinstreuer, C. and Zhang, Z. (2010) 'Airflow and Particle Transport in the Human Respiratory System', *Annual Review of Fluid Mechanics*, 42(Volume 42, 2010), pp. 301–334. Available at: https://doi.org/10.1146/annurev-fluid-121108-145453.

Koo, H.-K. *et al.* (2018) 'Small airways disease in mild and moderate chronic obstructive pulmonary disease: a cross-sectional study', *The Lancet. Respiratory Medicine*, 6(8), pp. 591–602. Available at: https://doi.org/10.1016/S2213-2600(18)30196-6.

Koshiyama, K. and Wada, S. (2015) 'Mathematical model of a heterogeneous pulmonary acinus structure', *Computers in Biology and Medicine*, 62, pp. 25–32. Available at: https://doi.org/10.1016/j.compbiomed.2015.03.032.

Kraft, M. *et al.* (2022) 'The role of small airway dysfunction in asthma control and exacerbations: a longitudinal, observational analysis using data from the ATLANTIS study', *The Lancet. Respiratory Medicine*, 10(7), pp. 661–668. Available at: https://doi.org/10.1016/S2213-2600(21)00536-1.

Krogh, M. (1915) 'The diffusion of gases through the lungs of man', *The Journal of Physiology*, 49(4), pp. 271–300.

Kumar, H. *et al.* (2013) 'Multiscale imaging and registration-driven model for pulmonary acinar mechanics in the mouse', *Journal of Applied Physiology (Bethesda, Md.: 1985)*, 114(8), pp. 971–978. Available at: https://doi.org/10.1152/japplphysiol.01136.2012.

Kuo, C., Jabbal, S. and Lipworth, B. (2019) 'I say IOS you say AOS: comparative bias in respiratory impedance measurements', *Lung*, 197(4), pp. 473–481. Available at: https://doi.org/10.1007/s00408-019-00247-y.

Lam, T. *et al.* (2025) 'A multidisciplinary approach towards modeling of a virtual human lung', *npj Systems Biology and Applications*, 11(1), p. 38. Available at: https://doi.org/10.1038/s41540-025-00517-x.

Lamas, D.J. *et al.* (2011) 'Delayed Access and Survival in Idiopathic Pulmonary Fibrosis: A Cohort Study', *American Journal of Respiratory and Critical Care Medicine*, 184(7), pp. 842–847. Available at: https://doi.org/10.1164/rccm.201104-0668OC.

Lambert, R.K. *et al.* (1982) 'A computational model for expiratory flow', *Journal of Applied Physiology*, 52(1), pp. 44–56. Available at: https://doi.org/10.1152/jappl.1982.52.1.44.

Lambert, R.K. and Beck, K.C. (2004) 'Airway area distribution from the forced expiration maneuver', *Journal of Applied Physiology (Bethesda, Md.: 1985)*, 97(2), pp. 570–578. Available at: https://doi.org/10.1152/japplphysiol.00912.2003.

Leiby, K.L., Raredon, M.S.B. and Niklason, L.E. (2020) 'Bioengineering the Blood-gas Barrier', *Comprehensive Physiology*, 10(2), pp. 415–452. Available at: https://doi.org/10.1002/cphy.c190026.

Lewis, B.M. *et al.* (1958) 'The measurement of pulmonary capillary blood volume and pulmonary membrane diffusing capacity in normal subjects; the effects of exercise and position', *The Journal of Clinical Investigation*, 37(7), pp. 1061–1070. Available at: https://doi.org/10.1172/JCI103687.

Li, X. *et al.* (2025) 'Digital twins as global learning health and disease models for preventive and personalized medicine', *Genome Medicine*, 17(1), p. 11. Available at: https://doi.org/10.1186/s13073-025-01435-7.

Li, Yuer *et al.* (2023) 'FVC/DLCO identifies pulmonary hypertension and predicts 5-year all-cause mortality in patients with COPD', *European Journal of Medical Research*, 28, p. 174. Available at: https://doi.org/10.1186/s40001-023-01130-6.

Litmanovich, D.E. *et al.* (2014) 'Multidetector Computed Tomographic Imaging in Chronic Obstructive Pulmonary Disease: Emphysema and Airways Assessment', *Radiologic Clinics of North America*, 52(1), pp. 137–154. Available at: https://doi.org/10.1016/j.rcl.2013.09.002.

Lu, L. *et al.* (2025) 'Associations of small airway dysfunction assessed by impulse oscillometry with lung function decline and exacerbations in participants with chronic obstructive pulmonary disease: A prospective cohort study in China', *Respiratory Medicine*, 241, p. 108075. Available at: https://doi.org/10.1016/j.rmed.2025.108075.

Lumb, A. and Thomas, C. (2021a) 'Distribution of pulmonary ventilation and perfusion', in L. Andrew and T. Caroline (eds) *Nunn and Lumb's Applied Respiratory Physiology*. Ninth Edition, pp. 88-110.e3. Available at: https://doi.org/10.1016/B978-0-7020-7908-5.00016-3.

Lumb, A. and Thomas, C. (2021b) *Elastic forces and lung volumes - Nunn and Lumb's Applied Respiratory Physiology - ClinicalKey Student*. Available at: https://www.clinicalkey.com/student/content/book/3-s2.0-B9780702079085000114 (Accessed: 4 June 2025).

Lumb, A. and Thomas, C. (2021c) *Nunn and Lumb's Applied Respiratory Physiology, Ninth Edition - ClinicalKey Student*. Available at:

https://www.clinicalkey.com/student/content/toc/3-s2.0-C20180006702 (Accessed: 22 March 2024).

Luo, X.Y. *et al.* (2004) 'LES modelling of flow in a simple airway model', *Medical Engineering & Physics*, 26(5), pp. 403–413. Available at: https://doi.org/10.1016/j.medengphy.2004.02.008.

Lutfi, M.F. (2017) 'The physiological basis and clinical significance of lung volume measurements', *Multidisciplinary Respiratory Medicine*, 12(1), p. 3. Available at: https://doi.org/10.1186/s40248-017-0084-5.

Malmberg, L.P. *et al.* (2008) 'Exercise-induced changes in respiratory impedance in young wheezy children and nonatopic controls', *Pediatric Pulmonology*, 43(6), pp. 538–544. Available at: https://doi.org/10.1002/ppul.20805.

Mannino, D.M. (2015) 'Biomarkers in COPD: the search continues!', *European Respiratory Journal*, 45(4), pp. 872–874. Available at: https://doi.org/10.1183/09031936.00236314.

Manoharan, A. *et al.* (2014) 'Small airway dysfunction is associated with poorer asthma control', *The European Respiratory Journal*, 44(5), pp. 1353–1355. Available at: https://doi.org/10.1183/09031936.00082314.

Mansur, A.H., Manney, S. and Ayres, J.G. (2008) 'Methacholine-induced asthma symptoms correlate with impulse oscillometry but not spirometry', *Respiratory Medicine*, 102(1), pp. 42–49. Available at: https://doi.org/10.1016/j.rmed.2007.08.007.

Mapel, D.W. *et al.* (2011) 'Severity of COPD at initial spirometry-confirmed diagnosis: data from medical charts and administrative claims', *International Journal of Chronic Obstructive Pulmonary Disease*, 6, pp. 573–581. Available at: https://doi.org/10.2147/COPD.S16975.

Marchal, F. and Hall, G.L. (2010) 'Forced oscillation technique', *Paediatric Lung Function*. European Respiratory Society, pp. 121–136. Available at: https://doi.org/10.1183/1025448x.00012109.

Marin, M.J. *et al.* (2024) 'An Introduction to the Complete Blood Count for Clinical Chemists: Red Blood Cells', *The Journal of Applied Laboratory Medicine*, 9(5), pp. 1025–1039. Available at: https://doi.org/10.1093/jalm/jfae031.

Matheson, A.M. *et al.* (2022) 'Persistent 129Xe MRI Pulmonary and CT Vascular Abnormalities in Symptomatic Individuals with Post-acute COVID-19 Syndrome', *Radiology*, 305(2), pp. 466–476. Available at: https://doi.org/10.1148/radiol.220492.

McClean, M.A. *et al.* (2011) 'Cut-points for response to mannitol challenges using the forced oscillation technique', *Respiratory Medicine*, 105(4), pp. 533–540. Available at: https://doi.org/10.1016/j.rmed.2010.10.013.

McGrath, M.W. and Thomson, M.L. (1959) 'The effect of age, body size and lung volume change on alveolar-capillary permeability and diffusing capacity in man', *The Journal of Physiology*, 146(3), pp. 572–582.

McIntosh, M.J. *et al.* (2023) '129Xe MRI Ventilation Defects in Asthma: What is the Upper Limit of Normal and Minimal Clinically Important Difference?', *Academic Radiology*, 30(12), pp. 3114–3123. Available at: https://doi.org/10.1016/j.acra.2023.03.010.

Meyer, F. *et al.* (2002) 'Peripheral airway obstruction in primary pulmonary hypertension', *Thorax*, 57(6), pp. 473–476. Available at: https://doi.org/10.1136/thorax.57.6.473.

Miller, M.R. *et al.* (2005) 'Standardisation of spirometry', *European Respiratory Journal*, 26(2), pp. 319–338. Available at: https://doi.org/10.1183/09031936.05.00034805.

Modi, P. and Cascella, M. (2024) 'Diffusing Capacity Of The Lungs For Carbon Monoxide', *StatPearls*. Treasure Island (FL): StatPearls Publishing. Available at: http://www.ncbi.nlm.nih.gov/books/NBK556149/ (Accessed: 22 March 2024).

Momtazmanesh, S. *et al.* (2023) 'Global burden of chronic respiratory diseases and risk factors, 1990–2019: an update from the Global Burden of Disease Study 2019', *eClinicalMedicine*, 59, p. 101936. Available at: https://doi.org/10.1016/j.eclinm.2023.101936.

Montesantos, S. *et al.* (2013) 'Airway Morphology From High Resolution Computed Tomography in Healthy Subjects and Patients With Moderate Persistent Asthma', *The Anatomical Record*, 296(6), pp. 852–866. Available at: https://doi.org/10.1002/ar.22695.

Moore, V.C. (2012) 'Spirometry: step by step', *Breathe*, 8(3), pp. 232–240. Available at: https://doi.org/10.1183/20734735.0021711.

Mori, K. *et al.* (2011) 'Colored 3-dimensional analyses of respiratory resistance and reactance in COPD and asthma', *COPD*, 8(6), pp. 456–463. Available at: https://doi.org/10.3109/15412555.2011.626818.

Morton, S.E. *et al.* (2018) 'A virtual patient model for mechanical ventilation', *Computer Methods and Programs in Biomedicine*, 165, pp. 77–87. Available at: https://doi.org/10.1016/j.cmpb.2018.08.004.

Myrianthefs, P. and Baltopoulos, G. (2013) 'A Higher Tidal Volume May Be Used for Athletes according to Measured FVC', *The Scientific World Journal*, 2013, p. 526138. Available at: https://doi.org/10.1155/2013/526138.

Nair, A., Ward, J. and Lipworth, B.J. (2011) 'Comparison of bronchodilator response in patients with asthma and healthy subjects using spirometry and oscillometry', *Annals of Allergy, Asthma & Immunology*, 107(4), pp. 317–322. Available at: https://doi.org/10.1016/j.anai.2011.07.011.

Naji, N. *et al.* (2013) 'Comparison of changes in lung function measured by plethymography and IOS after bronchoprovocation', *Respiratory Medicine*, 107(4), pp. 503–510. Available at: https://doi.org/10.1016/j.rmed.2012.12.022.

National Academies of Sciences, Engineering, and Medicine (2023) *Opportunities and Challenges for Digital Twins in Biomedical Research: Proceedings of a Workshop–in Brief | The National Academies Press*. Available at: https://nap.nationalacademies.org/catalog/26922/opportunities-and-challenges-for-digital-twins-in-biomedical-research-proceedings (Accessed: 11 August 2025).

Neelakantan, S. *et al.* (2022) 'Computational lung modelling in respiratory medicine', *Journal of the Royal Society Interface*, 19(191), p. 20220062. Available at: https://doi.org/10.1098/rsif.2022.0062.

Network, B.T.S.S.I.G. (2008) 'British Guideline on the Management of Asthma', *Thorax*, 63(Suppl 4), pp. iv1–iv121. Available at: https://doi.org/10.1136/thx.2008.097741.

Nielsen, K.G. and Bisgaard, H. (2000) 'The effect of inhaled budesonide on symptoms, lung function, and cold air and methacholine responsiveness in 2- to 5-year-old asthmatic children', *American Journal of Respiratory and Critical Care Medicine*, 162(4 Pt 1), pp. 1500–1506. Available at: https://doi.org/10.1164/ajrccm.162.4.2002019.

Oakes, J.M. *et al.* (2014) 'Airflow and particle deposition simulations in health and emphysema: from in vivo to in silico animal experiments', *Annals of Biomedical Engineering*, 42(4), pp. 899–914. Available at: https://doi.org/10.1007/s10439-013-0954-8.

Ochs, M. *et al.* (2004) 'The number of alveoli in the human lung', *American Journal of Respiratory and Critical Care Medicine*, 169(1), pp. 120–124. Available at: https://doi.org/10.1164/rccm.200308-1107OC.

Oliveira, C.L.N. *et al.* (2016) 'Entropy Production and the Pressure–Volume Curve of the Lung', *Frontiers in Physiology*, 7. Available at: https://doi.org/10.3389/fphys.2016.00073.

Oostveen, E. *et al.* (2003) 'The forced oscillation technique in clinical practice: methodology, recommendations and future developments', *European Respiratory Journal*, 22(6), pp. 1026–1041. Available at: https://doi.org/10.1183/09031936.03.00089403.

Orchard, C.H., Sanchez de Leon, R. and Sykes, M.K. (1983) 'The relationship between hypoxic pulmonary vasoconstriction and arterial oxygen tension in the intact dog.', *The Journal of Physiology*, 338, pp. 61–74. Available at: https://doi.org/10.1113/jphysiol.1983.sp014660.

O'Sullivan-Murphy, B., Driehuys, B. and Mammarappallil, J. (2022) 'MR Imaging for the Evaluation of Diffuse Lung Disease: Where Are We?', *Radiologic Clinics of North America*, 60(6), pp. 1021–1032. Available at: https://doi.org/10.1016/j.rcl.2022.06.007.

Paplinska-Goryca, M. *et al.* (2020) 'The Expressions of TSLP, IL-33, and IL-17A in Monocyte Derived Dendritic Cells from Asthma and COPD Patients are Related to Epithelial–Macrophage Interactions', *Cells*, 9(9), p. 1944. Available at: https://doi.org/10.3390/cells9091944.

Paredi, P. *et al.* (2010) 'Comparison of inspiratory and expiratory resistance and reactance in patients with asthma and chronic obstructive pulmonary disease', *Thorax*, 65(3), pp. 263–267. Available at: https://doi.org/10.1136/thx.2009.120790.

Park, H. *et al.* (2024) *Diffusing capacity as an independent predictor of acute exacerbations in chronic obstructive pulmonary disease | Scientific Reports*. Available at: https://www.nature.com/articles/s41598-024-51593-8 (Accessed: 17 June 2024).

Park, S.-W. *et al.* (2012) 'Air trapping is a major determinant of persistent airway obstruction in asthmatics', *Respiratory Medicine*, 106(6), pp. 786–793. Available at: https://doi.org/10.1016/j.rmed.2012.02.012.

Patte, C., Genet, M. and Chapelle, D. (2022) 'A quasi-static poromechanical model of the lungs', *Biomechanics and Modeling in Mechanobiology*, 21(2), pp. 527–551. Available at: https://doi.org/10.1007/s10237-021-01547-0.

Peacock, A.J. (1998) 'Oxygen at high altitude', *BMJ : British Medical Journal*, 317(7165), pp. 1063–1066.

Pellegrino, R. *et al.* (2005) 'Interpretative strategies for lung function tests', *European Respiratory Journal*, 26(5), pp. 948–968. Available at: https://doi.org/10.1183/09031936.05.00035205.

Pennati, F. *et al.* (2023) 'Micro-CT-derived ventilation biomarkers for the longitudinal assessment of pathology and response to therapy in a mouse model of lung fibrosis', *Scientific Reports*, 13(1), p. 4462. Available at: https://doi.org/10.1038/s41598-023-30402-8.

Pennati, F. *et al.* (2024) 'Multiphase micro-computed tomography reconstructions provide dynamic respiratory function in a mouse lung fibrosis model', *iScience*, 27(3), p. 109262. Available at: https://doi.org/10.1016/j.isci.2024.109262.

Petersson, J. and Glenny, R.W. (2014) 'Gas exchange and ventilation–perfusion relationships in the lung', *European Respiratory Journal*, 44(4), pp. 1023–1041. Available at: https://doi.org/10.1183/09031936.00037014.

Piascik, B *et al.* (2010) 'Materials, Structures, Mechanical Systems, andManufacturing Roadmap – Technology Area 12'.

Pilgrim-Morris, J.H. *et al.* (2025) 'A framework for modelling whole-lung and regional transfer factor of the lung for carbon monoxide using hyperpolarised xenon-129 lung magnetic resonance imaging', *ERJ open research*, 11(1), pp. 00442–02024. Available at: https://doi.org/10.1183/23120541.00442-2024.

Porsbjerg, C. *et al.* (2023) 'Asthma', *Lancet (London, England)*, 401(10379), pp. 858–873. Available at: https://doi.org/10.1016/S0140-6736(22)02125-0.

Postma, D.S. *et al.* (2019) 'Exploring the relevance and extent of small airways dysfunction in asthma (ATLANTIS): baseline data from a prospective cohort study', *The Lancet Respiratory Medicine*, 7(5), pp. 402–416. Available at: https://doi.org/10.1016/S2213-2600(19)30049-9.

Pozin, N. *et al.* (2017) 'A tree-parenchyma coupled model for lung ventilation simulation', *International Journal for Numerical Methods in Biomedical Engineering*, 33(11). Available at: https://doi.org/10.1002/cnm.2873.

Pugashetti, J.V. *et al.* (2023) 'Validation of Proposed Criteria for Progressive Pulmonary Fibrosis', *American Journal of Respiratory and Critical Care Medicine*, 207(1), pp. 69–76. Available at: https://doi.org/10.1164/rccm.202201-0124OC.

Quanjer, Philip H. *et al.* (2012) 'Multi-ethnic reference values for spirometry for the 3–95-yr age range: the global lung function 2012 equations', *European Respiratory Journal*, 40(6), pp. 1324–1343. Available at: https://doi.org/10.1183/09031936.00080312.

Rahimi-Gorji, M. *et al.* (2015) 'CFD simulation of airflow behavior and particle transport and deposition in different breathing conditions through the realistic model of human airways', *Journal of Molecular Liquids*, 209, pp. 121–133. Available at: https://doi.org/10.1016/j.molliq.2015.05.031.

Rastogi, D. *et al.* (2015) 'Inflammation, Metabolic Dysregulation, and Pulmonary Function among Obese Urban Adolescents with Asthma', *American Journal of Respiratory and Critical Care Medicine*, 191(2), pp. 149–160. Available at: https://doi.org/10.1164/rccm.201409-1587OC.

Ravikumar, P. *et al.* (2013) 'Separating in vivo mechanical stimuli for postpneumonectomy compensation: imaging and ultrastructural assessment', *Journal of Applied Physiology*, 114(8), pp. 961–970. Available at: https://doi.org/10.1152/japplphysiol.01394.2012.

Robinson, P.D., Latzin, P. and Gustafsson, P.M. (2010) 'Multiple-breath washout', *Paediatric Lung Function*. European Respiratory Society, pp. 87–104. Available at: https://doi.org/10.1183/1025448x.00011909.

Roth, C.J., Ismail, M., *et al.* (2017) 'A comprehensive computational human lung model incorporating inter-acinar dependencies: Application to spontaneous breathing and mechanical ventilation', *International Journal for Numerical Methods in Biomedical Engineering*, 33(1). Available at: https://doi.org/10.1002/cnm.2787.

Roth, C.J., Yoshihara, L., *et al.* (2017) 'Computational modelling of the respiratory system: Discussion of coupled modelling approaches and two recent extensions', *Computer Methods in Applied Mechanics and Engineering*, 314, pp. 473–493. Available at: https://doi.org/10.1016/j.cma.2016.08.010.

Rozen, D., Bracamonte, M. and Sergysels, R. (1983) 'Comparison between plethysmographic and forced oscillation techniques in the assessment of airflow obstruction', *Respiration; International Review of Thoracic Diseases*, 44(3), pp. 197–203. Available at: https://doi.org/10.1159/000194549.

Sarkar, M., Niranjan, N. and Banyal, P. (2017) 'Mechanisms of hypoxemia', *Lung India : Official Organ of Indian Chest Society*, 34(1), pp. 47–60. Available at: https://doi.org/10.4103/0970-2113.197116.

Schiffers, C. *et al.* (2022) 'Diagnostic work-up of asthma: more than spirometry', *European Respiratory Journal*, 60(suppl 66). Available at: https://doi.org/10.1183/13993003.congress-2022.909.

Schmekel, B. and Smith, H.J. (1997) 'The diagnostic capacity of forced oscillation and forced expiration techniques in identifying asthma by isocapnic hyperpnoea of cold air', *The European Respiratory Journal*, 10(10), pp. 2243–2249. Available at: https://doi.org/10.1183/09031936.97.10102243.

Schulze, J. *et al.* (2012) 'Methacholine challenge in young children as evaluated by spirometry and impulse oscillometry', *Respiratory Medicine*, 106(5), pp. 627–634. Available at: https://doi.org/10.1016/j.rmed.2012.01.007.

Shi, Y. *et al.* (2013) 'Peripheral airway impairment measured by oscillometry predicts loss of asthma control in children', *The Journal of Allergy and Clinical Immunology*, 131(3), pp. 718–723. Available at: https://doi.org/10.1016/j.jaci.2012.09.022.

Shim, S.S. *et al.* (2018) 'Lumen area change (Delta Lumen) between inspiratory and expiratory multidetector computed tomography as a measure of severe outcomes in asthmatic patients', *Journal of Allergy and Clinical Immunology*, 142(6), pp. 1773-1780.e9. Available at: https://doi.org/10.1016/j.jaci.2017.12.1004.

Singh, D. *et al.* (2023) 'Comparison of the Asthma Control Questionnaire and patient diaries in uncontrolled asthma', *ERJ Open Research*, 9(3). Available at: https://doi.org/10.1183/23120541.00104-2023.

Sivova, N. *et al.* (2013) 'Relevance of partitioning DLCO to detect pulmonary hypertension in systemic sclerosis', *PloS One*, 8(10), p. e78001. Available at: https://doi.org/10.1371/journal.pone.0078001.

Smith, H.J., Reinhold, P. and Goldman, M.D. (2005) 'Forced oscillation technique and impulse oscillometry', *Lung Function Testing*. European Respiratory Society, pp. 72–105. Available at: https://doi.org/10.1183/1025448x.00031005.

Soares, M. *et al.* (2018) 'Comparison of Forced and Impulse Oscillometry Measurements: A Clinical Population and Printed Airway Model Study.', *European Respiratory Journal*, 52(suppl 62). Available at: https://doi.org/10.1183/13993003.congress-2018.PA3390.

Soler, X. *et al.* (2018) 'Validity of the Asthma Control Test Questionnaire among Smoking Asthmatics', *The journal of allergy and clinical immunology. In practice*, 6(1), pp. 151–158. Available at: https://doi.org/10.1016/j.jaip.2017.05.010.

Solomon, Y. *et al.* (2022) 'Selected hematological abnormalities and their associated factors among asthmatic patients in Northwest Ethiopia: a cross-sectional study', *BMC Pulmonary Medicine*, 22(1), p. 228. Available at: https://doi.org/10.1186/s12890-022-02020-z.

Sorkness, R.L. *et al.* (2019) 'Compressive air trapping in asthma: effects of age, sex, and severity', *Journal of Applied Physiology*, 126(5), pp. 1265–1271. Available at: https://doi.org/10.1152/japplphysiol.00924.2018.

Spagnolo, P. *et al.* (2021) 'Early diagnosis of fibrotic interstitial lung disease: challenges and opportunities', *The Lancet Respiratory Medicine*, 9(9), pp. 1065–1076. Available at: https://doi.org/10.1016/S2213-2600(21)00017-5.

Stanojevic, S. *et al.* (2017) 'Official ERS technical standards: Global Lung Function Initiative reference values for the carbon monoxide transfer factor for Caucasians', *The European Respiratory Journal*, 50(3), p. 1700010. Available at: https://doi.org/10.1183/13993003.00010-2017.

Stanojevic, S. *et al.* (2022) 'ERS/ATS technical standard on interpretive strategies for routine lung function tests', *European Respiratory Journal*, 60(1). Available at: https://doi.org/10.1183/13993003.01499-2021.

Stanojevic, S., Bowerman, C. and Robinson, P. (2021) 'Multiple breath washout: measuring early manifestations of lung pathology', *Breathe*, 17(3), p. 210016. Available at: https://doi.org/10.1183/20734735.0016-2021.

Stern, J., Pier, J. and Litonjua, A.A. (2020) 'Asthma epidemiology and risk factors', *Seminars in Immunopathology*, 42(1), pp. 5–15. Available at: https://doi.org/10.1007/s00281-020-00785-1.

Strohl, K.P., Butler, J.P. and Malhotra, A. (2012) 'Mechanical Properties of the Upper Airway', *Comprehensive Physiology*, 2(3), pp. 1853–1872. Available at: https://doi.org/10.1002/cphy.c110053.

Subbarao, P. *et al.* (2015) 'Multiple-Breath Washout as a Lung Function Test in Cystic Fibrosis. A Cystic Fibrosis Foundation Workshop Report', *Annals of the American Thoracic Society*, 12(6), pp. 932–939. Available at: https://doi.org/10.1513/AnnalsATS.201501-021FR.

Sun, X.-G. *et al.* (2003) 'Pulmonary function in primary pulmonary hypertension', *Journal of the American College of Cardiology*, 41(6), pp. 1028–1035. Available at: https://doi.org/10.1016/S0735-1097(02)02964-9.

Sundbaum, J.K. *et al.* (2024) 'The Asthma Control Test as a predictive tool for hospitalization and death', *European Respiratory Journal*, 64(suppl 68). Available at: https://doi.org/10.1183/13993003.congress-2024.OA3766.

Suzuki, S. *et al.* (1984) 'Time-course of response in exercise-induced bronchoconstriction', *Annals of Allergy*, 53(4), pp. 341–346.

Svenningsen, S. *et al.* (2016) 'Is ventilation heterogeneity related to asthma control?', *European Respiratory Journal*, 48(2), pp. 370–379. Available at: https://doi.org/10.1183/13993003.00393-2016.

Sylvester, K.P. *et al.* (2020) 'ARTP statement on pulmonary function testing 2020', *BMJ Open Respiratory Research*, 7(1), p. e000575. Available at: https://doi.org/10.1136/bmjresp-2020-000575.

Szentes, B. *et al.* (2019) 'How does EQ-5D-5L perform in asthma patients?', *European Respiratory Journal*, 54(suppl 63). Available at: https://doi.org/10.1183/13993003.congress-2019.PA1968.

Szentes, B.L. *et al.* (2020) 'How does the EQ-5D-5L perform in asthma patients compared with an asthma-specific quality of life questionnaire?', *BMC Pulmonary Medicine*, 20(1), p. 168. Available at: https://doi.org/10.1186/s12890-020-01205-8.

Tanimura, K. *et al.* (2014) 'Comparison of two devices for respiratory impedance measurement using a forced oscillation technique: basic study using phantom models', *The Journal of Physiological Sciences*, 64(5), pp. 377–382. Available at: https://doi.org/10.1007/s12576-014-0329-4.

Tárnoki, D.L. *et al.* (2024) 'Lung imaging methods: indications, strengths and limitations', *Breathe*, 20(3), p. 230127. Available at: https://doi.org/10.1183/20734735.0127-2023.

Tashkin, D.P. *et al.* (2008) 'A 4-year trial of tiotropium in chronic obstructive pulmonary disease', *The New England Journal of Medicine*, 359(15), pp. 1543–1554. Available at: https://doi.org/10.1056/NEJMoa0805800.

Tawhai, M.H. and Bates, J.H.T. (2015) 'Computational models of lung diseases', *Drug Discovery Today: Disease Models*, 15, pp. 1–2. Available at: https://doi.org/10.1016/j.ddmod.2015.01.001.

Tawhai, M.H., Hoffman, E.A. and Lin, C.-L. (2009) 'The lung physiome: merging imaging-based measures with predictive computational models', *Wiley Interdisciplinary Reviews. Systems Biology and Medicine*, 1(1), pp. 61–72. Available at: https://doi.org/10.1002/wsbm.17.

Tawhai, M.H. and Lin, C.-L. (2010) 'Image-based modeling of lung structure and function', *Journal of magnetic resonance imaging : JMRI*, 32(6), pp. 1421–1431. Available at: https://doi.org/10.1002/jmri.22382.

The EuroQol Group (1990) 'EuroQol - a new facility for the measurement of health-related quality of life', *Health Policy*, 16(3), pp. 199–208. Available at: https://doi.org/10.1016/0168-8510(90)90421-9.

Thurston, G.B. (1952) 'Periodic Fluid Flow Through Circular Tubes', *The Journal of the Acoustical Society of America*, 24(6), pp. 653–656. Available at: https://doi.org/10.1121/1.1906949.

Trinick, R., Southern, K.W. and McNamara, P.S. (2012) 'Assessing the Liverpool Respiratory Symptom Questionnaire in children with cystic fibrosis', *European Respiratory Journal*, 39(4), pp. 899–905. Available at: https://doi.org/10.1183/09031936.00070311.

Tsuburai, T. *et al.* (2012) '[Use of forced oscillation technique to detect airflow limitations in adult Japanese asthmatics]', *Arerugi = [Allergy]*, 61(2), pp. 184–193.

Tsurikisawa, N. *et al.* (2015) 'Physiologic Airway Responses to Inhaled Histamine and Acetylcholine in Patients with Mild Asthma as Analyzed by Forced Oscillation', *Arerugi*, 64(7), pp. 952–970. Available at: https://doi.org/10.15036/arerugi.64.952.

Tuza, F.A. d´Alegria *et al.* (2020) 'Combined forced oscillation and fractional-order modeling in patients with work-related asthma: a case–control study analyzing respiratory biomechanics and diagnostic accuracy', *BioMedical Engineering OnLine*, 19(1), p. 93. Available at: https://doi.org/10.1186/s12938-020-00836-6.

Uematsu, M. *et al.* (2018) 'Association of Asthma Control Test (ACT) and Asthma Control Questionnaire (ACQ) with asthma exacerbation', *European Respiratory Journal*, 52(suppl 62). Available at: https://doi.org/10.1183/13993003.congress-2018.PA4436.

Usmani, O.S. *et al.* (2021) 'Seven Pillars of Small Airways Disease in Asthma and COPD: Supporting Opportunities for Novel Therapies', *Chest*, 160(1), pp. 114–134. Available at: https://doi.org/10.1016/j.chest.2021.03.047.

Van Noord, J.A. *et al.* (1989) 'Total Respiratory Resistance and Reactance as a Measurement of Response to Bronchial Challenge with Histamine', *American Review of Respiratory Disease*, 139(4), pp. 921–926. Available at: https://doi.org/10.1164/ajrccm/139.4.921.

Van Noord, J.A. *et al.* (1991) 'Total respiratory resistance and reactance in patients with asthma, chronic bronchitis, and emphysema', *The American Review of Respiratory Disease*, 143(5 Pt 1), pp. 922–927. Available at: https://doi.org/10.1164/ajrccm/143.5_Pt_1.922.

Van Sint Jan, S. and Geris, L. (2019) 'Modelling towards a more holistic medicine: The Virtual Physiological Human (VPH)', *Morphologie*, 103(343), pp. 127–130. Available at: https://doi.org/10.1016/j.morpho.2019.10.044.

Veneroni, C. *et al.* (2024) 'Diagnostic Potential of Oscillometry: A Population-based Approach', *American Journal of Respiratory and Critical Care Medicine*, 209(4), pp. 444–453. Available at: https://doi.org/10.1164/rccm.202306-0975OC.

Ventura, V. *et al.* (2023) 'Effect of Ambulatory Oxygen on the Respiratory Pattern during the 6 Min Walking Test in Patients with Interstitial Lung Diseases', *Biomedicines*, 11(7), p. 1834. Available at: https://doi.org/10.3390/biomedicines11071834.

Vestbo, J. *et al.* (2016) 'Fluticasone furoate and vilanterol and survival in chronic obstructive pulmonary disease with heightened cardiovascular risk (SUMMIT): a double-blind randomised controlled trial', *Lancet (London, England)*, 387(10030), pp. 1817–1826. Available at: https://doi.org/10.1016/S0140-6736(16)30069-1.

Viceconti, M. and Hunter, P. (2016) 'The Virtual Physiological Human: Ten Years After', *Annual Review of Biomedical Engineering*, 18(Volume 18, 2016), pp. 103–123. Available at: https://doi.org/10.1146/annurev-bioeng-110915-114742.

Wagner, P.D. (1981) 'Estimation of distributions of ventilation/perfusion ratios', *Annals of Biomedical Engineering*, 9(5), pp. 543–556. Available at: https://doi.org/10.1007/BF02364770.

Wall, W.A. and Rabczuk, T. (2008) 'Fluid–structure interaction in lower airways of CT-based lung geometries', *International Journal for Numerical Methods in Fluids*, 57(5), pp. 653–675. Available at: https://doi.org/10.1002/fld.1763.

Wang, W. *et al.* (2014) 'Can computer simulators accurately represent the pathophysiology of individual COPD patients?', *Intensive Care Medicine Experimental*, 2(1), p. 23. Available at: https://doi.org/10.1186/s40635-014-0023-0.

Weaver, L. *et al.* (2021) 'High risk of patient self-inflicted lung injury in COVID-19 with frequently encountered spontaneous breathing patterns: a computational modelling study', *Annals of Intensive Care*, 11(1), p. 109. Available at: https://doi.org/10.1186/s13613-021-00904-7.

Weibel, E.R. (2009) 'What makes a good lung?', *Swiss Medical Weekly*, 139(2728), pp. 375–386. Available at: https://doi.org/10.4414/smw.2009.12270.

Weibel, E.R. and Gomez, D.M. (1962) 'Architecture of the human lung. Use of quantitative methods establishes fundamental relations between size and number of lung structures', *Science (New York, N.Y.)*, 137(3530), pp. 577–585. Available at: https://doi.org/10.1126/science.137.3530.577.

Weibel, E.R. and Knight, B.W. (1964) 'A MORPHOMETRIC STUDY ON THE THICKNESS OF THE PULMONARY AIR-BLOOD BARRIER', *The Journal of Cell Biology*, 21(3), pp. 367–384. Available at: https://doi.org/10.1083/jcb.21.3.367.

Wesseling, G.J., Vanderhoven-Augustin, I.M. and Wouters, E.F. (1993) 'Forced oscillation technique and spirometry in cold air provocation tests', *Thorax*, 48(3), pp. 254–259. Available at: https://doi.org/10.1136/thx.48.3.254.

West, J.B., Dollery, C.T. and Naimark, A. (1964) 'Distribution of blood flow in isolated lung; relation to vascular and alveolar pressures', *Journal of Applied Physiology*, 19(4), pp. 713–724. Available at: https://doi.org/10.1152/jappl.1964.19.4.713.

Woolcock, A.J. and Read, J. (1966) 'Lung volumes in exacerbations of asthma', *The American Journal of Medicine*, 41(2), pp. 259–273. Available at: https://doi.org/10.1016/0002-9343(66)90021-0.

Wouters, E.F. *et al.* (1988) 'Contribution of impedance measurement of the respiratory system to bronchial challenge tests', *The Journal of Asthma: Official Journal of the Association for the Care of Asthma*, 25(5), pp. 259–267. Available at: https://doi.org/10.3109/02770908809073211.

Wyrwich, K.W. *et al.* (2011) 'Validation and agreement across four versions of the asthma control questionnaire in patients with persistent asthma', *Respiratory Medicine*, 105(5), pp. 698–712. Available at: https://doi.org/10.1016/j.rmed.2010.11.004.

Xiao, L. *et al.* (2013) 'A semiautomatic segmentation algorithm for extracting the complete structure of acini from synchrotron micro-CT images', *Computational and Mathematical Methods in Medicine*, 2013, p. 575086. Available at: https://doi.org/10.1155/2013/575086.

Yamada, Y. *et al.* (2020) 'Comparison of inspiratory and expiratory lung and lobe volumes among supine, standing, and sitting positions using conventional and upright CT', *Scientific Reports*, 10, p. 16203. Available at: https://doi.org/10.1038/s41598-020-73240-8.

Yamamoto, M. and Shimizu, K. (2025) 'Clinical interpretation of DLCO and KCO: From rationale to clinical and research applications', *Respiratory Investigation*, 63(3), pp. 358–364. Available at: https://doi.org/10.1016/j.resinv.2025.02.007.

Yang, S.-C. and Lin, B.-Y. (2010) 'Comparison of airway hyperreactivity in chronic obstructive pulmonary disease and asthma', *Chang Gung Medical Journal*, 33(5), pp. 515–523.

Yin, Y. *et al.* (2010) 'Simulation of pulmonary air flow with a subject-specific boundary condition', *Journal of Biomechanics*, 43(11), pp. 2159–2163. Available at: https://doi.org/10.1016/j.jbiomech.2010.03.048.

Zaw Thin, M. *et al.* (2023) 'Micro-CT acquisition and image processing to track and characterize pulmonary nodules in mice', *Nature Protocols*, 18(3), pp. 990–1015. Available at: https://doi.org/10.1038/s41596-022-00769-5.

Zhang, K. *et al.* (2024) 'Concepts and applications of digital twins in healthcare and medicine', *Patterns*, 5(8), p. 101028. Available at: https://doi.org/10.1016/j.patter.2024.101028.

Zhang, M. *et al.* (2021) 'Epithelial exosomal contactin-1 promotes monocyte-derived dendritic cell–dominant T-cell responses in asthma', *Journal of Allergy and Clinical Immunology*, 148(6), pp. 1545–1558. Available at: https://doi.org/10.1016/j.jaci.2021.04.025.

Zhang, X. *et al.* (2025) 'Assessment of ventilation heterogeneity and particle deposition in asthmatics using combined SPECT/CT imaging and computational modeling approaches', *European Journal of Pharmaceutical Sciences*, 209, p. 107093. Available at: https://doi.org/10.1016/j.ejps.2025.107093.

Zhang, X.-Y. *et al.* (2014) 'Full blood count parameters for the detection of asthma inflammatory phenotypes', *Clinical and Experimental Allergy: Journal of the British Society for Allergy and Clinical Immunology*, 44(9), pp. 1137–1145. Available at: https://doi.org/10.1111/cea.12345.

Zurita, P. and Hurtado, D.E. (2022) 'Computational modeling of capillary perfusion and gas exchange in alveolar tissue', *Computer Methods in Applied Mechanics and Engineering*, 399, p. 115418. Available at: https://doi.org/10.1016/j.cma.2022.115418.

7. Appendices - Code

7.1 Lambert's Scaling MATLAB code

```
%% scaling factor with Lambert's curves for radii
a_0 = [0.882, 0.882, 0.686, 0.546, 0.450, 0.370, 0.310, 0.255, 0.213,0.184, 0.153,
0.125, 0.100, 0.075, 0.057, 0.045, 0.039] ;
al_0 = [0.000011, 0.000011, 0.000051, 0.000080, 0.0001, 0.000125, 0.000142,
0.000159, 0.000174, 0.000184, 0.000194, 0.000206, 0.000218, 0.000226, 0.000233,
0.000239, 0.000243] *1000; % cm/H20 - units from: Airway area distribution from
the forced expiration manoeuvre
% n_1 = [0.5, 0.5, 0.6, 0.6, 0.7, 0.8, 0.9, 1, 1, 1, 1, 1, 1, 1, 1, 1, 1];
n_2 = [10, 10, 10, 10, 10, 10, 10, 10, 10, 10, 10, 9, 8, 8, 8, 7, 7];

%% Calculating a = A/A_m (fractional airway cross-sectional area available to air
flow)
P_tm = 7; % Lambert et al. 1982, fig 2 - assuming 70% of TLC, this occurs at P ~ 7
cm H2O (TLC is achieved as P->large)
P_2 = ( ( -n_2' .* (1 - a_0) ) / al_0 ) ;
a = 1 - (1 - a_0) .* ( (1 - (P_tm./P_2)').^(-n_2) ) ; % Airway area distribution
from the forced expiration manoeuvre

rscale = sqrt(a);

Hmax = max(Horsfield);

H = 0:Hmax;

W = 16 * ( 1 - H / Hmax );

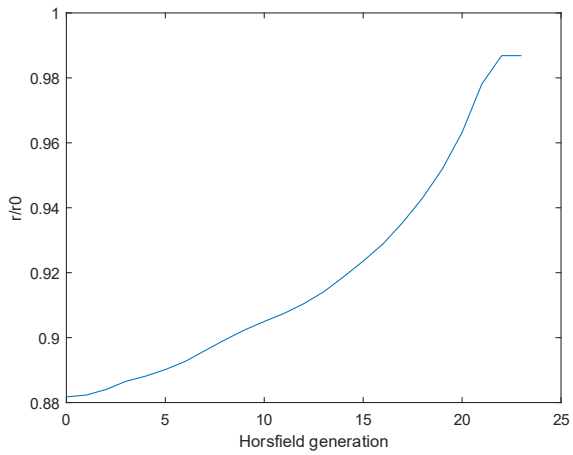
W1 = floor(W);
W2 = ceil(W);

rscaleH = rscale(W1+1) .* (W2 - W) + rscale(W2+1) .* (W - W1);

% Handle cases where W1 == W2
equalIndices = (W1 == W2);
rscaleH(equalIndices) = rscale(W1(equalIndices) + 1);

plot(H, rscaleH);
xlabel('Horsfield gen.');
ylabel('r/r0');

scaling_factor = rscaleH(Horsfield);
```



7.2 FOT Code

```
function [R5, R20, R520, X5, AX] = FOT_code(Branches, LowerBranches,...
    BranchLengths, frequencies, G, H)
 % [OutputIndices] = FOT_stripped_code(Branches, LowerBranches,
 % BranchLengths, frequencies) calculates total lung resistance and
 % reactance in the airway structure defined by Branches, BranchNodes,
 % LowerNodes, LowerBranches, at the given frequencies.
 % Inputs:
 % Branches: A Nx4 matrix, where each row defines a branch based on:
 % [Branch_Number, Proximal_Branch_Node, Distal_Branch_Node, Branch_Radius]
 % LowerBranches: A list of terminal branches.
 % BranchLengths: A vector of lengths of each branch in Branches.
 % frequencies: A vector of frequencies at which resistance and inertance
 % should be evaluated.
 % All input dimensions should be in metres (i.e. branch radii and lengths)
 % Outputs:
 % OutputIndices: A vector of 3 outputs, corresponding to:
 %[Res at 5Hz, Res at 20Hz, Reactance at 5Hz]
 % Written by Brody H Foy, Jan 2018
% BranchLengths = sqrt(sum((Branch_Nodes(Branches(:,2),2:4) -
Branch_Nodes(Branches(:,3),2:4)).^2,2));
% LowerBranches = lower_nodes - 1;
% frequencies = (1:25)';
 %% First define the relevant terminal boundary condition (constant-phase model).
% H = 5.81*98.0665*1e3; %Convert from cmH20/L/s to SI units [Pa/m^3]
% G = 1.22*98.0665*1e3; %Both values taken from Kaczka et al. (1997) 'Partitioning
airway ...' Used by Brody Foy previously

G = G*98.0665*1e3; %Convert from cmH20/L to SI units [Pa/m^3]
H = H*98.0665*1e3; %Convert from cmH20/L to SI units [Pa/m^3]

g = G*length(LowerBranches);
h = H*length(LowerBranches); %Multiply to disperse value over acinar regions

alpha = (2/pi)*atan(h/g); %Angle needed for constant-phase model
omega = (2*pi)*frequencies; %Angular frequencies

complex_i = sqrt(-1); %Defining the complex number
acinar_impedance = (g-complex_i*h)./(omega.^alpha); %The constant-phase model.

%% Now we recursively call the impedance calculation
total_impedance = recursive_impedance(Branches, 1, LowerBranches, BranchLengths,
 frequencies, acinar_impedance);
resistance = real(total_impedance)/(1e6)/0.098; %Convert from Pa/m^3/s to
cmH2O/L/s
inertance = imag(total_impedance)/(1e6)/0.098;

%% Account for shunting and chest wall if desired
account_for_shunt = 1; %Set to 0 to ignore

if account_for_shunt
    %% Add chest wall components (in series with lung)
    chest_resistance = 1.5; %Chest wall resistance (cmH2O/L/s)
    chest_inertance = 10.6./(2*pi.*frequencies); %Chest wall inertance

    resistance = resistance + chest_resistance;
    inertance = inertance + chest_inertance;
```

```
    %% Add cheek shunt component
    shunt_res_5Hz = 1.7*10.197; %Shunt resistance at 5Hz (cmH2O/L/s)
    shunt_res_20Hz = 1.3*10.197; % At 20Hz
    shunt_inert_5Hz = -4.5*10.197; %Shunt inertance at 5Hz (cmH2O/L/s)
    shunt_inert_20Hz = -1.15*10.197; % At 20Hz

    %Fit the shunt model resistance (shunt_res = a/(b + freq))
    bR = (20*shunt_res_20Hz - 5*shunt_res_5Hz)/(shunt_res_5Hz - shunt_res_20Hz);
    aR = shunt_res_5Hz*bR + 5*shunt_res_5Hz;
    shunt_res = aR./(bR + frequencies);

    % Fit the shunt model inertance (shunt_inert = a*log(freq) + b
    aX = (shunt_inert_5Hz - shunt_inert_20Hz)/(log(5) - log(20));
    bX = shunt_inert_5Hz - aX*log(5);
    shunt_inert = aX*log(frequencies) + bX;

    % Add combined effect (in parallel to lung)
    total_impedance = resistance + sqrt(-1)*inertance;
    shunt_impedance = shunt_res + sqrt(-1)*shunt_inert;
    total_impedance = 1./(1./shunt_impedance + 1./total_impedance);

    % Seperate back out
    resistance = real(total_impedance)*0.0980665; % Convert to kPa/L/s
    inertance = imag(total_impedance)*0.0980665;
end

%% Generate summary statistics
R5 = resistance(frequencies == 5);
R20 = resistance(frequencies == 20);
X5 = inertance(frequencies == 5);
% OutputIndices = [frequencies; resistance; inertance]';
R520 = R5 - R20;

n = length(inertance(inertance>0));
m = length((inertance(inertance(1,5:25)>0)));

if isempty(frequencies(1,5:25-n))
    AX = 0;
elseif inertance(inertance(1,5:25)>0) == 20
    AX = 0;
elseif isempty(inertance(inertance(1,5:25)<0))
    AX = 0;
elseif trapz(inertance(inertance(1,5:25)<0),frequencies(1,5:25-m))<0
    AX = 0;
else
    AX = trapz(inertance(inertance(1,5:25)<0),frequencies(1,5:25-m));
end
% Add figure here to plot resistance or inertance against
End

function total_impedance = recursive_impedance(Branches, CurrentBranch,...
    LowerBranches, BranchLength, frequencies, acinar_impedance)
%% This function recursively calls itself to iterate through the tree structure
% calculating the total impedance below (and including) the current branch.

%% Define the basic parameters for calculation
complex_i = sqrt(-1); %the imaginary unit
rho = 1.15; %Density of air (in SI units)
mu = 1.9e-5; %Viscosity of air (in SI units);
```

```
omega = 2*pi*frequencies;

%% Now calculate the impedance of the current branch (based on oscillatory flow)
rv = (omega*rho/mu).^(1/2).*Branches(CurrentBranch,4); %The boundary layer
thickness
J0 = besselj(0, rv*sqrt(-complex_i)); %The 0th and 1st Bessel functions
J1 = besselj(1, rv*sqrt(-complex_i));
FvExp = 2./(rv.*sqrt(-complex_i)).*(J1./J0);  %The exponential fourier component

% This corrects any NaNs that occur when evaluating J1/J0.
for j = 1:length(J0)
    if isinf(J0(j))&&(isinf(J1(j)))
        FvExp(j) = 0;
    end
end

FvExp_Length = (1- real(FvExp)).^2 + (imag(FvExp)).^2; %Length of the component.

resistance = -omega.*rho.*BranchLength(CurrentBranch)./...
    (pi.*Branches(CurrentBranch,4).^2).*(imag(FvExp))./FvExp_Length;
inertance =
rho.*BranchLength(CurrentBranch)./(pi.*Branches(CurrentBranch,4).^2)...
    .*(1-real(FvExp))./FvExp_Length;

branch_impedance = resistance + complex_i.*omega.*inertance;

%% Now iteratively sum over the branches below
if sum(LowerBranches == CurrentBranch)==1 %If we are at a terminal branch
    total_impedance = branch_impedance + acinar_impedance;
else
    CurrentNode = Branches(CurrentBranch,3); %find the distal node for the branch;
    [Daughters,~] = find(Branches(:,2)==CurrentNode);
    daughter_impedance = zeros(length(Daughters), length(frequencies));
    for j = 1:length(Daughters)
        total_impedance = recursive_impedance(Branches, Daughters(j),
LowerBranches,...
            BranchLength, frequencies, acinar_impedance);
            daughter_impedance(j,:) = total_impedance;
    end
    if length(Daughters) > 1
        total_impedance = branch_impedance + 1./(sum(1./daughter_impedance));
    else
        total_impedance = branch_impedance + daughter_impedance;
    end
end
end
```

7.3 MATLAB Function of V/Q Digital Twin

```
%% Function 1
function [DLCO, KCO] = Simulate_KCOnew(RV, TLC, Va_per, LungVols, PulmVol,
CapVols, D0_base, th, th_healthy, tRBC,tRBC_healthy)
%
%% Function 2
% function [DLCO, KCO] = Simulate_KCOnew(RV, TLC, Va_per, LungVols, PulmVol,
CapVols, D0_base, th_barrier, tRBC,th_RBC_barrier,th_scale)
%
% simulates a simple carbon monoxide gas transfer test using the input
% parameters, to generate DLCO and KCO values
%% INPUTS
% RV: Residual Volume of the lungs (in Litres)
% TLC: Total lung capacity (in Litres)
% Va_per: Percentage of TLC contributing to Alveolar Volume (%)
% LungVols: Relative sizes of different lung regions (4 regions by default,
%           corresponding to LUL, LLL, RUL+RML, RLL).
% PulmVol: The total capillary blood volume (in Litres)
% CapVols: Relative sizes of the different blood compartments (4 regions by
%           default, must be same size as LungVols)
% D0_base: The baseline alveolar-capillary C0 diffusion
% th: mean harmonic alveolar-capillary membrane thickness for each compartment
(µm) (4 regions by default,corresponding to LUL, LLL, RUL+RML, RLL)
% th_healthy: healthy mean harmonic alveolar-capillary membrane thickness (µm)
%
% tRBC: mean Red Blood Cell (RBC) membrane thickness for each compartment (nm) (4
regions by default,
%
corresponding to LUL, LLL, RUL+RML, RLL)
% tRBC_healthy : healthy mean Red Blood Cell (RBC) membrane thickness (nm)
%
%% OUTPUTS:
% DLCO: The diffusing capacity of the lungs
% KCO: The carbon monoxide transfer coefficient of the lungs

%% First double check that both LungVols and CapVols are scaled to have a sum of
1.
LungVols = LungVols(:)/sum(LungVols);
CapVols = CapVols(:)/sum(CapVols);

%% Define parameters that don't change across simulations
BHT = 8; %Length of the breath hold (standard value is 10s or 12s)
dt = 0.001; %Timestep size.
C0 = 0.003; % Initial C0 concentration

% Comment for PAH simulation
Va = TLC*Va_per;

%Uncomment for PAH
% Va = Va_per;
% Va_per = Va/TLC;

%%  Initialize data storage
TotalC_store = zeros(round(BHT/dt),1); %Store total CO concentrations

%% Calculate initial alveolar concentrations (post inhalation)
% New CO amount entering the lung compartment from Residual Volume (RV) to Vital
Capacity (VC) [TLC]
```

```
% is the difference between the two, minus the anatomical dead space (therefore
Va) times
% the volume of the part and concentration = C0*(TLC-RV)*Va_per*LungVol(i)
% New Volume of lung compartment post inhalation to Va = Va*LungVol(i)
% Therefore -> New CO Concentration at peak of expansion to Va end of inhalation
% LungC = New CO amount entered/ New Volume
% New because we started at Residual Volume
% LungC = C0*(TLC - RV)*Va_per*LungVol(i) / Va*LungVol(i) ->
% -> LungC = C0 * (TLC - FRC) * Va_per / Va

inhaled_air = TLC - RV;
dead_space = TLC - Va;

LungC = C0*(inhaled_air)*Va_per/Va*ones(4,1); % Initial alveolar CO Concentration
Dead_C = (C0*((inhaled_air)*(1-Va_per)))/(dead_space); % Concentration of CO in
the anatomical dead space

TotalC_store(1) = ((mean(LungC)*Va) + Dead_C*(dead_space))/TLC; % Total
Concentration of CO in Lung including Va and Anatomical Deadspace

counter = 2;

%% Loop over the duration of the breath hold
for t = 0:dt:BHT %for time increments of dt from 0 to BHT
    % Run calculation for each lobe
    for j = 1:4 %for each lung compartment 1 to 4
        % Calculate the capillary-volume-scaled diffusivity

        % To simulate DLCO and KCO for changes in Barrier and RBC membranes
        % permeation coefficients (AUCs from xenon 129 MRI), uncomment the
        % below and Function 1 at the top of the page
        % i.e. COVID-19
        D0_s = D0_base*(((((PulmVol*CapVols(j)/0.065))^(1/2))/(2^(1/2))) *
((Va/TLC)^(1/3))) * (th(j)/2 + tRBC(j)/2); %[L/s/mmHg]

        % for RBC:Barrier ratio - used in thesis for participant validation
        % in chapter 4 (MRI coupling)
        % uncomment Function 2 at the top of this page
        % function [DLCO, KCO] = Simulate_KCOnew(RV, TLC, Va_per, LungVols,
PulmVol, CapVols, D0_base, th_barrier, tRBC,th_RBC_barrier,th_scale)
        % D0_s = D0_base*(((((PulmVol*CapVols(j)/0.065))^(1/2))/(2^(1/2))) *
((Va/TLC)^(1/3)))* th_RBC_barrier(j)*th_scale; %[L/s/mmHg]

        % For all other simulations of DLCO and KCO, uncomment the below
        % i.e., Asthma, ILD, PH, Pneumonectomy
        D0_s = D0_base*(((((PulmVol*CapVols(j)/0.065))^(1/2))/(2^(1/2))) *
((Va/TLC)^(1/3))) * (th_healthy/th(j)); %[L/s/mmHg]

        Pacin = (760-47)*LungC(j); %Calculate the updated alveolar CO partial
pressure [mmHg]
        Pblood = 0; %Assume blood is an infinite sink (diffusion limited) and so
has a partial pressure of
        Compartment_COAmount = LungVols(j)*Va*LungC(j); %Convert CO concentration
in lung compartment to in litres [L] from percentage (%) [L]
        newCOAmount = Compartment_COAmount + dt*D0_s*(Pblood - Pacin); %Update CO
amount in lung compartment, based on diffusion [L]
        LungC(j) = newCOAmount/(LungVols(j)*Va);  %Calculate new CO concentrations
[%] in the lung compartments using the updated CO Amount [L]
    end
```

```
    TotalC_store(counter) = ((dot(LungC,LungVols)*Va)+Dead_C*(TLC-Va))/TLC; %Store
calculated concentrations for the cumulative time t - dot(LungC,LungVols) =
sum(LungC.*LungVols)
    counter = counter + 1;
end

%% Calculate DLCO and KCO
Ce = (dot(LungC,LungVols)*Va )/Va; % Calculation of the Final Concentration
Cx = C0*(inhaled_air)*Va_per/Va; %Initial alveolar Concentration
Pb = 760-47; % Alveolar Gas Pressure = Pacinous - P_Water_Vapour [mmHg]
kCO = log(Cx/Ce)/BHT; %Little kCO - Slope of Log-scaled graph of CO concentration
over Breath-hold time
DLCO = Va*kCO/Pb; %Calculating DLCO
DLCO = DLCO*1000*60; % Convert DLCO to mL/min/mmHg (traditional units)

% altitude = 10;
% Pb = 760  *(1 - 2.25577  * 10^(-5) *altitude)^5.25588;
% DLCO = DLCO*(0.505 + 0.00065*Pb);
% conversionLBTPS = 760/((273/310)*(Pb)); %
https://www.ncbi.nlm.nih.gov/books/NBK54114/?report=reader OR 1.2 from Neil's
paper
KCO = DLCO/(Va*1.2); % LBTPS [ml/min/mmHg/L]

%% Plotting the resultant curve (uncomment)
% hold on;
% plot([-2, -1, -1, 0, 0:dt:BHT]+2, [0, 0, C0, C0, TotalC_store(2:end)']/C0,
'LineWidth', 2)

% % First plotted
% Va_per = 40:10:100;
% for i = 1:length(Va_per)
% [DLCO(i), KCO(i)] = Simulate_KCOnew(1.5, 6, Va_per(i), [0.25, 0.25, 0.25, 0.25],
0.25, [0.25, 0.25, 0.25, 0.25], 4.675*10^(-4));
% end
% plot(Va_per, DLCO/DLCO(end))
% plot(Va_per, KCO/KCO(end))
```

7.4 MATLAB code for hypothetical disease simulations

```
clear; clc; close all;
load DLCO_AgeMspline_Male.mat
load DLCO_AgeMspline_Female.mat
load KCO_AgeMspline_Male.mat
load KCO_AgeMspline_Female.mat
load VA_AgeMspline_Male.mat
load VA_ageMspline_Female.mat
load TLC_Mspline_Male.mat
load TLC_Mspline_Female.mat
load RV_Mspline_Male.mat
load RV_Mspline_Female.mat

std_DLCO = zeros(80,1);
min_DLCO = zeros(80,1);
max_DLCO = zeros(80,1);
mean_DLCO = zeros(80,1);
std_KCO = zeros(80,1);
min_KCO = zeros(80,1);
max_KCO = zeros(80,1);
mean_KCO = zeros(80,1);

%% PAH
% sex = 2 ; % 1 = male
% H = 1.62; % Height in [m]
% A = 48;  % Age in years
%% Pneumonectomy
% sex = 1 ; % 1 = male
% H = 1.7; % Height in [m]
% A = 67;  % Age in years
%% Asthma
% sex = 2 ; % 1 = male
% H = 1.62; % Height in [m]
% A = 55.5;  % Age in years
% ILD
sex = 2 ; % 1 = male
H = 1.65; % Height in [m]
A = 52;  % Age in years
%% COVID-19
% sex = 2 ; % 1 = male
% H = 1.65; % Height in [m]
% A = 53;  % Age in years

% Input number
inputAge = A;
% Array of ages
ageArray = DLCO_AgeMspline_Male(:,2);
% Calculate the absolute differences between the input age and the array
ageDifferences = abs(ageArray - inputAge);
% Find the index of the minimum absolute difference
[~, minIndex] = min(ageDifferences);

% Get the closest age from the array
closestAge = ageArray(minIndex);
row = find(DLCO_AgeMspline_Male(:,2) == closestAge); %find row number where the
closet age reference values are located
% disp(['Closest age: ', num2str(closestAge)]);
```

```
if sex == 1 %if patient is male (1)
    MsplineRV_m = RV_Mspline_Male(row,2);
    MsplineTLC_m = TLC_Mspline_Male(row,2);
    RV =  exp(-2.37211+0.01346*A+0.01307*H*100 + MsplineRV_m);
    TLC =  exp(-10.5861+0.1433*log(A)+2.3155*log(H*100) + MsplineTLC_m);
    %     D0_base = 28/1000/60; % DM Membrane conductance Historical review: the
carbon monoxide diffusing capacity (DLCO) and its membrane (DM) and red cell
(θ/Vc)components
    MsplineDLCO_m = DLCO_AgeMspline_Male(row,3);
    MsplineVA_m = VA_AgeMspline_Male(row,3);
    D0_base = exp(-7.034920 + 2.018368 * log(H*100) - 0.012425*log(A) +
MsplineDLCO_m)/1000/60;
    VA = exp(-11.086573 + 2.430021 * log(H*100) + 0.097047*log(A) + MsplineVA_m);
    Va_per = VA/TLC;
    MsplineKCO_m = KCO_AgeMspline_Male(row,3);
    rKCO = exp(4.088408 - 0.415334*log(H*100) - 0.113166*log(A) + MsplineKCO_m); %
mL/min/mmHg/L

else % if patient is female
    MsplineRV_f = RV_Mspline_Female(row,2);
    MsplineTLC_f = TLC_Mspline_Female(row,2);
    RV =  exp(-2.50593+0.01307*A+0.01379*H*100+MsplineRV_f);
    TLC = exp(-10.1128+0.1062*log(A)+2.2259*log(H*100)+MsplineTLC_f);
    %     D0 = 3.465*10^(-4); % DLCO - Normal Predicted Values of Single-Breath
Diffusing Capacity of the Lung in Healthy Nonsmoking Adults (PMID: 3154613)
20.79mL/min/mmHg = 3.465*10^(-4) L/s/mmHg
    MsplineDLCO_f = DLCO_AgeMspline_Female(row,3);
    MsplineVA_f = VA_AgeMspline_Female(row,3);
    D0_base = exp(-5.159451+1.618697*log(H*100)-
0.015390*log(A)+MsplineDLCO_f)/1000/60;
    VA = exp(-9.873970 + 2.182316*log(H*100) + 0.082868*log(A) + MsplineVA_f);
    Va_per = VA/TLC;
    MsplineKCO_f = KCO_AgeMspline_Female(row,3);
    rKCO = exp(5.131492 - 0.645656*log(H*100) - 0.097395*log(A) + MsplineKCO_f); %
mL/min/mmHg/L
end

RV_per = RV/TLC;
% PulmVol = 0.269; %Pulmonary volume Taken from - Pulmonary Blood Volume and
Pulmonary Capillary Blood Volume in Valvular Heart Disease
PulmVol = 0.065;
% LungVols = [0.224, 0.243, 0.261, 0.272]; %Assumed ordered as LUL, LLL, RUL +
RML, RLL, Taken from Table 3 - Differences in Lung and Lobe Volumes between Supine
and Standing Positions Scanned with Conventional and Newly Developed 320-Detector-
Row Upright CT: Intra-Individual Comparison
LungVols = [0.23, 0.237, 0.264, 0.269];
LungVols = LungVols/sum(LungVols);
CapVols = LungVols; %Assumed relative pulmonary blood size (at default is same as
lung lobe size)
LungVols = LungVols(:)/sum(LungVols);
CapVols = CapVols(:)/sum(CapVols);
th_healthy = 0.77;
th = [th_healthy, th_healthy, th_healthy, th_healthy];
tRBC_healthy = 0.45;
tRBC = [tRBC_healthy, tRBC_healthy, tRBC_healthy, tRBC_healthy];

% First generate a reference value of DLCO and KCO, to compare against
% uncomment for PAH simulation
```

```
% [refDLCO, refKCO] = Simulate_KCOnew(RV/TLC, TLC, VA, LungVols, PulmVol, CapVols,
D0_base, th, th_healthy, tRBC, tRBC_healthy);

%uncomment for everything else
[refDLCO, refKCO] = Simulate_KCOnew(RV, TLC, Va_per, LungVols, PulmVol, CapVols,
D0_base, th, th_healthy, tRBC, tRBC_healthy);
%uncomment for GLI % predicted
% refDLCO = D0_base*1000*60;
% refKCO = rKCO;

%% Set up simulations for various scenarios
% In each scenario, we simulate over a grid of variables, and plot a
% heatmap of corresponding DLCO and KCO changes
%
% Valid values for sim_type are:
%
% Asthma : Compares changes RV, TLC, and VA/TLC
%
% Pneumonectomy: Compares changes in Pulmonary blood volume V_c, TLC, and RV
%
% ILD : Compares changes in TLC, Pulmonary blood volume V_c and
% Alveolar-Capillary membrane (ACM) thickness
%
% PAH : Compares changes in Alveolar Volume VA, Pulmonary blood volume V_c and RV
%
% COVID : Compares changes in RBC permeation coefficient analogue with
% blood-gas barrier permeation coefficient analogue

sim_type = 'COVID';
```

```
%% Series of cases for each file
if strcmp(sim_type, 'Asthma')
    % 2 SD from mean
    Va_per_grid = linspace(Va_per*0.78, Va_per*0.852, 51);
    TLC_grid = linspace(TLC*0.999, TLC*1.142, 51);
    % RV_grid = linspace((RV/TLC)*1.033, (RV/TLC)*1.166, 51); %This is RV/TLC
    RV_grid = linspace(0.25, 1, 51); %This is to change blood distribution in the
Lower Lobes which will be re-dristributed to the upper lobes
    DLCO = NaN(length(TLC_grid), length(Va_per_grid)); KCO = DLCO;
    % Create a 3D grid for the third input (PV_grid)
    [TLC_grid_3D, Va_per_grid_3D, RV_grid_3D] = meshgrid(TLC_grid, Va_per_grid,
RV_grid);

    % Loop through, calculate values
    for i = 1:length(TLC_grid)
        for j = 1:length(Va_per_grid)
            for k = 1:length(Va_per_grid)
                if Va_per_grid(j) < TLC_grid(i)
                    newCapVols = [0.23*RV_grid(k), 0.237, 0.264*RV_grid(k),
0.269];
                    [DLCO(i,j,k), KCO(i,j,k)] = Simulate_KCOnew(RV, TLC_grid(i),
Va_per_grid(j), LungVols, PulmVol, newCapVols, D0_base, th, th_healthy, tRBC,
tRBC_healthy);
                end
            end
        end
    end
    % Normalize the results for visualization
```

```
    DLCOp = 100 * DLCO / refDLCO;
    KCOp = 100 * KCO / refKCO;
    meanDLCO = mean(DLCOp, 'all');
    SD_DLCO = std(DLCOp, 0, 'all');
    minDLCO = min(DLCOp, [], 'all');
    maxDLCO = max(DLCOp, [], 'all');
    minrangeDLCO = meanDLCO - 2*SD_DLCO;
    maxrangeDLCO = meanDLCO + 2*SD_DLCO;
    outDLCO = sprintf('DLCO (%% of healthy) ILD - %.0f(%.0f-
%.0f)',meanDLCO,minrangeDLCO,maxrangeDLCO);
    disp(outDLCO)
    meanKCO = mean(KCOp, 'all');
    SD_KCO = std(KCOp, 0, 'all');
    minKCO = min(KCOp, [], 'all');
    maxKCO = max(KCOp, [], 'all');
    minrangeKCO = meanKCO - 2*SD_KCO;
    maxrangeKCO = meanKCO + 2*SD_KCO;
    outKCO = sprintf('KCO (%% of healthy) ILD - %.0f(%.0f-
%.0f)',meanKCO,minrangeKCO,maxrangeKCO);
    disp(outKCO)
    % Create a new figure with specified size
    figure('Position', [100, 100, 1150, 400]);
    % Create a 3D scatter plot
    subplot(1,2,1);
    scatter3(100*TLC_grid_3D(:)/TLC, 100*Va_per_grid_3D(:)/Va_per,
100*RV_grid_3D(:), 20, DLCOp(:), 'filled');
    xlabel('TLC (% of GLI input)');
    ylabel('VA/TLC (% of GLI Input)');
    zlabel('Perfused volume of LLs (% of Healthy)');
    M = sprintf('DLCO (%% of healthy) Asthma - %.0f(%.0f-
%.0f)',meanDLCO,minDLCO,maxDLCO);
    view(225,30)
    % Set the colormap to 'copper'
    colormap(hot);
    % Create a colorbar for DLCO
    cbar_dlco = colorbar;
    cbar_dlco.Ticks = linspace(min(cbar_dlco.Ticks), max(cbar_dlco.Ticks), 6);
    % bar = [KCOp(:) ; DLCOp(:)];
    % clim([min(bar), max(bar)]);
    % Customize the plot as needed
    title(M);
    % Adjust axis limits and set equal aspect ratio
    axis tight;
    set(gca, 'XTick', linspace(min(get(gca, 'XTick')), max(get(gca,'XTick')), 3));
    set(gca, 'YTick', linspace(min(get(gca, 'YTick')), max(get(gca,'YTick')), 3));
    set(gca, 'ZTick', linspace(min(get(gca, 'ZTick')), max(get(gca,'ZTick')), 3));
    % Create a 3D scatter plot
    subplot(1,2,2);
    scatter3(100*TLC_grid_3D(:)/TLC, 100*Va_per_grid_3D(:)/Va_per,
100*RV_grid_3D(:), 20, KCOp(:), 'filled');
    xlabel('TLC (% of GLI input)');
    ylabel('VA/TLC (% of GLI Input)');
    % zlabel('V_C distribution to LLs (% of Healthy)');
    zlabel('Perfused volume of LLs (% of Healthy)');
    N = sprintf('KCO (%% of healthy) Asthma - %.0f(%.0f-
%.0f)',meanKCO,minKCO,maxKCO);
    view(225,30)
    % Set the colormap to 'copper'
    colormap(hot);
```

```
    % Create a colorbar for DLCO
    cbar_kco = colorbar;
    cbar_kco.Ticks = linspace(min(cbar_kco.Ticks), max(cbar_kco.Ticks), 6);
    % bar = [KCOp(:) ; DLCOp(:)];
    % clim([min(bar), max(bar)]);
    % Customize the plot as needed
    title(N);
    % Adjust axis limits and set equal aspect ratio
    axis tight;
    set(gca, 'XTick', linspace(min(get(gca, 'XTick')), max(get(gca,'XTick')), 3));
    set(gca, 'YTick', linspace(min(get(gca, 'YTick')), max(get(gca,'YTick')), 3));
    set(gca, 'ZTick', linspace(min(get(gca, 'ZTick')), max(get(gca,'ZTick')), 3));
```

```
elseif strcmp(sim_type, 'ILD')
    % Setup grid
    %     Va_per_grid = linspace(Va_per*0.794, Va_per*0.904, 51);
    th_grid = linspace(th_healthy*1.31, th_healthy*2.22, 51);
    TLC_grid = linspace(TLC*0.65, TLC*1.23, 51);
    PV_grid = linspace(PulmVol*0.27, PulmVol*1.42, 51);
    % Create a 3D grid for the third input (PV_grid)
    [TLC_grid_3D, th_grid_3D, PV_grid_3D] = meshgrid(TLC_grid, th_grid, PV_grid);
    DLCO = NaN(size(TLC_grid_3D));
    KCO = NaN(size(TLC_grid_3D));
    % Loop through, calculate values
    for i = 1:length(TLC_grid)
        for j = 1:length(th_grid)
            for k = 1:length(PV_grid)
                if th_grid(j) < TLC_grid(i)
                    new_thickness = [th_grid(j), th_grid(j), th_grid(j),
th_grid(j)];
                    [DLCO(i,j,k), KCO(i,j,k)] = Simulate_KCOnew(RV, TLC_grid(i),
Va_per, LungVols, PV_grid(k), CapVols, D0_base, new_thickness, th_healthy, tRBC,
tRBC_healthy);
                end
            end
        end
    end
    % Normalize the results for visualization
    DLCOp = 100 * DLCO / refDLCO;
    KCOp = 100 * KCO / refKCO;

    meanDLCO = mean(DLCOp, 'all');
    SD_DLCO = std(DLCOp, 0, 'all');
    minDLCO = min(DLCOp, [], 'all');
    maxDLCO = max(DLCOp, [], 'all');
    minrangeDLCO = meanDLCO - 2*SD_DLCO;
    maxrangeDLCO = meanDLCO + 2*SD_DLCO;
    outDLCO = sprintf('DLCO (%% of healthy) ILD - %.0f(%.0f-
%.0f)',meanDLCO,minrangeDLCO,maxrangeDLCO);
    disp(outDLCO)
    meanKCO = mean(KCOp, 'all');
    SD_KCO = std(KCOp, 0, 'all');
    minKCO = min(KCOp, [], 'all');
    maxKCO = max(KCOp, [], 'all');
    minrangeKCO = meanKCO - 2*SD_KCO;
    maxrangeKCO = meanKCO + 2*SD_KCO;
    outKCO = sprintf('KCO (%% of healthy) ILD - %.0f(%.0f-
%.0f)',meanKCO,minrangeKCO,maxrangeKCO);
```

```
    disp(outKCO)
    % Create a new figure with specified size
    figure('Position', [100, 100, 1150, 400]);
    % Create a 3D scatter plot
    subplot(1,2,1);
    scatter3(100*TLC_grid_3D(:)/TLC, 100*th_grid_3D(:)/th_healthy,
100*PV_grid_3D(:)/PulmVol, 20, DLCOp(:), 'filled');
    xlabel('TLC (% of GLI input)');
    ylabel('ACM Thickness (% of healthy)');
    zlabel('V_c (% of healthy)');
    M = sprintf('DLCO (%% of healthy) ILD - %.0f(%.0f-
%.0f)',meanDLCO,minDLCO,maxDLCO);
    view(225,30)
    % Set the colormap to 'copper'
    colormap(hot);
    % Create a colorbar for DLCO
    cbar_dlco = colorbar;
    bar = [KCOp(:) ; DLCOp(:)];
    clim([min(bar), max(bar)]);
    % Customize the plot as needed
    title(M);
    % Adjust axis limits and set equal aspect ratio
    axis tight;
    set(gca, 'XTick', linspace(min(get(gca, 'XTick')), max(get(gca,'XTick')), 3));
    set(gca, 'YTick', linspace(min(get(gca, 'YTick')), max(get(gca,'YTick')), 3));
    set(gca, 'ZTick', linspace(min(get(gca, 'ZTick')), max(get(gca,'ZTick')), 3));
    % Create a 3D scatter plot
    subplot(1,2,2);
    scatter3(100*TLC_grid_3D(:)/TLC, 100*th_grid_3D(:)/th_healthy,
100*PV_grid_3D(:)/PulmVol, 20, KCOp(:), 'filled');
    xlabel('TLC (% of GLI input)');
    ylabel('ACM Thickness (% of healthy)');
    zlabel('V_c (% of healthy)');
    N = sprintf('KCO (%% of healthy) ILD - %.0f(%.0f-
%.0f)',meanKCO,minKCO,maxKCO);
    view(225,30)
    % Set the colormap to 'copper'
    colormap(hot);
    % Create a colorbar for DLCO
    cbar_kco = colorbar;
    cbar_kco.Ticks = linspace(min(cbar_kco.Ticks), max(cbar_kco.Ticks), 6);
    bar = [KCOp(:) ; DLCOp(:)];
    clim([min(bar), max(bar)]);
    % Customize the plot as needed
    title(N);
    % Adjust axis limits and set equal aspect ratio
    axis tight;
    set(gca, 'XTick', linspace(min(get(gca, 'XTick')), max(get(gca,'XTick')), 3));
    set(gca, 'YTick', linspace(min(get(gca, 'YTick')), max(get(gca,'YTick')), 3));
    set(gca, 'ZTick', linspace(min(get(gca, 'ZTick')), max(get(gca,'ZTick')), 3));
    % Create a new figure with specified size
    figure('Position', [100, 100, 1150, 400]);
```

```
elseif strcmp(sim_type, 'PAH')
    % Setup PV and TLC grid
    PV_grid = linspace(PulmVol*0.34, PulmVol*0.89, 51);
    % TLC_grid = linspace(TLC*0.82, TLC*1.1, 51);
    TLC_grid = linspace(TLC*0.63, TLC*1.22, 51);
```

```
    Va_grid = linspace(VA*0.55, VA*1.19, 51);
    RV_grid = linspace(RV*0.70, RV*1.66, 51);

    DLCO = NaN(length(TLC_grid), length(PV_grid)); KCO = DLCO;

    % Create a 3D grid for the third input (PV_grid)
    [Va_grid_3D, PV_grid_3D, RV_grid_3D] = meshgrid(Va_grid, PV_grid, RV_grid);

    % Loop through, calculate values
    for i = 1:length(Va_grid)
        for j = 1:length(PV_grid)
            for k = 1:length(RV_grid)
                if PV_grid(j) < TLC_grid(i)
                    [DLCO(i,j,k), KCO(i,j,k)] = Simulate_KCOnew(RV_grid(k), TLC,
Va_grid(i), LungVols, PV_grid(j), CapVols, D0_base, th, th_healthy, tRBC,
tRBC_healthy);
                end
            end
        end
    end
    DLCOp = 100 * DLCO / refDLCO;
    KCOp = 100 * KCO / refKCO;

    meanDLCO = mean(DLCOp, 'all');
    SD_DLCO = std(DLCOp, 0, 'all');
    minDLCO = min(DLCOp, [], 'all');
    maxDLCO = max(DLCOp, [], 'all');
    minrangeDLCO = meanDLCO - 2*SD_DLCO;
    maxrangeDLCO = meanDLCO + 2*SD_DLCO;
    outDLCO = sprintf('DLCO (%% of healthy) ILD - %.0f(%.0f-
%.0f)',meanDLCO,minrangeDLCO,maxrangeDLCO);
    disp(outDLCO)
    meanKCO = mean(KCOp, 'all');
    SD_KCO = std(KCOp, 0, 'all');
    minKCO = min(KCOp, [], 'all');
    maxKCO = max(KCOp, [], 'all');
    minrangeKCO = meanKCO - 2*SD_KCO;
    maxrangeKCO = meanKCO + 2*SD_KCO;
    outKCO = sprintf('KCO (%% of healthy) ILD - %.0f(%.0f-
%.0f)',meanKCO,minrangeKCO,maxrangeKCO);
    disp(outKCO)
    % Create a new figure with specified size
    figure('Position', [100, 100, 1150, 400]);
    % Create a 3D scatter plot for DLCO
    subplot(1,2,1);
    scatter3(100*Va_grid_3D(:)/VA, 100*PV_grid_3D(:)/PulmVol,
100*RV_grid_3D(:)/RV, 20, DLCOp(:), 'filled');
    xlabel('VA (% of GLI input)');
    ylabel('V_c (% of healthy)');
    zlabel('RV (% of GLI reference)');
    M = sprintf('DLCO (%% of healthy) PAH - %.0f(%.0f-%.0f)', meanDLCO, minDLCO,
maxDLCO);
    view(225,30)
    % Set the colormap to 'copper'
    colormap(hot);
    % % Create a colorbar for DLCO
    cbar_dlco = colorbar;
    bar = [KCOp(:) ; DLCOp(:)];
    clim([min(bar), max(bar)]);
```

```
    % Customize the plot as needed
    title(M);
    % Adjust axis limits and set equal aspect ratio
    axis tight;
    set(gca, 'XTick', linspace(min(get(gca, 'XTick')), max(get(gca,'XTick')), 3));
    set(gca, 'YTick', linspace(min(get(gca, 'YTick')), max(get(gca,'YTick')), 3));
    set(gca, 'ZTick', linspace(min(get(gca, 'ZTick')), max(get(gca,'ZTick')), 3));
    % daspect([1,1,1]);
    % Create a 3D scatter plot for KCO
    subplot(1,2,2);
    scatter3(100*Va_grid_3D(:)/VA, 100*PV_grid_3D(:)/PulmVol,
100*RV_grid_3D(:)/RV, 20, KCOp(:), 'filled');
    xlabel('VA (% of GLI input)');
    ylabel('V_c (% of healthy)');
    zlabel('RV (% of GLI reference)');
    N = sprintf('KCO (%% of healthy) PAH - %.0f(%.0f-%.0f)', meanKCO, minKCO,
maxKCO);
    view(225,30)
    % Set the colormap to 'copper'
    colormap(hot);
    % Create a colorbar for KCO using the same limits as DLCO
    cbar_kco = colorbar;
    cbar_kco.Ticks = linspace(min(cbar_kco.Ticks), max(cbar_kco.Ticks), 6);
    bar = [KCOp(:) ; DLCOp(:)];
    clim([min(bar), max(bar)]);
    % Customize the plot as needed
    title(N);
    % Adjust axis limits and set equal aspect ratio
    axis tight;
    set(gca, 'XTick', linspace(min(get(gca, 'XTick')), max(get(gca,'XTick')), 3));
    set(gca, 'YTick', linspace(min(get(gca, 'YTick')), max(get(gca,'YTick')), 3));
    set(gca, 'ZTick', linspace(min(get(gca, 'ZTick')), max(get(gca,'ZTick')), 3));
```

```
elseif strcmp(sim_type, 'Pneumonectomy')
    RightLung_grid = linspace(0.001, 1, 51);
    TLC_grid = linspace(0.32*TLC, TLC*0.84,51);
    RV_grid = linspace(0.30*RV, RV*0.82, 51);
    DLCO = NaN(length(RightLung_grid), length(TLC_grid)); KCO = DLCO;
    PulmVol_grid = linspace((0.23+0.237)*0.77*PulmVol, (0.23+0.237)*2.39*PulmVol,
51);
    % Create a 3D grid for the third input (PV_grid)
    [TLC_grid_3D, RV_grid_3D, PulmVol_grid_3D] = meshgrid(TLC_grid, RV_grid,
PulmVol_grid);

    for i = 1:length(TLC_grid)
        for j = 1:length(RV_grid)
            for k = 1:length(PulmVol_grid)
                % if RV_grid(j) < TLC_grid(i)
                    % newLungVols = [0.23, 0.237, RightLung_grid(i)*0.264,
RightLung_grid(i)*0.269]; %LUL, LLL, RUL + RML, RLL,
                    newLungVols = [0.23, 0.237, 0.0001, 0.0001]; %LUL, LLL, RUL +
RML, RLL,
                    newLungVols = newLungVols(:)/sum(newLungVols);
                    newCapVols = newLungVols;
                    [DLCO(i,j,k), KCO(i,j,k)] = Simulate_KCOnew(RV_grid(j),
TLC_grid(i), Va_per, newLungVols, PulmVol_grid(k), newCapVols, D0_base, th,
th_healthy, tRBC, tRBC_healthy);
                % end
```

```
            end
        end
    end
    % Normalize the results for visualization
    DLCOp = 100 * DLCO / refDLCO;
    KCOp = 100 * KCO / refKCO;
    meanDLCO = mean(DLCOp, 'all');
    SD_DLCO = std(DLCOp, 0, 'all');
    minDLCO = min(DLCOp, [], 'all');
    maxDLCO = max(DLCOp, [], 'all');
    minrangeDLCO = meanDLCO - 2*SD_DLCO;
    maxrangeDLCO = meanDLCO + 2*SD_DLCO;
    outDLCO = sprintf('DLCO (%% of healthy) ILD - %.0f(%.0f-
%.0f)',meanDLCO,minrangeDLCO,maxrangeDLCO);
    disp(outDLCO)
    meanKCO = mean(KCOp, 'all');
    SD_KCO = std(KCOp, 0, 'all');
    minKCO = min(KCOp, [], 'all');
    maxKCO = max(KCOp, [], 'all');
    minrangeKCO = meanKCO - 2*SD_KCO;
    maxrangeKCO = meanKCO + 2*SD_KCO;
    outKCO = sprintf('KCO (%% of healthy) ILD - %.0f(%.0f-
%.0f)',meanKCO,minrangeKCO,maxrangeKCO);
    disp(outKCO)
    % Create a new figure with specified size
    figure('Position', [100, 100, 1150, 400]);
    % Create a 3D scatter plot
    subplot(1,2,1);
    scatter3(100*TLC_grid_3D(:)/TLC, 100*RV_grid_3D(:)/RV,
100*PulmVol_grid_3D(:)/PulmVol, 20, DLCOp(:), 'filled');
    xlabel('TLC (% of GLI input)');
    ylabel('RV (% of GLI input)');
    zlabel('V_c (% of healthy)');
    M = sprintf('DLCO (%% of healthy) RL Pneumonectomy - %.0f(%.0f-
%.0f)',meanDLCO,minDLCO,maxDLCO);
    view(225,30)
    % Set the colormap to 'copper'
    colormap(hot);
    % % Create a colorbar for DLCO
    cbar_dlco = colorbar;
    cbar_dlco.Ticks = linspace(min(cbar_dlco.Ticks), max(cbar_dlco.Ticks), 6);
    % bar = [KCOp(:) ; DLCOp(:)];
    % clim([min(bar), max(bar)]);
    % Customize the plot as needed
    title(M);
    % Adjust axis limits and set equal aspect ratio
    axis tight;
    % Set number of ticks for the axes
    set(gca, 'XTick', linspace(min(get(gca, 'XTick')), max(get(gca,'XTick')), 3));
    set(gca, 'YTick', linspace(min(get(gca, 'YTick')), max(get(gca,'YTick')), 3));
    set(gca, 'ZTick', linspace(min(get(gca, 'ZTick')), max(get(gca,'ZTick')), 3));
    % Create a 3D scatter plot
    subplot(1,2,2);
    scatter3(100*TLC_grid_3D(:)/TLC, 100*RV_grid_3D(:)/RV,
100*PulmVol_grid_3D(:)/PulmVol, 20, KCOp(:), 'filled');
    xlabel('TLC (% of GLI input)');
    ylabel('RV (% of GLI input)');
    zlabel('V_c (% of healthy)');
```

```
    N = sprintf('KCO (%% of healthy) RL Pneumonectomy - %.0f(%.0f-
%.0f)',meanKCO,minKCO,maxKCO);
    view(225,30)
    % Set the colormap to 'copper'
    colormap(hot);
    % Create a colorbar for DLCO
    cbar_kco = colorbar;
    cbar_kco.Ticks = linspace(min(cbar_kco.Ticks), max(cbar_kco.Ticks), 6);
    % bar = [KCOp(:) ; DLCOp(:)];
    % clim([min(bar), max(bar)]);
    % Customize the plot as needed
    title(N);
    % Adjust axis limits and set equal aspect ratio
    axis tight;
    % Set number of ticks for the axes
    set(gca, 'XTick', linspace(min(get(gca, 'XTick')), max(get(gca,'XTick')), 3));
    set(gca, 'YTick', linspace(min(get(gca, 'YTick')), max(get(gca,'YTick')), 3));
    set(gca, 'ZTick', linspace(min(get(gca, 'ZTick')), max(get(gca,'ZTick')), 3));
```

```
elseif strcmp(sim_type, 'COVID')
    % RBC membrane
    tRBCnorm = 139;
    tRBCmin = (78-31)/tRBCnorm; %AUC
    tRBCmax = (103+39)/tRBCnorm; %AUC
    % Barrier Membrane
    thnorm = 340;
    thmin = (241-85)/thnorm; %AUC
    thmax = (340+133)/thnorm; %AUC
    % RBC:Barrier ratio
    rbcbarr_norm = 0.41;
    rbcbarr_min = (0.31-0.07)/rbcbarr_norm;
    rbcbarr_max = (0.6)/rbcbarr_norm;
    % values above taken from Figure 5, PMID: 35762891, Persistent 129Xe
    % MRI Pulmonary and CT Vasculat Abnormalities in Symptomatic
    % Individuals with Post-acute COVID-19 Syndrome
    % tRBC_grid = linspace(tRBC_healthy*(1+0.24), tRBC_healthy*(1+0.6), 51);
%Where, tRBC_healthy*(1+0.24) = (1 + RBC:Barrier min ratio) and
tRBC_healthy*(1+0.6) = (1 + RBC:Barrier max ratio) from same paper as above
    % tRBC_grid = linspace(tRBC_healthy*(1+tRBCmin), tRBC_healthy*(1+tRBCmax),
51);
    % tRBC_grid = linspace(tRBC_healthy*rbcbarr_min, tRBC_healthy*rbcbarr_max,
51);
    tRBC_grid = linspace(tRBC_healthy*tRBCmin, tRBC_healthy*tRBCmax, 51);
    th_grid = linspace(th_healthy*thmin, th_healthy*thmax, 51);
    DLCO = NaN(length(th_grid), length(tRBC_grid)); KCO = DLCO;
    % Loop through, calculate values
    for i = 1:length(th_grid)
        for j = 1:length(tRBC_grid)
                [DLCO(i,j), KCO(i,j)] = Simulate_KCOnew(RV, TLC, Va_per, LungVols,
PulmVol, CapVols, D0_base, [th_grid(i), th_grid(i), th_grid(i), th_grid(i)],
th_healthy, [tRBC_grid(j), tRBC_grid(j), tRBC_grid(j), tRBC_grid(j)],
tRBC_healthy);
        end
    end
    % Normalize the results for visualization
    DLCOp = 100 * DLCO / refDLCO;
    KCOp = 100 * KCO / refKCO;
    meanDLCO = mean(DLCOp, 'all');
```

```
    SD_DLCO = std(DLCOp, 0, 'all');
    minDLCO = min(DLCOp, [], 'all');
    maxDLCO = max(DLCOp, [], 'all');
    minrangeDLCO = meanDLCO - 2*SD_DLCO;
    maxrangeDLCO = meanDLCO + 2*SD_DLCO;
    outDLCO = sprintf('DLCO (%% of healthy) ILD - %.0f(%.0f-
%.0f)',meanDLCO,minrangeDLCO,maxrangeDLCO);
    disp(outDLCO)
    meanKCO = mean(KCOp, 'all');
    SD_KCO = std(KCOp, 0, 'all');
    minKCO = min(KCOp, [], 'all');
    maxKCO = max(KCOp, [], 'all');
    minrangeKCO = meanKCO - 2*SD_KCO;
    maxrangeKCO = meanKCO + 2*SD_KCO;
    outKCO = sprintf('KCO (%% of healthy) ILD - %.0f(%.0f-
%.0f)',meanKCO,minrangeKCO,maxrangeKCO);
    disp(outKCO)
    % Create a new figure with specified size
    figure('Position', [100, 100, 1150, 400]);
    % Create contour plot with interp shading, add contour lines, label
    subplot(1,2,1);
    pcolor(th_grid*100/th_healthy, tRBC_grid*100/tRBC_healthy, 100*DLCO'/refDLCO);
shading interp; hold on;
    contour(th_grid*100/th_healthy, tRBC_grid*100/tRBC_healthy, 100*DLCO'/refDLCO,
[50, 70, 90, 110, 130, 150], 'ShowText', true, 'LineWidth', 2, 'Color', [0,0,0]);
hold on;
    colorbar; xlabel('Barrier AUC (% of healthy)'); ylabel('RBC AUC (% of
healthy)'); title('DLCO (% of GLI Input)');
    plot(th_healthy, tRBC_healthy, 'k.', 'MarkerSize', 50); %Plot the reference
value
    M = sprintf('DLCO (%% of healthy) COVID-19 - %.0f(%.0f-
%.0f)',meanDLCO,minDLCO,maxDLCO);
    title(M);
    colormap(hot);
    subplot(1,2,2);
    pcolor(th_grid*100/th_healthy, tRBC_grid*100/tRBC_healthy, 100*KCO'/refKCO);
shading interp; hold on;
    contour(th_grid*100/th_healthy, tRBC_grid*100/tRBC_healthy, 100*KCO'/refKCO,
[50, 70, 90, 110, 130, 150], 'ShowText', true, 'LineWidth', 2, 'Color', [0,0,0]);
hold on;
    colorbar; xlabel('Barrier AUC (% of healthy)'); ylabel('RBC AUC (% of
healthy)'); title('KCO (% of GLI Input)');
    plot(th_healthy, tRBC_healthy, 'k.', 'MarkerSize', 50); %Plot the reference
value
    N = sprintf('KCO (%% of healthy) COVID-19 - %.0f(%.0f-
%.0f)',meanKCO,minKCO,maxKCO);
    title(N);
    colormap(hot);
end
```

7.5 MATLAB code for Figure 20

```
clear; clc; close all;
load DLCO_AgeMspline_Male.mat
load DLCO_AgeMspline_Female.mat
load KCO_AgeMspline_Male.mat
load KCO_AgeMspline_Female.mat
load VA_AgeMspline_Male.mat
load VA_ageMspline_Female.mat
load TLC_Mspline_Male.mat
load TLC_Mspline_Female.mat
load RV_Mspline_Male.mat
load RV_Mspline_Female.mat

std_DLCO = zeros(80,1);
min_DLCO = zeros(80,1);
max_DLCO = zeros(80,1);
mean_DLCO = zeros(80,1);
std_KCO = zeros(80,1);
min_KCO = zeros(80,1);
max_KCO = zeros(80,1);
mean_KCO = zeros(80,1);

sex = 1 ; % 1 = male
H = 1.70; % Height in [m]
A = 20;  % Age in years
% Input number
inputAge = A;
% Array of ages
ageArray = DLCO_AgeMspline_Male(:,2);
% Calculate the absolute differences between the input age and the array
ageDifferences = abs(ageArray - inputAge);
% Find the index of the minimum absolute difference
[~, minIndex] = min(ageDifferences);
% Get the closest age from the array
closestAge = ageArray(minIndex);
row = find(DLCO_AgeMspline_Male(:,2) == closestAge); %find row number where the
closet age reference values are located
% disp(['Closest age: ', num2str(closestAge)]);
if sex == 1 %if patient is male (1)
    MsplineRV_m = RV_Mspline_Male(row,2);
    MsplineTLC_m = TLC_Mspline_Male(row,2);
    RV =  exp(-2.37211+0.01346*A+0.01307*H*100 + MsplineRV_m);
    TLC =  exp(-10.5861+0.1433*log(A)+2.3155*log(H*100) + MsplineTLC_m);
    MsplineDLCO_m = DLCO_AgeMspline_Male(row,3);
    MsplineVA_m = VA_AgeMspline_Male(row,3);
    D0_base = exp(-7.034920+2.018368*log(H*100)-
0.012425*log(A)+MsplineDLCO_m)/1000/60;
    VA = exp(-11.086573+2.430021*log(H*100) + 0.097047*log(A)+MsplineVA_m);
    Va_per = VA/TLC;
else % if patient is female
    MsplineRV_f = RV_Mspline_Female(row,2);
    MsplineTLC_f = TLC_Mspline_Female(row,2);
    RV =  exp(-2.50593+0.01307*A+0.01379*H*100+MsplineRV_f);
    TLC = exp(-10.1128+0.1062*log(A)+2.2259*log(H*100)+MsplineTLC_f);
    MsplineDLCO_f = DLCO_AgeMspline_Female(row,3);
    MsplineVA_f = VA_AgeMspline_Female(row,3);
```

```
    D0_base = exp(-5.159451+1.618697*log(H*100)-
0.015390*log(A)+MsplineDLCO_f)/1000/60;
    VA = exp(-9.873970 + 2.182316*log(H*100) + 0.082868*log(A) + MsplineVA_f);
    Va_per = VA/TLC;
end

RV_per = RV/TLC;
PulmVol = 0.065;
LungVols = [0.23, 0.237, 0.264, 0.269]; % (sitting) Yamada, Yoshitake et al.
"Comparison of inspiratory and expiratory lung and lobe volumes among supine,
standing, and sitting positions using conventional and upright CT." Scientific
reports vol. 10,1 16203. 1 Oct. 2020, doi:10.1038/s41598-020-73240-8
LungVols = LungVols/sum(LungVols);
CapVols = LungVols; %Assumed relative pulmonary blood size (at default is same as
lung lobe size)
LungVols = LungVols(:)/sum(LungVols);
CapVols = CapVols(:)/sum(CapVols);
th_healthy = 0.62;
% th = 0.62;
th = [th_healthy, th_healthy, th_healthy, th_healthy];
tRBC_healthy = 0.45;
tRBC = [tRBC_healthy, tRBC_healthy, tRBC_healthy, tRBC_healthy];

% First we generate a reference value of DLCO and KCO, to compare against
[refDLCO, refKCO] = Simulate_KCOnew(RV, TLC, Va_per, LungVols, PulmVol, CapVols,
D0_base, th, th_healthy, tRBC, tRBC_healthy);
kcodlcoHEALTH = refKCO/refDLCO;
DLCO = zeros(6,1);
KCO = zeros(6,1);
% Va_per = 40:10:100;
Va_per = 0.35:0.01:0.94;
for i = 1:length(Va_per)
[DLCO(i), KCO(i)] = Simulate_KCOnew(RV, TLC, Va_per(i), LungVols, PulmVol,
CapVols, D0_base, th, th_healthy, tRBC, tRBC_healthy);
end

Vap = Va_per/0.94;
% Set the size of the plot
figure('Position', [100, 100, 560, 500]); % Adjust the values as needed
plot(Vap*100, DLCO/DLCO(end)*100,'-k', 'LineWidth', 2)
xlabel('Alveolar volume (VA/VA_T_L_C%)')
ylabel('DLCO as % DLCO at TLC')
% set(gca,'YScale','log')
ylim([50 100])
ax = gca;
ax.YTick = sort([100, 75, 50]);  % Increasing order
ax.YTickLabel = fliplr({'100', '75', '50'});  % Display in decreasing order
% set(gca, 'TickDir', 'out'); % Set tick direction outward
hold on
% figure(2)
yyaxis right
plot(Vap*100, KCO/KCO(end)*100,'--k', 'LineWidth', 2)
xlabel('Alveolar volume (VA/VA_T_L_C%)')
ylabel('KCO as % KCO at TLC')
legend('DLCO (Simulated)','KCO (Simulated)','Location','southeast','FontSize', 12)
ax = gca;
ax.YAxis(1).Color = 'k';
ax.YAxis(2).Color = 'k';
% set(gca,'YScale','log')
```

```
set(gca, 'XDir','reverse')
ylim([100 200])
ax.YTick = sort([200, 175, 150, 125, 100]);  % Increasing order
ax.YTickLabel = fliplr({'200', '175', '150', '125', '100'});  % Display in
decreasing order
% set(gca, 'TickDir', 'out'); % Set tick direction outward
ax.XTick = sort([100, 80, 60, 40]);  % Increasing order
ax.XTickLabel = fliplr({'100', '80', '60', '40'});  % Display in decreasing order
% set(gca, 'TickDir', 'out'); % Set tick direction outward
xlim([40 100])
 DLCOper = DLCO/DLCO(end)*100;
 KCOper = KCO/KCO(end)*100;

hold on
barColor = [0.2, 0.5, 0.8]; % Define your desired color, for example, light blue
% Define the range of x values
x = linspace(40, 100, 60);
% Define the second function
z = 0.43 + 0.57 ./ x * 100; % transforming z or KCO/KCOTLC a ratio, from
percentage by (dividing everything by 100, since our z axis is percentage)
multiplying x or VA/VATLC by 100

% Plot the second function on the left y-axis
yyaxis right;
ax1 = gca;
plot(x, z * 100, '--k', 'LineWidth', 2, 'DisplayName', 'KCO', 'Color',barColor);
ylabel('KCO as % KCO at TLC');
ylim([100 200]); % Set y-axis limits for the left axis

% Set the y-axis color to black
ax1.YColor = 'k';
yticks([100, 125, 150, 175, 200]); % Set custom ticks for the right axis

hold on;
% Plot the product of z-axis and x-axis on the left axis
product = z .* x;
yyaxis left;
ax2 = gca;
plot(x, product, '-k', 'LineWidth', 2, 'DisplayName', 'DLCO', 'Color',barColor);
ylabel('DLCO as % DLCO at TLC');
ylim([50 100]); % Set corrected y-axis limits for the right axis
% Set the y-axis color to black
ax2.YColor = 'k';
yticks([50, 75, 100]); % Set custom ticks for the left axis
% Add labels and title
xlabel('Alveolar volume (VA/VA_T_L_C%)');
% title('Plot of z = 0.43 + 0.57x and z \times x with Reversed X-Axis and Dual Y-
Axes');
set(gca, 'Xdir', 'reverse'); % Reverse the x-axis for the right axis
% Set custom ticks for the x-axis
xticks([40, 60, 80, 100]);
% Add legend
legend('Location', 'southeast','FontSize', 12);
% Show the plot
hold off;
mdldlco = fitlm(product,DLCOper);
R2dlco = mdldlco.Rsquared.Ordinary;
mdlkco = fitlm(z*100,KCOper);
R2kco = mdlkco.Rsquared.Ordinary;
```

8. Appendices - Permissions

Page No.	Type of work:	Name of work	Source of work	Copyright holder and contact	Permission requested on	I have permission yes /no	Permission note
27	Figure	Figure 2	Nunn's Applied Respiratory Physiology	Elsevier	27.06.2025	yes	RightsLink Printable Lisence